

**Computational studies of the interactions of biologically
active peptides with membrane**

Dissertation zur Erlangung des Doktorgrades Dr. rer. nat.

der Fakultät für Mathematik, Informatik und Naturwissenschaften

der Universität Hamburg

vorgelegt von Yana Gofman

Hamburg 2012

Die vorliegende Arbeit wurde von Januar 2008 bis Januar 2012 in der Abteilung Strukturforschung an Makromolekülen im Institut für Werkstoffforschung, Helmholtz-Zentrum Geesthacht unter der Anleitung von Frau Professor Dr. Regine Willumeit angefertigt.

Gutachter der Arbeit:

Prof. Dr. Ulrich Hahn

Prof. Dr. Regine Willumeit

Tag der Disputation: 23.03.2012

Table of contents

Summary	2
Zusammenfassung	3
General Introduction	4
Monte Carlo simulations model	14
Paper I: A combined pulse EPR and Monte Carlo simulation study provides molecular insight on peptide-membrane interactions.	28
Paper II: Interaction of an antimicrobial peptide with membranes: experiments and simulations with NKCS.	29
Paper III: Membrane interactions of novicidin, a novel antimicrobial peptide: phosphatidylglycerol promotes bilayer insertion.	30
Paper IV: W-band pulse EPR distance measurements in peptides using Gd ³⁺ -dipicolinic acid derivatives as spin labels.	31
Paper V: Membrane-integration of a mitochondrial signal-anchored protein does not require additional proteinaceous factors.	32
General Discussion: Limitations and Implications	33
Appendix A: Supplementary Material for Paper I	38
Appendix B: Supporting Material for Paper II	43
Appendix C: Supplementary Material for Paper III	47
Appendix D: Supplementary Material for Paper IV	49
Appendix E: Supplementary Material for Paper V	56
Acknowledgments	60
Declaration of Oath (Eidesstattliche Versicherung)	61
List of Hazardous Substances (Gefahrstoffliste)	62
List of Papers and Contribution	63
Curriculum Vitae	64

Summary

Biological membranes are complex and diverse systems, composed mostly of lipid and protein molecules. The molecules are packed heterogeneously and organized in a fluid mosaic, mutually affecting each other. Complex protein-lipids interactions have been investigated extensively with a wide range of biophysical and computational techniques. However, general principles of folding, energetics, stability and even structure of membrane proteins can be inferred from simpler peptide-membrane interactions. Increasing our understanding of peptide-membrane interactions is beneficial also for deciphering the mechanism of action of membrane-active peptides, such as antimicrobial and viral-fusion peptides.

This thesis includes 5 papers that summarize studies of peptide-membrane systems using a Monte Carlo (MC) simulations model. The simulations successfully reproduced available experimental data; in several cases they assisted in interpretation of the empirical results and guided further experiments. The first four papers of the thesis deal with antimicrobial peptides (AMPs), namely melittin, novicidin and NKCS, derived from natural killer cells. AMPs are found in the immunity system of various species, defending mostly against bacteria. AMPs act directly on the bacterial membrane, engaging a range of mechanisms. In an era in which bacteria acquired resistance to classical antibiotics, AMPs represent a new avenue to explore in the search for antibiotics of different types. The last paper is focused on a mitochondrial protein and elucidates mechanisms of its incorporation into mitochondrial outer membrane (MOM).

Zusammenfassung

Biologische Membranen sind komplex und vielfältig. Sie bestehen aus einer Vielzahl von Lipid- und Proteinmolekülen, die sich gegenseitig beeinflussen. Die komplizierten Protein-Lipid Interaktionen wurden ausgiebig mit einer Vielzahl von biophysikalischen und rechnergestützten Techniken untersucht, ein umfassendes Verständnis der Struktur-Funktionsbeziehung in Membranen ist jedoch bislang nicht erreicht worden. Allerdings können allgemeine Grundsätze der Faltung, der Energetik, der Stabilität und der Struktur von Membranproteinen aus einfacheren Peptid-Membran-Wechselwirkungen abgeleitet werden. Die Verbesserung unseres Verständnisses dieser Wechselwirkungen ist auch für die Entschlüsselung des Wirkmechanismus membranaktiver Peptide von Vorteil, die z. B. antimikrobielle Aktivität besitzen oder zur viralen Verschmelzung mit der Zielzelle benötigt werden.

Die vorliegende Arbeit beinhaltet 5 Publikationen, die Studien der Peptid-Membran-Wechselwirkungen mit Hilfe der Monte Carlo Simulation zusammenfassen. Die Simulationen haben erfolgreich verfügbare experimentelle Daten reproduziert; in einigen Fällen haben sie die Interpretation der empirischen Daten unterstützt und weiterführende Experimente vorhergesagt. Die ersten 4 Publikationen befassen sich mit den antimikrobiellen Peptiden (AMPs). Die *Publikationen I und IV* beschreiben Studien zu Melittin, einem AMP, das aus dem Gift der Honigbiene extrahiert wurde. *Publikation I* erörtert die Konformation und Orientierung des Melittin innerhalb der Lipidmembran; in Veröffentlichung *IV* wurde die Verwendung eines neuartigen Spinlabels zur Strukturbestimmung an Melittin getestet. Die Simulationen dienten dabei zur Erklärung der experimentellen Befunde. In *Publikation II* wird die computergestützte Verbesserung der antimikrobiellen Aktivität von NKCS beschrieben. Die Studien aus *Publikation III* beschreiben den Wirkmechanismus des Novicidin, das eine vorteilhafte Kombination aus effektiver antimikrobieller und niedriger hämolytischer Aktivität besitzt. Die letzte Publikation konzentriert sich auf ein mitochondriales Protein und seinen Einbau in die Mitochondrienmembran.

General Introduction

Biological membranes preserve the integrity of cells and organelles and act as physical barrier between the interior and external environment. Phospholipids and membrane proteins are the main components of biological membranes. In common cartoonish drawing of this architecture the bilayer is represented by two parallel lines, with ellipsoidal membrane proteins embedded in it. Clearly, this simplistic presentation is misleading and does not reflect the complexity, diversity and dynamics of the system. The “fluid mosaic model” presents a more realistic description of the system (1), with alternating membrane proteins, peripheral and integral, and lipid molecules of numerous and diverse types. The distribution of lipids and proteins is asymmetric, both laterally and between the two layers of the membrane, further adding to the heterogeneity and complexity of the system. Overall, biological membranes are, essentially, ensemble of enormous number of diverse components packed together. Inevitable preference between the various molecule types (2) can result in formation of so called lipids domains, or rafts; they usually have functional implications, for instance in cells division (3). Another outcome of the complex membrane architecture is mutual interaction of membrane proteins and lipids.

Membrane proteins exhibit one of two possible folds: β -barrels and bundles of α -helices (4). The formers are found only in the mitochondria, chloroplasts and Gram-negative bacteria outer membranes. Here I focus on α -helical proteins, which are widespread and much more common. Specifically, I focus on α -helical peptides and their interaction with lipids. In general, peptides are often utilized to study proteins-lipids interactions. Peptides can mimic the interaction of peripheral and transmembrane (TM) proteins with the membrane and, therefore, are used as simpler systems to study folding and insertion of larger membrane proteins into the hydrophobic

environment of lipids bilayer (5, 6). Moreover, the strategy of structure prediction of distinct TM segments is frequently taken, since the determination of whole TM proteins structure still is a complicated task (7, 8).

Several computational approaches are commonly applied for investigation of protein- and peptide-lipids interactions. The highest resolution method is molecular dynamics (MD) simulations, in which the molecules are described in atomic detail. MD provides detailed insights into the interactions, including the making and breaking of hydrogen bonds and salt bridges. However, this method has a limited simulations time scale and thus questionable ability to imitate biological processes. Still, MD simulations were effectively used to investigate many membrane-protein systems (9-11), as well as interactions of AMPs with membranes (12-14). Course-grained simulations employ similar approach as does MD, but groups of real atoms are represented as a single virtual particle, and the particles are connected by artificial bonds. Clearly, this leads to substantial speedup compared to atomistic simulations (15, 16). Additional approach is known as continuum solvent models, where the protein is described in atomic details, but the solvent (membrane and water) is presented as continuum environment with certain dielectric constant (17). The protein is treated as a rigid body; therefore, this approach is unable to elucidate the dynamics of peptides- and protein-lipids interactions and cannot trace conformational changes in the peptide/protein upon interaction with the membrane.

Monte-Carlo (MC) simulations have been previously demonstrated as an important tool in investigations of peptide-membrane interactions (18-26). Typically, the MC methods are based on a reduced representation of both peptides and membranes. As a result, the simulations do not provide atomistic details of the interaction, but allow comprehensive sampling of peptide's conformations and locations in the membrane. In this thesis the existing model of MC

simulations was utilized in order to investigate hydrophobic mismatch and α -helical AMPs. The model, described in details in the chapter “Monte Carlo simulations model”, was previously calibrated and tested on α -helical peptides, such as Magainin2, penetratine (26) and the M2 δ peptide, a TM segment from the acetylcholine receptor δ -subunit (25). The simulations successfully reproduced available empiric data and provided new insights on peptides-lipids interactions (25-27).

Antimicrobial peptides (AMPs)

Natural AMPs are part of the innate immunity system of a wide range of species including insects, amphibians, mammals and plants (28-30). These ubiquitously expressed peptides provide the first line of defense against various pathogens, including bacteria. AMPs share certain characteristics, like amphipathicity and overall positive charge that determines the selectivity of these peptides towards negatively charged bacterial cytoplasmic membrane (29). Acquired resistance of pathogenic bacteria to classical antibiotics is an increasing and still unsolved problem in health care, and AMPs are suggested as possible candidates to substitute the existing generation of antibiotics. Additional interest of the scientific community to AMPs is triggered also by their reported tumoricidal properties (31).

Although it is demonstrated that antimicrobial peptides act by direct destabilization of the bacterial membrane (28, 31-34), their precise mechanism of action is yet to be discovered. Various models of AMPs' mechanism of action have been described so far (31-35). In the carpet model, peptides bind to the phospholipid head groups in parallel to the membrane surface in a carpet-like fashion until a critical threshold concentration is reached. In the barrel-stave model,

peptides adopt TM conformation and form pores with their hydrophobic faces oriented towards the lipids and their hydrophilic faces oriented towards each other, i.e. pore funnel. In the toroidal pore model, peptides induce curvature in the membrane and the pore is lined with both peptides and lipids. The detergent-like model proposes that peptides intercalate in between the phospholipid head groups causing curvature strain and micellization at local regions of high peptides density. AMPs can display various mechanisms of action depending on the lipids composition and phase, peptide/lipid ratio and ionic strength of the solution (31-35). The action mechanism of AMPs depends also on their physicochemical properties, for instance hydrophobicity and charge distribution along the peptide sequence and structure.

Papers I and IV summarize studies of melittin, one of the most studied representatives of linear α -helical AMPs (36-38). This peptide is the principal toxic component of the venom of the honey bee (*Apis mellifera*) and is known for its strong cytolytic and antimicrobial activities. Melittin is composed of 26 amino acid residues (GIGAVLKVLTTGLPALISWIKRKRQQ) and includes both polar/charged and hydrophobic residues. Melittin, which is mostly a random coil in aqueous solutions, adopts an α -helical conformation with a kink in the middle upon interaction with the membrane (39). *Paper I* is dedicated to the conformation and orientation of melittin within lipids. The simulations correlated well with the results obtained via electron paramagnetic resonance (EPR) spectroscopy and guided further experiments (40). *Paper IV* describes tests of a new peptides label for EPR experiments. The label was tested on melittin in the aqueous phase, and the MC simulations were used as a ruler to verify the experimental data. Both works were performed in collaboration with Prof. Goldfarb's lab (The Weizmann Institute, Israel).

Paper II describes a work that was aimed to investigate the antimicrobial activity of NKCS derivatives. NKCS is an AMP derived from NK-lysin, a protein found in natural killer cells (NK-

cells) of the pig small intestine (41). Another derivative of NK-lysin, namely NK-2, was found effective against Gram-negative and Gram-positive bacteria (42, 43), yeasts (42), protozoan parasites (44) and also some cancer lines (45). In addition, NK-2 exhibited very low hemolytic activity and cytotoxicity against human cell lines (44). The replacement of a cysteine residue within the NK-2 sequence with a serine (C7S) resulted in NKCS, a peptide with an improved antibacterial activity relatively to NK-2. MC simulations of NKCS and its mutant variants were executed intending to improve its antimicrobial effect. The results were verified using small angle x-ray scattering, surface plasmon resonance and measurements of the antibacterial and hemolytic activity in cells. Circular dichroism (CD) spectroscopy was employed to estimate the peptides' helicity.

Paper III elaborates on the mechanism of action of novicidin, another AMP derived from the N-terminus of SMAP-29. The latter is from the cathelicidin family found in sheep (46, 47). Novicidin contains 18 residues (KNLRRRIIRKGIHIKKYF) and displays a favorable combination of effective antimicrobial activity and low hemolytic properties. While melittin's mechanism of action has been studied extensively (36), the interaction mode of novicidin was not known. To elucidate the mechanism of action, novicidin was simulated in membranes with various lipid compositions in terms of the fraction of charged and zwitterionic lipids. The data indicated that novicidin interacted marginally with zwitterionic bilayers, accounting for its low hemolytic activity. Negatively charged lipids, on the other hand, significantly increased the membrane-affinity of novicidin. The simulations results were accompanied by an array of biophysical techniques and biomimetic membrane assemblies performed in Prof. Jelinek's lab (Ben-Gurion University, Israel).

Proteins translocation into the mitochondrial outer membrane

Mitochondria are essential organelles of the eukaryotic cells. They produce the cells' main energy source adenosine triphosphate ATP (48). Mitochondria are made up of two membranes, the outer (MOM) and the inner (MIM) mitochondrial membrane. Proteins residing in the MOM mediate the interactions between the organelle and the rest of the cell. All these proteins are encoded in the nucleus and synthesized in the cytosol; their trafficking to the mitochondria is governed by the presence of various mitochondrial targeting signals (49). The translocation pathways into the MOM are diverse and vary between different proteins classes (reviewed in (49)). For instance, β -barrel proteins, unique to the mitochondria and chloroplasts, require the famous complex called the translocase of the outer mitochondrial (TOM). Several groups all over the world study the processes associated with proteins translocation to (and across) the MOM (49, 50).

In addition to the fascinating β -barrel proteins, α -helical proteins also reside in the MOM. Specifically, the so called signal-anchored proteins share a TM hydrophobic segment at the N-terminus that serves also as a mitochondrial targeting signal. The mechanism of their insertion into the MOM is not established. It was previously demonstrated that signal-anchored proteins do not require the TOM complex (51-53). However, possible involvement of another MOM protein, known or not, cannot be ruled out. In order to elucidate the mechanism of insertion of signal-anchored proteins into MOM, MC simulations of OM45, chosen as a model protein, were performed in bilayer mimicking the MOM. The results, together with plenty of experimental findings, suggest that signal-anchored proteins can be inserted into the MOM in a process that depends on the unique lipid composition of this membrane but is independent of additional

proteins. This project was performed in collaboration with lab of Prof. Rapaport (University of Tübingen, Germany). *Paper V* summarizes the details of the study.

References

1. Singer, S. J., and G. L. Nicolson. 1972. The fluid mosaic model of the structure of cell membranes. *Science* 175:720-731.
2. Engelman, D. M. 2005. Membranes are more mosaic than fluid. *Nature* 438:578-580.
3. Mukherjee, S., and F. R. Maxfield. 2004. Membrane domains. *Annu Rev Cell Dev Biol* 20:839-866.
4. Schushan, M., and N. Ben-Tal. 2010. Modeling and Validation of Transmembrane Protein Structures. In *Introduction to Protein Structure Prediction*. John Wiley & Sons, Inc. 369-401.
5. Hessa, T., H. Kim, K. Bihlmaier, C. Lundin, J. Boekel, H. Andersson, I. Nilsson, S. H. White, and G. von Heijne. 2005. Recognition of transmembrane helices by the endoplasmic reticulum translocon. *Nature* 433:377-381.
6. White, S. H., and G. von Heijne. 2008. How translocons select transmembrane helices. *Annu Rev Biophys* 37:23-42.
7. Lee, B. L., X. Li, Y. Liu, B. D. Sykes, and L. Fliegel. 2009. Structural and functional analysis of transmembrane XI of the NHE1 isoform of the Na⁺/H⁺ exchanger. *J Biol Chem* 284:11546-11556.
8. Reddy, T., X. Li, L. Fliegel, B. D. Sykes, and J. K. Rainey. 2010. Correlating structure, dynamics, and function in transmembrane segment VII of the Na⁺/H⁺ exchanger isoform 1. *Biochim Biophys Acta* 1798:94-104.
9. Gumbart, J., Y. Wang, A. Aksimentiev, E. Tajkhorshid, and K. Schulten. 2005. Molecular dynamics simulations of proteins in lipid bilayers. *Curr Opin Struct Biol* 15:423-431.
10. Roux, B., and K. Schulten. 2004. Computational studies of membrane channels. *Structure* 12:1343-1351.
11. Khalili-Araghi, F., J. Gumbart, P. C. Wen, M. Sotomayor, E. Tajkhorshid, and K. Schulten. 2009. Molecular dynamics simulations of membrane channels and transporters. *Curr Opin Struct Biol* 19:128-137.
12. Bond, P. J., and S. Khalid. 2010. Antimicrobial and cell-penetrating peptides: structure, assembly and mechanisms of membrane lysis via atomistic and coarse-grained molecular dynamics simulations. *Protein Pept Lett* 17:1313-1327.
13. Bolintineanu, D. S., and Y. N. Kaznessis. 2011. Computational studies of protegrin antimicrobial peptides: a review. *Peptides* 32:188-201.
14. Tieleman, D. P., and M. S. P. Sansom. 2001. Molecular dynamics simulations of antimicrobial peptides: From membrane binding to trans-membrane channels. *International Journal of Quantum Chemistry* 83:166-179.
15. Lindahl, E., and M. S. Sansom. 2008. Membrane proteins: molecular dynamics simulations. *Curr Opin Struct Biol* 18:425-431.

16. Sansom, M. S., K. A. Scott, and P. J. Bond. 2008. Coarse-grained simulation: a high-throughput computational approach to membrane proteins. *Biochem Soc Trans* 36:27-32.
17. Feig, M. 2008. Implicit Membrane Models for Membrane Protein Simulation. In *Molecular Modeling of Proteins*. 181-196.
18. Milik, M., and J. Skolnick. 1993. Insertion of peptide chains into lipid membranes: an off-lattice Monte Carlo dynamics model. *Proteins* 15:10-25.
19. Milik, M., and J. Skolnick. 1995. A Monte Carlo model of fd and Pf1 coat proteins in lipid membranes. *Biophys J* 69:1382-1386.
20. Baumgartner, A. 1996. Insertion and hairpin formation of membrane proteins: a Monte Carlo study. *Biophys J* 71:1248-1255.
21. Efremov, R. G., D. E. Nolde, G. Vergoten, and A. S. Arseniev. 1999. A solvent model for simulations of peptides in bilayers. II. Membrane-spanning alpha-helices. *Biophys J* 76:2460-2471.
22. Efremov, R. G., D. E. Nolde, G. Vergoten, and A. S. Arseniev. 1999. A solvent model for simulations of peptides in bilayers. I. Membrane-promoting alpha-helix formation. *Biophys J* 76:2448-2459.
23. Ducarme, P., M. Rahman, and R. Brasseur. 1998. IMPALA: a simple restraint field to simulate the biological membrane in molecular structure studies. *Proteins* 30:357-371.
24. Maddox, M. W., and M. L. Longo. 2002. A Monte Carlo study of peptide insertion into lipid bilayers: equilibrium conformations and insertion mechanisms. *Biophys J* 82:244-263.
25. Kessel, A., D. Shental-Bechor, T. Haliloglu, and N. Ben-Tal. 2003. Interactions of hydrophobic peptides with lipid bilayers: Monte Carlo simulations with M2delta. *Biophys J* 85:3431-3444.
26. Shental-Bechor, D., T. Haliloglu, and N. Ben-Tal. 2007. Interactions of cationic-hydrophobic peptides with lipid bilayers: a Monte Carlo simulation method. *Biophys J* 93:1858-1871.
27. Shental-Bechor, D., S. Kirca, N. Ben-Tal, and T. Haliloglu. 2005. Monte Carlo studies of folding, dynamics, and stability in alpha-helices. *Biophys J* 88:2391-2402.
28. Tossi, A., L. Sandri, and A. Giangaspero. 2000. Amphipathic, alpha-helical antimicrobial peptides. *Biopolymers* 55:4-30.
29. Zasloff, M. 2002. Antimicrobial peptides of multicellular organisms. *Nature* 415:389-395.
30. Bulet, P., R. Stocklin, and L. Menin. 2004. Anti-microbial peptides: from invertebrates to vertebrates. *Immunol Rev* 198:169-184.
31. Hoskin, D. W., and A. Ramamoorthy. 2008. Studies on anticancer activities of antimicrobial peptides. *Biochim Biophys Acta* 1778:357-375.
32. Oren, Z., and Y. Shai. 1998. Mode of action of linear amphipathic alpha-helical antimicrobial peptides. *Biopolymers* 47:451-463.
33. Shai, Y., and Z. Oren. 2001. From "carpet" mechanism to de-novo designed diastereomeric cell-selective antimicrobial peptides. *Peptides* 22:1629-1641.
34. Bechinger, B., and K. Lohner. 2006. Detergent-like actions of linear amphipathic cationic antimicrobial peptides. *Biochim Biophys Acta* 1758:1529-1539.
35. Matsuzaki, K., K. Sugishita, N. Ishibe, M. Ueha, S. Nakata, K. Miyajima, and R. M. Epand. 1998. Relationship of membrane curvature to the formation of pores by magainin 2. *Biochemistry* 37:11856-11863.

36. Raghuraman, H., and A. Chattopadhyay. 2007. Melittin: a membrane-active peptide with diverse functions. *Biosci Rep* 27:189-223.
37. Habermann, E. 1972. Bee and wasp venoms. *Science* 177:314-322.
38. Dempsey, C. E. 1990. The actions of melittin on membranes. *Biochim Biophys Acta* 1031:143-161.
39. Brown, L. R., W. Braun, A. Kumar, and K. Wuthrich. 1982. High resolution nuclear magnetic resonance studies of the conformation and orientation of melittin bound to a lipid-water interface. *Biophys J* 37:319-328.
40. Gordon-Grossman, M., Y. Gofman, H. Zimmermann, V. Frydman, Y. Shai, N. Ben-Tal, and D. Goldfarb. 2009. A combined pulse EPR and Monte Carlo simulation study provides molecular insight on peptide-membrane interactions. *J Phys Chem B* 113:12687-12695.
41. Andersson, M., H. Gunne, B. Agerberth, A. Boman, T. Bergman, R. Sillard, H. Jornvall, V. Mutt, B. Olsson, H. Wigzell, and et al. 1995. NK-lysin, a novel effector peptide of cytotoxic T and NK cells. Structure and cDNA cloning of the porcine form, induction by interleukin 2, antibacterial and antitumour activity. *EMBO J* 14:1615-1625.
42. Andra, J., and M. Leippe. 1999. Candidacidal activity of shortened synthetic analogs of amoebapores and NK-lysin. *Med Microbiol Immunol* 188:117-124.
43. Andra, J., D. Monreal, G. Martinez de Tejada, C. Olak, G. Brezesinski, S. S. Gomez, T. Goldmann, R. Bartels, K. Brandenburg, and I. Moriyon. 2007. Rationale for the design of shortened derivatives of the NK-lysin-derived antimicrobial peptide NK-2 with improved activity against Gram-negative pathogens. *J Biol Chem* 282:14719-14728.
44. Jacobs, T., H. Bruhn, I. Gaworski, B. Fleischer, and M. Leippe. 2003. NK-lysin and its shortened analog NK-2 exhibit potent activities against *Trypanosoma cruzi*. *Antimicrob Agents Chemother* 47:607-613.
45. Schroder-Borm, H., R. Willumeit, K. Brandenburg, and J. Andra. 2003. Molecular basis for membrane selectivity of NK-2, a potent peptide antibiotic derived from NK-lysin. *Biochim Biophys Acta* 1612:164-171.
46. Sawai, M. V., A. J. Waring, W. R. Kearney, P. B. McCray, Jr., W. R. Forsyth, R. I. Lehrer, and B. F. Tack. 2002. Impact of single-residue mutations on the structure and function of ovispirin/novispirin antimicrobial peptides. *Protein Eng* 15:225-232.
47. Wimmer, R., K. K. Andersen, B. Vad, M. Davidsen, S. Molgaard, L. W. Nesgaard, H. H. Kristensen, and D. E. Otzen. 2006. Versatile interactions of the antimicrobial peptide novispirin with detergents and lipids. *Biochemistry* 45:481-497.
48. Newmeyer, D. D., and S. Ferguson-Miller. 2003. Mitochondria: releasing power for life and unleashing the machineries of death. *Cell* 112:481-490.
49. Neupert, W., and J. M. Herrmann. 2007. Translocation of proteins into mitochondria. *Annu Rev Biochem* 76:723-749.
50. Mokranjac, D., and W. Neupert. 2009. Thirty years of protein translocation into mitochondria: unexpectedly complex and still puzzling. *Biochim Biophys Acta* 1793:33-41.
51. Schlossmann, J., and W. Neupert. 1995. Assembly of the preprotein receptor MOM72/MAS70 into the protein import complex of the outer membrane of mitochondria. *J Biol Chem* 270:27116-27121.

52. Ahting, U., T. Waizenegger, W. Neupert, and D. Rapaport. 2005. Signal-anchored proteins follow a unique insertion pathway into the outer membrane of mitochondria. *J Biol Chem* 280:48-53.
53. Meineke, B., G. Engl, C. Kemper, A. Vasiljev-Neumeyer, H. Paulitschke, and D. Rapaport. 2008. The outer membrane form of the mitochondrial protein Mcr1 follows a TOM-independent membrane insertion pathway. *FEBS Lett* 582:855-860.

Monte Carlo simulations model

This chapter summarizes the MC model that was introduced in references (1, 2) and exploited in my thesis.

Peptide representation

Each residue i is represented by two interaction sites corresponding to its α -carbon atom (C_i^α) and its side chain interaction center S_i (Fig. 1) (1). The latter were previously selected on the basis of the structure and energy characteristics of the amino acids (3). The peptide backbone was represented by virtual bonds connecting consecutive α -carbon atoms, as proposed by Flory and colleagues (4); a peptide of n residues has $N-1$ virtual bonds. Virtual bonds are highly stiff and were taken here as fixed at their equilibrium values of $3.81 \pm 0.03 \text{ \AA}$. The peptide backbone conformation was defined by the $2N-5$ dimensional vector $[\theta_2, \theta_3, \dots, \theta_{n-1}, \varphi_3, \varphi_4, \dots, \varphi_{N-1}]$ including $n-2$ virtual bond angles (θ_i) and $n-3$ dihedral angles (φ_i). The distance between S_i and C_i^α as well as θ_i^S , were fixed at their equilibrium values. Thus, the conformation of side chain i was expressed by the torsion angle (φ_i^S).

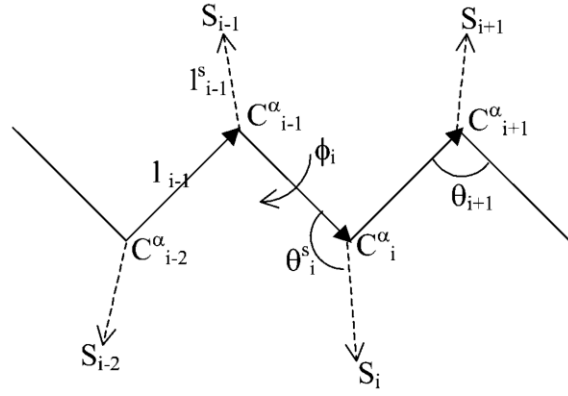


Figure 1. Schematic representation of the virtual bond model. A segment between backbone units C_{i-2}^{α} and C_{i+1}^{α} is shown. The site attached to the i^{th} α -carbon is marked as S_i . ϕ_i is the rotational angle of i^{th} virtual bond, connecting C_i^{α} and C_{i-1}^{α} . θ_i is the bond angle between virtual bonds i and $i+1$. θ_i^S is the side chain virtual bond vector pointing from C_i^{α} to S_i . ϕ_i^S is defined by C_{i-2}^{α} , C_{i-1}^{α} , C_i^{α} and S_i .

Membrane representation

The membrane was described using two parameters: hydrophobicity and surface charge. The hydrophobicity of the membrane (p) was proportional to the distance (z) between the interaction site and the bilayer midplane using a sigmoidal function:

$$p(z) = \frac{1}{1 + \exp(\eta(|z| - z_m))} \quad (1)$$

Where η determined the sharpness of the hydrophobicity profile and was previously set to $\eta = 1 \text{ \AA}^{-1}$ (1), and z_m represented the width of the hydrophobic region of a membrane monolayer. Fig. 2 shows a representative hydrophobicity profile of a membrane with $z_m = 15 \text{ \AA}$. The surface charge was located $(z_m + 5) \text{ \AA}$ from the membrane midplane.

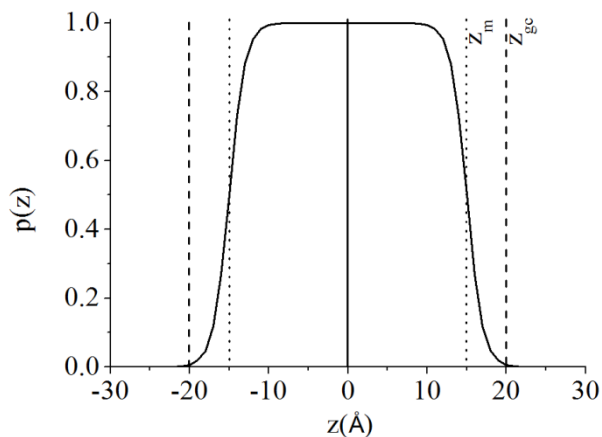


Figure 2. Membrane representation. $p(z)$ was calculated using Eq.1, with $z_m=15\text{\AA}$ and $\eta=1\text{\AA}^{-1}$ (solid line). The location of the surface charge is designated by the dashed lines; the hydrophobic region of the membrane is defined by the dotted lines.

Calculation of ΔG_{total}

The total free energy difference between a peptide in the aqueous phase and in the membrane (ΔG_{total}) can be divided into several terms as follows (5, 6):

$$\Delta G_{\text{total}} = \Delta G_{\text{con}} + \Delta G_{\text{def}} + \Delta G_{\text{Coul}} + \Delta G_{\text{sol}} + \Delta G_{\text{imm}} + \Delta G_{\text{lip}} \quad (2)$$

Calculation of ΔG_{con}

ΔG_{con} is the free energy change due to membrane-induced conformational changes in the peptide. At constant (absolute) temperature, T, it can be calculated as follows:

$$\Delta G_{\text{con}} = \Delta E - T\Delta S \quad (3)$$

where ΔE is the internal energy difference between the water- and membrane-bound states of the peptide. The internal energy is derived from a statistical potential based on

available 3-dimensional (3D) protein structures (3, 7). The energy function assigns a score (energy) to each peptide conformation according to the conformation's abundance in the Protein Data Bank (PDB). Common conformations are assigned high scores (low energy), while rare conformations are assigned lower scores (higher energy).

ΔS refers to the entropy difference between the water and membrane-bound states, while the entropy (S) in each state is determined by the distribution of the virtual bond rotations in the reduced peptide representation. To this end, the rotation space of each virtual bond was divided into 72 discrete intervals of 5° each. The entropy was estimated using the familiar “ $P \ln P$ ” relation:

$$S = \sum_{j=3}^{n-2} \sum_{i=1}^{72} P_{i,j} \ln(P_{i,j}) \quad (4)$$

Where $p_{i,j}$ is the probability of virtual bond j to be in the interval i . As the virtual bond rotations for the first and last two amino acids are not defined, these are omitted from the entropy calculation. The value of $p_{i,j}$ was estimated as

$$P_{i,j} = \frac{n_{i,j}}{N} \quad (5)$$

Where $n_{i,j}$ is the fraction of conformations out of the total number of conformations N in which a virtual bond j is in the interval i .

Calculation of ΔG_{def}

ΔG_{def} is the free energy penalty associated with fluctuations of the membrane width around its resting (native) value. Insertion of a rigid hydrophobic inclusion into a lipid bilayer may result in a deformation of the lipid bilayer to match the width of the

hydrocarbon region to the hydrophobic length of the inclusion, following the mattress model (8). The deformation involves a free energy penalty, ΔG_{def} , resulting from the compression or expansion of the lipid chains. ΔG_{def} has been calculated for lipid bilayers composed of lipids of various types using different methods and yielding similar values (8-14). For the MC model, the estimation of Fattal and Ben-Shaul (9) was chosen to estimate ΔG_{def} . Their calculations were based on a statistical-thermodynamic molecular model of the lipid chains and the fit of harmonic potential of the following form:

$$\Delta G_{\text{def}} = \omega (z_m - z_0)^2 \quad (6)$$

z_m and z_0 are the actual and native widths of a monolayer. ω is a harmonic force constant related to the membrane elasticity and is equal to $\omega = 0.22 \text{ kT}/\text{\AA}^2$ (9).

Calculation of ΔG_{coul}

ΔG_{Coul} stands for the Coulombic interactions between titratable residues of the peptide and the (negative) surface charge of the membrane. It is calculated using the Gouy-Chapman theory that describes how the electrostatic potential φ (measured in units of $k_B T/e$, where k_B is Boltzmann constant, T is the temperature, and e is electron charge) depends on the distance from the membrane surface in an electrolyte solution (15). To this end, the solution was considered neutral, containing monovalent salt. The protonation state of the side chains of the titratable residues in the solution is set according to $\text{pH} = 7$.

$$\varphi(z) = 2 \ln \frac{1 + \tanh(\Phi/4) \exp(\kappa(|z| - z_{GC}))}{1 - \tanh(\Phi/4) \exp(\kappa(|z| - z_{GC}))} \quad (7)$$

Where κ is the inverse of Debye length:

$$\kappa = \sqrt{\frac{2e^2 c^b}{k_B T \epsilon_0 \epsilon_r}} \quad (8)$$

c^b is the number of monovalent anions per unit volume in bulk, ϵ_0 is the permittivity in vacuum and ϵ_r is the dielectric constant in water (taken as 80). Φ is the potential on the plane of smeared charges; it depends on the charge density of the membrane σ and on the molarity of the solution $[K^+]$:

$$\sinh\left(\frac{\Phi}{2}\right) = \frac{\sigma}{\sqrt{8\epsilon_0 \epsilon_r k_B T N_A [K^+]}} \quad (9)$$

N_A is Avogadro number. σ was determined using the fraction of anionic lipids in the membrane f_a , valence of the lipids' charge Z and area occupied by one phospholipid in membrane A :

$$\sigma = \frac{f_a e Z}{A} \quad (10)$$

A titratable residue interacts Coulombically with the charged membrane only when the residue is in its charged form. However, due to the large desolvation free energy penalty associated with the transfer of a charge into hydrophobic environment, titratable residues typically are neutralized when approaching the nonpolar environment of the membrane. Therefore, the dependence of the charged state fraction of titratable residue i on its distance from the membrane midplane was arbitrarily described with a sigmoidal function $\chi_i(z)$, similar to the membrane polarity profile $p(z)$ in Eq. 1:

$$\chi_i(z) = 1 - \frac{1}{1 + \exp(\eta(|z| - h))} \quad (11)$$

Where η is the profile steepness, previously calibrated to 1 (2), and h is the distance between the membrane midplane and the torque point of the sigmoidal function, equals to

$(z_0-2)\text{\AA}$ (2). The electrostatic energy of interaction between titratable residue i and the charged membrane surface weighted by $\chi_i(z)$ could be calculated:

$$\begin{cases} \varphi_{-w_i}(z) = \varphi(z)\chi_i(z) \text{ when } |z| \geq z_{GC} \\ \varphi_{-w_i}(z) = \Phi\chi_i(z) \text{ when } |z| < z_{GC} \end{cases} \quad (12)$$

The energy of the electrostatic interaction of the whole peptide with the membrane was:

$$\Delta G_{coul} = \sum_1^i \varphi_{-w_i}(z)q_i \quad (13)$$

A full positive charge was assigned to the side-chain interaction site of Lys, Arg and to the α -carbon of the N-terminal. A full negative charge was assigned to the side-chain interaction site of Asp and Glu and the α -carbon of an unamidated C-terminal.

Calculation of ΔG_{sol} , ΔG_{imm} and ΔG_{lip}

ΔG_{sol} is the free energy of transfer of the peptide from water to the membrane. It accounts for electrostatic contributions resulting from changes in solvent polarity, as well as for nonpolar (hydrophobic) effects, which result both from differences in the van der Waals interactions of the peptide with the membrane and aqueous phases, and from solvent structure effects. ΔG_{imm} is the free energy penalty resulting from the confinement of the external translational and rotational motion of the peptide inside the membrane. ΔG_{lip} is the free energy penalty resulting from the interference of the peptide with the conformational freedom of the aliphatic chains of the lipids in the bilayer while the membrane retains its native width.

The sum of ΔG_{sol} , ΔG_{imm} and ΔG_{lip} is marked as ΔG_{SIL} , and in the MC simulations it is calculated by summing over the contributions of the individual amino acids. The free

energy of transfer of a specific residue i , i.e. $\Delta g_{SIL_i}(z)$, can be decomposed into contributions from its backbone Δg_{SIL}^b and side chain Δg_{SIL}^s . Thus, ΔG_{SIL} can be determined:

$$\Delta G_{SIL} = \sum_i p_i^b(z) \Delta g_i^b + p_i^s(z) \Delta g_i^s \quad (14)$$

The prefactors (p_i^b and p_i^s) in both terms represent the hydrophobicity of the environment at the interaction site, either α -carbon or side chain interaction center S_i . They are calculated according to Eq. 1.

Δg_i^s were calculated using the Kessel and Ben-Tal hydrophobicity scale (Table 1) (5). The scale accounts for the free energy of transfer of the amino acids, located in the center of a polyalanine α -helix, from the aqueous phase into the membrane midplane. In order to avoid the excessive penalty associated with the transfer of charged residues into the bilayer, in the model the titratable residues are neutralized gradually upon insertion into the membrane, so that a nearly neutral form is desolvated into the hydrophobic core. However, as described above, a gradual transition between the charged and neutral forms of titratable residues based on $\chi_i(z)$ (Eq.11) was introduced into the model. Therefore, for the neutral state of a titratable residue Δg_i^s was derived from the hydrophobicity scale (Table 1); for the charged state of a titratable residue Δg_i^s was taken as 64 kT (16):

$$\Delta g_{i-w}(z) = 64\chi_i(z)p_i^{crg}(z) + \Delta g_i(1 - \chi_i(z))p_i^{crg}(z) \quad (15)$$

$p_i^{crg}(z)$ is the polarity profile of the charged side chains solvation, a sigmoidal function similar to the hydrophobicity profile (Eq. 1):

$$p_i^{crg}(z) = \frac{1}{1 + \exp(\eta(|z| - h))} \quad (16)$$

The free energy of transfer of the peptide backbone from the aqueous phase into the membrane Δg_i^b was calculated using the following set of equations:

$$\begin{cases} \Delta g_i^b = \Delta g_i^{N-H} + f \times \Delta g_i^{C=O} & (i = 1, 2, 3) \\ \Delta g_i^b = f \times (\Delta g_i^{N-H} + \Delta g_i^{C=O}) & (i = 4, 5, \dots, n - 3) \\ \Delta g_i^b = \Delta g_i^{C=O} + f \times \Delta g_i^{N-H} & (i = n - 2, n - 1, n) \end{cases} \quad (17)$$

Where f is proportional to backbone deviations from the optimal α -helical conformation as observed by Bahar and Jernigan (3). It was assigned a value of zero for residues in their ideal α -helical conformations obtained at $\varphi_0 = -120^\circ$ (7); for these residues, the C=O and N-H backbone groups neutralized each other. The value of 1 was assigned to f for residues deviating significantly from the ideal α -helical conformation, e.g., residues that are in extended conformations. For these residues the free-energy penalty due to the transfer of both the C=O and N-H backbone groups are taken into account:

$$f = \frac{1}{2(2 - \exp((-1/\lambda^2)(\phi_i^- - \phi_0)^2) - \exp((-1/\lambda^2)(\phi_i^+ - \phi_0)^2))} \quad (18)$$

Obviously, the presence of Eq. 18 in the potential strongly enhances the formation of helical structures upon membrane association. γ is the standard deviation of the distribution of φ around its optimal value characterizing α -helical conformations, estimated as $\lambda = 30^\circ$ (7).

It is noteworthy that the stretches of three residues at the N- and C-termini were treated differently than the peptide core (Eq. 17). The free energy penalty associated with the transfer of the uncompensated hydrogen bonds of the N-H groups of the three residues at the N-terminal was taken into account regardless of the peptide conformation. Likewise, the free energy penalty due to the transfer of the uncompensated hydrogen bonds of the

C=O groups of the three residues at the C-terminal was also taken into account, regardless of the peptide conformation.

Amino acid	ΔG_i (kcal/mol)
I	-2.6
L	-2.6
F	-1.5
V	-1.2
A	-0.2
G	0.0
C	+0.4
S	+0.8
T	+1.1
M	+1.3
W	+1.3
P	+2.8
Y	+4.3
Q	+5.4
H	+6.8
K	+7.4
N	+7.7
E	+9.5
D	+11.5
R	+19.8
N-H	+1.8
C=O	+2.5

Table 1. A hydrophobicity scale representing free energies of transfer of each of the 20 amino acids from water into the center of the hydrocarbon region of a model lipid bilayer (Δg_i). The scale was computationally derived, as described in Kessel and Ben-Tal (2002) (5). The amino acid residues are presented using a single letter code. The values include the free-energy penalty due to the transfer of the backbone hydrogen bond from water into the membrane. The last two rows present an extra free-energy penalty associated with the transfer of unsatisfied backbone N-H and C=O hydrogen bonds from water to the membrane.

Generation of conformations

New conformations were generated by simultaneous random perturbations of φ_i , θ_i , φ_i^s :

$$\Delta(\varphi_i, \theta_i, \varphi_i^s) = \delta k(2r - 1) \quad (19)$$

Where r is a random number between 0 and 1; δk is the maximum variation of the respective coordinates: 3° for φ_i and 0.5° for θ_i and φ_i^s .

The peptide configuration was changed by external motions as described below. However, it is noteworthy that a set of randomly chosen conformational changes could also lead to slight changes in the peptide's orientation in the membrane.

Generation of configurations

External rigid body rotational and translational motions were carried out to change the peptide's configuration, i.e. its location in, and orientation with respect to, the membrane.

These motions were employed respectively as

$$\begin{cases} \alpha_{new} = \alpha_{old} + 2(r - 1)\delta\alpha_{max} \\ \cos\beta_{new} = \cos\beta_{old} + 2(r - 1)\delta\cos\beta_{max} \\ \gamma_{new} = \gamma_{old} + 2(r - 1)\delta\gamma_{max} \end{cases} \quad (20)$$

and

$$\mathbf{r}_{new} = \mathbf{r}_{old} + 2(r - 1)\delta d_{max} \quad (21)$$

where α , β , and γ are three Euler angles describing the orientation, and \mathbf{r} represents the Cartesian coordinates of the peptide's geometric center. $\delta\alpha$, $\delta\beta$, $\delta\gamma$ and δd_{max} ($=5^\circ$, 5° , 5° and 0.02\AA , respectively) were chosen to be maximum variations of the random

perturbations of α , β , γ and d . These parameters were determined by trial and error, such that the system will have enough time for internal relaxation but will not be trapped too often in local energy minima.

Additionally, the width of the membrane hydrophobic region was perturbed:

$$z_m = z_0 + \delta z(2r - 1) \quad (22)$$

δz , the maximum variation of a perturbation, was set to 0.5Å. Overall, the membrane width z_m was allowed to vary from its native value z_0 by up to 20% (17).

Sampling

To calculate the free energy change (Eq. 2), peptides simulations in water and in membrane environments were performed. A standard MC protocol was employed while acceptance of each move was based on the Metropolis criterion and the free energy difference between the new and old states (18). In water peptides were subjected solely to internal conformational modifications. In one MC cycle the number of internal modifications performed was equal to the number of residues in the peptide. Therefore, the acceptance criterion was based on $\Delta\Delta E$ (Eq. 3). In the membrane each MC cycle included additional external rigid body rotational and translational motions as described above. Thus, the acceptance criterion in this case was derived from the following free energy difference:

$$\Delta\Delta G_{total} = \Delta\Delta E + \Delta\Delta G_{SIL} + \Delta\Delta G_{def} + \Delta\Delta G_{coul} \quad (23)$$

To perform an extensive search in conformational space I performed 3-5 tests in both membrane and aqueous environments, while each test consisted of 500,000-900,000 MC cycles.

References

1. Kessel, A., D. Shental-Bechor, T. Haliloglu, and N. Ben-Tal. 2003. Interactions of hydrophobic peptides with lipid bilayers: Monte Carlo simulations with M2delta. *Biophys J* 85:3431-3444.
2. Shental-Bechor, D., T. Haliloglu, and N. Ben-Tal. 2007. Interactions of cationic-hydrophobic peptides with lipid bilayers: a Monte Carlo simulation method. *Biophys J* 93:1858-1871.
3. Bahar, I., and R. L. Jernigan. 1996. Coordination geometry of nonbonded residues in globular proteins. *Fold Des* 1:357-370.
4. Flory, P. J. 1969. *Statistical Mechanics of Chain Molecules*. Wiley-Interscience, New-York.
5. Kessel, A., and N. Ben-Tal. 2002. Free energy determinants of peptide association with lipid bilayers. In *Current Topics in Membranes*. T. J. M. Sidney A. Simon, editor. Academic Press. 205-253.
6. Ben-Tal, N., A. Ben-Shaul, A. Nicholls, and B. Honig. 1996. Free-energy determinants of alpha-helix insertion into lipid bilayers. *Biophys J* 70:1803-1812.
7. Bahar, I., M. Kaplan, and R. L. Jernigan. 1997. Short-range conformational energies, secondary structure propensities, and recognition of correct sequence-structure matches. *Proteins* 29:292-308.
8. Mouritsen, O. G., and M. Bloom. 1984. Mattress model of lipid-protein interactions in membranes. *Biophys J* 46:141-153.
9. Fattal, D. R., and A. Ben-Shaul. 1993. A molecular model for lipid-protein interaction in membranes: the role of hydrophobic mismatch. *Biophys J* 65:1795-1809.
10. Helfrich, P., and E. Jakobsson. 1990. Calculation of deformation energies and conformations in lipid membranes containing gramicidin channels. *Biophys J* 57:1075-1084.
11. Ben-Shaul, A., N. Ben-Tal, and B. Honig. 1996. Statistical thermodynamic analysis of peptide and protein insertion into lipid membranes. *Biophys J* 71:130-137.
12. Dan, N., and S. A. Safran. 1998. Effect of lipid characteristics on the structure of transmembrane proteins. *Biophys J* 75:1410-1414.
13. Nielsen, C., M. Goulian, and O. S. Andersen. 1998. Energetics of inclusion-induced bilayer deformations. *Biophys J* 74:1966-1983.
14. May, S., and A. Ben-Shaul. 1999. Molecular theory of lipid-protein interaction and the Lalpha-HII transition. *Biophys J* 76:751-767.
15. McLaughlin, S. 1989. The electrostatic properties of membranes. *Annu Rev Biophys Chem* 18:113-136.
16. Honig, B. H., and W. L. Hubbell. 1984. Stability of "salt bridges" in membrane proteins. *Proc Natl Acad Sci U S A* 81:5412-5416.
17. Marsh, D. 2008. Energetics of hydrophobic matching in lipid-protein interactions. *Biophys J* 94:3996-4013.
18. Metropolis, N., A. W. Rosenbluth, M. N. Rosenbluth, A. H. Teller, and E. Teller. 1953. Equation of State Calculations by Fast Computing Machines. *The Journal of Chemical Physics* 21:1087-1092.

Paper I: A combined pulse EPR and Monte Carlo simulation study provides molecular insight on peptide-membrane interactions.

Michal Gordon-Grossman, Yana Gofman, Herbert Zimmermann, Veronica Frydman, Yechiel Shai, Nir Ben-Tal and Daniella Goldfarb.

Michal Gordon-Grossman and Yana Gofman contributed equally to this work

Published in *J Phys Chem B*, 2009, 113(38):12687-12695

Reprinted with permission from “A combined pulse EPR and Monte Carlo simulation study provides molecular insight on peptide-membrane interactions”, Michal Gordon-Grossman et al., *The Journal of Physical Chemistry B*, American Chemical Society, Sep 1, 2009. Copyright (2009), American Chemical Society.

A Combined Pulse EPR and Monte Carlo Simulation Study Provides Molecular Insight on Peptide–Membrane Interactions

Michal Gordon-Grossman,^{†,‡} Yana Gofman,^{‡,§,||} Herbert Zimmermann,[⊥] Veronica Frydman,[#] Yechiel Shai,[∇] Nir Ben-Tal,^{*,||} and Daniella Goldfarb^{*,†}

Departments of Chemical Physics, Chemical Infrastructure Unit, Biological Chemistry, The Weizmann Institute of Science, Rehovot, Israel 76100, GKSS Research Center, Geesthacht, Germany 21502, Max-Planck Institute for Medical Research, Heidelberg, Germany, and Department of Biochemistry, The George S. Wise Faculty of Life Sciences, Tel-Aviv University, Tel-Aviv, Israel 69978

Received: June 1, 2009; Revised Manuscript Received: July 28, 2009

We present a new approach to obtain details on the distribution and average structure and locations of membrane-associated peptides. The approach combines (i) pulse double electron–electron resonance (DEER) to determine intramolecular distances between residues in spin labeled peptides, (ii) electron spin echo envelope modulation (ESEEM) experiments to measure water exposure and the direct interaction of spin labeled peptides with deuterium nuclei on the phospholipid molecules, and (iii) Monte Carlo (MC) simulations to derive the peptide–membrane populations, energetics, and average conformation of the native peptide and mutants mimicking the spin labeling. To demonstrate the approach, we investigated the membrane-bound and solution state of the well-known antimicrobial peptide melittin, used as a model system. A good agreement was obtained between the experimental results and the MC simulations regarding the distribution of distances between the labeled amino acids, the side chain mobility, and the peptide’s orientation. A good agreement in the extent of membrane penetration of amino acids in the peptide core was obtained as well, but the EPR data reported a somewhat deeper membrane penetration of the termini compared to the simulations. Overall, melittin adsorbed on the membrane surface, in a monomeric state, as an amphipatic helix with its hydrophobic residues in the hydrocarbon region of the membrane and its charged and polar residues in the lipid headgroup region.

Introduction

Key biological processes involve interactions between peptides and the cell membrane, and many biophysical approaches have been used to characterize these interactions. One of the prominent methods used to this end is electron paramagnetic resonance (EPR) spectroscopy. The EPR measurements are based on site directed spin labeling,^{1–3} where a nitroxide side chain, like methanethiosulfonate (MTSL), is introduced at a desired site in the protein/peptide via cysteine substitution mutagenesis. Spin labels can also be attached to phospholipid molecules, thus allowing the examination of changes in membrane ordering and fluidity upon the introduction of a peptide/protein.⁴ The line shape of the EPR spectrum of nitroxide radicals is highly sensitive to the degree of the side chain mobility, whereas the nitrogen hyperfine coupling and the *g*-values, particularly the *g*_{xx} component, sense the polarity^{2,3} and proticity of its close environment.⁵ In addition, increased relaxation rates due to the presence of paramagnetic quenchers provide information about the solvent accessibility and the insertion depth in membranes.^{2,6–8} Additional broadening due

to the introduction of a second spin label provides distance information in the range 7–20 Å.^{3,9,10} The analysis of the accessibility, mobility, and polarity measurements is well established and can be used to reveal the secondary structure and the general location and orientation of the peptide relative to the membrane.^{2,11}

Pulse double electron–electron resonance (DEER) measurements extend the distances accessible by EPR methods to 70 Å,^{12–14} and have been applied in a number of investigations of peptide/protein–membrane interactions.^{15–20} Electron spin echo envelope modulation (ESEEM) is yet another well established technique designed to measure weak hyperfine interactions between unpaired electrons and nearby nuclei that can be further interpreted in terms of distances.^{21–23} Although it is a technique commonly used in studies of the coordination shells of metal ions, it has been scarcely applied in the context of protein/peptide–membrane interactions. Recently, ESEEM has been used to derive the water penetration depth in membranes.^{16,24,25} We have previously shown that peptide–membrane interactions can be identified by combining ESEEM induced by D₂O and ²H in specifically labeled lipid molecules.²⁶ In that preliminary study, which was a proof of principle, the peptides were labeled in one position only.

While EPR techniques provide a wealth of structural information, they do not give directly the atomic level structure but rather provide constraints that can be correlated or combined with modeling techniques. Monte Carlo (MC) simulations have been previously demonstrated to be an important tool in the investigation of peptide–membrane interactions.^{27–34} Typically, the MC methods are based on a reduced representation, which enables comprehensive sampling of peptide conformations and

* Corresponding authors. E-mail: Daniella.goldfarb@weizmann.ac.il (D.G.); NirB@tauex.tau.ac.il (N.B.-T.).

[†] Department of Chemical Physics, The Weizmann Institute of Science.

[‡] Michal Gordon-Grossman and Yana Gofman contributed equally to this work.

[§] GKSS Research Center.

^{||} Tel-Aviv University.

[⊥] Max-Planck Institute for Medical Research.

[#] Department of Chemical Infrastructure Unit, The Weizmann Institute of Science.

[∇] Department of Biological Chemistry, The Weizmann Institute of Science.

locations in the membrane in an accelerated manner. This approach allows overcoming the current limited computer power, which often restricts molecular dynamics (MD) simulations, another computational tool often used in the research of the interactions of peptides with lipid bilayers.

In this work, we combined EPR experiments, CW-EPR, ESEEM, and DEER with MC simulations to explore peptide–membrane interactions in molecular detail. To demonstrate the effectiveness of the new approach, we chose melittin, a commonly used model for the investigation of peptide–membrane interactions. We studied its interactions with large unilamellar vesicles (LUVs), consisting of the zwitterionic dipalmitoylphosphatidylcholine (DPPC) and monovalent ion phosphatidylglycerol (PG) at 7:3 molecular ratio. The MC simulations were used to rationalize the experimental results and help in their interpretation on the one hand, and the experimental results served as tests for the predictive power of the simulations on the other. The MC protocol we employed has been developed, tested, and used to study the membrane interactions of peptides, such as magainin2, penetratine,³⁵ and the M2 δ transmembrane segment from the acetylcholine receptor subunit.³⁶ The simulations were carried out both on native and mutated melittin, corresponding to the experiments, in order to determine their structure and orientation in both water and membrane and to elucidate any effect of the spin labeling on the structure.

Melittin, a 26-residue antimicrobial peptide, is the major component of honeybee (*Apis mellifera*) venom.³⁷ The structure of melittin has been investigated under various conditions using X-ray crystallography^{38,39} and NMR (nuclear magnetic resonance) techniques.^{40–43} The crystal structure shows that the peptide forms a tetramer, with each subunit comprising two α -helical segments connected by a hinge at residues 11 and 12 with a kink of $\sim 120^\circ$.³⁹ Apolar residues forming the core of the tetramer are almost completely shielded from the solvent by the hydrophilic side chains and the polypeptide backbones. NMR studies of melittin bound to dodecylphosphocholine (DPC) micelles revealed a rod-like α -helical conformation similar to the crystal structure.^{40,41}

In spite of the significant number of studies examining the orientation of melittin within the membrane, it is still a controversial subject. It was observed that melittin's orientation is affected by various factors. Melittin can be oriented either perpendicular or parallel to the membrane surface, depending on pH, temperature, phospholipid composition, and peptide concentration.⁴⁴ Several studies showed that melittin can adopt a surface-parallel, transmembrane, or pseudotransmembrane orientation in neutral membranes (discussed in ref 44). By contrast, only surface orientation was observed in membranes containing negatively charged lipids.⁴⁴ The surface orientation of melittin is characterized by apolar residues facing the hydrophobic core of the membrane and polar residues facing the aqueous phase.^{40,41}

Our results showed that, upon membrane binding, melittin undergoes conformational changes from a primarily random coil, with some helical content at the C-terminus, to a helical structure. We also show that at low concentrations melittin is oriented parallel to the membrane surface. Examination of specific residue location revealed that all the charged (and highly polar) residues are exposed to the aqueous phase, while hydrophobic amino acids are immersed in the membrane, as anticipated on the basis of empirical data. The distances between the labels measured by DEER and the membrane-penetration depth of the residues in the peptide core, determined by ESEEM, correlated well with the MC simulations. However, melittin's

TABLE 1: Peptide Designations and Sequences^a

sequence	peptide designation
GIGAVLKVLTTGLPALISWIKRKRQQ	Melittin
<u>C</u> GIGAVLKVLTTGLPALISWIKRKRQQ	mel-N
G <u>I</u> C <u>A</u> VLKVLTTGLPALISWIKRKRQQ	mel-C ₃
GIGAVLKVLTTGLPCLISWIKRKRQQ	mel-C ₁₅
GIGAVLKVLTTGLPALICWIKRKRQQ	mel-C ₁₈
GIGAVLKVLTTGLPALISWIKRKRQQ <u>C</u>	mel-C ₂₇
<u>C</u> GIGAVLKVLTTGLPCLISWIKRKRQQ	mel-NC ₁₅
GIGAVLKVLTTGLPCLISWIKRKRQQ <u>C</u>	mel-C ₁₅ C ₂₇
GICAVLKVLTTGLPALICWIKRKRQQ	mel-C ₃ C ₁₈
<u>C</u> GIGAVLKVLTTGLPALISWIKRKRQQ <u>C</u>	mel-NC ₂₇

^a The position of the spin label is indicated by C.

termini were found to penetrate somewhat deeper into the membrane than predicted by the MC simulations.

Experimental Methods

Materials. The phospholipids dipalmitoylphosphatidylcholine (DPPC) (Sigma) and egg phosphatidylglycerol (PG) (Lipid products) were used as is. 1,2-Dipalmitoyl-*sn*-glycero-3-phosphocholine-*N,N,N*-trimethyl-*d*₉ (DPPC-*d*₉) was synthesized as reported earlier, and the isotopic purity was found to be better than 98%.⁴⁵ Per-deuterated alkyl chain DPPC (DPPC-*d*₆₂) was purchased from Avanti Polar Lipids Inc. MTSL (1-oxyl-2,2,5,5-tetramethyl-3-pyrroline-3-methyl) methanethiosulfonate was from Toronto Research Chemicals, Ontario, CA. The spin probes 3-(carboxy)-2,2,5, 5-tetramethyl-1-pyrrolidinyloxy (Proxy) and 5-doxyl-stearic acid (5DSA) were purchased from Aldrich. 1,2-dipalmitoyl-*sn*-glycero-3-phospho (TEMPO) choline (HPCSP) and 1-palmitoyl-2-stearoyl-(10-DOXYL)-*sn*-glycero-3-phosphocholine (10PCSP) were purchased from Avanti Polar Lipids Inc. 1-Palmitoyl-2-stearoyl-(5-DOXYL)-*sn*-glycero-3-phosphocholine (5PCSP) was synthesized according to the procedure described earlier.⁴⁶ Materials for peptide synthesis and purification appear in the Supporting Information.

Peptide Synthesis and Labeling. Peptides were synthesized by a solid phase method on rink amide MBHA resin (0.68 mequiv) by using an ABI 433A automatic peptide synthesizer. The principles of peptide-resin cleavage and peptide purification have been described elsewhere,²⁶ and detailed information appears in the Supporting Information. The peptides were labeled with MTSL as reported earlier.² Labeled peptides were shown to be homogeneous by analytical HPLC (>97%, by weight) and were analyzed by electrospray mass spectroscopy. Table 1 lists all of the spin labeled peptides prepared and their designations.

Sample Preparation. A dry phospholipid mixture of DPPC/PG (7:3 w/w), DPPC-*d*₉/PG (7:3 w/w), or DPPC-*d*₆₂/PG (7:3 w/w) was dissolved in a CHCl₃/MeOH mixture (2:1, v/v). Each of the spin labeled phospholipids 5, 10, HPCSP, 5DSA, or Proxy were added from a stock solution to the DPPC/PG (7:3 w/w) or the DPPC-*d*₉/PG (7:3 w/w) solution to give 1% by weight. The solvents were evaporated under a nitrogen stream. A lipid suspension was prepared by vortex and sonication of the lipids in deuterated or nondeuterated phosphate buffer to give a final concentration of 5 mg/mL. Once the sample is fully hydrated, large unilamellar vesicles (LUVs) were prepared by extrusion with an Avastin LiposoFast extruder.⁴⁷ The peptides were added to the LUV solution to give a peptide concentration of 0.16 mM and a peptide–lipid molar ratio of 1/200 in order to ensure maximum binding of the peptides to the LUVs, as determined previously.⁴⁸ The concentration of spin labeled peptides in the water–glycerol (30%) solution was 0.35 mM. All samples for

DEER measurements were prepared in D₂O solutions to extend the phase memory time. Samples for DEER and ESEEM measurements were prepared as follows: after equilibration, approximately 30–40 μ l of each were rapidly frozen by insertion of the EPR tube (2.7 mm i.d. and 3.7 mm o.d.) into liquid nitrogen. Thereafter, the samples remained frozen.

Spectroscopic Measurements. All CW X-band (9.5 GHz) measurements were performed at room temperature (23–25 °C) on a Bruker ELEXSYS 500 spectrometer, using flat cells or a couple of round quartz capillaries (0.6 i.d. \times 0.84 o.d., VitroCom Inc.). ESEEM and DEER experiments were carried out at 50 K on a Bruker ELEXSYS E580 spectrometer (9.5 GHz) using the ER4118X-MS-5X probehead with a split ring resonator (5 mm sample access). The constant time four-pulse DEER experiment⁴⁹ was employed, and the experimental details are given in the Supporting Information. Distance distributions were obtained from the dipolar time evolution data by DeerAnalysis2008 software.⁵⁰ Tikhonov regularization was performed with L curve computation, and the regularization parameter was set to 10, 100, or 1000.

The ESEEM experiments were done using the three-pulse pulse sequence $\pi/2$ - τ - $\pi/2$ - T - $\pi/2$ - τ -echo, with a repetition rate of 3 ms and four-step phase cycle.⁵¹ All measurements were performed at a field corresponding to the maximum echo intensity, and the $\pi/2$ and π microwave pulse lengths were 16 and 32 ns, respectively. The τ -value was optimized for maximum modulation depth ($\tau = 1/(2\nu_1) \sim 224$ ns, where ν_1 is the ²H Larmor frequency). The time interval T was incremented in 20 ns steps starting at 40 ns. Fourier transformation of the ESEEM (FT-ESEEM) trace was carried out as follows: after phase correction and normalization, the background decay of the normalized data was subtracted using a polynomial fit; then, the data was apodized with a Hamming window, and zero filling to 512 points was performed followed by FT and cross-term averaging.⁵² All ESEEM traces were treated identically. The number of accumulations was 30–300 depending on the modulation depth.

We have chosen the intensity of the ²H peak, $I(^2\text{H})$, in the FT-ESEEM as a measure for the modulation depth. The ²H peak is composed of a narrow component due to remote deuterium nuclei and a broad component due to water molecules that form H-bonds with the NO group.²⁵ The data analysis in the present study took into account only the narrow spectral constituent.

Computational Methods

MC simulations of melittin in water and membrane were performed as described previously.^{35,36,53} In brief, melittin was described in a reduced way, in which each amino acid was represented by two sites, corresponding to its α -carbon and side chain. The hydrocarbon region of the membrane was represented as a smooth profile of 30 Å width. A negative surface charge, representing the molecular fraction of PG, was located on both sides of the membrane at a distance of 20 Å from the midplane, corresponding to the location of the lipid phosphate groups.³⁵ To calculate the free energy of the peptide in water and in the membrane, four simulations consisting of 900 000 Monte Carlo cycles were conducted. The total free energy of membrane association (ΔG_{total}) was calculated as the difference between the free energies of a peptide in the aqueous phase and in the membrane, using the following equation.³⁵

$$\Delta G_{\text{total}} = \Delta G_{\text{con}} + \Delta G_{\text{sol}} + \Delta G_{\text{imm}} + \Delta G_{\text{lip}} + \Delta G_{\text{def}} + \Delta G_{\text{coul}} \quad (1)$$

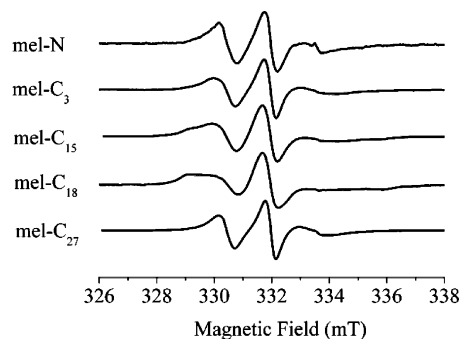


Figure 1. X-band EPR spectra of melittin that is labeled in various positions along the peptide in the presence of LUVs.

In eq 1, ΔG_{con} stands for the change in the free energy due to membrane-induced conformational changes, ΔG_{sol} is the free energy of transfer of the peptide from the aqueous environment to the membrane, ΔG_{imm} accounts for immobilization of the peptide in the membrane, ΔG_{lip} accounts for the free energy due to the change in the conformational freedom of the lipid chains, ΔG_{def} accounts for the membrane deformation associated with peptide incorporation into the membrane, and ΔG_{coul} stands for Coulombic attraction between charged amino acids and the (negative) membrane surface charge. The data of each simulation was used to calculate the tilt angle and penetration depth of the peptide with respect to the membrane plane, and the free energy of membrane association, by averaging over the values obtained in all of the cycles. The penetration depth was calculated as the average over conformations of the distance between the geometric center of the peptide and the membrane midplane. The tilt angle was estimated on the basis of the angle between the peptide's end-to-end vector and the membrane's surface. The reported values are the averages over all of the simulations \pm standard deviations among the values of the different runs.

Melittin's initial structure was taken from Protein Data Bank (PDB) entry 2MLT. Labeling of melittin with MTSL at different positions (Table 1) was mimicked by leucine. This is based on the observation that MTSL is hydrophobic and its free energy of transfer from water into the membrane is very similar to that of leucine.^{36,54} The initial structures of the labeled peptides were obtained by modifying the native structure using the NEST methodology,⁵⁵ with default parameters. The simulations were performed in 30% acidic membranes unless stated otherwise. The helical content of the peptides was calculated as in ref 53.

Experimental Results

CW-EPR Measurements. Figure 1 presents the room temperature CW EPR spectra of the melittin singly labeled mutants in the presence of LUVs. It shows that in the presence of LUVs the label's mobility decreases from the ends of the peptide to its center, with mel-C₁₈ being the most rigid and the N- and C-terminus labels being the most mobile. Comparison of these spectra and the spectra in solution (Figure S1, Supporting Information) shows that the spectra with the LUVs are always considerably broader due to slower tumbling rates, confirming that melittin is bound to the membrane. The spectra of the doubly labeled peptide were approximately a superposition of the spectra of the corresponding singly labeled peptides (Figure S1, Supporting Information).

DEER Measurements—The Reference System. DEER measurements, in the presence and absence of LUVs, were carried out for four double mutants (Table 1). To ensure that

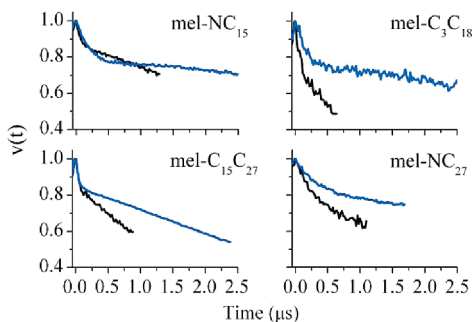


Figure 2. Normalized DEER decays for the doubly labeled melittin peptides within DPPC/PG/D₂O LUVs (black) and in D₂O/30% glycerol solution (blue). The corresponding distance distributions are shown in Figure 3.

the DEER decay (excluding the background decay) obtained from the LUV solutions is owing to intra- and not inter-peptide interactions due to aggregation, we have compared the DEER trace obtained from a singly labeled melittin, mel-C₁₅, with that of a doubly labeled melittin, mel-C₁₅C₂₇ (Figure S2, Supporting Information). The DEER kinetics of mel-C₁₅ could be best fitted with an exponential decay of a dimensionality of 2.14, which is consistent with a two-dimensional distribution of peptide on the LUV surface. The difference between the time domain traces of the singly and doubly labeled peptides clearly showed that, for peptide/phospholipids = 1/200, the dipolar interactions, determined after background subtraction, are intramolecular and that melittin is in a monomeric state.

The time-domain DEER traces of the doubly labeled melittin in solutions with and without LUVs are shown in Figure 2. In all cases, the background decay was significantly faster in the presence of LUVs, although the peptide concentration was lower (0.35 mM vs 0.16 mM, respectively). This is expected because the peptides are not distributed isotropically throughout the solution but are concentrated on the LUVs such that the local concentration is higher than the bulk concentration.⁵⁶ The enhanced contribution of the background decay affected also the signal-to-noise ratio and prevented measurements at long times (Figure S3, Supporting Information).

Figure 3 shows the distance distribution obtained from the DEER measurements in the aqueous phase and in LUV solutions. The fine structures (peaks) appearing in some of the distance distributions are most probably artifacts of the regularization due to noise and should be considered as part of the total width of the distribution. It is evident that, on average, the membrane-bound peptide is shorter than in the aqueous phase, and the overall distance distribution is narrower. The smallest difference was observed for mel-C₁₅C₂₇, where the distance distributions with and without the LUVs are very close. Single-peak distributions were observed in both cases, which are centered on distances of 20 and 22.5 Å, respectively. The distances are similar to the distance between the corresponding α -carbons of Ala15 and Gln26 in the X-ray structure,^{38,39} suggesting that the peptide core is helical even in the aqueous solution. The similarity between the center of the distance distribution of the bound peptides and the corresponding distances in the overall crystal structure (Figure 3) suggests that the average conformation is helical.

While the DEER measurements report the average conformation of melittin in the aqueous phase and in association with LUVs, they do not reveal the penetration depth into the membrane and the orientation of the peptide in the membrane. This information was derived from the ESEEM experiments described next.

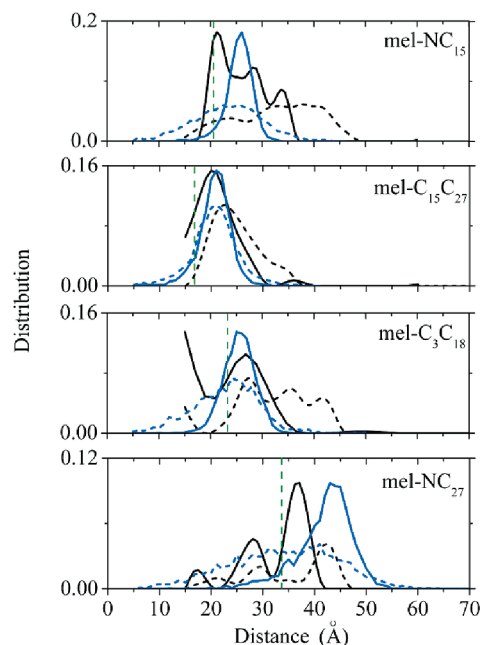


Figure 3. Distance distribution obtained from the DEER traces (black) shown in Figure 2 for the four double mutants studied with (solid) and without (dashed) LUVs. The experimental results were normalized to the maximum of the MC results. The blue (solid and dashed) lines are the results of the MC simulations obtained from the corresponding Leu double mutants. The vertical green line represents the corresponding distance between α -carbons in the crystal structure.^{38,39}

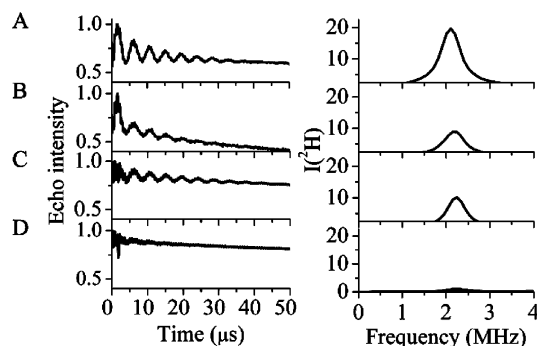


Figure 4. Three-pulse ESEEM time domain traces of mel-C₂₇ in (A) 70% D₂O/30% glycerol, (B) DPPC/PG/D₂O LUVs, (C) DPPC-*d*₆₂/PG LUVs, and (D) DPPC-*d*₉/PG LUVs and their corresponding FT-ESEEM spectra.

ESEEM Measurements—The Reference System. Figure 4 shows examples of time domain ESEEM traces and FT-ESEEM spectra of mel-C₂₇ in a D₂O buffer, with LUVs in a deuterated buffer and with deuterated LUVs. These show the range of ²H modulation depth that can be observed. The modulation depth is expressed in the intensity of the ²H peak in the FT-ESEEM spectrum, given by $I(^2\text{H})$. In general, the larger $I(^2\text{H})$ is, the higher is the ²H density around the spin label. To correlate $I(^2\text{H})$ with the insertion depth of the spin label in the peptide, a proper reference is required.

The reference chosen was spin labeled phospholipid molecules (Figure 5). The spin label in HPCSP senses the polar headgroup region, 5PCSP probes the region below the phosphate group toward the membrane, and 10PCSP the hydrocarbon region. These spin probes were introduced in minute amounts to the phospholipid solutions prior to the preparation of the LUVs. Earlier reports showed that the addition of melittin to DPPC/PG model membranes changed the modulation depth experienced by 5, 7, and 16DSA (doxyl-stearic acid spin

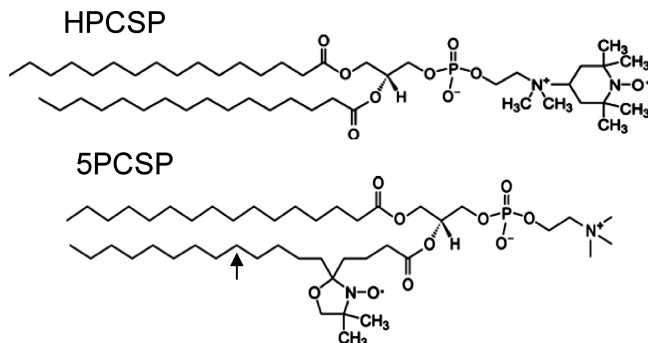


Figure 5. Structures of the HPCSP and 5PCSP spin labeled phospholipids. The 10PCSP probe is similar to 5PCSP with the nitroxide spin label in the position marked by the arrow.

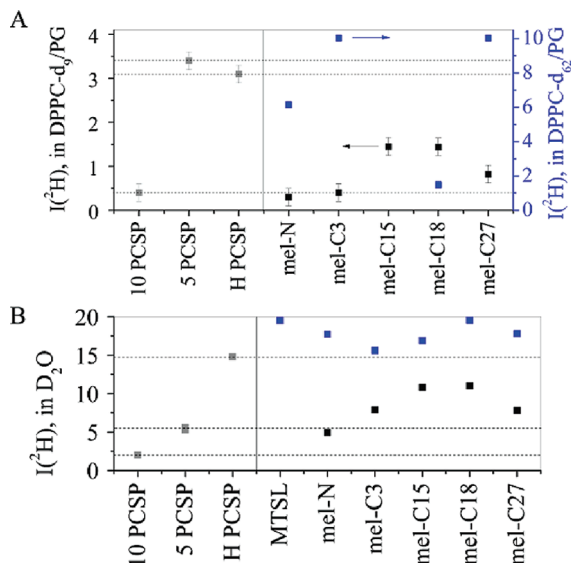


Figure 6. $I(^2\text{H})$ value of labeled melittin within (A) DPPC- d_9 /PG (black squares) and DPPC- d_{62} /PG (blue squares). (B) DPPC/PG/ D_2O LUVs (black squares) compared to the unbound labeled melittin and free MTSL, in 70% D_2O /30% glycerol (blue squares). The spin labeled phospholipids reference in the presence of melittin (gray squares) is also shown for comparison in DPPC- d_9 /PG and DPPC/PG/ D_2O LUVs. The dotted lines indicate the $I(^2\text{H})_{n\text{-PCSP}}$ ($n = \text{H}, 5, 10$) values. The standard errors are marked, but sometimes they are smaller than the symbols.

labels).²⁶ Accordingly, we compared the $I(^2\text{H})$ values of the PCSP spin probes in the various types of deuterated LUV solutions with and without melittin (Figure S4, Supporting Information). Due to a small, but significant observed difference we used the results of the samples with melittin as the reference.

Figure 6 shows the dependence of $I(^2\text{H})$ on the spin-label position in the phospholipids in samples of LUVs/ D_2O and DPPC- d_9 /PG LUVs with melittin (non-labeled). Earlier calculations showed that $I(^2\text{H})$ should exhibit an approximate linear dependence down (or up) to ~ 10 Å from the deuterated layer in DPPC- d_9 /PG LUVs.²⁵ For the deuterated LUVs, the trend $I(^2\text{H})_{\text{HPCSP}} \sim I(^2\text{H})_{\text{5PCSP}} \gg I(^2\text{H})_{\text{10PCSP}} \sim 0$ is observed. The similar values for HPCSP and 5PCSP confirm the bend of the polar headgroup region with respect to the alkyl chain.⁵⁷ For the LUV/ D_2O samples, the trend of $I(^2\text{H})$ is $I(^2\text{H})_{\text{HPCSP}} I(^2\text{H})_{\text{5PCSP}} > I(^2\text{H})_{\text{10PCSP}}$ (Figure 6B). The close $I(^2\text{H})$ values for 5PCSP and 10PCSP are a consequence of the sigmoid shape of the polarity profile within the membrane.²⁵

Orientation and Location of Melittin within the Membrane. A plot of $I(^2\text{H})$ vs the spin label position in the peptide in DPPC- d_9 /PG LUVs is presented in Figure 6A. It shows that

labels in the center of the peptide, attached to C_{15} and C_{18} , have the highest $I(^2\text{H})$ values, while those at the ends show lower values. These results on their own are not sufficient for locating the peptide relative to the membrane because low values of $I(^2\text{H})$ could arise from a residue that is buried in the hydrophobic region of the membrane or is situated in the aqueous phase, not interacting with the membrane at all. Therefore, the $I(^2\text{H})$ values of the spin labeled peptides in LUVs/ D_2O are essential to complement the picture and differentiate these two options. The results are depicted in Figure 6b, demonstrating a trend very similar to that observed with the DPPC- d_9 /PG LUVs.

Figure 6B also shows the dependence of the $I(^2\text{H})$ values of the spin labeled peptides in a D_2O buffer along with that of a free MTSL, which represents the highest possible $I(^2\text{H})$ value. The scatter of the points is much larger than the experimental error and reveals that different residues experience a different water exposure in solution. Here, mel-C₁₈ experiences the largest exposure to water, while mel-C₃, the lowest. The difference between the degrees of water exposure of the amino acids might indicate that melittin is partially structured even in solution. Alternatively, the differences can also be due to exchangeable protons in amino acids in the close vicinity of the label. Upon the addition of LUVs, all peptides exhibit a considerable reduction in $I(^2\text{H})$ of D_2O , confirming the binding to the LUVs.

The combined D_2O , DPPC- d_9 ESEEM results indicate that the spin labels in mel-C₁₈ and mel-C₁₅ are exposed to the solvent, whereas the N- and C-termini are somewhat deeper in the membrane. In order to substantiate this observation, ESEEM measurements were carried out also with DPPC- d_{62} . The results presented in Figure 6A show that, among the labeled peptides, mel-C₁₈ is the furthest away from the hydrophobic region, while the termini are the closest.

Computational Results

Free Energy of Melittin–Membrane Association. We first examined the dependence of the free energy of melittin–membrane association on the lipid composition and the ionic strength. We performed MC simulations of the interaction of melittin with membranes containing different proportions of anionic lipids (Figure S5A, Supporting Information). As anticipated, increasing the fraction of the acidic lipids increased the Coulombic interaction between them and melittin’s basic residues and the magnitude of the free energy of melittin–membrane association, i.e., increased affinity. In contrast, increasing the ionic strength decreased the magnitude of the association free energy of melittin with the membrane, due to the shielding effect of the cations (Figure S5B, Supporting Information).

We then compared the experimentally obtained association free energy of melittin⁵⁸ with unilamellar phosphocholine (zwitterionic) vesicles with the corresponding calculated value of melittin interaction with a neutral membrane. The computed value of -15.1 ± 0.6 kT (Figure S5A, Supporting Information) is slightly lower than the experimental value of about -11.8 to -13.6 kT.⁵⁸ We also compared our results to MD simulations of melittin within a membrane containing 10% anionic (and 90% zwitterionic) lipids.⁵⁹ The free energy value of melittin–membrane association of the MD simulation was -21.7 kT in excellent agreement with the -21.1 ± 0.6 kT value of our MC calculations (Figure S5A, Supporting Information).

It is noteworthy that changes in the proportion of anionic lipids and the ionic strength did not affect melittin’s helicity, penetration depth, and orientation relative to the membrane (Figure S6, Supporting Information).

TABLE 2: Thermodynamic Parameters for the Membrane Association of Native and Modified Melittin, Calculated on the Basis of the MC Simulations^a

peptide designation	z (Å)	tilt (deg)	ΔG_{total} (kT)	ΔG_{conf} (kT)
melittin	18.5 ± 0.1	$93 \pm (<1)$	$-29 \pm (<1)$	$-1 \pm (<1)$
mel-NC ₁₅	17.4 ± 0.1	$96 \pm (<1)$	$-38 \pm (<1)$	$-5 \pm (<1)$
mel-C ₁₅ C ₂₇	$18.2 \pm (<0.1)$	95 ± 1	$-29 \pm (<1)$	$2 \pm (<1)$
mel-C ₃ C ₁₈	17.2 ± 0.1	104 ± 1	$-29 \pm (<1)$	$1 \pm (<1)$
mel-NC ₂₇	$18.5 \pm (<0.1)$	$95 \pm (<1)$	$-37 \pm (<1)$	$-6 \pm (<1)$

^a Each value is represented as an average \pm standard deviation. The penetration depth, z , is calculated as the average distance between the peptide's α -carbon and the membrane midplane. The tilt angle, tilt, is calculated as the angle between the peptide's end-to-end vector and the membrane normal. ΔG_{total} is the total free energy change upon membrane association; ΔG_{conf} stands for the free energy change due to the membrane-induced conformational changes in the peptide (eq 1).

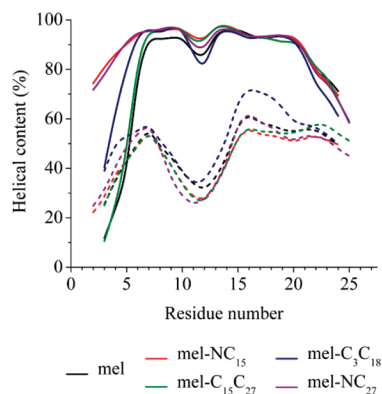


Figure 7. Calculated helical content of native and Leu-modified melittin. The dotted curves show the results of simulations in the aqueous phase, and the continuous curves refer to the membrane simulations. The results obtained with the label (represented as Leu) at different amino acids are plotted using different colors according to the legend.

Native vs Labeled Melittin. We conducted MC simulations of the interactions of native and mutant melittin peptides with model membranes, composed of 30% acidic lipids, and correlated the results with the experimental data presented above (Table 2). In the MC simulations, the interactions between pairs of amino acids are described using statistical (knowledge-based) potentials, derived from known protein structures.⁶⁰ Since there is no data that enables the derivation of similar potential terms for the spin probe, we were forced to represent it as an amino acid. Fortunately, the probe and leucine share very similar polarity and membrane partitioning.^{54,61} Thus, the cysteine side chains with the nitroxide probes, positioned as designated in Table 1, were substituted by leucine in the simulations.

Overall, the native and “labeled” melittin peptides showed the same membrane behavior. They all adsorbed onto the membrane surface at an angle of 93 – 103° with respect to the membrane normal (Table 2) at an approximately helical conformation (Figure 7), and penetrated into the membrane to the same extent (distance of 17.2 – 18.5 Å from the bilayer midplane; Table 2). Additionally, they all assumed conformations in which the hydrophobic amino acids were embedded in the hydrocarbon region of the membrane and the polar and charged residues interacted with the aqueous phase or the water–membrane interface (Figure 8). Thus, the leucine mutation, representing the spin label, did not appear to alter melittin's mode of interaction with the membrane significantly.

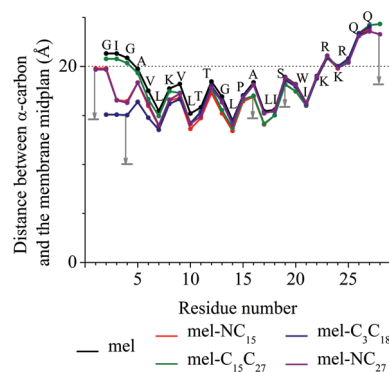


Figure 8. Location of native and mutant melittin near the membrane. The average distance of the α -carbon atoms from the membrane midplane in the MC simulations is shown for each residue. The gray arrows refer to the location of the NO group of the probe (see text). The corresponding rms fluctuations (Figure S7, Supporting Information) indicate that the termini are more flexible than the core, as anticipated.

However, along with the similarities, there are some differences between certain modified peptides and native melittin. For example, the free energy of membrane association of the mel-NC₁₅ and mel-NC₂₇ peptides was larger in magnitude than that of native melittin (Table 2). This is attributed to the free energy change due to membrane-induced conformational changes in the peptide, ΔG_{conf} , while other energetical terms were similar. We therefore investigated the helicity of native melittin and the mutants.

We calculated the helical content of the native and modified peptides in the aqueous phase and in the membrane (Figure 7). As anticipated, the peptides exhibited a significant increase in their helical content upon membrane association. The native and “labeled” peptides sampled similar conformations in the aqueous phase. However, the N-terminus of mel-NC₁₅ and mel-NC₂₇ had higher helical content in the membrane than the rest of the peptides (Figure 7). Since these were the only peptides with an N-terminal “label”, we concluded that the incorporation of a hydrophobic “label” (i.e., a leucine residue) at this position in melittin pulled the N-terminal deeper into the membrane and increased the helicity. This led to an increase of the magnitude of the free energy change due to membrane-induced conformational changes (in the peptide) and the total association free energy of these two peptides in comparison to the rest (Table 2). The analysis of the prevalent conformations of the melittin mutants, presented below, supports this conclusion. In contrast, the incorporation of the “label” into the C-terminus of melittin did not increase the helicity. This is attributed, in part, to the fact that the C-terminus is too polar to partition into the membrane even after the addition of the hydrophobic “probe”.

Melittin Structure, Orientation, and Penetration Depth.

Figure 3 shows the distribution of distances between the α -carbon atoms of the “labeled” residues observed in the MC simulations in comparison with the DEER experiments of the various melittin mutants. The experimental and computational results correlate well. The distance distribution is wider in water than in membrane in all cases, which is consistent with the anticipation that, roughly speaking, melittin is a random coil in solution and it becomes ordered upon membrane interaction (Figure 7). Mel-C₁₅C₂₇ showed the least significant broadening of the distance distribution in water relative to membrane, similar to the experiment. This is probably due to the fact that the helical content of the C-terminal is high in water (Figure 7). In general, the agreement between the DEER results and the MC simula-

tions is better for the membrane-associated peptide than for the peptide in solution.

Figure 8 shows the average location of the α -carbon atoms of the amino acids of native and modified melittin within the membrane. As mentioned above, all peptides adsorbed onto the membrane surface in similar conformation, orientation, and location. The C-terminus, containing some charged residues, is exposed to water. In native and in most of the modified melittin peptides, the N-terminus is located in the membrane–water interface. The only exception is mel-C₃C₁₈, for which the incorporation of the “label” (leucine) instead of Gly3 caused deeper penetration of the N-terminus into the membrane as compared to the rest of the peptides. Overall, the MC simulations are qualitatively consistent with the experiments concerning the locations of C₃, C₁₅, and C₁₈ (Figure 6). However, it appears that the termini penetrate deeper into the membrane according to the ESEEM experiments than in the simulations. This discrepancy will be discussed next.

Discussion

In the following, we first discuss the implications and current limitations of the ESEEM techniques for deriving peptide insertion depth in membranes. This is followed by a discussion of the restrictions of the MC simulations. We then depict the results of the combined approach that helps to reduce the limitations of each technique separately.

Implications and Limitations of the ESEEM Technique.

In order to estimate the insertion depth of the peptide into the membrane from the $I(^2\text{H})$ values, we used references based on spin labeled phospholipids. The comparison of the reference spin probes in LUVs/D₂O and DPPC-*d*₉ LUVs leads to conflicting results regarding the insertion depth. The DPPC-*d*₉ LUV measurements suggest a deeper penetration depth than the D₂O results (Figure 6), although overall, both give the same melittin conformation. It is worth mentioning that a similar conflict was observed in our earlier study that focused on mel-N only.²⁶ To reconcile the discrepancy, we then suggested that the N-terminus is close to the membrane surface region and adapts a conformation where the spin label at the N-terminus has limited water exposure. However, this explanation is inconsistent with the more complete data set presented above. We think that the reason for this inconsistency is that spin labeled phospholipids are not a proper reference system for deuterated LUVs. Problems in using labeled lipids in accessibility studies were previously pointed out by Nielsen et al.⁶ These were associated with wide variations in the probe conformation that complicated interpretation, and the disorder that may be introduced by the label, especially near the bilayer midplane. In addition, spin labeled lipids cannot account for the changes in the modulation depth associated with the volume of the peptide and the excluded volume associated with it. The volume of spin labeled melittin may change the number of phospholipid molecules in the vicinity of its spin label, thus effectively reducing their local density in this region. This would lead to lower $I(^2\text{H})$ values, which are misinterpreted as a deeper penetration. D₂O molecules, on the other hand, are small and mobile, and they should be less affected by the excluded volume. We therefore consider the D₂O reference to be more reliable. Accordingly, the spin labels in mel-C₁₅ and mel-C₁₈ are not buried deeper than position 5 of the phospholipid (Figure 6). This is also supported by the MC simulation. The simulation shows that the α -carbon of Ser18 is ~ 18 Å from the membrane midplane (Figure 8), which is above the fifth position in the alkyl chain. Although we have accounted for changes in D₂O

distribution in the membrane due to the insertion of melittin by using as a reference spin labeled phospholipids in LUVs in the presence of melittin, possible contributions to the modulation depth from exchangeable protons of the backbone and in side chains were not considered. For example, in a recent study, modulations due to D₂O were observed for a buried residue in a membrane protein.⁶² The above reservations call for a search for a better reference system, free from the above concerns. One possibility would be a transmembrane helix, as used by Nielsen et al.⁶

The penetration depth of spin labeled peptides/proteins into membranes is commonly obtained by the combined effect of paramagnetic quenchers situated selectively in the solvent and hydrophobic regions.^{6,20,63} In principle, the ESEEM methodology presented here provides the same type of information. However, there are two principal advantages. First, the data is derived directly from interactions between peptides and deuterated membrane and not through the effect of a “third party”, namely, the quencher. While per-deuterated lipids may differ from the protonated counterpart,⁶⁴ the use of specifically deuterated lipids, like DPPC-*d*₉, is more innocent because only a few protons are replaced. A second advantage is that the modulation depth can be analyzed quantitatively. We have already reported a simple model for such an analysis,²⁶ but it should be tested against a known good reference system for calibration. Two disadvantages of the ESEEM approach are that it requires frozen solutions, similar to DEER, and the use of specifically deuterated membranes, which is costly and requires special synthetic efforts.

The secondary structure of peptides/proteins in membranes, particularly helices, can be determined by solid state NMR of aligned samples using the PISEMA method.⁶⁵ The major advantage of this method is that it is label free; namely, no chemical modifications are involved, and one sample provides the information needed as opposed to the EPR methodology that requires the preparation of many mutants. Some disadvantages relative to the DEER/ESEEM approach are the much lower sensitivity, 3–9 mM of protein are required in NMR⁶⁶ as compared to 0.1–0.2 mM in EPR, and the need for well oriented samples which complicates sample preparation.

Limitations of the MC Simulations. The free energy component that described the (membrane-induced) conformational changes in the peptide is derived from the proteins' three-dimensional structures, and includes only native amino acids.⁶⁰ However, the EPR techniques included labeling of melittin with MTSL. As the spin probe could not have been taken into account, it was approximated by a leucine residue of comparable hydrophobicity.^{54,61} Consequently, the length of the probe and its other unique characteristics were not taken into consideration in the model.

An additional limitation of the model is related to the implicit description of the peptide, where each residue is represented by two interaction sites. The simplicity makes the simulations computationally feasible. However, it involves inaccuracies in the calculations, especially those related to the solvation free energy (eq 1), which strongly depends on the location of each atom. Moreover, the reduced representation leads to undefined torsion angles of the two residues at both ends of the peptide. This results in an increased flexibility of the chain ends and reduction of the stability of the α -helical conformation in the terminal segments. Accordingly, the helical content is reduced, causing desolvation of the termini. This limitation could be the reason for the discrepancy between experiment and computation regarding the peptide termini (see below).

Experimental vs Computational Results. There is good correlation between the EPR results and the MC simulations concerning the mobility. Both methods show that in the membrane-associated state the peptide ends are significantly more mobile than the core (see Figure S7 (Supporting Information), which shows the rms fluctuations of the α -carbon atoms).

The experimentally obtained distance distributions correlated well with those of the MC simulations (Figure 3). Both show a considerable narrowing of the distributions upon membrane binding. For mel-C₁₅C₂₇, however, the change was relatively small. There is also good agreement between the experimental data and simulation concerning the average distance between the α -carbon atoms (Figure 3). However, in the aqueous phase, the experimentally determined average distances are somewhat higher than the predicted values (Figure 3). Naturally, the distance measured between two MTSL labels is not the same as that determined from the α - (or β -) carbon atoms in the native peptide due to the length and the motional freedom of the label. A recent comparison of distances measured by EPR and the corresponding distances between the β -carbon atoms obtained from the crystal structures of T4-lysozyme and a comparative model of α A-crystallin showed that the difference may vary between -4 and 12 Å with an average of about $0-4$ Å.⁶⁷ Thus, the anticipation is that the measured distances between labels would appear inflated in the aqueous solution compared to the membrane, where the peptide is, in essence, restricted to the helical state.

The experimental distance distribution of mel-C₃C₁₈ is high at $r = 15-20$ Å (Figure 3) which is not reproduced by the MC simulation. This sample was the hardest to measure in terms of signal-to-noise ratio, and therefore, it was acquired for the shortest decay time. It could be that the short distances observed are artifacts due to difficulties associated with the removal of background.

Finally, we discuss the peptide orientation and location within the membrane. The MC simulations yielded an average structure of a continuous α -helix with relatively disrupted termini (Figure 7). The overall conformation is “banana-shaped” with the helix core embedded in the membrane and the termini exposed to the water/lipid polar headgroups (Figure 8). There is a rather good agreement with the ESEEM results in the relative penetration depth of mel-C₃, C₁₅, and C₁₈, while there is some disagreement regarding the N- and C-termini. In comparison to the MC simulations, the ESEEM results suggest a deeper penetration of the termini.

An earlier molecular dynamics simulation showed that MTSL has a clear hydrophobic bias.⁶⁸ Thus, when facing the membrane, the nitrogen of the probe protrudes about $5-6$ Å deeper than the α -carbon atom of the labeled residue.⁶⁸ Conversely, because of steric hindrance, a probe that is introduced at the water-accessible side of the helix would insert only about 2 Å deeper into the membrane than the α -carbon atom. Accordingly, to account for this hydrophobic bias, we added $2-6$ Å to the predicted depth of the α -carbon atoms depending on their location on the helix (Figure 8, gray arrows). Nevertheless, this correction was not sufficient to account for the discrepancy regarding the location of the N- and C-termini spin labels. The discrepancy can be due to either some uncertainties in the MC simulation regarding the peptide ends, as discussed above, or some additional bias of the spin labeling at the peptide ends. This suggests that spin labeling at the ends of the peptide may not be as innocent as desired.

Since the termini appeared to be mobile both in experiment and in simulation, and because of the high energy penalty associated with the transfer of the polar/charged termini from the aqueous phase into the membrane, we suggest that in the

native peptide they reside somewhere in the polar headgroup region of the membrane.

Conclusions

We have presented an approach that combines pulse EPR techniques and MC simulations to obtain the population and prevalent conformation, location, and orientation of membrane-bound peptides. The approach was demonstrated on melittin within a negatively charged membrane. We found that at the peptide/phospholipids ratio of 1:200 melittin is in a monomeric state and adapts an α -helical conformation, primarily parallel to the membrane surface. The obtained configuration of melittin in the membrane is characterized by polar and charged residues facing the solvent, whereas the hydrophobic amino acids penetrate deeper into the membrane. In solution, melittin is mostly disordered, though its C-terminus does have some helical character. We obtained a very good agreement between the distance distributions and the penetration depth of the residues in the peptide core. However, the experimental results showed deeper membrane penetration of the N- and C-termini than predicted by the MC simulations. This could arise from specific effects of the spin labels or from inaccuracies of the MC simulations in the peptide ends. Nevertheless, the experimental results and simulations correlate very well. Their combination provides detailed and more inclusive results that are in agreement with previous findings. Therefore, this approach can be used for further investigation of peptide–membrane interactions. Furthermore, MC simulations may be used to guide the design of EPR experiments both for phrasing of testable hypotheses regarding the structure of the peptide in the aqueous phase and the membrane, and by suggesting the optimal residues for spin labeling.

Acknowledgment. This work was supported, in part, by the ISF-VATAT Converging technologies program, by the Minerva Foundation (D.G.), and by the European Commission under the sixth Framework Programme through the Marie-Curie Action: BIOCONTROL, contract number MCRTN - 33439 (N.B.-T., Y.G.). D.G. holds the Erich Klieger Professorial chair in Chemical Physics.

Supporting Information Available: Peptide synthesis details. Six figures showing X-band EPR spectra of melittin, DEER traces and distance distributions obtained from the singly and doubly labeled melittin, normalized DEER decays after background removal for the doubly labeled melittin peptides, the $I(^2\text{H})$ values of the spin probes examined in this work in deuterated membranes and D₂O with and without melittin, the calculated free energy of melittin–membrane association as a function of the fraction of anionic lipids (at a constant ionic strength of 0.1 M) and the ionic strength, and calculated rms fluctuations of the α -carbon atoms of native melittin in association with a membrane. This material is available free of charge via the Internet at <http://pubs.acs.org>.

Note Added after Print Publication. This paper was published on the Web on September 2, 2009, and in the September 24, 2009, issue. Due to a production error, Figures 7 and 8 were incorrect. The electronic version was corrected and reposted to the Web issue on October 14, 2009. An Addition and Correction was also published (DOI: 10.1021/jp909559d).

References and Notes

- (1) Steinhoff, H. J. *Front. Biosci.* **2002**, *7*, c97.
- (2) Hubbell, W. L.; Gross, A.; Langen, R.; Lietzow, M. A. *Curr. Opin. Struct. Biol.* **1998**, *8*, 649.

- (3) Fanucci, G. E.; Cafiso, D. S. *Curr. Opin. Struct. Biol.* **2006**, *16*, 644.
- (4) Anbazhagan, V.; Vijay, N.; Kleinschmidt, J. H.; Marsh, D. *Biochemistry* **2008**, *47*, 8414.
- (5) Steinhoff, H.; Savitsky, A.; Wegener, C.; Pfeiffer, M.; Plato, M.; Mobius, K. *Biochim. Biophys. Acta* **2000**, *1457*, 253.
- (6) Nielsen, R. D.; Che, K.; Gelb, M. H.; Robinson, B. H. *J. Am. Chem. Soc.* **2005**, *127*, 6430.
- (7) Hustedt, E. J.; Beth, A. H. *Biological Magnetic Resonance: Structural information from CW-EPR spectra of dipolar coupled nitroxide spin labels*, 2000.
- (8) Han, X.; Bushweller, J. H.; Cafiso, D. S.; Tamm, L. K. *Nat. Struct. Biol.* **2001**, *8*, 715.
- (9) Steinhoff, H. *J. Biol. Chem.* **2004**, *385*, 913.
- (10) Hubbell, W. L.; Cafiso, D. S.; Altenbach, C. *Nat. Struct. Biol.* **2000**, *7*, 735.
- (11) Altenbach, C.; Greenhalgh, D. A.; Khorana, H. G.; Hubbell, W. L. *Proc. Natl. Acad. Sci. U.S.A.* **1994**, *91*, 1667.
- (12) Schiemann, O.; Prisner, T. F. *Q. Rev. Biophys.* **2007**, *40*, 1.
- (13) Jeschke, G.; Polyhach, Y. *Phys. Chem. Chem. Phys.* **2007**, *9*, 1895.
- (14) Borbat, P. P.; Freed, J. H. *Methods Enzymol.* **2007**, *423*, 52.
- (15) Milov, A. D.; Erilov, D. A.; Salnikov, E. S.; Tsvetkov, Y. D.; Formaggio, F.; Toniolo, C.; Raap, J. *Phys. Chem. Chem. Phys.* **2005**, *7* (8), 1794.
- (16) Salnikov, E. S.; Erilov, D. A.; Milov, A. D.; Tsvetkov, Y. D.; Peggion, C.; Formaggio, F.; Toniolo, C.; Raap, J.; Dzuba, S. A. *Biophys. J.* **2006**, *91*, 1532.
- (17) Hustedt, E. J.; Beth, A. H. *Biological Magnetic Resonance*, 2000, *19*; Eds. Berliner, L. J., Eaton, S. S., Eaton, G. R., Eds.; Kluwer Academic/Plenum Publishers: New York; pp 155.
- (18) Drescher, M.; Veldhuis, G.; van Rooijen, B. D.; Milikisyan, S.; Subramaniam, V.; Huber, M. *J. Am. Chem. Soc.* **2008**, *130*, 7796.
- (19) Georgieva, E. R.; Ramlall, T. F.; Borbat, P. P.; Freed, J. H.; Eliezer, D. *J. Am. Chem. Soc.* **2008**, *130*, 12856.
- (20) Jao, C. C.; Hegde, B. G.; Chen, J.; Haworth, I. S.; Langen, R. *Proc. Natl. Acad. Sci. U.S.A.* **2008**, *105*, 19666.
- (21) Dikanov, S. A.; Tsvetkov, Y. D. *Electron Spin Echo Envelope Modulation (ESEEM) Spectroscopy*; CRC Press: Boca Raton, FL, 1992.
- (22) Kevan, L.; Schwartz, R. N. Modulation of electron spin-echo decay in solids. *Time domain electron spin resonance*; John Wiley & Sons: New-York, 1979; p 279.
- (23) Schweiger, A.; Jeschke, G. Nuclear modulation effect I: basic experiments. *Principles of pulse electron paramagnetic resonance*; Oxford University Press: New York, 2001.
- (24) Bartucci, R.; Erilov, D. A.; Guzzi, R.; Sportelli, L.; Dzuba, S. A.; Marsh, D. *Chem. Phys. Lipids* **2006**, *141*, 142.
- (25) Erilov, D. A.; Bartucci, R.; Guzzi, R.; Shubin, A. A.; Maryasov, A. G.; Marsh, D.; Dzuba, S. A.; Sportelli, L. *J. Phys. Chem. B* **2005**, *109*, 12003.
- (26) Carmieli, R.; Papo, N.; Zimmermann, H.; Potapov, A.; Shai, Y.; Goldfarb, D. *Biophys. J.* **2006**, *90*, 492.
- (27) Milik, M.; Skolnick, J. *Proteins* **1993**, *15*, 10.
- (28) Baumgartner, A. *Biophys. J.* **1996**, *71*, 1248.
- (29) Ducarme, P.; Rahman, M.; Brasseur, R. *Proteins* **1998**, *30*, 357.
- (30) Efremov, R. G.; Nolde, D. E.; Vergoten, G.; Arseniev, A. S. *Biophys. J.* **1999**, *76*, 2448.
- (31) Maddox, M. W.; Longo, M. L. *Biophys. J.* **2002**, *82*, 244.
- (32) Veresov, V. G.; Davidovskii, A. I. *Eur. Biophys. J.* **2007**, *37*, 19.
- (33) Tzliil, S.; Murray, D.; Ben-Shaul, A. *Biophys. J.* **2008**, *95*, 1745.
- (34) Wee, C. L.; Sansom, M. S.; Reich, S.; Akhmatskaya, E. *J. Phys. Chem. B* **2008**, *112*, 5710.
- (35) Shental-Bechor, D.; Haliloglu, T.; Ben-Tal, N. *Biophys. J.* **2007**, *93*, 1858.
- (36) Kessel, A.; Shental-Bechor, D.; Haliloglu, T.; Ben-Tal, N. *Biophys. J.* **2003**, *85*, 3431.
- (37) Habermann, E. *Science* **1972**, *177*, 314.
- (38) Terwilliger, T. C.; Eisenberg, D. *J. Biol. Chem.* **1982**, *257*, 6010.
- (39) Terwilliger, T. C.; Eisenberg, D. *J. Biol. Chem.* **1982**, *257*, 6016.
- (40) Brown, L. R.; Braun, W.; Kumar, A.; Wuthrich, K. *Biophys. J.* **1982**, *37*, 319.
- (41) Inagaki, F.; Shimada, I.; Kawaguchi, K.; Hirano, M.; Terasawa, I.; Ikura, T.; Go, N. *Biochemistry* **1989**, *28*, 5985.
- (42) Okada, A.; Wakamatsu, K.; Miyazawa, T.; Higashijima, T. *Biochemistry* **1994**, *33*, 9438.
- (43) Lam, Y. H.; Wassall, S. R.; Morton, C. J.; Smith, R.; Separovic, F. *Biophys. J.* **2001**, *81*, 2752.
- (44) Raghuraman, H.; Chattopadhyay, A. *Biosci. Rep.* **2007**, *27*, 189.
- (45) Eibl, H. *Proc. Natl. Acad. Sci. U.S.A.* **1978**, *75*, 4074.
- (46) Fellmann, P.; Zachowski, A.; Devaux, P. F. *Methods Mol. Biol.* **1994**, *27*, 161.
- (47) MacDonald, R. C.; MacDonald, R. I.; Menco, B. P.; Takeshita, K.; Subbarao, N. K.; Hu, L. R. *Biochim. Biophys. Acta* **1991**, *1061*, 297.
- (48) Papo, N.; Shai, Y. *Biochemistry* **2003**, *42*, 458.
- (49) Pannier, M.; Veit, S.; Godt, A.; Jeschke, G.; Spiess, H. W. *J. Magn. Reson.* **2000**, *142*, 331.
- (50) Jeschke, G.; Chechik, V.; Ionita, P.; Godt, A.; Zimmermann, H.; Bahman, J.; Timmel, C. R.; Hilger, D.; Jung, H. *Appl. Magn. Reson.* **2006**, *30* (3–4), 473.
- (51) Fauth, J. M.; Schweiger, A.; Braunschweiler, L.; Forrer, J.; Ernst, R. R. *J. Magn. Reson.* **1986**, *66*, 74.
- (52) Van Doorslaer, S.; Sierra, G. A.; Schweiger, A. *J. Magn. Reson.* **1999**, *136*, 152.
- (53) Shental-Bechor, D.; Kirca, S.; Ben-Tal, N.; Haliloglu, T. *Biophys. J.* **2005**, *88*, 2391.
- (54) Yu, Y. G.; Thorgeirsson, T. E.; Shin, Y. K. *Biochemistry* **1994**, *33*, 14221.
- (55) Petrey, D.; Xiang, Z.; Tang, C. L.; Xie, L.; Gimpelev, M.; Mitros, T.; Soto, C. S.; Goldsmith-Fischman, S.; Kernysky, A.; Schlessinger, A.; Koh, I. Y.; Alexov, E.; Honig, B. *Proteins* **2003**, *53*, 430.
- (56) Ruthstein, S.; Goldfarb, D. *J. Phys. Chem. C* **2008**, *112* (18), 7102.
- (57) Zanker, P. P.; Jeschke, G.; Goldfarb, D. *J. Chem. Phys.* **2005**, *122*, 024515.
- (58) Ladokhin, A. S.; White, S. H. *Biochim. Biophys. Acta* **2001**, *1514*, 253.
- (59) Lazaridis, T. *Proteins* **2005**, *58*, 518.
- (60) Bahar, I.; Jernigan, R. L. *J. Mol. Biol.* **1997**, *266*, 195.
- (61) Sammalkorpi, M.; Lazaridis, T. *Biophys. J.* **2007**, *92*, 10.
- (62) Volkov, A.; Dockter, C.; Bund, T.; Paulsen, H.; Jeschke, G. *Biophys. J.* **2009**, *96*, 1124.
- (63) Macosko, J. C.; Kim, C. H.; Shin, Y. K. *J. Mol. Biol.* **1997**, *267*, 1139.
- (64) Aussenac, F.; Laguerre, M.; Schmitter, J. M.; Dufourc, E. J. *Langmuir* **2003**, *19*, 10468.
- (65) Opella, S. J.; Nevzorov, A.; Mesleb, M. F.; Marassi, F. M. *Biochem. Cell Biol.* **2002**, *80*, 597.
- (66) De Angelis, A. A.; Howell, S. C.; Nevzorov, A. A.; Opella, S. J. *J. Am. Chem. Soc.* **2006**, *128*, 12256.
- (67) Alexander, N.; Bortolus, M.; Al-Mestarihi, A.; McHaourab, H.; Meiler, J. *Structure* **2008**, *16*, 181.
- (68) Sammalkorpi, M.; Lazaridis, T. *Biochim. Biophys. Acta* **2007**, *1768*, 30.

**Paper II: Interaction of an antimicrobial peptide with membranes:
experiments and simulations with NKCS.**

Yana Gofman, Sebastian Linser, Agnieszka Rzeszutek, Dalit Shental-Bechor, Sergio S. Funari,
Nir Ben-Tal and Regine Willumeit

Published in *J Phys Chem B*, 2010, 114(12):4230-4237.

Reprinted with permission from “Interaction of an antimicrobial peptide with membranes: experiments and simulations with NKCS”, Yana Gofman et al., *The Journal of Physical Chemistry B*, American Chemical Society, Apr 1, 2010. Copyright (2010), American Chemical Society.

Interaction of an Antimicrobial Peptide with Membranes: Experiments and Simulations with NKCS

Yana Gofman,[†] Sebastian Linser,[†] Agnieszka Rzeszutek,[†] Dalit Shental-Bechor,[‡] Sergio S. Funari,[§] Nir Ben-Tal,^{*‡} and Regine Willumeit^{*‡}

GKSS Research Center, 21502 Geesthacht, Germany, Department of Biochemistry, The George S. Wise Faculty of Life Sciences, Tel-Aviv University, Ramat-Aviv, 69978 Tel-Aviv, Israel, and Hasylab, DESY, 22603 Hamburg, Germany

Received: September 23, 2009; Revised Manuscript Received: January 6, 2010

We used Monte Carlo simulations and biophysical measurements to study the interaction of NKCS, a derivative of the antimicrobial peptide NK-2, with a 1-palmitoyl-2-oleoyl-*sn*-glycero-3-phosphoethanolamine (POPE) membrane. The simulations showed that NKCS adsorbed on the membrane surface and the dominant conformation featured two amphipathic helices connected by a hinge region. We designed two mutants in the hinge to investigate the interplay between helicity and membrane affinity. Simulations with a Leu-to-Pro substitution showed that the helicity and membrane affinity of the mutant (NKCS-[LP]) decreased. Two Ala residues were added to NKCS to produce a sequence that is compatible with a continuous amphipathic helix structure (NKCS-[AA]), and the simulations showed that the mutant adsorbed on the membrane surface with a particularly high affinity. The circular dichroism spectra of the three peptides also showed that NKCS-[LP] is the least helical and NKCS-[AA] is the most. However, the activity of the peptides, determined in terms of their antimicrobial potency and influence on the temperature of the transition of the lipid to hexagonal phase, displayed a complex behavior: NKCS-[LP] was the least potent and had the smallest influence on the transition temperature, and NKCS was the most potent and had the largest effect on the temperature.

Introduction

After half a century of almost complete control over microbial infections, the past decade has brought a worldwide resurgence of infectious diseases due to the evolution of antibiotic-resistant strains at an alarming rate.^{1,2} As a potential class of novel antimicrobial agents, animal-derived antimicrobial peptides (AMP) have recently emerged.^{3–5} These peptides are fast and lethal toward a broad spectrum of pathogens but are quite harmless to eukaryotic cells. Some AMPs also possess anti-cancer and antiviral activity, as well as the capacity to manipulate the innate immune response.³ The first generation of antimicrobial peptides is already at the edge of application.^{4,6} However, the dose effective *in vitro* is very close to the toxic dose in animal models, indicating that a concerted effort to understand the interaction of antibacterial peptides with their target membrane is of utmost importance.

The precise mechanism of action of antimicrobial peptides and the molecular basis for their selective cytotoxicity are not fully understood. Data suggest that, regardless of their origin and the diversity in their primary and secondary structure, the antimicrobial activity of the peptides is a result of direct interactions with the phospholipids of the pathogens' membrane rather than association with a specific receptor. It is generally believed that most antimicrobial peptides lyse their target cell by the destabilization of the cytoplasmic membrane.^{3,7–10} The selectivity of the cytolytic mechanism is assumed to stem from inherent differences in the lipid composition of the target cells.¹⁰

The NK-2 peptide, corresponding to residues 39–65 of the NK-lysin protein, has been investigated extensively due to its high antimicrobial^{11–13} and anticancer qualities¹⁴ as well as low hemolytic activity.¹¹ The peptide was found to reduce the transition temperature of the lipid bilayer in a concentration dependent manner by up to 10 °C.¹⁵ The replacement of cysteine residue within the NK-2 sequence with a serine (C7S), resulted in a peptide with an improved antibacterial activity referred to as NKCS in the current study.¹⁶ Both peptides are randomly coiled in water and adopt a helical structure upon interaction with the lipid bilayer.^{11,16}

Several approaches are used to investigate the interaction between antibacterial peptides and lipid membranes. These include biophysical studies using techniques such as differential scanning calorimetry (DSC),¹⁷ Fourier transform infrared (FTIR) spectroscopy,¹⁸ circular dichroism (CD) spectroscopy,¹⁹ scattering techniques (X-ray and neutron scattering),^{17,20} NMR,²¹ and surface plasmon resonance (SPR),²² as well as computational studies including molecular dynamics simulations,^{23,24} continuum solvent models,^{25,26} and Monte Carlo (MC) simulations.^{27–34} In this work we characterized the interactions between the cationic peptide NKCS and 1-palmitoyl-2-oleoyl-*sn*-glycero-3-phosphoethanolamine (POPE) membranes. We employed small-angle X-ray scattering (SAXS) and SPR along with measurements of the antibacterial and hemolytic activity in cells. We used CD spectroscopy to estimate the peptide's helicity. In addition, we performed MC simulations of NKCS and its derivatives in a POPE membrane.^{35–38}

Phosphoethanolamine (PE) is a prominent example for the capability of a lipid to create nonbilayer forms such as hexagonal phases. Under suitable conditions even cubic structures are formed.^{39,40} The local formation of nonbilayer structures is a prerequisite for the fusion and division of cell membranes when,

* Corresponding authors. E-mail: N.B.-T., NirB@tauex.tau.ac.il; R.W., Regine.Willumeit@gkss.de.

[†] GKSS Research Center.

[‡] Tel-Aviv University.

[§] Hasylab.

TABLE 1: Amino Acid Sequences of the Peptides

NKCS	KILRGVSKKIMRT	FLRRISKDILTGKK
NKCS-[LP]	KILRGVSKKIMRT	FPRRISKDILTGKK
NKCS-[AA]	KILRGVSKKIMRTAAFLRRISKDILTGKK	

^aThe changes are marked in bold fonts.

for very short periods of time, these structures are built in a living system.⁴¹ The fraction of PE in the cytoplasmic membrane varies between, e.g., 69% of the total phospholipid in *Escherichia coli*,⁴² 10% in *Bacillus subtilis*,⁴³ and 0% in *Staphylococcus aureus*.⁴⁴ Even though PE is not always the most abundant lipid in bacterial membranes, it interacts strongly with cationic peptides, leading to changes in the phase transition temperature. Specifically, magainin⁴⁵ and its analog MSI-78⁴⁶ show a significant increase in the lipid hexagonal phase transition temperature, whereas gramicidin,⁴⁷ alamethicin,⁴⁸ and the wasp venom peptide mastoparan⁴⁹ reduce the temperature.

The central hypothesis of this paper is that simple structural features, such as α -helicity and amphipathicity can be used to interpret changes in the membrane affinity of NKCS. We design two mutants, NKCS-[AA] and NKCS-[LP], to examine it, and to correlate the membrane affinity and activity of the peptides. We show that NKCS, NKCS-[AA], and NKCS-[LP] are, in essence, random coils in the aqueous solution. Upon membrane association, NKCS and NKCS-[AA] assume helical conformations, while the helical content of NKCS-[LP] stays low. This is demonstrated both in the CD spectroscopy studies and in the simulations. However, the assumption that the biological activity of a peptide increases with its membrane affinity might not always be true. For example, NKCS-[AA] and NKCS-[LP] manifest similar activities despite significant changes in the values of their calculated membrane-association free energies.

Theoretical Calculations

Monte Carlo simulations of the interaction of a peptide molecule with POPE membranes were performed as described previously.^{35–38} The peptide was described using a reduced representation with each amino acid represented as two interaction sites, one corresponding to the α -carbon and the other to the side chain. The initial conformations of the peptides were modeled using the Nest program,⁵⁰ based on the structure of NK-lysine from the Protein Data Bank (entry 1NKL, model 1). The lipid membrane was approximated as a hydrophobic profile, corresponding to the hydrocarbon region of the membrane. The model membrane included also surface charges, corresponding to the polar headgroups, which interacted electrostatically with the titratable residues of the peptide, depending on their protonation state, using the Gouy–Chapman potential. A more detailed computational protocol is available in the Supporting Information.

Materials and Methods

Peptides. The peptide NKCS and its derivatives were synthesized by Biosyntan (Berlin, Germany). All three peptides carry a net charge of +10 (calculated by counting the N-terminus, lysine, histidine, and arginine as positive charges and counting aspartate as a negative charge; the C-termini are amidated). The sequences are shown in Table 1. The choice of peptides is explicated in Discussion. The purity of 95% was guaranteed by analytical RP-HPLC (Lichrospher 100 RP 18, 5 μ m columns, Merck, Darmstadt, Germany) and MALDI-TOF (Bruker Daltonik GmbH, Bremen, Germany) performed by the company.

Melittin was purchased from Sigma-Aldrich (Deisenhofen, Germany). It was used to compare its known hemolytic activity with that of the investigated peptides.⁵¹

The peptides were stored at -20 °C. Directly before use they were dissolved in double distilled water to a final concentration of 1 mM. Between the experiments the peptide solutions were also stored at -20 °C.

Lipid. The phospholipid POPE was purchased from Sigma-Aldrich (Deisenhofen, Germany) and stored airtight in the freezer at -20 °C.

Circular Dichroism (CD). CD data were acquired with a JASCO CD spectrophotometer (JASCO, Gross-Umstadt, Germany) using quartz cuvettes with an optical path length of 0.1 cm. The CD was measured between 260 and 185 nm with a 0.5 nm step resolution and a 1 nm bandwidth. The counting rate was 50 nm/min with 4 s response time. Each spectrum was a sum of at least three scans to improve the signal/noise ratio. The detergent, sodium dodecyl sulfate (SDS) (Fluka, St. Louis, MO), which mimics some characteristics of biological membranes, was added to the cuvette with final concentrations of 1 and 10 mM in double distilled water before the peptides were added. As references, the spectra of double distilled water and SDS at the respective concentration were subtracted from the measurements with peptides. All spectra were collected for a concentration of 60 μ M peptide in double distilled water. The molar ratio of peptide to SDS was 1:17 (for 1 mM SDS) and 1:167 (10 mM SDS).

Surface Plasmon Resonance (SPR). Surface plasmon resonance phenomenon allows performing the real-time measurements of the adhesion of molecules to the biomimetic surfaces. The SPR detector detects the changes in optical properties at the sensor surface coated with the ligand due to the adsorption and desorption of the solute.⁵²

The SPR apparatus BIAcore X (GE Healthcare, Freiburg, Germany) was equipped with an internal injection system (500 μ L Hamilton syringe). The running buffer was a 10 mM sodium phosphate buffer (pH 7.4), and the flow rate was 5 μ L/min for all experiments. We used the BIAcore L1 chip, which was composed of a thin dextran matrix modified by lipophilic compounds on a gold surface where the lipid vesicles could be captured.⁵³ All solutions were freshly prepared, degassed, and filtered through 0.22 μ m pores. The experiments were done at the room temperature (RT). After the system was cleaned according to the manufacturer's instructions, the BIAcore X apparatus was left running overnight using Milli-Q water as eluent to thoroughly wash all liquid-handling parts of the instrument. The L1 chip was then installed, and the surface was cleaned by an injection of the nonionic detergent *N*-octyl β -D-glucopyranoside (50 μ L, 40 mM).

The phospholipid POPE was dissolved in a methanol/chloroform (Merck, Darmstadt, Germany) (1/2, v/v) solution. The solvent was slowly removed by a constant stream of nitrogen. The resulting lipid film was dried in a vacuum oven at 40 °C overnight. Just before the experiments, the lipid films were hydrated in buffer. To form multilamellar vesicles of POPE, sodium phosphate buffer (Merck, Darmstadt, Germany) was added at the room temperature to the lipid films and a small amount of glass beads was put into the vials. After vortexing for 1 min, the solution was incubated for 2 h at 28 °C, while every 30 min the sample was vortexed. Then the solution was cooled to RT and POPE vesicles (100 μ L, 1 mM) were applied to the chip surface. To remove artifacts, NaOH (5 μ L, 10 mM) was injected, which resulted in a stable baseline corresponding to the lipid bilayer linked to the chip surface. The thickness of

TABLE 2: Average Binding Free Energy and Fraction of All, “Inner” and “Outer” Conformations of NKCS, NKCS-[LP], and NKCS-[AA] Predicted by the MC Simulations^a

peptide	conformations	calculated membrane-association energy (<i>kT</i>)	fraction (%)	measured membrane-association energy (<i>kT</i>)
NKCS	inner	-21.6 ± 1.8	85 ± 3	-18.5 ± 1.1 ($n = 6$)
	outer	-6.5 ± 0.7	15 ± 3	
	all	-20.5 ± 1.9	100	
NKCS-[LP]	inner	-17.3 ± 1.6	64 ± 2	-16.1 ± 0.3 ($n = 5$)
	outer	-10.9 ± 1.0	36 ± 2	
	all	-16.0 ± 1.0	100	
NKCS-[AA]	inner	-34.3 ± 0.4	99.8 ± 0.2	-25.7 ± 0.3 ($n = 5$)
	outer	38.9 ± 19.0	0.2 ± 0.2	
	all	-34.3 ± 0.4	100	

^a For comparison, the average binding energies of the peptides to POPE measured using SPR are presented in the last column. The number of experiments, n , is indicated in parentheses. All values are shown as average \pm standard deviation.

the bilayer was calculated by assuming that 1000 RU (response units) correspond to 1 nm layer thickness.⁵⁴ This bilayer was subsequently used as a model membrane surface to study the peptide–membrane interactions. For all peptides, 50 μ L of a 1 μ M solution was injected while the adsorption and desorption of the peptide was observed until it resulted in a stable signal. Finally, NaOH was injected to wash all unbound compounds away. All measurements were performed in triplicates.

Small Angle X-ray Scattering (SAXS). The POPE vesicles were prepared as described above with a final concentration of 25 mg/mL. After 30 min at room temperature, mixing with the appropriate peptide solution followed. The measurements were performed at the A2 beamline at HASYLAB, DESY. It ran with a wavelength $\lambda = 0.15$ nm and covered a scattering vector $s = 1/d = (2 \sin \theta)/\lambda$ ($2\theta =$ scattering angle, $d =$ lattice spacing) from 1×10^{-2} to 0.5 nm^{-1} . The calibration for the SAXS pattern was done by measuring rat tail tendon (repeat distance 65 nm, standard at beamline A2) in addition to silver behenate ($[\text{CH}_3(\text{CH}_2)_2\text{OCOO}-\text{Ag}]$, repeat distance 5.838 nm, made available at beamline A2). The samples were measured in a temperature-controlled sample holder, where the temperature was varied with an increase of 2 $^\circ\text{C}/\text{min}$ and the data were collected for 10 s per measurement.

The data were normalized with respect to the primary beam and the background (buffer measurement). The positions of the diffraction peaks were determined using the OTOKO software.⁵⁵ The repeat distances were calculated from the peak positions based on the rat tail tendon and silver behenate calibration.

Antibacterial Assay. The *Escherichia coli* strain K12 (ATCC 23716), the *Staphylococcus carnosus* strain (ATCC 51365), and the *Bacillus subtilis* strain (ATCC 6051) (all bacteria were obtained from DSMZ, Braunschweig, Germany) were cultivated in the respective medium at 37 $^\circ\text{C}$ with shaking at 160 rpm to reach the log-phase. The peptides were 2-fold serial diluted and 10 μ L of the log-phase bacteria suspension containing 100 colony forming units (CFU) was added to 90 μ L of the peptide solution to measure the antibacterial activity by a microdilution susceptibility test. The density of the bacteria suspension was measured photometrically at 620 nm wavelength with a microplate reader (Tecan, Crailsheim, Germany). Values of the minimal inhibitory concentration (MIC) were defined as the concentration of the highest dilution of the peptides at which the bacteria growth was completely suppressed.

Hemolysis. To measure the hemolytic activity of the peptides, fresh (maximum storage time was 2 days) human blood (group 0 rhesus positive), was centrifuged for 3 min at 2000 rpm. The supernatant was discarded and the pellet washed with phosphate buffered saline (PBS) three times. The erythrocytes pellet was subsequently diluted with MES buffer (20 mM morpholinoet-

hanesulfonic acid, 140 mM NaCl, pH 5.5 (Merck, Darmstadt, Germany)) until 20 μ L of this suspension added to 980 μ L of double distilled water gave the absorbance 1.4 at the wavelength of 412 nm, which equaled 5×10^8 cells/mL. The peptides were diluted in MES buffer to the desired concentrations before 20 μ L of the erythrocyte suspension was added to 80 μ L of peptide solution. As the control, 20 μ L of erythrocyte suspension was mixed with 80 μ L of double distilled water, expecting 100% lysis of the erythrocytes. The negative control was made by mixing 20 μ L of erythrocyte suspension and 80 μ L of MES buffer. After all samples were carefully mixed, the suspensions were incubated for 30 min at 37 $^\circ\text{C}$. Directly after incubation the samples were stored on ice and MES buffer (900 μ L) was added. All suspensions were centrifuged for 10 min at 2000 rpm to separate intact erythrocytes. Finally, the absorbance was measured with a spectrometer (Tecan, Crailsheim, Germany) at 412 nm wavelength.

Simulation Results

We conducted preliminary MC simulations of NKCS in the aqueous phase and within a POPE membrane and analyzed the structural and free energy determinants of the membrane association. The peptide adsorbed on the membrane surface with an association free energy of -20.5 kT (Table 2). A close look at the predicted conformations of the peptide showed a mixture of two main groups (Figure 1A). In the first (Figure 1A), which we called “the inner group of conformations”, the peptide was partially dissolved in the membrane. The nonpolar residues were immersed in the hydrophobic region of the membrane, whereas the polar and charged residues were located in water, in close proximity to the membrane surface charge. Most of the conformations were helical with a distortion (hinge) in residues Thr-13 and Phe-14 (Figure 1B). In the second, outer, group of NKCS conformations, the peptide was randomly coiled and located, in essence, outside the membrane. This group of conformations resembled in its low helix content the conformations that were observed in the aqueous phase. The lysine and arginine residues pointed toward the slightly negatively charged membrane surface, whereas the nonpolar residues of the peptide faced the aqueous phase and did not interact with the membrane.

The free energy of membrane-association of the NKCS “inner” conformations was significantly lower (i.e., more favorable) than that of the “outer” ones (Table 2). Free energy decomposition suggested that the difference is mainly due to desolvation of the nonpolar residues (Supporting Information Table S1). These were embedded in the membrane in the inner conformations and interacted favorably with the hydrocarbon region whereas in the outer conformations they faced the solvent.

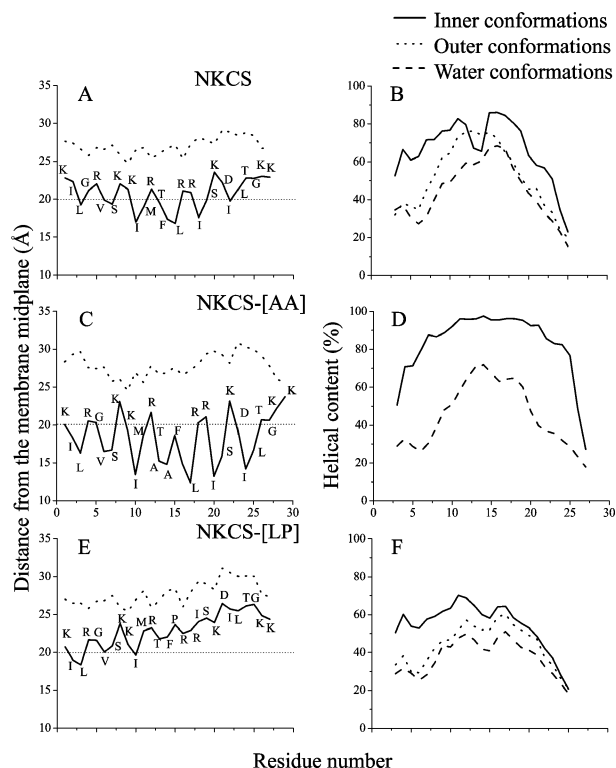


Figure 1. Location of the inner and outer conformations of (A) NKCS, (C) NKCS-[AA], and (E) NKCS-[LP] near the membrane. The average distance of the α -carbon atoms from the membrane midplane in the MC simulations is shown for each residue. The horizontal dotted line marks the location of the lipids polar heads. The calculated helical content of (B) NKCS, (D) NKCS-[AA], and (F) NKCS-[LP] in the aqueous phase and near the membrane. Inner, outer, and water conformations are represented with different curves, as indicated. The helical content of the outer group of NKCS-[AA] is not shown since there were only 6 conformations (out of 3600). In all cases the helical content of the water conformations was the lowest and that of the inner conformations highest.

Additionally, the membrane-induced helix formation, as well as close electrostatic interactions between positively charged residues and the negatively charged membrane surface, made the “inner” group of conformations more favorable (Supporting Information Table S1).

On the basis of the preliminary simulations, we hypothesized that the membrane affinity depends on the compatibility of NKCS’s sequence with an amphipathic helix structure and designed two peptides to examine this possibility (Table 1). In the first (NKCS-[AA]) we added two consecutive Ala residues into the hinge region of NKCS. With this, the polypeptide sequence becomes compatible with an amphipathic helix structure (Figure 2B) and the anticipation was that its membrane affinity would increase. Indeed, the simulations showed that the vast majority of the conformations, above 99% of total (Table 2), were embedded in the membrane with nonpolar residues within the hydrophobic core and the polar residues in the aqueous phase (Figure 1C). The helical content of these conformations was much higher than that of the original peptide and the only distortions were in the termini (Figure 1D). Reassuringly, the membrane affinity of NKCS-[AA] was much stronger than that of the original peptide (Table 2), as we hoped.

As a negative control experiment, we also designed a second variant (NKCS-[LP]) in which Leu-15 was replaced with a Pro. The idea was to interfere further with the helical structure of the peptide, thereby reducing its membrane affinity. Indeed, the

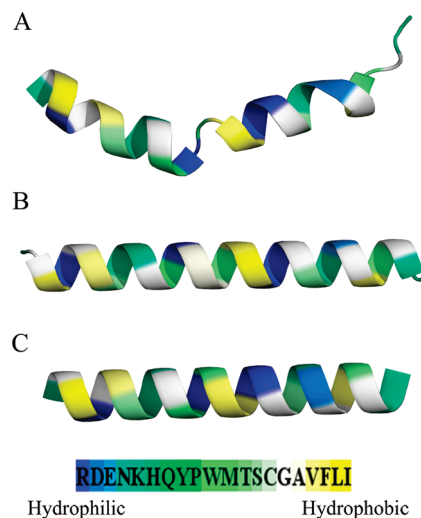


Figure 2. Compatibility of the peptide sequence with an amphipathic helical structure. The peptide is represented as ribbons colored according to the hydrophobicity scale in the bar. (A) Representative structure of NKCS in an “inner” conformation, obtained from the MC simulations in the membrane. The view is from the membrane surface upward, and the structure features two short amphipathic helices, connected by a hinge. (B) NKCS-[AA], constructed as a canonical α -helix. In contrast to NKCS, the sequence of NKCS-[AA] is consistent with the amphipathic helix structure. This is indeed the predominant conformation of the peptide in association with the membrane. The view is from the membrane plan upward, as in “A”. (C) NKCS in a (hypothetical) canonical α -helix conformation. It is evident from the picture that the hydrophobic and polar/charged amino acids are spread in all directions and the conformation is not amphipathic. That is, NKCS’s amino acid sequence is not compatible with an amphipathic helix structure.

NKCS-[LP] peptide associated with the membrane with less negative free energy than the original peptide NKCS (Table 2). Also here it was possible to distinguish between two groups of conformations. The outer group resembled that of NKCS in orientation and helical content. In both, the N-terminus up to Thr-13 was on average adsorbed on the surface of the membrane (Figure 1A,E) with quite high helical content (Figure 1B,F). The C-terminal region of NKCS-[LP], however, was located in the aqueous phase, and somewhat distorted, by design, due to the presence of Pro-15. Besides disruption of the α -helix, Pro-15 lowered the kink’s flexibility, making the amphipathic arrangement of the peptide even less plausible than that of the original peptide.

To summarize, the conformations of the three peptides investigated in the simulations could be divided into two groups. The inner conformations were helical to various degrees, and amphipathic, with nonpolar residues facing the membrane. The outer conformations were much less helical and the interaction of the peptide with the membrane was maintained only by the Coulombic attraction between the positively charged Arg and Lys residues of the peptide with the membrane surface charge. According to the simulations, the membrane affinity of the peptide depended on the compatibility of its sequence with the amphipathic helix structure, in agreement with our hypothesis. Next we describe experiments that characterize the helicity of the three peptides and examine their membrane affinity and activity.

Experimental Results

CD Spectroscopy. To characterize the structure of NKCS, NKCS-[LP], and NKCS-[AA], we carried out CD experiments in the presence and absence of SDS. According to our results,

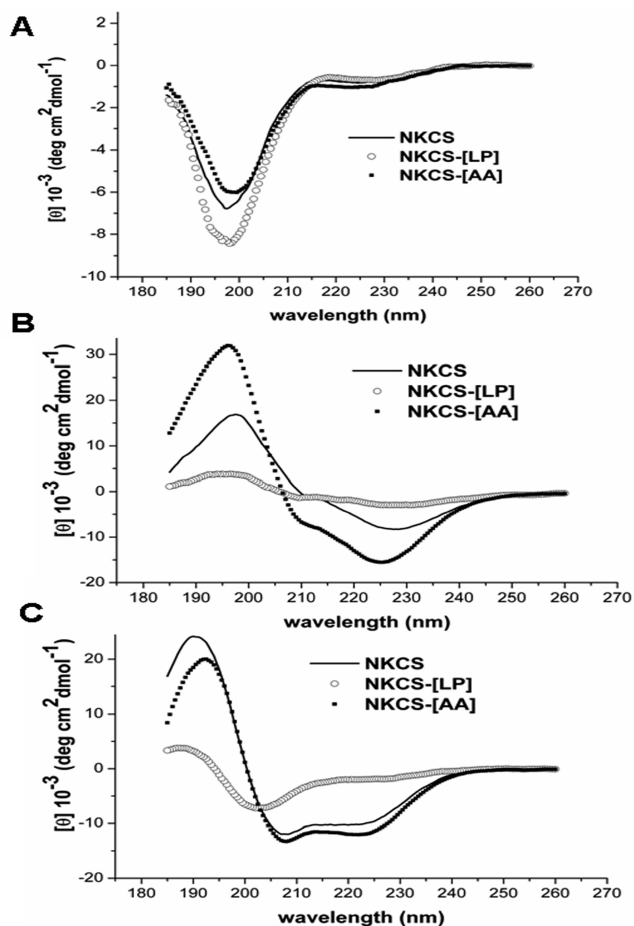


Figure 3. (A) CD measurements of NKCS and its derivatives in double distilled water. Negative bands in the region 198–200 nm and positive bands in the range 216–218 nm indicate disordered peptide structures. CD measurements of NKCS and its derivatives mixed with 1 mM (B) and 10 mM (C) SDS. The low concentration of detergent induced the adoption of ordered structures. At 10 mM SDS, NKCS and NKCS-[AA] clearly fold into α -helices (positive bands at 190–192 nm, negative bands at 208 and 222 nm). NKCS-[LP] is a mixture of β -sheet and random coils.

the three peptides were randomly coiled in water (Figure 3A). After the addition of the negatively charged SDS detergent, the adoption of a secondary structure was visible. Below the critical micelle concentration (CMC) of SDS, which is 8 mM, the peptides showed a preference toward the α -helical conformation (Figure 3B). The strong signal of NKCS-[AA] indicated a higher helical content in comparison with the two other peptides. At an SDS concentration above the CMC (10 mM), the helicity of NKCS and NKCS-[AA] increased (Figure 3C), but NKCS-[LP] seemed to adopt a mixture of random coils and β structures.

SPR. The interaction between the peptides and the lipid bilayer was investigated using the SPR method. The successful coating of the BIAcore L1 chip by POPE was documented by the increase in the response units from 18200 to 24000 after rinsing with NaOH to wash away the unbound lipids (Figure 4A). The increase corresponded to a layer of thickness of 58 Å, similar to the thickness of a hydrated membrane obtained on the basis of SAXS measurements.

After injection of NKCS, a strong adsorption of the peptide was visible followed by a very slow desorption (Figure 4A). Such a behavior suggested a strong interaction between the peptide and POPE bilayers. The thickness of the peptide layer was estimated as 14 Å, corresponding to the diameter of an α -helix.^{56,57} A different picture was observed after injection of

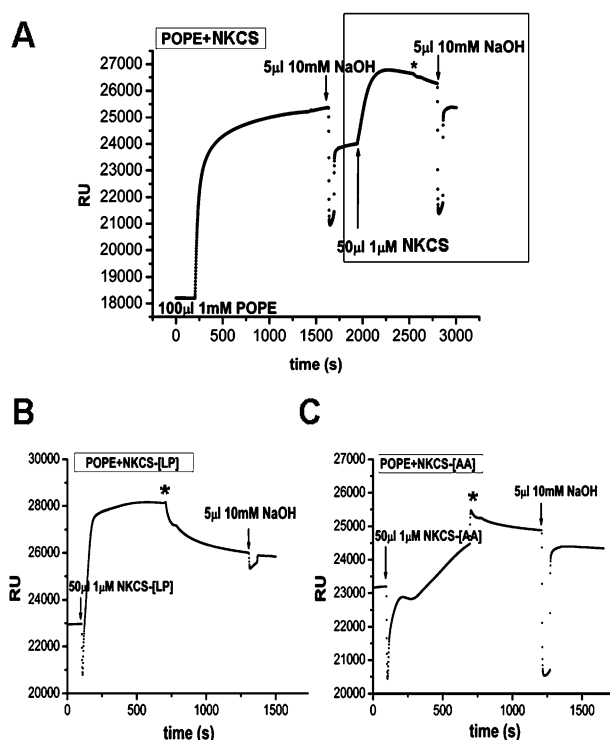


Figure 4. SPR measurements of the (A) NKCS, (B) NKCS-[LP], and (C) NKCS-[AA] peptides. Injections of POPE, NaOH, and peptides are indicated. The frame highlights the time range of the peptide–membrane interaction of NKCS with POPE. The onset was normalized to zero for NKCS-[LP] and NKCS-[AA]. The asterisks mark the end of the peptide injection and the beginning of peptide desorption. RU = response units.

NKCS-[LP] (Figure 4B). The peptide also adsorbed quickly. However, its desorption was very fast, which is indicative of a weaker affinity to the membrane than NKCS. The measurement allowed to estimate the peptide layer thickness as 29 Å.

The interaction of NKCS-[AA] with the POPE bilayer was more complicated (Figure 4C). After the injection of the peptide, its adsorption was very fast and strong but turned into a short desorption after 100 s. After an additional 80 s, a peptide adsorption occurred again. When the injection ended a slow desorption was observed. From the reference units (RU) one could approximate a peptide layer thickness of 12 Å, which corresponds to a single peptide layer. However, it should be stated that the determination of layer thickness from RU is a very difficult task and the reported values should be taken only as approximations.

For comparison, we determined the peptides' membrane affinity from the SPR sensograms, following previous studies.^{22,58} The obtained values were similar to the computationally predicted ones, i.e., $-18.5kT$, $-16.1kT$, and $-25.7kT$ for NKCS, NKCS-[LP], and NKCS-[AA], respectively (Table 2).

SAXS Measurements. SAXS measurements were performed to investigate the influence of the peptides on the repeat distance (sum of lipid bilayer thickness and water layer between two lipid bilayers) and the inverse hexagonal phase transitions of POPE. All peptides changed the inverse hexagonal phase transition temperature of POPE liposomes (Supporting Information Figure S1 and Table 3) whereas the repeat distance, which was determined to be 55 ± 9 Å at 37 °C for POPE, remained the same within the error for all experiments (data not shown). All tested peptides shifted the transition temperature to higher values in a concentration dependent manner (Table 3). There

TABLE 3: Increase of the Inverse Hexagonal Phase Transition Temperature of a POPE Vesicles upon Interaction with NKCS Derivatives, Expressed as ΔT ($^{\circ}\text{C}$)^a

molar ratio [lipid/peptide]	NKCS	NKCS-[AA]	NKCS-[LP]
1000:1	4	3	4
300:1	10	5	5
100:1		9	6

^a The aggregation of the sample POPE + NKCS in the molar ratio of 100:1 was so strong that the transfer into the measurement capillary was not possible.

TABLE 4: Antibacterial Activity of NKCS, NKCS-[AA], and NKCS-[LP] against *E. coli*, *S. carnosus*, and *B. subtilis* Determined as MIC (Minimal Inhibitory Concentration, μM)

peptide	<i>E. coli</i>	<i>S. carnosus</i>	<i>B. subtilis</i>
NKCS	0.63	2.5	1.25
NKCS-[AA]	1.25	2.5	2.5
NKCS-[LP]	2.5	5	5
melittin	2.5	0.63	0.63

was no effect on the pretransition between the gel and liquid crystalline phase for any of the peptides (data not shown).

Antibacterial and Hemolytic Activity. The three peptides NKCS, NKCS-[LP], and NKCS-[AA] and melittin (as a control) were tested against one Gram-negative and two Gram-positive bacteria strains and human erythrocytes. NKCS and its derivatives exhibited a good antibacterial activity against both types of bacteria, though they were slightly more active against the Gram-negative *E. coli* (Table 4). NKCS-[LP] showed an activity similar to that of melittin against *E. coli*, while NKCS and NKCS-[AA] were more potent. For the Gram-positive strains the minimal inhibitory concentration (MIC) of the three NKCS-based peptides was higher than the MIC of melittin. The peptides showed low hemolytic activity in comparison to melittin. At the very high concentration of 100 μM , the NKCS-[LP] and NKCS-[AA] derivatives caused lysis of 44.5% and 36.9% of red blood cells, respectively. The hemolytic activity of NKCS reached only 19.6% (Supporting Information Figure S2).

Discussion

In the present study we designed two cationic peptides based on NKCS, the 27-amino-acid fragment encompassing the membrane-active core region of NK-lysin. Their antibacterial and hemolytic activities, secondary structure, and interactions with model POPE membranes were investigated. The experiments were inspired by MC simulations.

Despite the overall good agreement between calculations and experiments in this study, it should be noted that our computational model has inherent limitations owing to its simplification of the complexity of the peptide–membrane interaction. First, the model treats the interaction of a single peptide molecule with the lipid bilayer and is not suitable (in its current form) for the study of peptide concentration effects, which are key to the understanding of antimicrobial peptide’s membranolytic. Thus, the simulations are suitable only for results obtained at low peptide concentration. Second, the model membrane is planar (although free to change its width). Thus, membrane curvature effects, which are anticipated in the presence of POPE lipids, cannot be simulated. Third, both the peptide and membrane are described using a reduced representation, providing a procedure that is computationally feasible. However, it does not allow studies of specific peptide–lipid interactions in atomic details. Hydrogen bonds and salt bridges between the

peptide and lipid, as well as the exact stereochemistry of the interaction, are not taken into account explicitly.

According to previous studies,¹⁶ our CD measurements, and the MC simulations, NKCS was mostly unstructured in water but adopted an α -helical conformation in the membrane-mimetic environment. Moreover, the simulations of the peptide in POPE membranes showed a helix disruption at residues Thr-13 and Leu-14. The origin of this break in the helicity becomes clear when the peptide was presented as a canonical α -helix (Figure 2C). Two distinct hydrophobic faces, of the N- and C-termini, are oriented in different directions; i.e., the hydrophobic moments of the termini do not point in the same direction. Upon membrane interaction, this would not be a favorable conformation. However, the analysis of the computationally predicted inner conformations revealed that the kink in the middle allowed a deviation from a regular α -helix to a conformation with an improved amphipathic organization of the peptide. The kink enabled the helices in the N- and C-termini to align their hydrophobic moments so that the hydrophobic regions of both were oriented toward the membrane (Figure 2A).

The replacement of Leu-15 with Pro in NKCS-[LP] was assumed to perturb the α -helix even further, and both the CD measurements and the simulations supported this notion. NKCS-[LP] was found to be significantly less helical than NKCS, which can explain the reduced membrane affinity of this peptide in comparison to NKCS (Table 2). The weaker helicity of NKCS-[LP] can be correlated with the lower impact on the inverse hexagonal phase transition of POPE. Moreover, the SPR experiment showed a peptide layer of 29 Å, which is larger than the diameter of an α -helix.^{56,57} This result can be correlated with the MC simulations that showed that while NKCS-[LP]’s N-terminus was embedded in the membrane, the C-terminus fluctuated above the surface (Figure 1E), resulting in an apparent thicker peptide layer.

The addition of two Ala residues into the sequence of NKCS was surmised to increase the α -helicity and improve the amphipathicity of the peptide, creating a single uninterrupted hydrophobic face (NKCS-[AA]; Figure 2B). The SPR experiments showed an association of NKCS-[AA] with the POPE membrane. The measured peptide layer thickness of 12 Å corresponds, approximately, to the average diameter of an α -helix, in agreement with the MC simulations. The computed and measured membrane-association free energy of NKCS-[AA] was much more negative (favorable) than that of NKCS (Table 2). Thus, we expected NKCS-[AA] to interfere more strongly with the membrane structure and to be more active against bacteria. However, the SAXS studies at various lipid–peptide ratios revealed consistently that the impact of NKCS-[AA] on the POPE bilayer structure was weaker than that of NKCS. The results also showed that NKCS-[AA] was slightly less active against bacteria than NKCS.

The three peptides shifted the temperature of inverse hexagonal phase transition to higher values. Observations of the peptide-induced lipids phase behavior can give an indication about membrane disruption. A temperature reduction suggests the generation of a negative membrane curvature whereas a high transition temperature indicates stiffening of the membrane and the induction of a positive curvature. The POPE lipid promotes spontaneous negative curvature,⁵⁹ and the adsorption of NKCS and its derivatives balanced this tendency and stabilized the bilayer. When the threshold concentration of the peptide was reached, a strong perturbation of the membrane occurred, leading eventually to lysis.^{17,60}

This study was performed to examine the hypothesis that α -helicity and amphipathicity are the major structural features determining the membrane affinity of cationic antimicrobial peptides. We designed two peptides, based on the primary structure of NKCS. By exchanging (NKCS-[LP]) or inserting amino acids (NKCS-[AA]), we altered the α -helical content and amphipathicity of the peptide. Our CD and SPR measurements were in keeping with the Monte Carlo simulations regarding the secondary structure and membrane affinity of the peptides. Moreover, NKCS-[LP] showed a decreased antimicrobial activity and weak influence on POPE's hexagonal phase transition temperature, in comparison to NKCS, which correlated well with its lower (calculated and measured) membrane affinity. In contrast, the increase in the membrane affinity of the NKCS-[AA] peptide in comparison to that of NKCS did not result in increased membrane-lytic potency. Quite the contrary, the peptide was slightly less active than the original NKCS (Tables 3 and 4).

Antimicrobial and membranolytic activity correlate with membrane affinity; the affinity must be high enough for the peptide to associate with the membrane. Indeed, NKCS-[LP], which showed a reduced membrane affinity in comparison to NKCS also exhibited a reduced activity. However, NKCS-[AA] demonstrated approximately the same activity as NKCS in spite of its increased membrane affinity, implying that activity depends also on other factors. Perhaps the membrane adsorption of a kinked peptide, such as NKCS, can cause more significant membrane disruption than a perfect α -helix, such as NKCS-[AA]. In this respect, it is noteworthy that a cyclic analog of melittin (which retained the overall helical structure) showed reduced membrane affinity but increased activity.⁶¹

Conclusions

Overall, the present study demonstrates how the interplay between simulations and experiments can be combined to provide a molecular picture of the membrane interaction of NKCS. The next challenge is to understand the mechanism of membrane lysis. For that, it is necessary to replace the crude representation of the membrane that was used here by a molecular (perhaps even atomistic) model.

Acknowledgment. We gratefully acknowledge the assistance of Sadasivam Jeganathan (Max-Planck-Arbeitsgruppe "Zytoskelett" of Prof. Dr. E. Mandelkow in Hamburg) for CD measurements. We thank Prof. Dr. P. Dubrue from the Department of Organic Chemistry at Ghent University for supporting us with the SPR knowledge and equipment. This work was financially supported by the European Commission under the sixth Framework Program through the Marie-Curie Action: BIOCONTROL, contract number MCRTN-33439 and German-Israeli Foundation for Scientific Research and Development, grant number 831/2004.

Supporting Information Available: Detailed description of computational methods, a table of energy decomposition data, and two figures showing SAXS patterns and hemolytic activity diagram are provided. This material is available free of charge via the Internet at <http://pubs.acs.org>.

References and Notes

- (1) Cohen, M. L. *Science* **1992**, *257*, 1050–5.
- (2) Hamilton-Miller, J. M. *Int. J. Antimicrob. Agents* **2004**, *23*, 209–12.
- (3) Powers, J. P.; Hancock, R. E. *Peptides* **2003**, *24*, 1681–91.
- (4) Bush, K.; Macielag, M.; Weidner-Wells, M. *Curr. Opin. Microbiol.* **2004**, *7*, 466–76.
- (5) Shai, Y. *Curr. Pharm. Des.* **2002**, *8*, 715–25.
- (6) Zasloff, M. *Nature* **2002**, *415*, 389–95.
- (7) Epand, R. M.; Shai, Y.; Segrest, J. P.; Anantharamaiah, G. M. *Biopolymers* **1995**, *37*, 319–38.
- (8) Shai, Y. *Trends Biochem. Sci.* **1995**, *20*, 460–4.
- (9) Shai, Y.; Oren, Z. *Peptides* **2001**, *22*, 1629–41.
- (10) Matsuzaki, K. *Biochim. Biophys. Acta* **1999**, *1462*, 1–10.
- (11) Andra, J.; Leippe, M. *Med. Microbiol. Immunol.* **1999**, *188*, 117–24.
- (12) Jacobs, T.; Bruhn, H.; Gaworski, I.; Fleischer, B.; Leippe, M. *Antimicrob. Agents Chemother.* **2003**, *47*, 607–13.
- (13) Olak, C.; Muentert, A.; Andra, J.; Brezesinski, G. *J. Pept. Sci.* **2008**, *14*, 510–7.
- (14) Schroder-Born, H.; Bakalova, R.; Andra, J. *FEBS Lett.* **2005**, *579*, 6128–34.
- (15) Willumeit, R.; Kumpugdee, M.; Funari, S. S.; Lohner, K.; Navas, B. P.; Brandenburg, K.; Linser, S.; Andra, J. *Biochim. Biophys. Acta* **2005**, *1669*, 125–34.
- (16) Andra, J.; Monreal, D.; Martinez de Tejada, G.; Olak, C.; Brezesinski, G.; Gomez, S. S.; Goldmann, T.; Bartels, R.; Brandenburg, K.; Moriyon, I. *J. Biol. Chem.* **2007**, *282*, 14719–28.
- (17) Lohner, K.; Prenner, E. J. *Biochim. Biophys. Acta* **1999**, *1462*, 141–56.
- (18) Haris, P. I.; Chapman, D. *Biopolymers* **1995**, *37*, 251–63.
- (19) Ladokhin, A. S.; Selsted, M. E.; White, S. H. *Biophys. J.* **1997**, *72*, 794–805.
- (20) Salditt, T.; Li, C.; Spaar, A. *Biochim. Biophys. Acta* **2006**, *1758*, 1483–98.
- (21) Bechinger, B. *Biochim. Biophys. Acta* **1999**, *1462*, 157–83.
- (22) Papo, N.; Shai, Y. *Biochemistry* **2003**, *42*, 458–66.
- (23) La Rocca, P.; Biggin, P. C.; Tieleman, D. P.; Sansom, M. S. *Biochim. Biophys. Acta* **1999**, *1462*, 185–200.
- (24) Forrest, L. R.; Sansom, M. S. *Curr. Opin. Struct. Biol.* **2000**, *10*, 174–81.
- (25) Kessel, A.; Cafiso, D. S.; Ben-Tal, N. *Biophys. J.* **2000**, *78*, 571–83.
- (26) Kessel, A.; Haliloglu, T.; Ben-Tal, N. *Biophys. J.* **2003**, *85*, 3687–95.
- (27) Milik, M.; Skolnick, J. *Proteins* **1993**, *15*, 10–25.
- (28) Baumgartner, A. *Biophys. J.* **1996**, *71*, 1248–55.
- (29) Efremov, R. G.; Nolde, D. E.; Vergoten, G.; Arseniev, A. S. *Biophys. J.* **1999**, *76*, 2448–59.
- (30) Ducarme, P.; Rahman, M.; Brasseur, R. *Proteins* **1998**, *30*, 357–71.
- (31) Maddox, M. W.; Longo, M. L. *Biophys. J.* **2002**, *82*, 244–63.
- (32) Veresov, V. G.; Davidovskii, A. I. *Eur. Biophys. J.* **2007**, *37*, 19–33.
- (33) Tzllil, S.; Murray, D.; Ben-Shaul, A. *Biophys. J.* **2008**, *95*, 1745–57.
- (34) Wee, C. L.; Sansom, M. S.; Reich, S.; Akhmatkaya, E. *J. Phys. Chem. B* **2008**, *112*, 5710–7.
- (35) Kessel, A.; Shental-Bechor, D.; Haliloglu, T.; Ben-Tal, N. *Biophys. J.* **2003**, *85*, 3431–44.
- (36) Shental-Bechor, D.; Kirca, S.; Ben-Tal, N.; Haliloglu, T. *Biophys. J.* **2005**, *88*, 2391–402.
- (37) Shental-Bechor, D.; Haliloglu, T.; Ben-Tal, N. *Biophys. J.* **2007**, *93*, 1858–71.
- (38) Gordon-Grossman, M.; Gofman, Y.; Zimmermann, H.; Frydman, V.; Shai, Y.; Ben-Tal, N.; Goldfarb, D. *J. Phys. Chem. B* **2009**, *113*, 12687–95.
- (39) Wang, X.; Quinn, P. J. *Biochim. Biophys. Acta* **2002**, *1564*, 66–72.
- (40) Siegel, D. P. *Biophys. J.* **2006**, *91*, 608–18.
- (41) van den Brink-van der Laan, E.; Killian, J. A.; de Kruijff, B. *Biochim. Biophys. Acta* **2004**, *1666*, 275–88.
- (42) Ames, G. F. J. *Bacteriol.* **1968**, *95*, 833–43.
- (43) Bishop, D. G.; Rutberg, L.; Samuelsson, B. *Eur. J. Biochem.* **1967**, *2*, 448–53.
- (44) Koch, H. U.; Haas, R.; Fischer, W. *Eur. J. Biochem.* **1984**, *138*, 357–63.
- (45) Matsuzaki, K.; Sugishita, K.; Ishibe, N.; Ueha, M.; Nakata, S.; Miyajima, K.; Epand, R. M. *Biochemistry* **1998**, *37*, 11856–63.
- (46) Hallock, K. J.; Lee, D. K.; Ramamoorthy, A. *Biophys. J.* **2003**, *84*, 3052–60.
- (47) Szule, J. A.; Rand, R. P. *Biophys. J.* **2003**, *85*, 1702–12.
- (48) Angelova, A.; Ionov, R.; Koch, M. H.; Rapp, G. *Arch. Biochem. Biophys.* **2000**, *378*, 93–106.
- (49) Tytler, E. M.; Segrest, J. P.; Epand, R. M.; Nie, S. Q.; Epand, R. F.; Mishra, V. K.; Venkatachalapathi, Y. V.; Anantharamaiah, G. M. *J. Biol. Chem.* **1993**, *268*, 22112–8.

- (50) Petrey, D.; Xiang, Z.; Tang, C. L.; Xie, L.; Gimpelev, M.; Mitros, T.; Soto, C. S.; Goldsmith-Fischman, S.; Kernytsky, A.; Schlessinger, A.; Koh, I. Y.; Alexov, E.; Honig, B. *Proteins* **2003**, *53*, 430–5.
- (51) Blondelle, S. E.; Houghten, R. A. *Pept. Res.* **1991**, *4*, 12–8.
- (52) Hall, K.; Mozsolits, H.; Aguilar, M. I. *Lett. Pept. Sci.* **2003**, *10*, 475–485.
- (53) Cooper, M. A.; Hansson, A.; Lofas, S.; Williams, D. H. *Anal. Biochem.* **2000**, *277*, 196–205.
- (54) *Real-Time Analysis of biomolecular interactions: applications of BIACORE*; Nagata, K., Handa, H., Eds.; Springer Publishing Co.: New York, 2000.
- (55) Boulin, C.; Kempf, R.; Koch, M. H. J.; McLaughlin, S. M. *Nucl. Instrum. Methods.* **1986**, *249*, 399–407.

- (56) Vie, V.; Van Mau, N.; Chaloin, L.; Lesniewska, E.; Le Grimellec, C.; Heitz, F. *Biophys. J.* **2000**, *78*, 846–56.
- (57) Ambroggio, E. E.; Separovic, F.; Bowie, J.; Fidelio, G. D. *Biochim. Biophys. Acta* **2004**, *1664*, 31–7.
- (58) Mozsolits, H.; Thomas, W. G.; Aguilar, M. I. *J. Pept. Sci.* **2003**, *9*, 77–89.
- (59) Fuller, N.; Rand, R. P. *Biophys. J.* **2001**, *81*, 243–54.
- (60) Bechinger, B.; Lohner, K. *Biochim. Biophys. Acta* **2006**, *1758*, 1529–39.
- (61) Unger, T.; Oren, Z.; Shai, Y. *Biochemistry* **2001**, *40*, 6388–97.

JP909154Y

Paper III: Membrane interactions of novicidin, a novel antimicrobial peptide: phosphatidylglycerol promotes bilayer insertion.

Jerzy Dorosz, Yana Gofman, Sofiya Kulusheva, Daniel Otzen, Nir Ben-Tal, Niels Chr. Nielsen, Raz Jelinek

Published in *J Phys Chem B*, 2009, 114(34):11053-11060.

Reprinted with permission from “Membrane interactions of novicidin, a novel antimicrobial peptide: phosphatidylglycerol promotes bilayer insertion”, Jerzy Dorosz et al., *The Journal of Physical Chemistry B*, American Chemical Society, Sep 1, 2009. Copyright (2009), American Chemical Society.

Membrane Interactions of Novicidin, a Novel Antimicrobial Peptide: Phosphatidylglycerol Promotes Bilayer Insertion

Jerzy Dorosz,^{†,‡} Yana Gofman,^{§,||} Sofiya Kolusheva,[†] Daniel Otzen,[⊥] Nir Ben-Tal,^{||} Niels Chr. Nielsen,[‡] and Raz Jelinek^{*,†}

Department of Chemistry and Ilse Katz Institute for Nanotechnology, Ben Gurion University, Beer Sheva 84105, Israel, Center for Insoluble Protein Structures (inSPIN), Interdisciplinary Nanoscience Center (iNANO) and Department of Chemistry, Aarhus University, DK-8000 Aarhus C, Denmark, GKSS Research Center, Geesthacht 21502, Germany, Department of Biochemistry and Molecular Biology, The George S. Wise Faculty of Life Sciences, Tel Aviv University, Ramat Aviv 69978, Israel, and Center for Insoluble Protein Structures (inSPIN), Interdisciplinary Nanoscience Center (iNANO) and Department of Molecular Biology, Gustav Wieds Vej 10C, Aarhus University, DK-8000 Aarhus C, Denmark

Received: June 7, 2010; Revised Manuscript Received: July 22, 2010

Novicidin is an antimicrobial peptide derived from ovispirin, a cationic peptide which originated from the ovine cathelicidin SMAP-29. Novicidin, however, has been designed to minimize the cytotoxic properties of SMAP-29 and ovispirin toward achieving potential therapeutic applications. We present an analysis of membrane interactions and lipid bilayer penetration of novicidin, using an array of biophysical techniques and biomimetic membrane assemblies, complemented by Monte Carlo (MC) simulations. The data indicate that novicidin interacts minimally with zwitterionic bilayers, accounting for its low hemolytic activity. Negatively charged phosphatidylglycerol, on the other hand, plays a significant role in initiating membrane binding of novicidin, and promotes peptide insertion into the interface between the lipid headgroups and the acyl chains. The significant insertion into bilayers containing negative phospholipids might explain the enhanced antibacterial properties of novicidin. Overall, this study highlights two distinct outcomes for membrane interactions of novicidin, and points to a combination between electrostatic attraction to the lipid/water interface and penetration into the subsurface lipid headgroups region as important determinants for the biological activity of novicidin.

1. Introduction

Antimicrobial peptides (AMPs) are essential components of innate immunity in multicellular organisms due to their selectivity and rapid response, crucial for encountering the fast proliferation of microorganisms.^{1–3} Studying and developing new AMPs has become particularly important in the light of the emergence of antibiotic-resistant bacterial strains. Although these peptides display high amino-acid sequence diversity, they generally encompass short peptides (12–60 residues),⁴ and seem to possess two common characteristics: amphiphilicity (approximately 50% hydrophobic residues) and net positive charge (2–9 lysine or arginine residues).⁵ Many AMPs do not exhibit ordered structures in water; however, they adopt specific secondary structures in membrane environments, a transformation that is believed to be a major factor in their antimicrobial activity.⁶ However, in a recent work on antimicrobial peptide mimics,⁷ the requirement of a defined secondary structure as a critical factor of antimicrobial activity has been challenged.

Numerous studies have aimed to decipher the modes of action of AMPs and their specificity for bacterial cells rather than host cells.^{8,9} The amphiphilic properties of AMPs generally enhance their affinity to lipid membranes, which are believed to be their initial, and most likely primary targets.⁹ In particular, the positive charge of AMPs is believed to contribute to peptide specificity toward *bacterial* membranes, which are enriched in anionic lipids, in contrast to the more neutral surfaces of mammalian cells.^{1,8,9}

Antimicrobial peptides have been shown to form membrane pores, which are believed to cause leakage of important metabolites and lead to bacterial cell death. Two different types of membrane pores have been described, namely, a barrel-stave pore (observed for alamethicin), where the pore is lined solely with the peptide,^{10,11} and a toroidal pore (for many helical, amphipathic peptides such as magainin) in which the peptide induces a curvature in the membrane and the pore is lined with both peptide and lipids.^{12,13} Dermaseptin on the other hand has been shown to self-associate in the presence of anionic lipids, forming a “carpet” at the membrane’s surface, which breaks after the peptide reaches a critical concentration.¹¹

A more general description has been proposed by Huang et al.,¹⁴ according to which a peptide can exist in one of two possible states: inactive, parallel to the membrane surface and active, transmembrane state, depending on the relative peptide/lipid proportion in the membrane. For lower peptide/lipid ratios, the energetically favored orientation is parallel to the membrane and the peptide is embedded on the interface region between hydrophobic acyl chains and hydrophilic lipid headgroups. At

* To whom correspondence should be addressed. E-mail: razj@bgu.ac.il. Phone: +972-8-6428665. Fax: +972-8-6472943.

[†] Ben Gurion University.

[‡] Center for Insoluble Protein Structures (inSPIN), Interdisciplinary Nanoscience Center (iNANO) and Department of Chemistry, Aarhus University.

[§] GKSS Research Center.

^{||} Tel Aviv University.

[⊥] Center for Insoluble Protein Structures (inSPIN), Interdisciplinary Nanoscience Center (iNANO) and Department of Molecular Biology, Aarhus University.

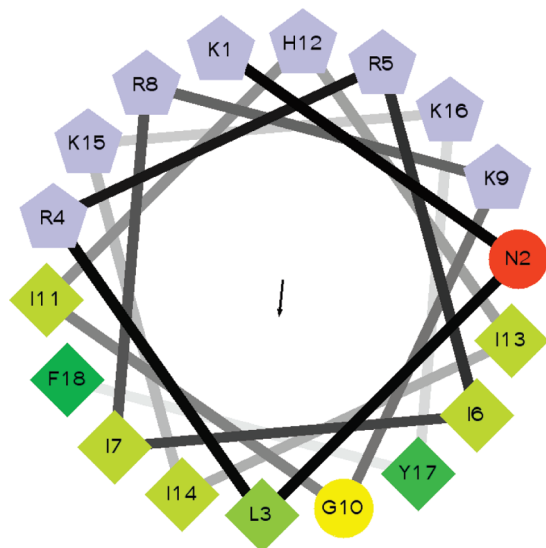


Figure 1. Helical wheel projection of novicidin. All lysine and arginine residues (gray color) are located at one side of the amphipathic helix, whereas the hydrophobic residues (yellow-green color) are facing the opposite side. The vector in the middle of the wheel represents the hydrophobic moment of the molecule. The image was created using wheel.pl software, version 1.4.

higher peptide/lipid ratios, a transmembrane orientation is preferred which allows the peptide to assemble and to form oligomeric pores. Another proposed model for AMP action—the “detergent-like” model—takes into account the geometry of the lipid molecules intercalated by an amphiphilic peptide which induces a curvature strain in the lipid bilayer, therefore acting like a detergent molecule and disrupting the membrane.¹⁵ Recent nuclear magnetic resonance (NMR) and molecular dynamics (MD)-based studies of alamethicin in phospholipid bilayers, micelles, and bicelles^{16,17} indicate that AMPs display a very high degree of flexibility in their membrane binding conformations which may be important for different modes of action.

Ovispirin is a synthetic peptide derived from the N-terminus of the sheep cathelicidin SMAP-29.^{18,19} Ovispirin (sequence KNLRRIIRKIIHIIKKYK) is highly cytolytic, and thus, its applicability as a potential AMP is limited.¹⁸ This observation has prompted an effort by Novozymes A/S to develop peptide variants with reduced activity toward mammalian cells. A double amino acid substitution I10G and G18F produced *novicidin*, a peptide displaying a favorable combination of effective antimicrobial activity and low hemolytic properties. Assuming the peptide adopts an ideal α -helical structure, the distribution of positively charged and hydrophobic residues in the sequence results in a highly amphipathic structure (Figure 1). The helical-wheel representation of novicidin suggests a high affinity of the peptide to anionic lipids that could counterbalance the repulsion of positively charged residues, and points to an interesting profile of membrane interactions. Here, we present a comprehensive investigation of the biological activity and membrane interactions of novicidin, with the goal of shedding light upon its cell selectivity and mechanism of action.

2. Materials and Methods

2.1. Materials. Novicidin was generously provided by Dr. Hans Henrik Kristensen (Novozymes A/S).

Melittin was purchased from Sigma-Aldrich. All phospholipids, including 1,2-dimyristoyl-*sn*-glycerophosphocholine (DMPC), 1,2-dimyristoyl-*sn*-glycero-3-phospho-(1'-*rac*-glycerol) (DMPG) sodium salt, and ESR probe 1-palmitoyl-2-

stearoyl-(10-*doxyl*)-*sn*-glycero-3-phosphocholine, were purchased from Avanti Polar Lipids, Inc. (Alabaster, AL). Stock solutions (40 and 20 mM for DMPC and DMPG, respectively) were prepared by dissolution of the phospholipids in chloroform: ethanol 1:1 mixtures, and were kept at $-20\text{ }^{\circ}\text{C}$. For monolayer experiments, phospholipid stock solutions of 1 mM were used. Stock solution of the ESR probe was prepared by dissolution in ethanol to a final concentration of 1 mg/mL and stored at $-20\text{ }^{\circ}\text{C}$.

The diacetylene monomer 10,12-tricosadiynoic acid was obtained from Alpha Aesar, Lancaster Synthesis (Lancashire, England). 60 mM stock solution was prepared by dissolution of 10,12-tricosadiynoic acid in chloroform:ethanol mixture and stored at $-20\text{ }^{\circ}\text{C}$.

2.2. Hemolysis Assay. 1 mL of fresh blood from a human donor was centrifuged at 4000g to separate erythrocytes from blood plasma. Erythrocytes were washed four to five times with PBS and centrifuged at 4000g, until no trace of free hemoglobin was visible in the supernatant. The pellet of red blood cells was resuspended in 10 mL of PBS (therefore diluting the initial portion of erythrocytes 10 times) and treated with a range of 2-fold dilutions of novicidin and melittin and incubated for 30 min at $37\text{ }^{\circ}\text{C}$ with gentle shaking (100 rpm). As a positive control (100% lysis), we used a sample treated with 1% Triton X100. The suspension was centrifuged (4000g) to separate intact red blood cells from the supernatant. The amount of free hemoglobin in the supernatant was determined by measuring the absorbance at 560 nm. Each experiment comprised two independent measurements, and the experiments were repeated twice. These four measurements were the basis for the calculation of SD.

2.3. Antibacterial Assay. Three different bacteria strains were used to determine the killing efficiency of the novicidin: *Escherichia coli* BL21 and *Salmonella enterica ser. typhimurium* (Gram-negative) and *Bacillus cereus* wild type (Gram-positive). Bacteria were cultured at $37\text{ }^{\circ}\text{C}$ in LB medium to reach an optical density of 0.4–0.6 at 560 nm (midlog phase) and then diluted 1000 times and subsequently transferred to a 96-well microplate (Greiner) followed by treatment with a range of 2-fold dilutions of antimicrobial substances: two highly positively charged peptides (novicidin and bee-venom-derived melittin) and a conventional antibiotic (streptomycin). Bacteria were incubated at $37\text{ }^{\circ}\text{C}$ for 16 h (overnight) with shaking (200 rpm). After incubation, the optical density (at 560 nm) was measured to estimate the growth inhibition. The MIC 50 was a concentration, which caused a decrease of optical density by 50% compared with the control. The experiment comprised two independent measurements, and was repeated two times, yielding a mean value \pm SD.

2.4. Monolayer Adsorption Experiments. The experiments were performed at $25\text{ }^{\circ}\text{C}$ using a Nima 312D Teflon trough (Nima Technology Ltd., Coventry, U.K.). The absorption isotherms ($\Delta\pi$ -time) were monitored throughout the duration of the experiment using a Nima PS4, Wilhelmy plate sensor. Lipid monolayers at different surface pressures were formed by deposition of the lipid solutions at the air-water interface of the dipping well (total volume of 50 mL). After 15 min of solvent evaporation and equilibration, the peptide was injected into the water subphase, below the preformed lipid monolayer through a thin, vertical tube, to reach 200 ng/mL (87 nM) concentration followed by 2–3 h of incubation with gentle stirring.

2.5. Lipid Vesicle Preparation. Phospholipid stock solutions in chloroform:ethanol 1:1 mixture were transferred to a glass

tube and evaporated under vacuum for several hours. In the liposomes for ESR experiments, the doxyl probe (1-palmitoyl-2-stearoyl-(10-doxyl)-sn-glycero-3-phosphocholine) constituted 2% of all lipids (molar ratio). The lipid film formed on a glass surface was hydrated by incubation in Tris buffer for a few minutes followed by probe sonication on a Misonix Incorporated sonicator (Farmingdale, NY). The suspensions were incubated at room temperature for 60 min and centrifuged at 5000g to remove titanium particles.

2.6. Polydiacetylene (PDA)/Phospholipid Vesicles. 10,12-Tricosadiynoic acid and the phospholipids, dissolved in ethanol:chloroform 1:1, were mixed in a glass tube in 3:2 ratio (diacetylene:lipids) and dried *in vacuo*. The resulting lipid film was hydrated with deionized water and sonicated using a Misonix Incorporated sonicator (Farmingdale, NY). The tubes were heated to 70 °C during the sonication process. The vesicle suspension was cooled to room temperature and incubated overnight at 4 °C followed by polymerization by UV irradiation at 254 nm for 20–30 s to create polydiacetylene (PDA).

2.7. PDA Fluorescence. PDA/phospholipid vesicles were mixed with various amounts of peptide followed by addition of Tris buffer and filled with water to 1 mL. Final concentrations: lipids 30 μM , Tris 1.5 mM, novicidin (3.48–0.435 μM ; peptide:lipid ratio 1:8–1:70). The solution was transferred to a 1 mL quartz cuvette, and the fluorescence emission spectra were taken (530–700 nm) with the excitation wavelength 488 nm. Spectra were baselined, and the emission intensity at 560 nm was plotted as a function of the peptide concentration, creating a titration curve.

2.8. Tyrosine Fluorescence. Internal fluorescence of novicidin was measured in quartz cuvette (1 mL volume) using an FL-920 spectrofluorimeter (Edinburgh, U.K.). The excitation wavelength was set to 279 nm, emission spectra were taken from 295 to 360 nm, and each spectrum was corrected by baseline subtraction using the appropriate peptide-free liposome solution. The suspension of liposomes (1 mM total lipid concentration) was mixed with Tris buffer (final concentration 1.5 mM, pH 8), and then, the peptide was added. The volume was filled to 1 mL using deionized water. The novicidin concentration remained constant for all measurements (3.5 μM), and the peptide to lipid ratio (from approximately 1:2 to 1:60) was varied by changing the volume of added liposomes.

2.9. Circular Dichroism (CD). The vesicle suspension (1 mM) was mixed with the Tris buffer (50 mM, pH 8.0) first, and then, the peptide was added (2 mg/mL). Final concentrations used: Tris 5 mM, novicidin 0.1 mg/mL (43.5 μM), and lipids 435 μM . Peptide concentration was determined after the measurement using the BCA method. Solutions were placed into a demountable, quartz cuvette with 0.1 cm path length, and spectra were obtained using a Jasco J-815 CD spectrometer (Jasco Spectroscopic Co., Hachioji City, Japan) using the following settings: spectrum range 185–260 nm, scanning speed 10 nm/min, integration time 4 s, and data pitch 1 nm.

2.10. Electron Spin Resonance (ESR). Vesicles containing 2% of DOXYL probe were mixed with Tris buffer (pH 7.4) and the peptide (final concentrations: lipids 0.5 mM, Tris 25 mM, novicidin 14.3 μM). Samples were placed in a 20 mm length, 1 mm internal-diameter quartz capillary, and ESR spectra were recorded on a Bruker EMX-220 digital X-band spectrometer at room temperature. Amplitudes of 12.5 and 100 kHz, modulation, and microwave power level were selected at subcritical values (0.5 G and 20 mW, respectively) to obtain the best signal-to-noise ratio. Processing of the ESR spectra was carried out using Bruker WIN-EPR software.

TABLE 1: Antibacterial and Hemolytic Activities of Novicidin

compound	minimal inhibitory concentration (MIC, μM)			hemolytic activity (IC50, μM)
	<i>E. coli</i> BL21	<i>S. enterica ser. Typhimurium</i>	<i>B. cereus</i>	
novicidin	0.65 \pm 0.3	1.4 \pm 0.4	1.4 \pm 1.0	>50
melittin	2.2 \pm 0.7	0.4 \pm 0.2	1.0 \pm 0.5	1.6 \pm 0.5
streptomycin	20 \pm 7	86 \pm 26	3.5 \pm 1.7	n/a

The rotational correlation time was calculated according to the equation

$$\tau_c = 6.65 \cdot \Delta H_{+1} [(I_{+1}/I_{-1})^{1/2} - 1] \cdot 10^{-10} \quad (\text{s})$$

where I_{+1}/I_{-1} corresponds to the amplitude of low- and high-field components and ΔH_{+1} is the width of the low-field component of the spectra.²⁰

2.11. Monte Carlo (MC) Simulations. MC simulations of novicidin were performed according to methodologies described previously.^{21–25} Novicidin was depicted in a reduced way, in which each amino acid was represented by two interaction sites, corresponding to the α -carbon and side chain. These interaction sites, as well as sequential α -carbons, were connected by virtual bonds. The hydrophobicity of the membrane was represented as a smooth profile of 30 Å width, corresponding to the hydrocarbon region of phosphatidylcholine (PC) and phosphatidylglycerol (PG) membranes. A negative surface charge was located on both sides of the membrane at a distance of 20 Å from the midplane. Its magnitude corresponded to the fraction of acidic lipids (0, 20, 50, and 100 mol %, in accordance with the experiments). The solution was considered neutral with monovalent salt at a concentration of 0.1 M. Novicidin's initial structure was modeled using the Scap methodology²⁶ and Protein Data Bank entry 1HU6¹⁸ as a template. To calculate the free energy of the peptide in water and in the membrane, four simulations consisting of 900 000 Monte Carlo cycles were conducted. In the simulations in water, the peptide was subjected to internal conformational modifications only, while in the membrane simulations the peptide was additionally allowed to change its location and orientation relative to the membrane. The total free energy of membrane association was calculated as the difference between the free energies of the peptide in water and in the membrane. A detailed description of the energetic terms included can be found in the Supporting Information. The helical content of novicidin was calculated as described in ref 22.

3. Results

3.1. Biological Activity. Table 1 summarizes the hemolytic and antimicrobial properties of novicidin, evaluated by commonly used Gram-negative and Gram-positive bacterial species. For comparison, we also outline in Table 1 the hemolytic and antimicrobial properties of melittin, a widely studied cytolytic peptide,²⁷ and streptomycin, a conventional antibiotic.²⁸ The low minimal inhibitory concentrations (MICs) recorded for novicidin (Table 1) attest to its effective antibacterial properties. A recent study recording the antibacterial properties of novicidin against an array of *Listeria monocytogenes* and *Staphylococcus aureus* strains similarly reported low MICs for the peptide.²⁹ Table 1 also confirms the low hemolytic activity of novicidin; the recorded IC50 of the peptide (>50 μM) is significantly higher than that of melittin (1.6 μM).

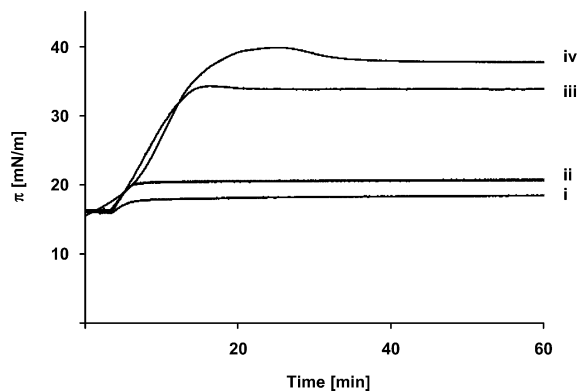


Figure 2. Isothermal adsorption of novicidin onto phospholipid monolayers. Adsorption isotherms of 87 nM novicidin injected under preformed phospholipid monolayers (initial monolayer pressure 16 mN/m): (i) DMPC; (ii) DMPC:DMPG 4:1; (iii) DMPC:DMPG 1:1; (iv) DMPG. The increase in the surface pressure of monolayers containing anionic phospholipids indicates enhanced penetration of the peptide into monolayers containing negative phospholipids. Almost no surface pressure change was recorded for the zwitterionic monolayer, indicating very weak interaction. The experimental sample size was $n = 2$.

The biological (both hemolytic and antibacterial) activities of cationic AMPs are believed to be strongly associated with their *membrane interactions*.^{9,30} We applied several biophysical techniques designed to characterize the binding and insertion of novicidin into model phospholipid membranes. The data, presented and discussed below, help to shed light on the likely mechanisms of antibacterial action and cell specificity of novicidin.

3.2. Biophysical Characterization. Figure 2 depicts isothermal adsorption experiments in which 87 nM novicidin was injected underneath lipid monolayers deposited at the air/water interface.³¹ Langmuir monolayers of lipids have been widely employed as useful biomimetic assemblies;^{32,33} in particular, numerous studies have focused on the analysis of peptide incorporation into lipid monolayers as models for peptide/membrane interactions.^{34,35} The adsorption isotherms depicted in Figure 2 demonstrate the dramatic effect of the phospholipid headgroup charge upon novicidin adsorption and penetration into the lipid monolayers.

The adsorption isotherm in Figure 2,i shows a negligible increase in surface pressure following injection of novicidin underneath a monolayer comprising the zwitterionic phospholipid dimyristoylphosphatidylcholine (DMPC). This result indicates a minimal insertion of novicidin into the DMPC monolayer. Importantly, Figure 2 demonstrates that when the monolayer contained a higher concentration of dimyristoylphosphatidylglycerol (DMPG), a negatively charged phospholipid, more pronounced incorporation of novicidin within the monolayer occurred, giving rise to higher surface pressures. This observation highlights not only the pronounced affinity of the peptide to monolayers containing anionic lipids but particularly the fact that the peptide *inserted* into the DMPG-containing monolayers. Such interpretation is also consistent with our previous investigations indicating that novicidin adopts secondary structure elements allowing for lipid incorporation.³⁶

While Figure 2 indicates that negatively charged DMPG significantly promotes insertion of novicidin into lipid monolayers at the air/water interface, additional experiments were carried out to evaluate the extent of insertion of the peptide into lipid bilayers, which is the actual organization of lipid molecules within physiological membranes. Figure 3 illustrates the application of a biomimetic lipid/polymer assay to explore

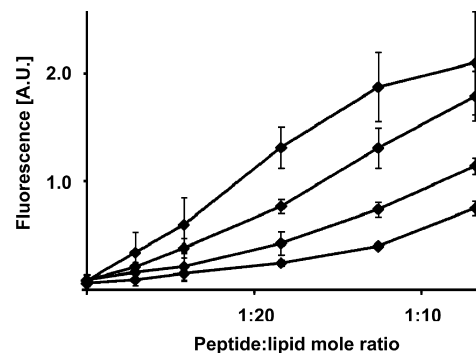


Figure 3. Fluorescence dose-response curves of lipid/PDA vesicles. Novicidin induces perturbations of phospholipid/PDA bilayer vesicles leading to induction of fluorescence emission at 560 nm. Differences in fluorescence emission in various lipid compositions are dependent upon the degree of penetration of the peptide: (i) DMPC:PDA 2:3 (mole ratio); (ii) DMPC:DMPG:PDA 1.6:0.4:3; (iii) DMPC:DMPG:PDA 1:1:3; (iv) DMPG:PDA 2:3. The experimental sample size was $n = 2$.

the relationship between the extent of bilayer insertion and lipid composition. Specifically, Figure 3 presents fluorescence dose response curves recorded following incubation of novicidin with phospholipid/polydiacetylene (PDA) vesicles. PDA is a unique chromatic polymer which undergoes visible *blue-red* transformations as well as *fluorescence emission* induced by varied molecular interactions.³⁷ In particular, mixed vesicles comprising PDA and lipid molecules have been previously used for analysis of membrane interactions of antimicrobial peptides and other membrane-associated molecules.³⁷⁻³⁹ In such lipid/PDA vesicle systems, interactions of membrane-active molecules resulting in disruption of the lipid bilayer led to significantly enhanced fluorescence emission from the associated PDA polymer matrix. Furthermore, the chromatic response of the vesicles can be employed to distinguish between *surface interactions* of tested peptides on the one hand and *subsurface insertion* on the other hand, based upon the relative *steepness* of the dose-response curves.⁴⁰

Figure 3 depicts the effect of the anionic phospholipid DMPG in phospholipid/PDA vesicles on the mode of interaction of novicidin with the membrane. *Steeper* dose response curves were observed following incubation of novicidin with vesicles containing *less* DMPG. For example, 15 μ M novicidin induced a relative fluorescence of 1.0 (arbitrary units, a.u.) in DMPC/PDA (2:3 mol ratio) vesicles (Figure 3,i), while the same concentration gave rise to less than 0.4 a.u. in a solution of DMPC/DMPG/PDA (1:1:3) vesicles (Figure 3,ii). These results can be explained according to the extent of novicidin interaction with the vesicle surface. In the DMPC/PDA biomimetic membrane, novicidin is most likely associated with the PDA headgroups (which are negatively charged), giving rise to the *steeper* dose response curve (Figure 3,i). In comparison, in vesicles containing more DMPG, a significant fraction of novicidin is probably immersed within the DMPG domains, overall leading to *less* surface perturbation of the PDA matrix and consequently giving rise to a more *moderate* curve compared to DMPC/PDA.

Previous studies have indicated that the fluorescence emission induced in lipid/PDA systems is ascribed to *surface perturbations* of the vesicles.³⁷ Accordingly, the fluorescence results in Figure 3 suggest that DMPG promotes *deeper insertion* of novicidin beyond the bilayer surface, giving rise to relatively lower fluorescence responses, while DMPC causes a higher degree of *surface binding* leading to higher chromatic response. Indeed, the most moderate fluorescence dose response curve

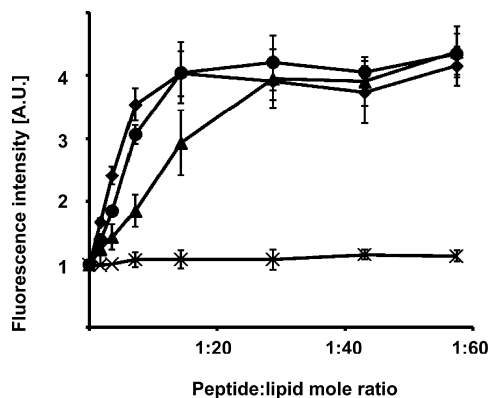


Figure 4. Tyrosine fluorescence titration curves. Titration with liposomes containing different ratios of DMPG vs DMPC. Novicidin interaction induces an increase of fluorescence emission at 304 nm (Y17) due to penetration of the peptide into the lipid bilayer. (x) DMPC; (▲) DMPC:DMPG (4:1 mol ratio); (●) DMPC:DMPG (1:1); (◆) DMPG. The experimental sample size was $n = 6$.

was apparent when novicidin was incubated with DMPG/PDA vesicles (Figure 3,iv).

Tyrosine fluorescence data depicted in Figure 4 lend support to the interpretation of the chromatic lipid/PDA assay results, confirming that DMPG promoted more pronounced incorporation of novicidin into the bilayer. Aromatic amino acids such as tryptophane and tyrosine have been shown to localize preferentially at the membrane interface (headgroup region).^{41,42} In particular, the fluorescence emission of tyrosine has been shown to exhibit pronounced sensitivity to the hydrophobicity of its microenvironment.⁴³ Indeed, Tyr fluorescence spectroscopy is regularly employed to evaluate the extent of peptide interactions with lipids.⁴⁴

Novicidin has one Tyr residue in position 17. The tyrosine fluorescence titration data in Figure 4 confirm that novicidin did not penetrate into DMPC bilayers, yielding almost unchanged fluorescence emission as the lipid:peptide ratio increased (Figure 4, crosses). However, significantly higher fluorescence was recorded when novicidin was added to vesicles comprising, in addition to DMPC, also the negatively charged DMPG. Similar to the chromatic assay results in Figure 3, Figure 4 demonstrates that higher abundance of DMPG within the vesicles correlated with greater insertion of novicidin beyond the lipid/water interface. Indeed, the highest increase in tyrosine fluorescence emission was observed when novicidin was added to DMPC:DMPG (1:1 mol ratio) vesicles and to pure DMPG vesicles, respectively (Figure 4, filled circles and filled diamonds, respectively).

To corroborate the fluorescence data in Figures 3 and 4, which point to a direct relationship between DMPG content and bilayer insertion, and probe the approximate depth of peptide insertion into the bilayer, we further carried out electron spin resonance (ESR) spectroscopy experiments utilizing phospholipid vesicles which additionally included phosphatidylcholine displaying a doxyl spin probe in position 10 of the acyl chain (PC-10-DS, Table 2). Table 2 depicts the effect of novicidin upon the rotational correlation times of the doxyl residue, denoted τ_c , which are highly sensitive to the local dynamical properties of the spin-probe within the lipid bilayer.⁴⁵

Table 2 demonstrates that addition of novicidin resulted in dramatic transformations of the τ_c values. Particularly important, changes of the rotational correlation times were clearly dependent upon the presence of DMPG in the vesicles. Specifically, in 10-DS-PC/DMPC (1:50 mol ratio) vesicles, incubation with

TABLE 2: ESR Data—Rotational Correlation Times, τ_c , of PC-10-DS Incorporated into the Phospholipid Vesicles^a

	τ_c (ns)	
	control	novicidin
DMPC	2.63	2.73
DMPC:DMPG 4:1	2.21	3.79
DMPG	1.93	7.80

^a SD values were less than 10%.

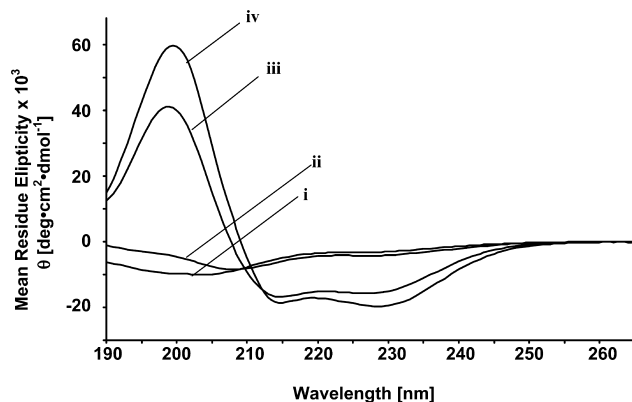


Figure 5. Circular dichroism (CD). Far UV CD spectra of novicidin in different environments: (i) Tris buffer; (ii) DMPC; (iii) DMPC:DMPG 4:1; (iv) DMPG. Novicidin adopts an α -helical structure when incubated with negatively charged liposomes (iii and iv), whereas it is unstructured in the buffer (i). The spectrum obtained for DMPC vesicles (ii) differs from the one in the buffer (i), exhibiting a higher signal in the region corresponding to a positive band characteristic for the α -helix and a slightly lower signal in the region corresponding to a negative band of the helical structure, indicating a minor structural change of the peptide.

novicidin yielded a minimal change to τ_c from 2.63 to 2.73 ns (Table 2), consistent with the proposed *surface localization* of novicidin in bilayers comprising only DMPC. However, almost a 2-fold increase in correlation time compared to the control vesicles, from 2.21 to 3.79 ns, was apparent when novicidin was added to 10-DS-PC/DMPC/DMPG (1:25:25) vesicles, and a 4-fold greater τ_c was recorded when the peptide was incubated with 10-DS-PC/DMPG (1:50) vesicles. The increase in τ_c is indicative of the slower mobility of the spin probes and underscores lower membrane fluidity.⁴⁶ Accordingly, since the doxyl residue in 10-DS-PC is localized closer to the middle of the lipid acyl chains, the τ_c data likely indicate that novicidin insertion into the headgroup/acyl chain interface affects the bilayer interior, possibly through penetration of the side-chains of hydrophobic residues, such as leucine and isoleucine, into the hydrocarbon region of the bilayer.

While Figures 2–4 and Table 2 highlight the relationship between novicidin membrane penetration and the abundance of the negatively charged phospholipid DMPG as compared to zwitterionic DMPC, we further assessed the consequences of membrane interactions upon the peptide *structure*. Figure 5 depicts circular dichroism (CD) spectra of novicidin incubated with different vesicle systems. In a buffer solution (no lipids present), the CD spectrum of novicidin (Figure 5,i) exhibits a pronounced dip at around 198 nm, indicative of a predominant random coil structure. The CD trace of novicidin incubated with DMPC vesicles (Figure 5,ii), although slightly different than the peptide in the buffer solution, similarly points to a highly disordered conformation of the peptide. It should be pointed out, however, that the CD spectra in buffer (Figure 5i) and in PC (Figure 5i) are different, especially in the region 190–205

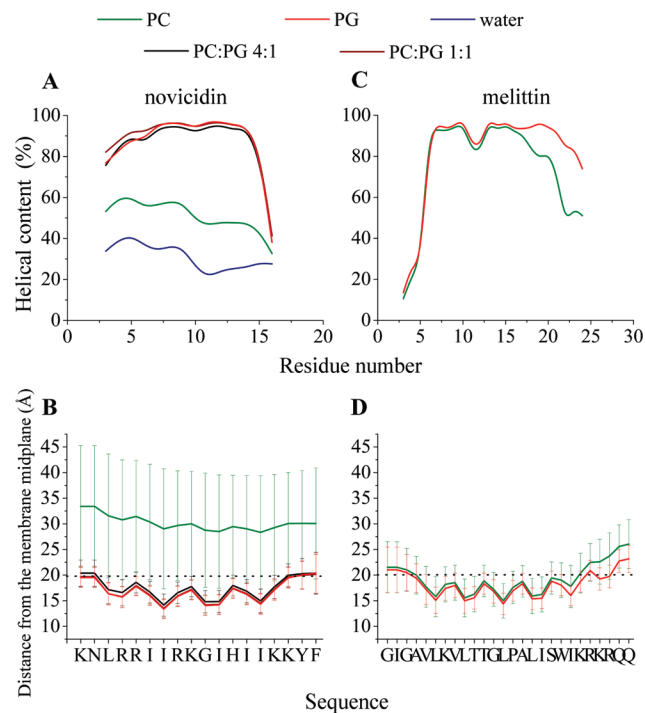


Figure 6. Peptide helicity and location of the α -carbon atoms in the lipid bilayer based on Monte Carlo simulations. The curves obtained for water solution and bilayers comprising different lipid compositions are depicted in different colors. (A, C) The calculated helical content of novocidin (A) and melittin (C) in the aqueous phase and lipid bilayers. (B, D) Average conformations of novocidin (B) and melittin (D) in the lipid bilayer determined as the average distance of each residue α -carbon from the bilayer midplane. The error bars mark the standard deviations. For clarity, the error bars of novocidin in DMPC:DMPG 1:1 and DMPC:DMPG 4:1 are omitted. The residues are indicated using a one-letter code. The horizontal dotted line marks the location of the phosphate group of the lipid polar heads.

nm. In PC, the signal is more positive (displaying a spectral maximum at around 195 nm) than in buffer. Furthermore, the minima at 208 and 222 nm (helix signature) are somewhat more pronounced in PC than in water. These differences are small but experimentally significant, and possibly point to a residual helical structure in the presence of DMPC vesicles.

The CD results reveal a dip at around 220 appearing in the spectra as the DMPG content in the vesicles gradually increased (Figure 5,iii–iv). CD traces featuring dips at around 208 and 222 nm generally point to the formation of a helical peptide conformation.⁴⁷ This result confirms the empirical prediction that the anionic membranes would induce the α -helical structure of novocidin. Indeed, many cationic AMPs exhibit a general tendency to adopt helical structures upon interactions with the negatively charged membranes.^{6,30}

3.3. Monte Carlo Simulations. The results of Monte Carlo (MC) simulations, depicted in Figures 6 and 7, provide a computational chemistry framework for the experimental data and their interpretation. The calculated helical contents of novocidin in water and in bilayers of different lipid compositions correlate well with the CD spectra. Novocidin is, in essence, randomly coiled in water (Figure 6A). The helicity of novocidin only slightly increased due to the surface interaction with a neutral (DMPC) lipid bilayer and markedly increased with the addition of negatively charged lipids (DMPG) (Figure 6A). In comparison, melittin which is less charged and more hydrophobic exhibits high helicity both in the charged and neutral lipid bilayers (Figure 6C).

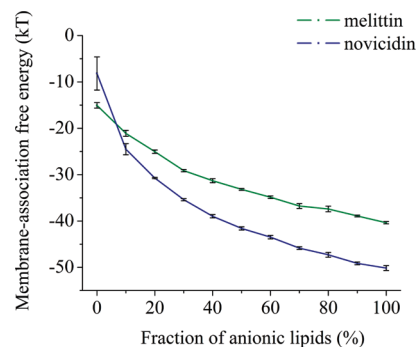


Figure 7. Calculated free energy of membrane association of novocidin (blue) and melittin (green) as a function of the fraction of anionic lipids in the bilayer. The error bars indicate the standard deviation. Please notice that for the most part the error bars are smaller than the marks of the data points.

The orientation of novocidin within bilayers of various lipid compositions was estimated on the basis of the average distances of the residues from the membrane midplane (Figure 6B). Figure 6B shows that in all cases the peptide backbone was approximately parallel to the bilayer surface. In a purely neutral membrane (corresponding to a DMPC lipid bilayer), novocidin interacted very weakly with the membrane (membrane-association free energy of about -8 kT) and, for the most part, remained in the aqueous phase approximately 30 Å from the bilayer midplane (Figure 6B).

The incorporation of negative surface charge into the bilayer (the model's representation of the negatively charged DMPG lipids) led to penetration of novocidin into the headgroup region of the membrane. This location was favorable, since it enabled the hydrophobic residues to be buried in the hydrocarbon region of the membrane, while the positively charged residues interacted through Coulomb attraction with the negative membrane-surface charge. The charged and polar residues remained in the water–bilayer interface to minimize the desolvation penalty associated with their transfer into the hydrophobic region of the membrane. A similar conformation was previously described for melittin²⁴ (Figure 6D), as well as for NKCS and two derivatives.²⁵ In addition, the position of the tyrosine residue (Tyr-17) at the membrane interface region is in agreement with previous reports.^{41,42} However, in contrast to melittin, novocidin did not partition into the polar headgroup region in a pure PC membrane and its penetration was dependent on the presence of the negatively charged lipids. This property was manifested also by NKCS and its two derivatives.²⁵ Figure 6B also points to the greater flexibility of the *C-terminus* of the peptide (e.g., larger error bars), likely induced by electrostatic repulsion between asparagine and the negatively charged phospholipids in the bilayer.

Figure 7 confirms that the membrane-association free energy of novocidin increased with the fraction of negatively charged lipids. It also shows a comparison of the novocidin data with previous simulations of melittin within bilayers of different compositions.²⁴ In both cases, the calculated free energy values correlated well with the experimentally estimated hemolytic and antibiotic activity data (Table 1). Novocidin's MIC against bacteria is comparable to the MIC of melittin (Table 1). This observation correlates with the similar penetration depth of both peptides into negatively charged membranes, despite novocidin's lower (more favorable) binding free energy to the negatively charged lipids, relative to melittin (Figure 6D). Although the association energy of melittin to negatively charged membranes is higher than that of novocidin, it is still low enough to

effectively bind, and penetrate bacterial membranes (containing 20–40% of anionic lipids for Gram-negative bacteria and up to 100% negatively charged lipids for Gram-positive bacteria⁴⁸) at the concentrations used. Likewise, the higher (less favorable) free energy of novicidin association with the neutral bilayer could be ascribed to its lower hemolytic activity in comparison to melittin. Moreover, the average conformations of novicidin and melittin within a neutral lipid bilayer support this notion (Figure 6B and D). While melittin was immersed within the uncharged bilayer, novicidin remained only loosely associated with the membrane's surface.

4. Discussion

A primary question pertaining to the biological activity of novicidin concerns the factors affecting its significant antimicrobial activity on the one hand and diminished hemolytic action on the other hand. The experimental data and MC simulations provide a framework for understanding both cell selectivity and bacterial toxicity. In particular, our results point to the role of negatively charged lipids, specifically phosphatidylglycerol, as determining membrane insertion of novicidin.

The data presented here underscore a significant effect of negatively charged phospholipids upon binding and insertion of novicidin into membrane bilayers. Indeed, the presence of DMPG was found to constitute an essential prerequisite for novicidin attachment and penetration into lipid bilayers. This observation, combined with the lack of helical structure and negligible insertion of novicidin into pure zwitterionic lipid bilayers, might explain the selectivity of the peptide toward bacterial cells, which generally display a much higher abundance of negatively charged phospholipids in their membranes.⁴⁸ Diminished membrane interactions of AMPs with zwitterionic lipids have been widely observed and are believed to account for their low hemolytic activities.^{49,50} Similarly, binding of cationic AMPs to negatively charged lipids has been reported in varied membrane systems mimicking bacterial membranes.^{51,52}

The differences between melittin and novicidin both in the biological context (Table 1) as well as the MC calculations pertaining to membrane localization (Figure 6) are noteworthy. Specifically, the ability of melittin to insert into zwitterionic membranes and consequent hemolytic activity most likely emanates from its specific distribution of hydrophobic and positively charged residues in the sequence and its overall hydrophobicity. These properties are reflected in the lower (more negative) energy of melittin association with neutral membranes compared to novicidin. Melittin contains five positively charged residues, mostly clustered at the N-terminus, and 11 hydrophobic residues (I, L, V, F, and A). Novicidin, on the other hand, has seven cationic residues distributed evenly along the peptide and seven hydrophobic residues. The higher portion of hydrophobic amino acids presumably assures melittin's interaction with zwitterionic membranes.

Interestingly, ovispirin, another peptide that has the same ratio of hydrophobic vs charged amino acids as novicidin, exhibits high hemolytic and cytotoxic properties.¹⁸ Indeed, our MC simulations showed that ovispirin associates with neutral lipids (Supporting Information, Figure S1A). The differences between the novicidin and ovispirin constitute Gly vs Ile at position 10 and Phe vs Gly at position 18. Roughly speaking, these substitutions preserve the overall hydrophobicity level of the peptide. However, the effect of the substitution in position 10 is more pronounced, since it is much closer to the membrane than position 18. The important role of the G10I substitution is further supported by another close relative: the novispirin peptide

which has only one of the two substitutions, F18G. The MC simulations, as well as experimental data,¹⁸ showed that novispirin has a weak affinity for and does not insert into a neutral bilayer (Supporting Information, Figure S1B).

Further to these arguments, it has been suggested that hemolysis of eukaryotic cells by AMPs is not solely dependent on the electrostatic attraction to the membrane but requires peptide penetration into the hydrophobic core of the membrane and simultaneous α -helix formation.^{6,30} An interesting example demonstrating this phenomenon is dermaseptin B2, which adopts a helical structure in zwitterionic membranes and is therefore highly cytolytic. A variant of dermaseptin lacking the hydrophobic C-terminal part (crucial for adopting a helical conformation in zwitterionic membranes) remains unordered in phosphatidylcholine vesicles and, more significantly, has very low cytolytic properties.⁵³ A recent study on the cationic peptide pardaxin has demonstrated a dependence of the secondary structure and the mode of action upon membrane composition.⁵⁴ Pardaxin adopted a helical conformation in zwitterionic DOPC vesicles and permeabilized the bilayer through a "barrel-stave" mechanism, whereas in anionic vesicles (DOPC/PG) the peptide disrupted the membrane via the "carpet" mechanism. The ability of pardaxin to form an α -helix in zwitterionic membranes is likely to be the key to the cytolytic activity, since its diastereoisomer, which is unable to adopt a helical conformation, is nonhemolytic.⁵⁵ Unlike the cytolytic peptide pardaxin, novicidin *did not* adopt a helical structure upon interaction with zwitterionic membranes (Figures 5,ii and 6A) and did not penetrate into the bilayer (Figures 2–4). This conclusion accounts for novicidin's very low hemolytic activity (Table 1).

In addition to modulation of the membrane specificity of novicidin, the experiments point to an important role of negatively charged phospholipids in promoting insertion of novicidin into the interface between the hydrophilic headgroups and the hydrophobic tails of the lipids. The incorporation of novicidin within DMPG-containing bilayers was evident through application of the biophysical techniques employed, including the chromatic lipid/PDA assay (Figure 2), tyrosine fluorescence (Figure 3), and ESR (Table 2). Folding of novicidin into a pronounced helical conformation upon interaction with DMPG vesicles (Figures 4 and 5B) provides a structural framework for insertion of the peptide into the bilayer, rather than localization only at the lipid/water interface.

Insertion of novicidin into the headgroup region, promoted by negatively charged phospholipids and a serious membrane perturbation, may well be the underlying mechanism for the antibacterial action of the peptide. Subsurface bilayer penetration has been previously observed for some cationic peptides.^{56,57} In conclusion, this investigation reveals the critical role of the phospholipid headgroup charge in determining the biological activity of novicidin, a novel antimicrobial peptide, particularly as the molecular determinant for discrimination between mammalian and bacterial membranes.

Acknowledgment. This research project has been supported by the European Commission under the sixth Framework Program through the Marie-Curie Action: BIOCONTROL, contract number MCRTN – 33439. We are grateful to Dr. Hans Henrik Kristensen for providing novicidin. Support from the Danish National Research Foundation is also acknowledged.

Supporting Information Available: Details of energy calculations for the Monte Carlo simulations are presented as well as the location of novispirin and ovispirin peptides in

neutral lipid membranes. This material is available free of charge via the Internet at <http://pubs.acs.org>.

References and Notes

- Zasloff, M. *Nature* **2002**, *415*, 389–395.
- Bulet, P.; Stöcklin, R.; Menin, L. *Immunol. Rev.* **2004**, *198*, 169–184.
- Hancock, R. E.; Diamond, G. *Trends Microbiol.* **2000**, *8*, 402–410.
- Yount, N. Y.; Bayer, A. S.; Xiong, Y. Q.; Yeaman, M. R. *Biopolymers* **2006**, *84*, 435–458.
- Brown, K. L.; Hancock, R. E. W. *Curr. Opin. Immunol.* **2006**, *18*, 24–30.
- Jiang, Z.; Vasil, A. I.; Hale, J. D.; Hancock, R. E. W.; Vasil, M. L.; Hodges, R. S. *Biopolymers* **2008**, *90*, 369–383.
- Rotem, S.; Mor, A. *Biochim. Biophys. Acta* **2009**, *1788*, 1582–1592.
- Matsuzaki, K. *Biochim. Biophys. Acta* **1999**, *1462*, 1–10.
- Shai, Y. *Biochim. Biophys. Acta* **1999**, *1462*, 55–70.
- He, K.; Ludtke, S. J.; Huang, H. W.; Worcester, D. L. *Biochemistry* **1995**, *34*, 15614–15618.
- Oren, Z.; Shai, Y. *Biopolymers* **1998**, *47*, 451–463.
- Matsuzaki, K.; Murase, O.; Fujii, N.; Miyajima, K. *Biochemistry* **1996**, *35*, 11361–11368.
- Ludtke, S. J.; He, K.; Heller, W. T.; Harroun, T. A.; Yang, L.; Huang, H. W. *Biochemistry* **1996**, *35*, 13723–13728.
- Huang, H. W. *Biochemistry* **2000**, *39*, 8347–8352.
- Bechinger, B.; Lohner, K. *Biochim. Biophys. Acta* **2006**, *1758*, 1529–1539.
- Dittmer, J.; Thøgersen, L.; Underhaug, J.; Bertelsen, K.; Vosegaard, T.; Pedersen, J. M.; Schjøtt, B.; Tajkhorshid, E.; Skrydstrup, T.; Nielsen, N. C. *J. Phys. Chem. B* **2009**, *113*, 6928–6937.
- Bertelsen, K.; Paaske, B.; Thøgersen, L.; Tajkhorshid, E.; Schjøtt, B.; Skrydstrup, T.; Nielsen, N. C.; Vosegaard, T. *J. Am. Chem. Soc.* **2009**, *131*, 18335–18342.
- Sawai, M. V.; Waring, A. J.; Kearney, W. R.; McCray, P. B. J.; Forsyth, W. R.; Lehrer, R. I.; Tack, B. F. *Protein Eng.* **2002**, *15*, 225–232.
- Wimmer, R.; Andersen, K. K.; Vad, B.; Davidsen, M.; Mølgaard, S.; Nesgaard, L. W.; Kristensen, H. H.; Otzen, D. E. *Biochemistry* **2006**, *45*, 481–497.
- Freed, J. H.; Fraenkel, G. K. *J. Chem. Phys.* **1963**, *39*, 326–348.
- Kessel, A.; Shental-Bechor, D.; Haliloglu, T.; Ben-Tal, N. *Biophys. J.* **2003**, *85*, 3431–3444.
- Shental-Bechor, D.; Kirca, S.; Ben-Tal, N.; Haliloglu, T. *Biophys. J.* **2005**, *88*, 2391–2402.
- Shental-Bechor, D.; Haliloglu, T.; Ben-Tal, N. *Biophys. J.* **2007**, *93*, 1858–1871.
- Gordon-Grossman, M.; Gofman, Y.; Zimmermann, H.; Frydman, V.; Shai, Y.; Ben-Tal, N.; Goldfarb, D. *J. Phys. Chem. B* **2009**, *113*, 12687–12695.
- Gofman, Y.; Linser, S.; Rzeszutek, A.; Shental-Bechor, D.; Funari, S. S.; Ben-Tal, N.; Willumeit, R. *J. Phys. Chem. B* **2010**, *114*, 4230–4237.
- Xiang, Z.; Honig, B. *J. Mol. Biol.* **2001**, *311*, 421–430.
- Blondelle, S. E.; Houghten, R. A. *Biochemistry* **1991**, *30*, 4671–4678.
- Berkman, S.; Henry, R. J.; Housewright, R. D. *J. Bacteriol.* **1947**, *53*, 567–574.
- Gottlieb, C. T.; Thomsen, L. E.; Ingmer, H.; Mygind, P. H.; Kristensen, H.; Gram, L. *BMC Microbiol.* **2008**, *8*, 205.
- Chen, Y.; Guarnieri, M. T.; Vasil, A. I.; Vasil, M. L.; Mant, C. T.; Hodges, R. S. *Antimicrob. Agents Chemother.* **2007**, *51*, 1398–1406.
- Maget-Dana, R. *Biochim. Biophys. Acta* **1999**, *1462*, 109–140.
- Brockman, H. *Curr. Opin. Struct. Biol.* **1999**, *9*, 438–443.
- Brezesinski, G.; Möhwald, H. *Adv. Colloid Interface Sci.* **2003**, *100–102*, 563–584.
- Vié, V.; Van Mau, N.; Chaloin, L.; Lesniewska, E.; Le Grimmellec, C.; Heitz, F. *Biophys. J.* **2000**, *78*, 846–856.
- Volinsky, R.; Kolusheva, S.; Berman, A.; Jelinek, R. *Biochim. Biophys. Acta* **2006**, *1758*, 1393–1407.
- Vad, B.; Thomsen, L. A.; Bertelsen, K.; Franzmann, M.; Pedersen, J. M.; Nielsen, S. B.; Vosegaard, T.; Valnickova, Z.; Skrydstrup, T.; Enghild, J. J.; et al. *Biochim. Biophys. Acta* **2010**, *1804*, 806–820.
- Kolusheva, S.; Shahal, T.; Jelinek, R. *Biochemistry* **2000**, *39*, 15851–15859.
- Katz, M.; Tsubery, H.; Kolusheva, S.; Shames, A.; Fridkin, M.; Jelinek, R. *Biochem. J.* **2003**, *375*, 405–413.
- Satchell, D. P.; Sheynis, T.; Shirafuji, Y.; Kolusheva, S.; Ouellette, A. J.; Jelinek, R. *J. Biol. Chem.* **2003**, *278*, 13838–13846.
- Sheynis, T.; Sykora, J.; Benda, A.; Kolusheva, S.; Hof, M.; Jelinek, R. *Eur. J. Biochem.* **2003**, *270*, 4478–4487.
- Wimley, W. C.; White, S. H. *Nat. Struct. Biol.* **1996**, *3*, 842–848.
- Yau, W. M.; Wimley, W. C.; Gawrisch, K.; White, S. H. *Biochemistry* **1998**, *37*, 14713–14718.
- Giancotti, V.; Quadrioglio, F.; Cowgill, R. W.; Crane-Robinson, C. *Biochim. Biophys. Acta* **1980**, *624*, 60–65.
- Lerche, M. H.; Kragelund, B. B.; Bech, L. M.; Poulsen, F. M. *Structure* **1997**, *5*, 291–306.
- Takahashi, T.; Noji, S.; Erbe, E. F.; Steere, R. L.; Kon, H. *Biophys. J.* **1986**, *49*, 403–410.
- Viriyaraj, A.; Kashiwagi, H.; Ueno, M. *Chem. Pharm. Bull.* **2005**, *53*, 1140–1146.
- Johnson, W. C. *J. Annu. Rev. Biophys. Biophys. Chem.* **1988**, *17*, 145–166.
- Epand, R. M.; Epand, R. F. *Biochim. Biophys. Acta* **2009**, *1788*, 289–294.
- Gazit, E.; Boman, A.; Boman, H. G.; Shai, Y. *Biochemistry* **1995**, *34*, 11479–11488.
- Dathe, M.; Meyer, J.; Beyermann, M.; Maul, B.; Hoischen, C.; Bienert, M. *Biochim. Biophys. Acta* **2002**, *1558*, 171–186.
- Matsuzaki, K.; Harada, M.; Funakoshi, S.; Fujii, N.; Miyajima, K. *Biochim. Biophys. Acta* **1991**, *1063*, 162–170.
- Abraham, T.; Lewis, R. N. A. H.; Hodges, R. S.; McElhaney, R. N. *Biochemistry* **2005**, *44*, 11279–11285.
- Joanne, P.; Galanth, C.; Goasdoué, N.; Nicolas, P.; Sagan, S.; Lavielle, S.; Chassaing, G.; El Amri, C.; Alves, I. D. *Biochim. Biophys. Acta* **2009**, *1788*, 1772–1781.
- Vad, B. S.; Bertelsen, K.; Johansen, C. H.; Pedersen, J. M.; Skrydstrup, T.; Nielsen, N. C.; Otzen, D. E. *Biophys. J.* **2010**, *98*, 576–585.
- Shai, Y.; Oren, Z. *J. Biol. Chem.* **1996**, *271*, 7305–7308.
- Breukink, E.; van Kraaij, C.; van Dalen, A.; Demel, R. A.; Siezen, R. J.; de Kruijff, B.; Kuipers, O. P. *Biochemistry* **1998**, *37*, 8153–8162.
- Christiaens, B.; Symoens, S.; Verheyden, S.; Engelborghs, Y.; Joliot, A.; Prochiantz, A.; Vandekerckhove, J.; Rosseneu, M.; Vanloo, B. *Eur. J. Biochem.* **2002**, *269*, 2918–2926.

JP1052248

Paper IV: W-band pulse EPR distance measurements in peptides using Gd³⁺-dipicolinic acid derivatives as spin labels.

Michal Gordon – Grossman, Ilia Kaminker, Yana Gofman, Yechiel Shai and Daniella Goldfarb.

Published in *Phys Chem Chem Phys*, 2011, 13(22):10771-10780.

Reproduced by permission of the PCCP Owner Societies from “W-band pulse EPR distance measurements in peptides using Gd³⁺-dipicolinic acid derivatives as spin labels”, Michal Gordon – Grossman et al., *Physical Chemistry Chemical Physics*, Royal Society of Chemistry, May 9, 2011. Copyright (2011), Royal Society of Chemistry (<http://pubs.rsc.org/en/Content/ArticleLanding/2011/CP/c1cp00011j>).

Cite this: *Phys. Chem. Chem. Phys.*, 2011, **13**, 10771–10780

www.rsc.org/pccp

PAPER

W-Band pulse EPR distance measurements in peptides using Gd^{3+} -dipicolinic acid derivatives as spin labels†

Michal Gordon-Grossman,^a Ilia Kaminker,^a Yana Gofman,^b Yechiel Shai^c and Daniella Goldfarb^{*a}

Received 4th January 2011, Accepted 30th March 2011

DOI: 10.1039/c1cp00011j

We present high field DEER (double electron–electron resonance) distance measurements using Gd^{3+} ($S = 7/2$) spin labels for probing peptides' conformations in solution. The motivation for using Gd^{3+} spin labels as an alternative for the standard nitroxide spin labels is the sensitivity improvement they offer because of their very intense EPR signal at high magnetic fields. Gd^{3+} was coordinated by dipicolinic acid derivative (4MMDPA) tags that were covalently attached to two cysteine thiol groups. Cysteines were introduced in positions 15 and 27 of the peptide melittin and then two types of spin labeled melittins were prepared, one labeled with two nitroxide spin labels and the other with two 4MMDPA– Gd^{3+} labels. Both types were subjected to W-band (95 GHz, 3.5 T) DEER measurements. For the Gd^{3+} labeled peptide we explored the effect of the solution molar ratio of Gd^{3+} and the labeled peptide, the temperature, and the maximum dipolar evolution time T on the DEER modulation depth. We found that the optimization of the $[\text{Gd}^{3+}]/[\text{Tag}]$ ratio is crucial because excess Gd^{3+} masked the DEER effect and too little Gd^{3+} resulted in the formation of Gd^{3+} -tag₂ complexes, generating peptide dimers. In addition, we observed that the DEER modulation depth is sensitive to spectral diffusion processes even at Gd^{3+} concentrations as low as 0.2 mM and therefore experimental conditions should be chosen to minimize it as it decreases the DEER effect. Finally, the distance between the two Gd^{3+} ions, 3.4 nm, was found to be longer by 1.2 nm than the distance between the two nitroxides. The origin and implications of this difference are discussed.

Introduction

Site directed spin-labeling combined with electron paramagnetic resonance (EPR) is a common method for determining structural and dynamic properties of peptides and proteins. This method

usually involves cysteine mutation and the attachment of a nitroxide spin label through the formation of a disulfide bond (referred to as site directed spin labeling).¹ In the last decade measurements of distances between two nitroxide spin labels in biomacromolecules by pulse EPR techniques have attracted considerable attention due to the ability to measure distances in the range of 1.5–8 nm.^{2–9} Such measurements rely on the determination of the dipolar coupling between the two spins, which is inversely proportional to the cube of their interspin distance. Usually distance measurements on nitroxide labeled biomacromolecules are carried out on pulse X-band spectrometers using the four-pulse DEER sequence (Fig. 1a).¹⁰ The minimal concentration of spin labeled molecules is usually ~0.05–0.1 mM, the amount of sample needed is approximately 40–100 μl and the time required to obtain good quality time domain traces is 12–24 hours.^{6,10} Sensitivity improvement has been recently reported for Q-band measurements¹¹ or by using perdeuterated proteins¹² which exhibit a considerably longer phase memory time compared to natural abundance samples.

Recently, Gd^{3+} ($S = 7/2$) spin labels have been suggested as an alternative to nitroxide spin labels for high magnetic field measurements where high spin Gd^{3+} offers a number of

^a Department of Chemical Physics, Weizmann Institute of Science, Rehovot, 76100, Israel. E-mail: daniella.goldfarb@weizmann.ac.il

^b Helmholtz-Zentrum, 21502 Geesthacht, Germany

^c Department of Biological Chemistry, Weizmann Institute of Science, Rehovot, 76100, Israel

† Electronic supplementary information (ESI) available: The details of the titration of 4MMDPA–melC₁₅C₂₇ with Gd^{3+} , showing the UV-Vis spectra of the titration with arsenazo and the titration curve obtained at $\lambda = 650$ nm for the arsenazo– Gd^{3+} complex. The speciation of Gd^{3+} –(4MMDPA)_{1–3} in solution. W-Band ED-EPR spectra of frozen solution of Gd^{3+} –(4MMDPA) as a function of $[\text{Gd}^{3+}]/[4\text{MMDPA}]$, W-band ED-EPR spectra and the corresponding simulations of aquo Gd^{3+} and Gd^{3+} –(4MMDPA) 1 : 100. The experimental details of ¹H ENDOR measurements and ¹H ENDOR spectra of frozen solutions of Gd^{3+} –4MMDPA with different $[\text{Gd}^{3+}]/[4\text{MMDPA}]$ ratios. A comparison of the W-band ED-EPR spectra of Gd^{3+} –(4MMDPA) with different $[\text{Gd}^{3+}]/[4\text{MMDPA}]$, where $[\text{Gd}^{3+}] = 0.1$ mM, and of 4MMDPA–melC₁₅C₂₇ with Gd^{3+} for $R = 1:2, 1:1.25$ and $1:0.7$, at constant $[4\text{MMDPA}] = 0.2$ mM. Details of relaxation time measurements and DEER control measurements details. See DOI: 10.1039/c1cp00011j

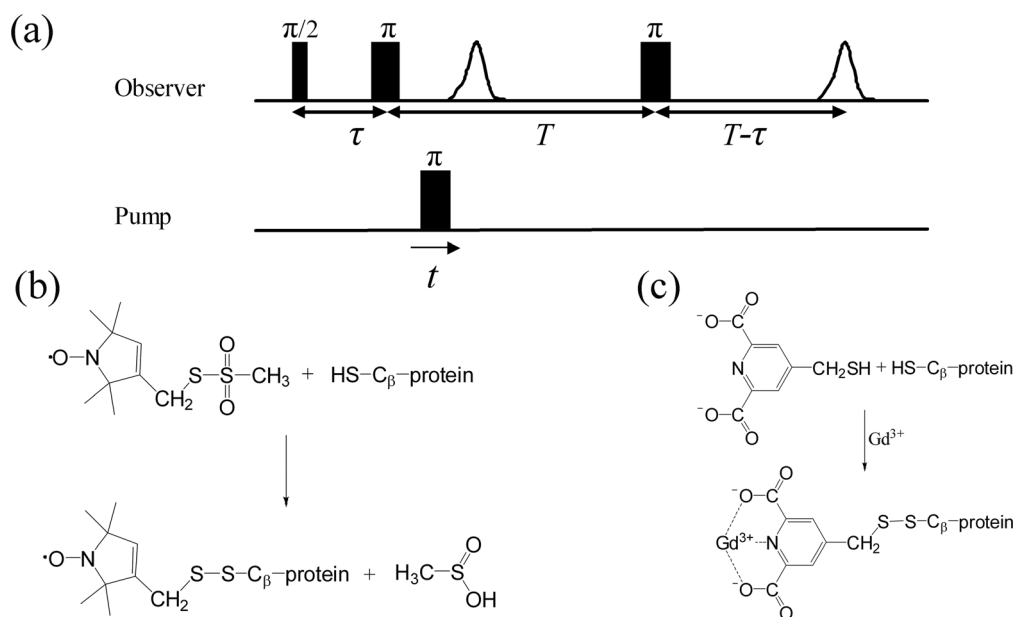


Fig. 1 (a) The four pulse DEER sequence used in this work. (b) The conjugation reaction of MTSL with a cysteine residue, generating the nitroxide labeled peptide. (c) The reaction yielding Gd^{3+} -4MMDPA labeled peptide.

advantages.^{13–16} Distance measurements on a pair of nitroxides at high fields are of course possible and it has higher (absolute) sensitivity than possible at the X-band per single measurement, provided that the spectrometer can produce short enough microwave pulses.^{13,17} The difficulty of such measurements is the data analysis required for the extraction of the distance distribution. At high fields the nitroxide g -anisotropy becomes resolved and because the microwave pulses excite only a fraction of the EPR spectrum only a subset of molecules with selected orientations with respect to the external magnetic field contributes to the DEER trace. This is referred to as orientation selection^{18–20} and it has to be taken into account explicitly in the extraction of the distance distribution from the DEER data.^{19–26} This requires a series of measurements at several positions along the EPR powder pattern and a rather complex data analysis.

The EPR spectrum of the $| -1/2 \rangle \rightarrow | 1/2 \rangle$ central transition of Gd^{3+} narrows with increasing external magnetic field, B_0 , thus increasing sensitivity. Moreover, the isotropic g value of Gd^{3+} , the second order contribution of the zero field splitting (ZFS) to the central transition and the relatively large distribution of the ZFS parameters (D , E)²⁷ circumvent the problem of orientation selection. Earlier measurements on a rigid bis- Gd^{3+} complex have shown that at Ka- and W-band (32 and 95 GHz respectively) the central transition can be treated as an effective $S = 1/2$ system and that data analysis can be carried out as done for a pair of nitroxides ($S = 1/2$) using the DeerAnalysis software.¹⁵ Recently it has been demonstrated that proteins can be labeled with Gd^{3+} binding tags that are covalently attached to cysteines (see Fig. 1b and c), as in site directed spin labeling, and that distance distributions can be readily extracted from W-band DEER measurements.¹³ The tag used was a dipicolinic acid derivative that has been designed as a lanthanide tag for paramagnetic NMR.²⁸ These DEER measurements were carried out on 2–3 μl of 0.05–0.1 mM

protein solutions. This is a significant improvement over the standard X-band measurements in terms of sample quantity, without compromising the simplicity of data analysis. This work also revealed two difficulties, the sensitivity of the DEER effect to the presence of Gd^{3+} that is free in solution and not attached to the protein tags and the lower than expected modulation depth.^{13–15}

In the present work we continue to explore the new approach of distance measurements using Gd^{3+} spin labels, focusing on peptides and addressing the problems described above and other issues unique to peptides. As a model peptide we used melittin, a common model for antimicrobial peptides (see sequence in Table 1)^{29–31} that we labeled with two Gd^{3+} ions using a 4-mercaptopropionic acid (4MMDPA) tag which coordinates Gd^{3+} (binding constant in the nanomolar affinity)³² and can be readily attached to a cysteine thiol group *via* a disulfide bridge, similar to nitroxides (Fig 1b and c).²⁸ We present W-band DEER measurements as a function of the $[\text{Gd}^{3+}]/[4\text{MMDPA-melittin}]$ ratio, temperature and the dipolar evolution time interval, T , followed by a discussion of the optimum sample preparation and measurements conditions. Next, similar DEER measurements performed on melittin doubly labeled with nitroxides are described and the distance distributions obtained for the nitroxides and Gd^{3+} labels are compared. The differences are accounted for through Monte-Carlo (MC) simulations.

Table 1 Peptides designations and sequences. The position of the spin label (or the amino acid mimicking it) is indicated by underscore

Peptide designation	Sequence
Native melittin	GIGAVLKVLTTGLPALISWIKRKRQQ
mel-C ₁₅ C ₂₇	GIGAVLKVLTTGLPCLISWIKRKRQQC
mel-K ₁₅ K ₂₇	GIGAVLKVLTTGLPKLISWIKRKRQQK
mel-H ₁₅ H ₂₇	GIGAVLKVLTTGLPHLISWIKRKRQQH

Experimental methods

Materials

4-Mercaptomethyl-dipicolinic acid (4MMDPA) for peptide labeling was purchased from Latvian Institute of Organic Synthesis. 5,5'-Dithiobis-(2-nitrobenzoic acid) (DTNB), used for the procedure of ligation of 4MMDPA to the peptide, was purchased from Sigma-Aldrich. 1-Oxyl-2,2,5,5-tetramethyl-3-pyrroline-3-methyl, methanethiosulfonate (MTSL) was purchased from Toronto Research Chemicals, Ontario, Arsenazo III Beckman[®], 2,2-(1,8-dihydroxy-3,6-disulfonaphthylene-2,7-bisazo) bisbenzenearsonic acid, was purchased from Fluka. It was used in titrations aiming at determining the amount of 4MMDPA labeled melittin in solution. Perdeuterated glycerol-d₈ was purchased from Cambridge Isotope Laboratories.

Peptide spin labeling and purification

Melittin with cysteines in positions 15 and 27 (mel-C₁₅C₂₇) was prepared as described previously (see sequence in Table 1).⁷ Melittin was labeled with MTSL through attachment to the cysteine SH group at positions 15 and 27 as reported earlier.⁷ Site-specific labeling of the melittin with Gd³⁺ was done through 4MMDPA. The ligation of 4MMDPA to the purified peptide was done according to a procedure reported in the literature.²⁸ The labeled peptide product was purified by RF-HPLC with the same analytical column that was used for the unlabeled peptide. The peptide was analyzed by electrospray mass spectroscopy to confirm its composition and molecular weight. The ligated-peptides were lyophilized and then weighted and stored in a freezer at -20 °C.

Sample preparation

The amount of Gd³⁺ added to 4MMDPA-mel-C₁₅C₂₇ for DEER measurements was determined from a titration with the colorimetric indicator arsenazo^{33,34} as described in the ESI.† According to the titration curve, see ESI†, Fig. S1b, three Gd³⁺-4MMDPA-melC₁₅C₂₇ samples were prepared. GdCl₃ and the labeled peptide were dissolved in doubly distilled water (DDW) to give different $R = [\text{Gd}^{3+}]/[\text{4MMDPA-tag}]$ molar ratios of 1:0.7, 1:1.25, and 1:2. These doubly labeled peptides were lyophilized and then weighted and stored in a freezer at -20 °C. The labeled peptides were then dissolved in 7:3 D₂O: glycerol-d₈ solution followed by vortex and sonication for approximately one minute. The final total peptide concentration was 0.1 mM where the total Gd³⁺ concentrations were 0.1, 0.16 and 0.28 mM for $R = 1:2, 1:1.25, \text{ and } 1:0.7$, respectively.

For the X-band DEER measurements, approximately 40 μl of the samples were rapidly frozen by insertion of the EPR tube (2.7 mm id and 3.7 mm od) into liquid nitrogen. Samples for W-band DEER measurements were prepared similarly but in quartz capillaries (0.6 mm id × 0.84 mm od, VitroCom Inc.). Thereafter, the samples remained frozen in liquid nitrogen.

Spectroscopic measurements

X-Band (9.5 GHz) DEER measurements

DEER experiments were carried out at 50 K on a Bruker ELEXSYS E580 spectrometer using the EN4118X-MD-4 probe head. The constant time four-pulse DEER experiment, shown in Fig. 1a, was employed with a $+x/-x$ phase cycle on the first pulse and averaging over 25 increments of τ ($\tau = 400$ ns, $\Delta\tau = 8$ ns) to suppress nuclear modulations.¹⁰ The echo was measured as a function of t , while T was kept constant. The pump frequency, ν_{pump} , was set to the center of the resonator bandwidth and the external magnetic field was set to the maximum of the nitroxide spectrum at the pump frequency. The observer frequency, ν_{obs} , was set at 60 MHz higher than ν_{pump} . The length of all MW pulses was 40 ns, where different amplitudes were used for π and $\pi/2$ pulses, and the dwell time was 20 ns. The number of shots per point and scan number were 30 and 56, respectively, and the repetition time was 7 ms. Total accumulation time for the data set was approximately 12 h.

W-Band (95 GHz) measurements

W-Band DEER measurements were performed on a home-built spectrometer.³⁵ Gd³⁺ labeled peptides were measured at 10 K and 25 K, whereas nitroxide labeled samples were measured at 40 K. The four pulse DEER sequence was employed (see Fig 1a) where the separations between the pump and observer frequencies ($\Delta\nu$) were 65 MHz and 78 MHz for the nitroxide and Gd³⁺ samples, respectively. For the nitroxide samples the observe $\pi/2$ and π pulses were 40 and 80 ns and the pump pulse duration was 25 ns. For the Gd³⁺ samples the observe $\pi/2$ and π pulses were 15 and 30 ns and the pump pulse duration was 12.5 ns or 15 ns. DEER traces were summed over eight τ values starting with 350 ns for nitroxide samples and 250 ns for Gd³⁺ samples and incremented by a step of $\Delta\tau_1 = 12.5$ ns. An eight step phase cycle was employed: $\pi/2_{\text{obs}} + x, -x, +x, -x, +x, -x, +x, -x; \pi_{\text{obs}} + x, +x, +x, +x, -x, -x, -x, -x; \pi_{\text{pump}} + x, +x, -x, -x, +x, +x, -x, -x; \pi_{\text{obs}} + x, +x, +x, +x, +x, +x, +x, +x$. The receiver phase cycle was $+, -, +, -, +, -, +, -$. The repetition time was 100 μs for the Gd³⁺ samples and 20 ms for the nitroxide samples. The phase cycling was needed to remove various instrumental artifacts and pulse imperfection.

Accumulation times were 1–6 h and 4–12 h for the Gd³⁺ and nitroxide labeled peptides, respectively, depending on the delay time, T . Distance distributions were obtained from the dipolar time evolution data at X- and W-band using the DeerAnalysis2009 software.³⁶ The background decay was fitted to an homogenous decay with a dimension of 3. Tikhonov regularization was performed with L curve computation and the regularization parameter was set to 100 or 1000.

Echo detected (ED) EPR spectra of the nitroxide labeled peptides were recorded at 40 K using $\pi/2$ and π pulses of 60 ns and 120 ns, respectively, with $\tau = 300$ ns and a repetition time of 20 ms. ED-EPR spectra of Gd³⁺ samples were recorded at 10 K and at 25 K, and the $\pi/2$ and π pulses were 30 ns and 60 ns, respectively, with a repetition time of 3 ms.

Two-pulse echo decay measurements, $\pi/2-\tau-\pi-\tau$ -echo, to measure the phase memory time of Gd^{3+} samples were carried out at 10 K and 25 K, with the experimental values described above. The repetition time was 3 ms and two-step phase cycling was carried out. All measurements were performed at a field corresponding to the maximum echo intensity of the Gd^{3+} .

Saturation recovery ($t_s-T-\pi/2-\tau-\pi-\tau$ -echo) was employed for measuring the spin-lattice relaxation time with a repetition rate of 3 ms. A two-step phase cycling, where the $\pi/2$ pulse was cycled with 0° , 180° was employed. All measurements were performed at a field corresponding to the maximum echo intensity, with a saturation pulse length, t_s , of 1.5 ms that was optimized by increasing its length with full power until no change in the recovery trace was observed. The echo detection $\pi/2$ and π microwave pulse lengths were 60 ns and 120 ns, respectively.

Computational methods

Monte-Carlo (MC) simulations of the peptides were performed according to the methodology described previously.^{7,37,38} The peptides were represented by two interaction sites for each amino acid, corresponding to the α -carbon and side chain. These interaction sites, as well as sequential α -carbons, were connected by virtual bonds. To explore the possible conformations of the peptides in water, 3 simulations consisting of 500 000 MC cycles were conducted. New peptide structures were generated by simultaneously perturbing the generalized coordinates. The maximal step of the virtual backbone torsion angle was 3° , while the maximal step for both the side-chain torsion angle and its angle with respect to the backbone was 0.5° . The evaluation of the conformations was performed using a statistical potential based on available 3D structures.³⁹ The energy function assigns a score (energy) to each conformation of the peptide according to its abundance in the Protein Data Bank (PDB). Common conformations received high scores (low energy) while rare conformations received lower scores (higher energy).

Melittin's initial structure was taken from PDB entry 2MLT. As the label used in the experimental procedures, namely Gd^{3+} -4MMDPA, was not present in the statistical potential used,³⁹ it was substituted by either Lys or His (Table 1). These amino acids were chosen because of their positive charge, similar to the label. The initial structures of the labeled peptides (Table 1) were obtained by modifying the native structure using the NEST methodology, with default parameters.⁴⁰

The helical content of the peptides was calculated as described by Shental-Bechor *et al.*, 2005.⁴¹ A residue was considered to be in a helical state if the dihedral angles of the two adjacent virtual bonds lie within the interval $-120^\circ \pm 30^\circ$. The dihedral angles were defined by four consecutive α -carbons.⁴¹ The first and last two residues were excluded since the rotational angles of the peptide's ends cannot be defined.

The data from the simulations were used to calculate distance distribution between the labels, meaning His15 and

His27 or Lys15 and Lys27. In the case of unlabeled melittin, the distance distribution was calculated between Pro14 and Gln26. Since we used a reduced representation for the peptides, we defined the distance between two residues as the distance between two sites corresponding to side chains. For His the side chain site was defined at the center of the imidazole ring; for Lys it was defined at the ϵ -amino group; for Gln it was defined at the amide group; for Pro it was defined at the average location between β -, γ - and Δ -carbons.³⁷

Melittin labeled with Gd^{3+} -4MMDPA

The EPR spectrum and relaxation times

Melittin was labeled at positions 15 and 27 (mel- $\text{C}_{15}\text{C}_{27}$) with either two 4MMDPA tags or two nitroxide spin labels, as shown in Fig. 1b and c. Based on the titration of 4MMDPA-mel $\text{C}_{15}\text{C}_{27}$ with Gd^{3+} in the presence of arsenazo (Fig. S1, ESI[†]), we prepared three samples of doubly labeled peptide with $[\text{Gd}^{3+}]/[4\text{MMDPA-mel-C}_{15}\text{C}_{27}]$ ratios of 1:0.35, 1:0.63 and 1:1, which correspond to $R = [\text{Gd}^{3+}]/[4\text{MMDPA-tag}]$ ratios of 1:0.7, 1:1.25 and 1:2, respectively, assuming 100% labeling. In all three samples the concentration of the labeled peptide was 0.1 mM. The W-band ED-EPR spectra of these three samples are depicted in Fig. 2. The lineshapes of the three samples are clearly different. The spectrum of the $R = 1:0.7$ sample shows the dominance of a narrower central transition, as well as a narrower background due to the Gd^{3+} transitions other than the central transition. The spectrum of the $R = 1:1.25$ sample is broader than that of the $R = 1:0.7$ sample, but it is not as wide as that of the $R = 1:2$ sample. The observed differences in lineshapes are attributed to the presence of different species in solution with relative amounts that are determined by $[\text{Gd}^{3+}]$, $[4\text{MMDPA tags}]$ and the corresponding binding constants. Comparison of these spectra with spectra of Gd^{3+} -4MMDPA (just the tag, not the labeled peptide) with different ratios of

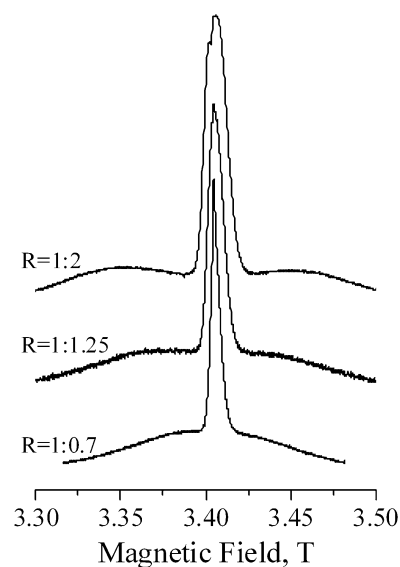


Fig. 2 W-Band ED-EPR spectra (25 K) of solutions of Gd^{3+} -4MMDPA-mel $\text{C}_{15}\text{C}_{27}$ with $[\text{Gd}^{3+}]/[4\text{MMDPA-tag}] = R = 1:2, 1:1.25, \text{ and } 1:0.7$.

[Gd³⁺]/[4MMDPA] helped to account for the differences (Fig. S2–S6, ESI†). For $R = 1:0.7$ there is a significant contribution from aquo Gd³⁺ (approximately 40% according to calculations presented in Fig. S2a, ESI†). Due to its smaller D value ($D = 850$ MHz, see Fig. S4a, ESI†), its central transition is narrow and dominates the spectrum of the $R = 1:0.7$ sample. The broader spectrum of $R = 1:1.25$ is attributed to a reduction in the amount of free Gd³⁺ and the increase of the amount of the Gd³⁺–4MMDPA complexes (estimated around 67% according to calculations, see Fig. S2a, ESI†) which have larger D values. Finally, for $R = 1:2$ there is a deficiency of Gd³⁺, free Gd³⁺ is no longer present and there is a major contribution from Gd³⁺–4MMDPA₂ complexes (approximately 72% according to calculation, see Fig. S2a, ESI†) that have even larger D . The free Gd³⁺ present in the $R = 1:1.25$ sample is not a consequence of a too small binding constant but due to a large equilibrium constant for the Gd³⁺–(4MMDPA)₂ complex.

Gd³⁺ can coordinate 1–3 tags, however for peptide bound tags, due to steric hindrance, it is more likely to coordinate one or two tags, either from the same peptide molecule (intra-molecular complex) or from different peptides (inter-molecular) forming dimers. Clearly, neither is desired. While the formation of intra- and inter-peptide complexes is plausible for peptides, which are relatively small and highly flexible in solution, this is less likely for proteins. The formation of intra-peptide Gd³⁺ complexes does not contribute to the pair-wise DEER effect and therefore is not of concern. In the ESI† (Fig. S2–S6) we present a more detailed discussion of the speciation of the Gd³⁺–4MMDPA_{*n*} ($n = 0–3$) complexes in solution based on the available equilibrium constants³² and measurements of ED-EPR and ¹H ENDOR (electron–nuclear double resonance) spectra as a function of the [Gd³⁺]/[4MMDPA] ratio. The ENDOR spectra were used to count the number of water ligands and from this we deduced what types of complexes are present in the frozen solution.⁴²

The relative intensity of the central transition and the broad background is temperature dependent because of the Boltzman distribution (see Fig. 3). The relaxation times of Gd³⁺ are also temperature dependent. The phase memory time obtained from the two pulse echo decay (see Fig. S7a, ESI†) and the spin–lattice relaxation time determined from saturation recovery measurements at 25 K and 10 K (see Fig. S7b, ESI†) are listed in Table 2. The saturation recovery data were fitted with a bi exponential function yielding a long time constant attributed to the spin lattice relaxation time, T_1 , and a shorter one. The latter could have residual contribution from spectral diffusion and it can also be associated with transitions other than the central transition. As will be shown later these values should be taken into consideration when optimizing DEER measurements because they affect the S/N ratio.

DEER measurements

Effect of [Gd³⁺]/[4MMDPA–melC₁₅C₂₇]. Prior to DEER measurements on melittin doubly labeled with 4MMDPA–Gd³⁺ we verified that melittin does not bind Gd³⁺ specifically such that it can contribute to the pair

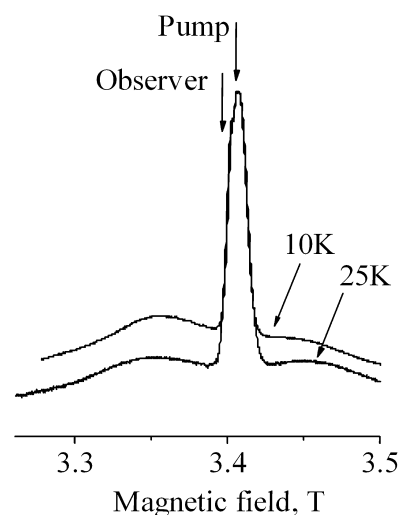


Fig. 3 W-Band ED-EPR spectra of a solution of Gd³⁺–4MMDPA–melC₁₅C₂₇ with $R = 1:1.25$, normalized to the maximum echo intensity, measured at 10 K and 25 K. The positions of the pump and observer pulses in the DEER measurements are shown in the figure.

Table 2 The relative populations of the $M_s = \pm 1/2$ levels, the calculated λ_n and λ_{ef} , the experimental DEER modulation depth, λ_{exp} , and the relaxation times of the $R = 1:1.25$ sample

	$P(-1/2)$	$P(1/2)$	λ_n	λ_{ef}	λ_{exp}^a	$T_M/\mu s$	$T_1^b/\mu s$
10 K	0.096	0.061	0.176	0.028	0.022	3.6	100 (22)
25 K	0.105	0.126	0.150	0.035	0.017	2.6	91 (12)

^a Determined from the DEER traces recorded with $T = 2 \mu s$. ^b The value in parentheses corresponds to the shorter time constant.

distance distribution. For this purpose we have carried out DEER measurements on a solution of GdCl₃ (0.2 mM) with and without melittin (0.4 mM). The ED-EPR spectra and the homogenous decay of the DEER traces of the two samples were found to be the same. Hence, we conclude that Gd³⁺ does not bind to unlabeled melittin (see Fig. S8, ESI†).

W-Band DEER traces of Gd³⁺–4MMDPA–melC₁₅C₂₇ with $R = 1:0.7$, $1:1.25$ and $1:2$ are shown in Fig. 4. In these measurements the frequency of the pump pulse was set to the maximum of the central $|-1/2\rangle \rightarrow |1/2\rangle$ transition, while that of the observer pulse was shifted by $\Delta\nu = 78$ MHz (see arrows in Fig. 3). The sample with $R = 1:0.7$ shows just a monotonous decay without any modulations indicative of a specific pair-wise dipolar interaction. We attribute this to the presence of a significant amount of aquo Gd³⁺ in solution. Because of the narrower central transition of aquo Gd³⁺ its relative contributions to the observer spins and particularly to the pump spins are larger than its actual relative amount in the sample. Therefore, it practically masks any specific pair wise modulation in the DEER trace. Reduction of R to $1:1.25$, where the relative amount of the free aquo Gd³⁺ is considerably reduced, revealed the specific pair-wise dipolar modulation as shown in Fig. 4a. The data after background removal are shown in Fig. 4b and the obtained distance distribution, Fig. 4c, exhibits a maximum at 3.4 nm. The DEER trace of the $R = 1:2$ sample reveals a deeper

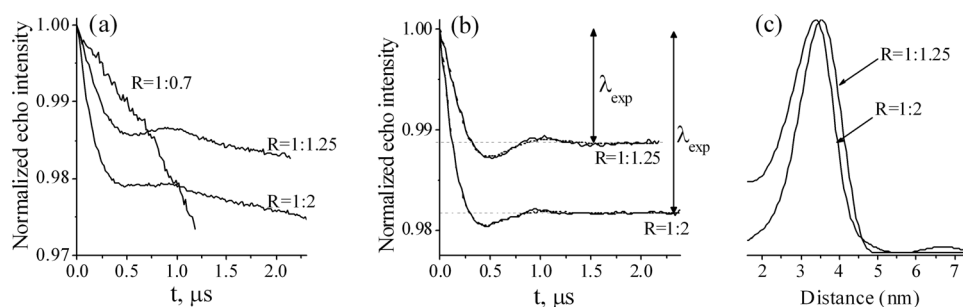


Fig. 4 (a) W-Band four pulse DEER traces of Gd^{3+} -4MMDPA-melC₁₅C₂₇ with $R = 1:2$ (10 K), $1:1.25$ (10 K) and $1:0.7$ (25 K). (b) The corresponding four pulse DEER traces after background removal obtained for $R = 1:2$ and $1:1.25$ and the fitted data obtained with the distance distributions shown in (c). λ_{exp} are noted in (b).

modulation (1.7% compared to 1.2%), and the distance distribution, although very similar to the $R = 1:1.25$ sample, is shifted to 3.3 nm and exhibits some higher intensities at lower distances. These differences are attributed to short distances obtained from peptide dimers due to the formation of Gd^{3+} -4MMDPA₂ complexes, as discussed in the previous section. The deeper modulation depth arises from the absence of free Gd^{3+} in solution and from contributions from three spin interactions in the dimers that have deeper modulations than pairs.^{43,44}

Effect of temperature and time interval T . To further explore the influence of experimental parameters on the modulation depth we carried out DEER measurements on the $R = 1:1.25$ sample at different temperatures and different time intervals T , recalling that the maximum value of t is $T - \tau$. For Gd^{3+} , the four pulse echo intensity $V(t)$ is given by:⁴⁵

$$V(t) \propto V(0)(1 - \lambda_{\text{ef}}(1 - \cos \omega_{\text{dd}}t)) \quad (1)$$

where ω_{dd} is the dipolar frequency and λ_{ef} is the probability to flip a B spin. Equation 1 corresponds to the DEER trace after background removal. Assuming that the contributions to the DEER trace come only from spin pairs with $M_S = \pm 1/2$ and taking into account only the lineshape of the central transition, the nominal value of λ , λ_n , can be calculated using the following:^{14,46}

$$\lambda_n = \int \frac{\omega_1^2}{\Omega^2} \sin^2 \left[\frac{\Omega}{2} t_p \right] g(\Delta\omega) d(\Delta\omega) \quad (2)$$

$$\Omega^2 = \omega_1^2 + \Delta\omega^2 \quad (3)$$

In eqn (2) and (3) $\Delta\omega$ is the off resonance relative to the pump pulse frequency, t_p is the pump pulse duration, $g(\Delta\omega)$ is the EPR lineshape of the central transition and the MW field amplitude ω_1 can be determined from nutation measurements. λ_{ef} is obtained from λ_n and the relative populations of the $M_S = \pm 1/2$ levels, $P = P_{1/2} + P_{-1/2}$, according to $\lambda_{\text{ef}} = P\lambda_n$.^{14,15} In Table 2 we list the λ_{ef} values calculated for the $R = 1:1.25$ sample at 10 K and 25 K and the experimental values, λ_{exp} , obtained from the asymptotic value of $V(t)$ (see eqn (1)). DEER traces are shown in Fig. 5.

This calculation of λ_{ef} is valid when the contributions of the broad background to the pumped B spins are negligible or if it has been subtracted.^{14,15} This assumption is better fulfilled at 25 K than at 10 K. Therefore, λ_n and λ_{exp} at 10 K should be taken as an upper limit due to contributions of the other transitions. In principle, λ_{ef} can be calculated directly from the lineshape of the full spectrum, provided that the broad tails in the upper and lower field edges are recorded and taken into account. Table 2 shows that the calculated λ_{ef} are larger than the experimental values, similar to earlier reports.^{14,15} Moreover, the expected λ_{ef} (25 K) > λ_{ef} (10 K) relation is opposite to that observed experimentally. The lower than expected λ_{exp} can be due to the presence of free Gd^{3+} , but this should have the same effect at 10 K and 25 K. The presence of short distances that cannot be probed by the pumped pulse should reduce the experimental modulation depth.^{9,13,47} This, however, seems unlikely in this particular sample considering the pump pulse length and the distance distribution obtained. Moreover, it should not depend on temperature.

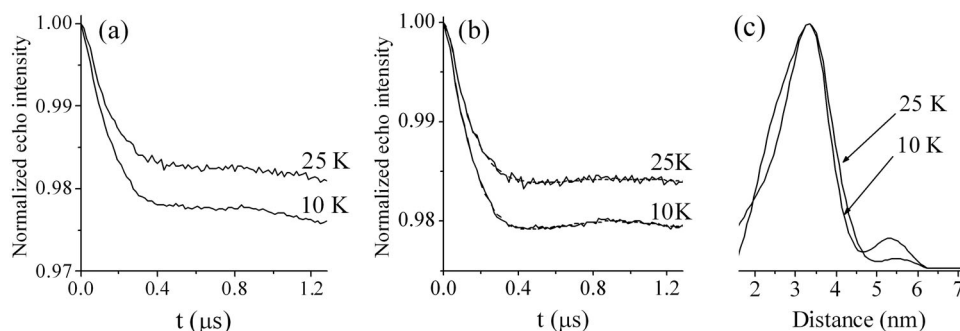


Fig. 5 (a) W-Band four pulse DEER traces of Gd^{3+} -4MMDPA-melC₁₅C₂₇ with $R = 1:1.25$, measured at 10 K and 25 K, $T = 2 \mu\text{s}$. (b) The corresponding traces after background removal and data fitting (dashed), with the distance distribution shown in (c).

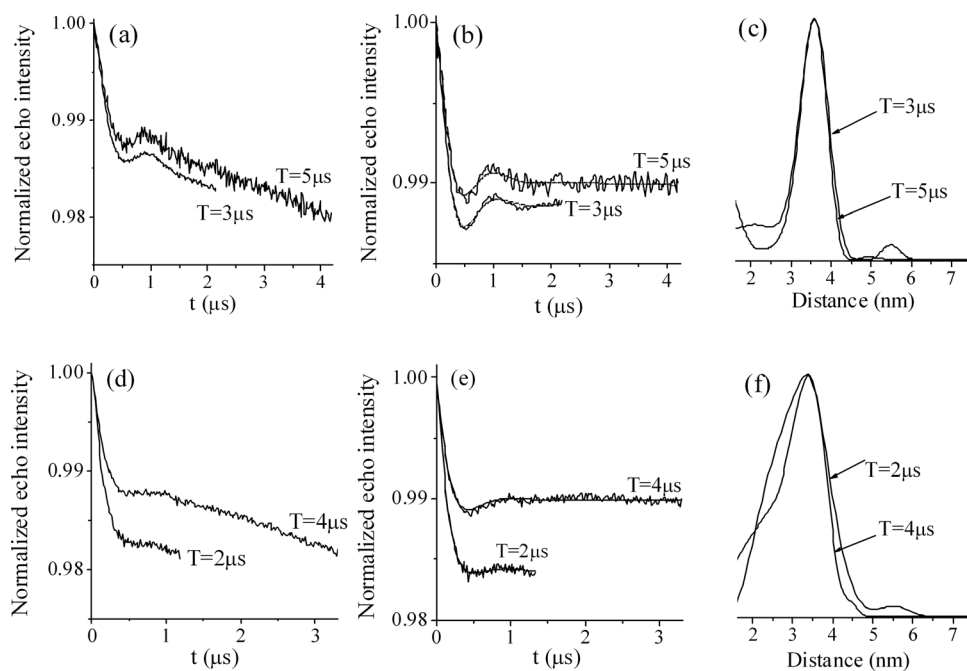


Fig. 6 (a) W-Band four pulse DEER traces of Gd^{3+} -4MMDPA-mel $\text{C}_{15}\text{C}_{27}$ with $R = 1:1.25$ with $T = 3 \mu\text{s}$ and $T = 5 \mu\text{s}$ measured at 10 K. (b) The corresponding traces after background removal and data fitting (dashed), with the distance distribution shown in (c). (d-f) The same as (a-c) for $T = 2$ and $4 \mu\text{s}$ at 25 K.

We also examined the effect of the time interval, T , at both temperatures, on λ_{exp} as shown in Fig. 6. Here we see that for both temperatures the longer T is the lower λ_{exp} is, the change being larger at 25 K. The T and temperature dependence of λ_{exp} suggest that it contains contributions from spin dynamics. This will be discussed in more detail later. All the DEER measurements carried out under the various conditions described above gave a distance distribution with a maximum at 3.4 nm with some variations in width attributed to differences in S/N and variation in background removal. The latter is highly sensitive to the total duration of the DEER trace.

Melittin labeled with nitroxides

We have also carried out W-band DEER measurements on mel- $\text{C}_{15}\text{C}_{27}$ labeled with nitroxides. The echo detected EPR spectrum of this sample is shown in Fig. 7a. Here

measurements were carried out at several positions for the observer and pump pulses and the results are shown in Fig. 7b. The distance distributions obtained from the three traces are shown in Fig. 7c. They all exhibit a maximum at 2.5 nm and vary a little in their total width and in the intensity and position of a shoulder between 3–4 nm. These are further compared to the distance distribution obtained from X-band measurements,⁷ where the maximum of the distance distribution is observed at 2.2 nm. There could be several reasons for the different distance distributions obtained at X- and W-band. The first, and most likely, is the presence of some orientation selection at the W-band. The other two reasons concern the differences in pulse durations. It is well known that the bandwidth of the pump pulse should exceed the dipolar frequency, ω_{dd} , in order to observe dipolar modulations. Therefore too long pump pulses will miss contributions from short distances.^{3,47} This argument, however,

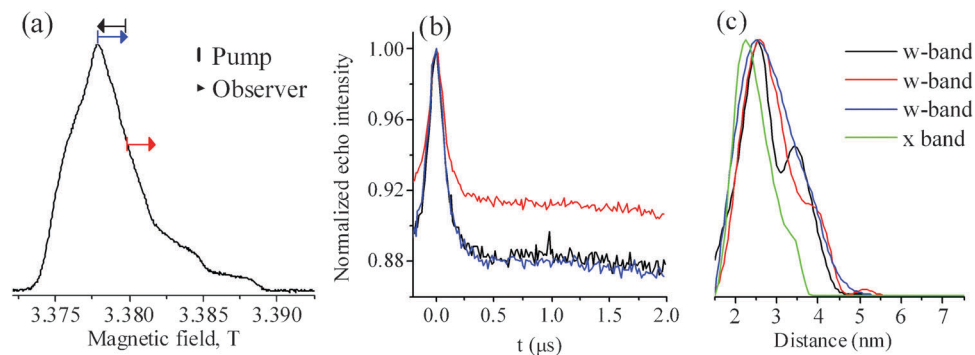


Fig. 7 (a) W-Band ED-EPR spectrum (25 K) of a solution of 0.1 mM nitroxide labeled mel- $\text{C}_{15}\text{C}_{27}$. (b) The raw W-band (25 K) DEER traces obtained at different observer and pump frequencies, and the corresponding (c) distance distributions along with that measured at the X-band (40 K). The positions of pump (beginning of arrow) and observer (end of arrow) pulses are shown in (a) (color coded).

is not relevant as the pump pulse duration in the X-band measurements (40 ns) was longer than in the W-Band measurements (25 ns) and therefore short distances should have been missed at the X-band and not W-band. It was shown that the duration of the observer pulses is also important and too long pulses can also lead to reduced contributions from short distances.⁴⁷ The observer pulses in the W-band measurements were longer (40, 80 ns) than in the X-band measurements (40, 40 ns) and we cannot exclude that this had an effect.

Discussion

We have shown that similar to proteins,¹³ peptides can be labeled with Gd^{3+} -4MMDPA for nanoscale distance measurements using DEER at the W-band and that the sensitivity of such measurements is high. The concentration of the doubly labeled melittin in this study was 0.1 mM and the DEER traces were acquired within 1–6 h depending on the time interval, T , chosen. Increasing the measurement time to 12–24 h, as customarily done at X-band DEER measurements of nitroxides, would allow reducing the concentration to 50–60 μM . Taking into account that the sample volume is about 2–3 μl this is a significant improvement in terms of sample quantity over the standard X-band measurements. The low modulation depth of the Gd^{3+} DEER traces is compensated for by the very intense EPR signal and the efficient signal averaging.

The maximum of the distance distribution obtained with the nitroxide labels is nonetheless significantly shorter (~ 1.2 nm) than that obtained with the Gd^{3+} tags at the same positions; 2.2 nm compared to 3.4 nm. Earlier MC simulations and X-band DEER measurements on nitroxide labeled melittin showed that residues 15–25 are significantly helical.⁷ The Gd^{3+} -4MMDPA has a total charge of +1, as opposed to the rather hydrophobic nitroxide spin label. To verify the effect of the positive charge in positions 15 and 27 on the peptide conformation the cysteines were replaced with the charged amino acids, Lys and His, and MC simulations were carried out. In general, the simulations showed that the helical content of the mutant peptides was similar to that of the native peptide (Fig. 8a). However, the helical content of residues 14 to 17 of the mutants was a bit lower than the native peptide

although this is probably related to the substitution of Ala15 that has high preference of α -helical structures.⁴⁸ For the Lys modification, the helical content of the residues at the C-terminus increased a little comparing to His characterized by lower propensity to form α -helix.³⁹

The calculated distance distribution between α -carbons of melittin labeled at positions 15 and 27 is shown in Fig. 8b and between the side chains is given in Fig. 8c. The distances are similar to the NO–NO distances in nitroxide labeled mel-C₁₅C₂₇. Additionally, the simulations show that the average backbone structure has not been altered significantly, however a difference in distance distribution between side chains for the native peptide and the His modification is observed. We hypothesize that the rigidity and bulkiness of His side chains are the reason for the detected variation in the distance distribution. In contrast, the distance between the flexible and long Lys side chains is on average similar to the distance between the α -carbons. This suggests that changes in the conformation of the side chain occurred. Therefore, we attribute the differences in the Gd^{3+} - Gd^{3+} and NO–NO distances to differences of the tether orientation relative to the backbone and consider the extreme case where the tethers orient in opposite directions. In our earlier work on two Gd labeled proteins¹³ we measured 0.9 nm difference between the Gd^{3+} - Gd^{3+} and NO–NO distances, which is not much smaller than the 1.2 nm reported here. In this work the Gd^{3+} - Gd^{3+} measured distance was well reproduced by a rotameric library of the Gd^{3+} tag superimposed on the NMR structure for the two different proteins. In the case of peptides, that are significantly more flexible than proteins, an increase of 0.3 nm in the difference is not unexpected.

We also made some simple model calculations to show that the Gd^{3+} - Gd^{3+} distances are within a physically plausible range. For this purpose we used the crystal structure of melittin⁴⁹ which comprises two helices with a bent. This is a crude simplification but sufficient to determine lower limits. In the crystal structure the distance between the two $C\alpha$ atoms with the spin labels attached is 1.93 nm. The “lengths” of the labels are as follows: the $C\alpha$ -N distance in the Gd label is 0.84–0.87 nm, depending on the conformation; to this one has to add the N- Gd distance which is about 0.2 nm. The $C\alpha$ -O distance in the nitroxide label is in the range of 0.83 to 1.0 nm, depending on the conformation. With these values the

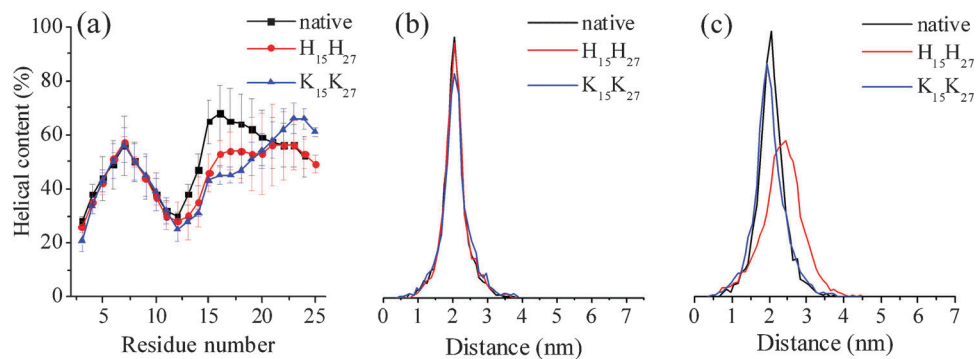


Fig. 8 MC simulations. (a) The calculated helical content of native melittin (black), His (red) and Lys (blue) modified peptides in aqueous phase. The corresponding distance distributions between the α -carbons (b) and the side chains (c) of amino acids 14 and 26 in native melittin and 15 and 27 in modified peptides. The standard deviation is represented by the error bars.

estimated range of distances between the Gd labels attached to melittin can be up to 4.0 nm (distance between the two Gd ions); for the nitroxide label the distance between the two oxygens can be up to 3.7 nm. We then attached the labels on melittin and “played” with their conformations to find the most distant and the closest approach of the labels, given the structure of melittin; namely the labels do not clash with other side chains of the peptide and adopt common torsion angles. The ranges that we got are ~ 0.9 – 3.9 nm for the Gd label (approximate distance between Gd ions) and 1.1 – 3.6 nm for the nitroxide labels (distance between O atoms). These values are within the range measured.

This observed difference in the distance between the two types of labels, both here and in the proteins,¹³ suggests that it may be informative to carry out complementary measurements using two types of labels as a method for increasing the number of constraints when deriving structures of biomolecules.

So far the major inconvenience in using Gd^{3+} spin labeling for distance measurements was the effect of the free Gd^{3+} in solution. Free Gd^{3+} in solution may arise from the addition of too much Gd^{3+} in the case that the degree of 4MMDPA labeling is not known and due to the possibility of forming Gd^{3+} –(4MMDPA)₂ complexes. Another problem is that deficiency of Gd^{3+} leads to significant amounts of Gd^{3+} –(4MMDPA)₂ complexes. This generates peptide dimers and contributions of unwanted distances to the distance distributions as well as effects due to interactions between more than two spins.⁴³ This problem is unique to peptides, which are small and flexible, and is unlikely to occur in proteins labeled with 4MMDPA. To avoid the problem of excess free Gd^{3+} , or deficiency of Gd^{3+} , the concentration of the tags attached to the peptide should be known. In this work this was determined by titration in the presence of arsenazo. This test, however, uses some peptide (5×10^{-4} μmol) and in practice reduces sensitivity as it increases the amount of peptide needed. Our limited experience shows that for 4MMDPA tags, a ratio of $[\text{Gd}^{3+}]/[\text{tag}] \approx 0.6$ – 0.8 is optimum because it shifts the equilibrium towards bound Gd^{3+} . The problems mentioned above can be eliminated all together by designing a tag that has a high binding constant with a large number of ligating atoms, such as DOTA (tetra-azacyclododecane tetraacetic)¹⁶ and DTPA (diethylenetriamine pentaacetic acid), which saturate the coordination sites of Gd^{3+} .

The experimental DEER effect, often referred to as the modulation depth (λ_{exp}), was found to be lower than that expected from consideration of pump pulse bandwidth relative to the whole spectral width (λ_{ef}), as observed earlier.^{13–15} Furthermore, we observed that λ_{exp} depends on temperature and the interval T . The temperature dependence is expected because the relative intensity of the central transition changes with temperature. However, the dependence observed was opposite than expected. We attribute both the T and the temperature dependence to spin dynamics, namely stochastic spin flips of the pumped spin B occurring during the period between the pump pulse and the echo detection. The pump pulse inserted at time t after the first π pulse (see Fig. 1) flips the spin of one of the dipolar coupled pair spins, B, and thereby changing the frequency of the coupled A spin

(observed spin). Because of the different evolution frequencies during the period $T-t$, not all A spins originally excited will refocus and the echo intensity is modulated with ω_{dd} . As mentioned earlier, the depth of the modulation is determined by the probability to flip the B spins, given by λ_{ef} , assuming that no further flips take place. This is usually the case for nitroxides at low temperatures. Any process that leads to random flips of the pumped spins B, referred to as spectral diffusion, will lead to a decrease in the modulation depth λ_{ef} . Such a process can be spin–lattice relaxation, which is indeed rather short for Gd^{3+} but probably not short enough to account alone for the observed reduction in λ_{ef} . Another process that can cause random B spin flips is flip–flops due to the dipolar interaction with spins that do not participate in the DEER experiments all together (spin diffusion). This is caused by the pseudo-secular term of the dipolar Hamiltonian. For effective spin diffusion the frequencies of the two spins participating in the flip–flop process should have similar resonance frequencies.¹⁷ DEER data acquired with shorter T values will experience less random B spin flips as compared to longer T , as indeed observed experimentally. As effective flip–flops occur between spins with close resonant frequencies, the process is expected to be more effective for spin pairs with $M_s = \pm 1/2$ because of the narrow central transition. Accordingly, the relatively more intense central transition at 25 K should result in more effective spin flip–flops. It turns out that for the samples studied in this work this effect overcomes the decrease in populations of the $M_s = \pm 1/2$ levels at 10 K that leads to a decrease in λ_{ef} at 10 K such that the highest DEER effect is observed at 10 K and not 25 K. The fast component observed in the T_1 measurements, though shorter at 25 K, is yet too slow to account for the low λ_{exp} and therefore cannot be attributed solely to spectral diffusion rate.

The effect of T_1 driven random flips of spin B is, in a way, reminiscent of the relaxation-induced dipolar modulation enhancement (RIDME) experiment,^{50,51} where modulations due to electron–electron dipolar interaction are induced by longitudinal relaxation flips of the B spins during a long enough and fixed time interval T . In RIDME T_1 and T should have the same order of magnitude, and there is no need for a pump pulse. There,⁵⁰ it was shown that the relative intensity of the dipolar peak of imidazoline biradical increases with longer T , whereas in our examples, the effect is the opposite as the random flips destroy the modulation induced by the pump pulse. The understanding of the effect of spectral diffusion on the modulation depth of high spin Gd^{3+} pairs requires future systematic investigations exploring temperature, concentration and linewidth dependencies along with the development of the necessary theoretical framework.

Conclusions

We have demonstrated W-band DEER distance measurements between a pair of Gd^{3+} spin labels in a peptide with high sensitivity. A caveat in these measurements is that the molar $[\text{Gd}^{3+}]/[\text{4MMDPA tag}]$ ratio has to be around 0.6 – 0.8 to avoid free Gd^{3+} that masks the DEER effect on the one hand, and the formation of peptide dimers on the other. We have also showed that the modulation depth is not only determined

by the spectral bandwidth of the pump pulse as compared to EPR spectral width, but it is also sensitive to random flips of the pumped B spins due to spectral diffusion processes that decrease the modulation depth. Therefore, for the particular samples investigated in this work a temperature measurement of 10 K was preferred over 25 K, where the relative intensity of the central transition is higher.

The Gd^{3+} – Gd^{3+} distance in Gd^{3+} –4MMDPA–mel- $\text{C}_{15}\text{C}_{27}$, 3.4 nm, is 1.2 nm longer than NO–NO distances in nitroxide labeled mel- $\text{C}_{15}\text{C}_{27}$. This difference was attributed to the different orientations and conformations of the nitroxide and Gd^{3+} labels due to their different properties. This suggests that two types of labels that can provide complementary structural information may be a new future approach. In addition, Gd^{3+} is rather robust and may withstand oxidation or reduction conditions that a nitroxide does not.

Acknowledgements

This work was supported, in part, by the ISF-VATAT Converging technologies program and by the Minerva Foundation. DG holds the Erich Klieger Professorial chair in Chemical Physics. YG was supported by the European Commission under the sixth Framework Programme through the Marie-Curie Action: BIOCONTROL, contract number MCRTN – 33439. We thank Gottfried Otting for helpful discussion regarding the peptide labeling. We thank Prof. Ben-Tal Nir for his support concerning the MC simulations and his comments regarding this manuscript and Dr Miri Eisenstein for her help with the modeling of spin labels on the melittin crystal structure.

References

- W. L. Hubbell, A. Gross, R. Langen and M. A. Lietzow, *Curr. Opin. Struct. Biol.*, 1998, **8**, 649.
- P. P. Borbat, H. S. McHaourab and J. H. Freed, *J. Am. Chem. Soc.*, 2002, **124**, 5304.
- G. Jeschke and Y. Polyhach, *Phys. Chem. Chem. Phys.*, 2007, **9**, 1895.
- O. Schiemann, N. Piton, J. Plackmeyer, B. E. Bode, T. F. Prisner and J. W. Engels, *Nat. Protoc.*, 2007, **2**, 904.
- E. R. Georgieva, T. F. Ramlall, P. P. Borbat, J. H. Freed and D. Eliezer, *J. Am. Chem. Soc.*, 2008, **130**, 12856.
- O. Schiemann and T. F. Prisner, *Q. Rev. Biophys.*, 2007, **40**, 1.
- M. Gordon-Grossman, Y. Gofman, H. Zimmermann, V. Frydman, Y. Shai, N. Ben-Tal and D. Goldfarb, *J. Phys. Chem. B*, 2009, **113**, 12687.
- E. J. Hustedt and A. H. Beth, *Annu. Rev. Biophys. Biomol. Struct.*, 1999, **28**, 129.
- J. E. Banham, C. M. Baker, S. Ceola, I. J. Day, G. H. Grant, E. J. Groenen, C. T. Rodgers, G. Jeschke and C. R. Timmel, *J. Magn. Reson.*, 2008, **191**, 202.
- M. Pannier, S. Veit, A. Godt, G. Jeschke and H. W. Spiess, *J. Magn. Reson.*, 2000, **142**, 331.
- H. Ghimire, R. M. McCarrick, D. E. Budil and G. A. Lorigan, *Biochemistry*, 2009, **48**(25), 5782.
- R. Ward, A. Bowman, E. Sozudogru, H. El-Mkami, T. Owen-Hughes and D. G. Norman, *J. Magn. Reson.*, 2010, **207**, 164.
- A. Potapov, H. Yagi, T. Huber, S. Jergic, N. E. Dixon, G. Otting and D. Goldfarb, *J. Am. Chem. Soc.*, 2010, **132**, 9040.
- A. M. Raitsimring, C. Gunanathan, A. Potapov, I. Efremenko, J. M. Martin, D. Milstein and D. Goldfarb, *J. Am. Chem. Soc.*, 2007, **129**, 14138.
- A. Potapov, Y. Song, T. J. Meade, D. Goldfarb, A. V. Astashkin and A. Raitsimring, *J. Magn. Reson.*, 2010, **205**, 38.
- Y. Song, T. J. Meade, A. V. Astashkin, E. L. Klein, J. H. Enemark and A. Raitsimring, *J. Magn. Reson.*, 2011, **210**, 59.
- P. A. Cruickshank, D. R. Bolton, D. A. Robertson, R. I. Hunter, R. J. Wylde and G. M. Smith, *Rev. Sci. Instrum.*, 2009, **80**, 103102.
- R. G. Larsen and D. J. Singel, *J. Chem. Phys.*, 1993, **98**(7), 5134.
- Y. Polyhach, A. Godt, C. Bauer and G. Jeschke, *J. Magn. Reson.*, 2007, **185**, 118.
- V. P. Denysenkov, T. F. Prisner, J. Stubbe and M. Bennati, *Proc. Natl. Acad. Sci. U. S. A.*, 2006, **103**, 13386.
- O. Schiemann, P. Cekan, D. Margraf, T. F. Prisner and S. T. Sigurdsson, *Angew. Chem., Int. Ed.*, 2009, **48**, 3292.
- Z. Yang, J. Becker and S. Saxena, *J. Magn. Reson.*, 2007, **188**, 337.
- B. E. Bode, J. Plackmeyer, T. F. Prisner and O. Schiemann, *J. Phys. Chem. A*, 2008, **112**, 5064.
- J. E. Lovett, A. M. Bowen, C. R. Timmel, M. W. Jones, J. R. Dilworth, D. Caprotti, S. G. Bell, L. L. Wong and J. Harmer, *Phys. Chem. Chem. Phys.*, 2009, **11**, 6840.
- B. Endeward, J. A. Butterwick, R. MacKinnon and T. F. Prisner, *J. Am. Chem. Soc.*, 2009, **131**, 15246.
- Z. Yang, D. Kise and S. Saxena, *J. Phys. Chem. B*, 2010, **114**, 6165.
- A. M. Raitsimring, A. V. Astashkin, O. G. Poluektov and P. Caravan, *Appl. Magn. Reson.*, 2005, **28**, 281.
- X. C. Su, B. Man, S. Beeren, H. Liang, S. Simonsen, C. Schmitz, T. Huber, B. A. Messerle and G. Otting, *J. Am. Chem. Soc.*, 2008, **130**, 10486.
- P. Mendez-Samperio, *Peptides*, 2008, **29**, 1836.
- L. R. Brown, J. Lauterwein and K. Wüthrich, *Biochim. Biophys. Acta*, 1980, **622**, 231.
- A. Okada, K. Wakamatsu, T. Miyazawa and T. Higashijima, *Biochemistry*, 1994, **33**, 9438.
- I. Grenthe, *J. Am. Chem. Soc.*, 1961, **83**, 360.
- T. N. Nagaraja, R. L. Croxen, S. Panda, R. A. Knight, K. A. Keenan, S. L. Brown, J. D. Fenstermacher and J. R. Ewing, *J. Neurosci. Methods*, 2006, **157**, 238.
- S. Gouin and F. M. Winnik, *Bioconjugate Chem.*, 2001, **12**, 372.
- D. Goldfarb, Y. Lipkin, A. Potapov, Y. Gorodetsky, B. Epel, A. M. Raitsimring, M. Radoul and I. Kaminker, *J. Magn. Reson.*, 2008, **194**, 8.
- G. Jeschke, V. Chechik, P. Ionita, A. Godt, H. Zimmermann, J. Bahman, C. R. Timmel, D. Hilger and H. Jung, *Appl. Magn. Reson.*, 2006, **30**, 473.
- A. Kessel, D. Shental-Bechor, T. Haliloglu and N. Ben-Tal, *Biophys. J.*, 2003, **85**, 3431.
- D. Shental-Bechor, T. Haliloglu and N. Ben-Tal, *Biophys. J.*, 2007, **93**, 1858.
- I. Bahar and R. L. Jernigan, *J. Mol. Biol.*, 1997, **266**, 195.
- D. Petrey, Z. Xiang, C. L. Tang, L. Xie, M. Gimpelev, T. Mitros, C. S. Soto, S. Goldsmith-Fischman, A. Kernysky, A. Schlessinger, I. Y. Koh, E. Alexov and B. Honig, *Proteins: Struct., Funct., Genet.*, 2003, **53**, 430.
- D. Shental-Bechor, S. Kirca, N. Ben-Tal and T. Haliloglu, *Biophys. J.*, 2005, **88**, 2391.
- A. V. Astashkin, A. M. Raitsimring and P. Caravan, *J. Phys. Chem. A*, 2004, **108**, 1990.
- G. Jeschke, M. Sajid, M. Schulte and A. Godt, *Phys. Chem. Chem. Phys.*, 2009, **11**, 6580.
- B. E. Bode, D. Margraf, J. Plackmeyer, G. Durner, T. F. Prisner and O. Schiemann, *J. Am. Chem. Soc.*, 2007, **129**, 6736.
- A. D. Milov, A. G. Maryasov and Y. D. Tsvetkov, *Appl. Magn. Reson.*, 1998, **15**, 107.
- K. M. Salikhov, S. A. Dzuba and A. M. Raitsimring, *J. Magn. Reson.*, 1981, **42**, 255.
- A. Milov, B. Naumov and Y. Tsvetkov, *Appl. Magn. Reson.*, 2004, **26**, 587.
- I. Bahar, M. Kaplan and R. L. Jernigan, *Proteins: Struct., Funct., Genet.*, 1997, **29**, 292.
- T. C. Terwilliger and D. Eisenberg, *J. Biol. Chem.*, 1982, **257**, 6016.
- L. V. Kulik, S. A. Dzuba, I. A. Grigoryev and Y. D. Tsvetkov, *Chem. Phys. Lett.*, 2001, **343**, 315.
- S. Milikisyants, F. Scarpelli, M. G. Finguerra, M. Ubbink and M. Huber, *J. Magn. Reson.*, 2009, **201**, 48.

Paper V: Membrane-integration of a mitochondrial signal-anchored protein does not require additional proteinaceous factors.

Elisa Merklinger, Yana Gofman, Alexej Kedrov, Arnold J.M. Driessen, Nir Ben-Tal, Yechiel Shai and Doron Rapaport

Published in *Biochem J*, 2011.

Reproduced by permission of the Biochemical Society from “Membrane-integration of a mitochondrial signal-anchored protein does not require additional proteinaceous factors”, Elisa Merklinger et al., *Biochemical Journal*, The Biochemical Society, 2011. Copyright (2011), the Biochemical Society.

Membrane integration of a mitochondrial signal-anchored protein does not require additional proteinaceous factors

Elisa MERKLINGER^{*}, Yana GOFMAN[†], Alexej KEDROV[‡], Arnold J. M. DRIESSEN[‡], Nir BEN-TAL[§], Yechiel SHAI[¶] and Doron RAPAPORT^{*1}

^{*}Interfaculty Institute of Biochemistry, Hoppe-Seyler-Strasse 4, University of Tübingen, 72076 Tübingen, Germany, [†]Helmholtz-Zentrum, Max-Planck-Strasse 1, 21502 Geesthacht, Germany, [‡]Department of Molecular Microbiology, Groningen Biomolecular Sciences and Biotechnology Institute and the Zernike Institute for Advanced Materials, University of Groningen, 9747 AG Groningen, The Netherlands, [§]Department of Biochemistry and Molecular Biology, The George S. Wise Faculty of Life Sciences, Tel Aviv University, Tel Aviv 69978, Israel, and [¶]Department of Biological Chemistry, The Weizmann Institute of Science, Rehovot 76100, Israel

The MOM (mitochondrial outer membrane) contains SA (signal-anchored) proteins that bear at their N-terminus a single hydrophobic segment that serves as both a mitochondrial targeting signal and an anchor at the membrane. These proteins, like the vast majority of mitochondrial proteins, are encoded in the nucleus and have to be imported into the organelle. Currently, the mechanisms by which they are targeted to and inserted into the OM (outer membrane) are unclear. To shed light on these issues, we employed a recombinant version of the SA protein OM45 and a synthetic peptide corresponding to its signal-anchor segment. Both forms are associated with isolated mitochondria independently of cytosolic factors. Interaction with mitochondria was diminished when a mutated form of

the signal-anchor was employed. We demonstrate that the signal-anchor peptide acquires an α -helical structure in a lipid environment and adopted a TM (transmembrane) topology within artificial lipid bilayers. Moreover, the peptide's affinity to artificial membranes with OM-like lipid composition was much higher than that of membranes with ER (endoplasmic reticulum)-like lipid composition. Collectively, our results suggest that SA proteins are specifically inserted into the MOM by a process that is not dependent on additional proteins, but is rather facilitated by the distinct lipid composition of this membrane.

Key words: ergosterol, mitochondrion, outer membrane, signal-anchored protein (SA protein).

INTRODUCTION

Proteins residing in the MOM (mitochondrial outer membrane) facilitate various interactions between the organelle and the rest of the eukaryotic cell. All of these proteins are encoded in the nucleus and synthesized on cytosolic ribosomes. In contrast with most mitochondrial proteins that contain N-terminal cleavable mitochondrial presequences, all MOM proteins carry internal non-cleavable targeting and sorting signals [1–3]. These signals assure their specific targeting to the organelle and insertion into the lipid bilayer.

MOM proteins can be divided into those that contain only one TM (transmembrane) domain and those that are embedded in the membrane with several α -helical segments or as β -barrel structure. The SA (signal-anchored) proteins, which belong to the first group, owe their name to a short portion of their N-terminus that serves as both a mitochondrial targeting signal and an anchor to the MOM [4]. The large remaining portion of the protein is exposed to the cytosol. Verified members of this family in fungi include the receptor components of the TOM (translocase of outer mitochondrial membrane) complex, Tom20 and Tom70, and two additional proteins: OM45 (outer membrane 45) and the OM isoform of Mcr1 (momMcr1). The targeting signal of these proteins consists of the TM segment and positively charged flanking regions [3,4].

A topologically related group are the tail-anchored OM proteins that have an α -helical TM domain in their C-terminus and a

large N-terminally positioned domain, exposed to the cytosol [5]. The targeting signal in these proteins and their mechanism of membrane integration was studied in some detail [6–9]. However, whereas the targeting information in tail-anchored proteins resides in the C-terminus, meaning that they have to be inserted into the membrane by a post-translational mechanism, some recognition of the N-terminal signal-anchor segment can occur while the rest of the polypeptide chain is still being synthesized. Hence, the biogenesis process of SA proteins can be completely different from that of the tail-anchored proteins.

Several lines of evidence suggest that import of SA protein does not require any of the known import components. First, it was demonstrated that mitochondrial targeting of Tom20 and Tom70 is not affected by either blocking the import receptors by specific antibodies or removing them upon proteolytic treatment [10,11]. Similarly, membrane insertion of SA proteins appears to be independent of the import pore formed by the TOM complex [11–13]. Despite the aforementioned similarities, it appears as if SA proteins do not share a common mechanism of targeting and insertion. Whereas OM45 and momMcr1 follow a still uncharacterized membrane integration pathway, the Tom receptors seem to use another pathway. It was proposed that another OM protein, Mim1 promotes both insertion of Tom20 and Tom70 into the OM and their final assembly into the TOM core complex [14–16]. Considering the observations described above, we previously suggested that proteins such as OM45 and momMcr1 can be inserted into the OM in a process that does not

Abbreviations used: ATR-FTIR, attenuated total reflectance-Fourier transform IR; CL, cardiolipin; DCM, dichloromethane; DIEA, N,N-diisopropylethylamine; DMF, dimethylformamide; ER, endoplasmic reticulum; Fmoc, fluorenylmethoxycarbonyl; ITC, isothermal titration calorimetry; LPC, L- α -lysophosphatidylcholine; LUV, large unilamellar vesicle; MBHA, p-methylbenzhydrylamine; MC, Monte Carlo; MOM, mitochondrial outer membrane; NBD-F, 7-nitrobenz-2-oxa-1,3-diazole fluoride; OM, outer membrane; PC, phosphatidylcholine; PE, phosphatidylethanolamine; PI, phosphatidylinositol; PS, phosphatidylserine; SA, signal-anchored; TAMRA, 6-carboxytetramethylrhodamine; TFA, trifluoroacetic acid; TM, transmembrane; TOM, translocase of outer mitochondrial membrane.

¹ To whom correspondence should be addressed (email doron.rapaport@uni-tuebingen.de).

require the assistance of the known import components [13,17]. However, this model does not exclude the possibility that an as yet unknown OM protein is involved, and our detailed understanding of the mechanisms that govern the membrane integration of these proteins is still rather vague.

In order to shed light on the biogenesis of this special group of proteins, we used a recombinant OM45 protein and synthesized a peptide corresponding to the signal-anchor segment of the protein. Both forms, but not their mutated variants, were able to associate with isolated mitochondria. Our results indicate that the OM45 peptide can adopt an α -helical conformation in a lipid environment and can tightly bind to protein-free phospholipid bilayers. Importantly, the low ergosterol content of the MOM appears to play an important role in the biogenesis process. Taken together, our findings support a mechanism where SA proteins can be inserted into the MOM in a process that depends on the unique lipid composition of this membrane, but is independent of additional proteins.

EXPERIMENTAL

Materials

Rink amide-MBHA (p-methylbenzhydrylamine) resin and Fmoc (fluoren-9-ylmethoxycarbonyl) amino acids were obtained from Calbiochem-Novabiochem. Other reagents used for peptide synthesis included TFA (trifluoroacetic acid), piperidine, DIEA (*N,N*-diisopropylethylamine), NMM (*N*-methylmorpholine), HOBT (*N*-hydroxybenzotriazole hydrate), HBTU [2-(1*H*-benzotriazol-1-yl)-1,1,3,3-tetramethyluronium hexafluorophosphate], DCM (dichloromethane; peptide synthesis grade) and DMF (dimethylformamide; peptide synthesis grade) (all from Biolab). 4-Chloro-NBD-F (7-nitrobenz-2-oxa-1,3-diazole fluoride) was purchased from Sigma and TAMRA (6-carboxytetramethylrhodamine) succinimidyl ester was from Molecular Probes. Egg LPC (L- α -lysophosphatidylcholine) and PI (phosphatidylinositol) were purchased from Sigma, PC (phosphatidylcholine), PE (phosphatidylethanolamine), PS (phosphatidylserine) and CL (cardiolipin) (diphosphatidylglycerol) were from Avanti, and ergosterol was from Larodan.

Construction and purification of recombinant proteins

DNA sequences encoding either full-length OM45, its cytosolic domain (lacking residues 1–38) or a mutant version of the full-length protein (R4E, K26E) were cloned into the vector pET28a (Novagen), which includes a C-terminal His₆ tag. The constructs were transformed into *Escherichia coli* cells (Rosetta2 DE3) and grown at 37 °C to D_{600} of 0.6 before protein expression was induced with 0.5 mM isopropyl β -D-thiogalactoside. Cells were grown for an additional 4 h at 30 °C and harvested by centrifugation. Next, the cells were resuspended in lysis buffer (50 mM sodium phosphate, 300 mM sodium chloride and 10 mM imidazole, pH 8.0) and lysis was performed by shaking for 1 h at 4 °C in the presence of PMSF, lysozyme and RNase followed by sonification. The homogenate was centrifuged and the supernatant was loaded on to a column containing Ni-NTA (Ni²⁺-nitrilotriacetate)-agarose beads (Qiagen) and washed with 20 ml of lysis buffer with 20 mM imidazole. Elution of the protein was accomplished with 300 mM imidazole in lysis buffer. Purity and homogeneity of the proteins were confirmed by SDS/PAGE.

Peptide synthesis, fluorescent labelling and purification

Peptides were synthesized by an Fmoc solid-phase method on Rink amide resin. Cleavage of the peptides from the MBHA resin

resulted in the amidation of the C-terminus. To label the peptides, the Fmoc protecting group at the N-terminus of the resin-bound peptides was removed by incubation with piperidine. All of the other reactive amine groups of the attached peptides were kept protected under these conditions. The resin-bound peptides were washed twice with DMF, and then treated with either NBD-F or TAMRA in anhydrous DMF containing 2% DIEA, leading to the formation of a resin-bound N-NBD or N-rhodamine peptide respectively. After 1 h (NBD) or 24 h (TAMRA), the resin was washed with DMF and then with methylene chloride. To label the ϵ -amino group of Lys²⁶ with the NBD group, the following procedure was applied. The MTT [3-(4,5-dimethylthiazol-2-yl)-2,5-diphenyl-2*H*-tetrazolium bromide] side chain protecting group, was removed under mild acidic conditions (2 \times 1 min of 5% TFA in DCM and 30 min of 1% TFA in DCM), enabling the conjugation of the fluorophore after capping of the N-terminus with 1 M acetic anhydride and 0.3 M triethylamine in anhydrous DMF.

All of the peptides were purified by RP-HPLC (reversed-phase-HPLC) on a C4 RP Bio-Rad semi-preparative column. The column was eluted with a 40 min linear gradient of acetonitrile in water, containing 0.05% TFA, at a flow rate of 1.8 ml/min. The purified peptides were further subjected to electrospray MS to confirm their molecular mass.

Binding of recombinant proteins and synthetic peptides to isolated mitochondria

Isolated mitochondria (20 μ g) were incubated in SEM buffer (250 mM sucrose, 1 mM EDTA and 10 mM Mops-KOH, pH 7.2) in the presence or absence of 100 mM KCl with 4 μ g of recombinant purified OM45 proteins for 20 min at room temperature (21 °C) and subsequently layered over a 60% (w/v) sucrose cushion. After centrifugation (40 000 g, 40 min, 4 °C) the supernatant was removed and proteins were precipitated. The layer between the cushion and the supernatant (5% of total volume) was diluted and centrifuged (20 000 g, 15 min, 4 °C). All fractions were subjected to SDS/PAGE and Western blot analysis. For the mitochondria-peptide interaction, 1 μ M fluorescently labelled peptide was used and 100 μ l fractions were collected. All fractions were analysed for their fluorescence and were analysed by SDS/PAGE and immunodecoration.

Preparation of LUVs (large unilamellar vesicles)

Thin films of a mixture of PC, PE, PI, CL and PS (molar ratio of 46:35:13:4:2 respectively) for OM-like LUVs or of PC, PE, PI, PS (54:25:11:10 respectively) containing 0.18 mol of ergosterol/mol of phospholipids for ER (endoplasmic reticulum)-like LUVs were generated from a solution of the lipids in a 2:1 (v/v) mixture of chloroform/methanol that was dried during rotation. The films were freeze-dried overnight, sealed with Ar(g), and stored at -20 °C. To form vesicles, the films were suspended in PBS and vortex-mixed for 1.5 min. The lipid suspension underwent five cycles of freezing-thawing and then vesicles were extruded through polycarbonate membranes with 1.0 and then 0.2 μ m pore diameters. The shape and size of the formed LUVs were verified by negative-staining electron microscopy.

Fluorescence measurements

Changes in the fluorescence of NBD-labelled peptides were measured upon binding to vesicles. LUVs (100 μ M final concentration) were added to 400 μ l of PBS containing 1 μ M NBD-labelled peptide. Fluorescence measurements were

performed at room temperature, with λ_{ex} set at 467 nm (10 nm slit) and λ_{em} scan at 500–600 nm (10 nm slits) or set constant at 530 nm. The extent of insertion was measured by adding increasing amounts of LUVs to a fixed amount of peptide (0.2–1 μM). After the signal reached a plateau, proteinase K (125 $\mu\text{g/ml}$ final concentration) was added.

ITC (isothermal titration calorimetry)

ITC was performed using an ITC₂₀₀ microcalorimeter (MicroCal; GE Healthcare). Small aliquots (3 μl) of the SA-peptide solution (20 μM) were injected into a solution of LUVs (2 mM) in a cell volume of $\sim 200 \mu\text{l}$. Alternatively, small aliquots of an LUV solution (4 mM) were injected into a solution of peptide (10 μM). Control experiments included titration of peptide into buffer solution, injection of vesicle solution into buffer and the addition of buffer into LUV solution. The heat released upon dilution, determined in these control experiments was subtracted from the heat of the peptide–liposome binding reactions. Binding isotherms were integrated and analysed using Origin[®]7 software according to a ‘one binding site’ model.

Further methods are described in the Supplementary Online Data (available at <http://www.BiochemJ.org/bj/442/bj4420381add.htm>).

RESULTS

Recombinant OM45 and a signal-anchor peptide specifically bind isolated mitochondria

To study binding of SA proteins to the MOM in the absence of cytosolic chaperones, we used the MOM SA protein OM45 as a model protein. To follow binding, we analysed the sedimentation behaviour on a sucrose cushion of isolated organelle, recombinant His₆-tagged OM45 purified from *E. coli* cells, and a mixture containing both components. Three fractions were collected after centrifugation: (i) an upper fraction that contains soluble unbound proteins, (ii) a middle fraction, where mitochondria was enriched, collected from the interface between the sucrose cushion and the buffer and (iii) a lower fraction that contained the pellet. Free OM45 was mainly present at the top fraction of the gradient, whereas a subpopulation of free OM45 molecules was also detected in the lower pellet fraction (Figure 1A). We suggest that this latter population represents aggregated molecules. Incubation of the recombinant protein with isolated mitochondria in the presence of 100 mM salt prior to centrifugation resulted in co-migration of these components in the middle fraction. In contrast, a protein corresponding to the cytosolic domain of OM45 did not bind to the isolated organelle under these conditions (Figure 1A). Notably, the binding of full-length OM45 was not affected by trypsin-mediated removal of the exposed domains of protease-sensitive mitochondrial surface receptors (Figure 1A).

To verify the specificity of this binding assay, we used a recombinant variant of OM45 where Arg⁴ and Lys²⁶ within the signal-anchor segment were changed to Glu⁴ and Glu²⁶, thus changing the net charge of the regions flanking the TM helix from +5 to +1. We previously observed that these mutations dramatically reduced the ability of the corresponding signal-anchor to mediate insertion of a model protein into the MOM [18]. In contrast with the native protein that was detected primarily in the bound fraction, a large portion of the mutated protein remained in the upper unbound fraction (Figure 1B). Hence, in accordance with our previous observation, the mutated protein demonstrates a reduced capacity to interact with isolated mitochondria. We next asked whether the mitochondria-associated OM45 is only

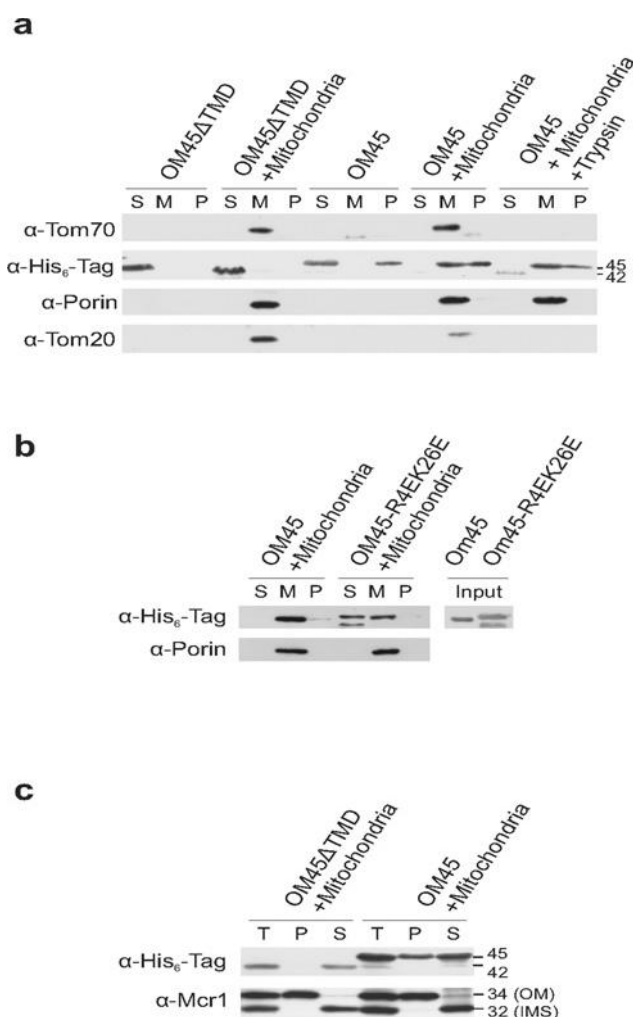


Figure 1 Binding of the OM45 protein to mitochondria

(a) Recombinant full-length OM45 protein (OM45) or its cytosolic domain (OM45ΔTMD) were loaded on a sucrose cushion either alone or after pre-incubation with mitochondria (20 μg) in a buffer containing 100 mM KCl. In one sample, mitochondria pretreated with trypsin was used. Three fractions were collected after centrifugation: supernatant (S), a middle fraction (M) containing the mitochondria and a lower fraction in the cushion (P). The samples were analysed by SDS/PAGE and immunodecorated with antibodies against the His₆-tag, Tom70 and Tom20 (exposed OM receptor proteins), and porin (membrane-embedded OM protein). (b) Recombinant full-length OM45 or its charge variant (OM45-R4EK26E) were treated as described in (a). Proteins before loading on to the sucrose cushion were analysed (right-hand panel). (c) Recombinant full-length OM45 protein or its cytosolic domain was incubated with mitochondria in a buffer lacking salt. The samples were treated as described in (a) and the middle fraction was collected and halved. One aliquot was left untreated (T), whereas the second aliquot was subjected first to alkaline extraction and then centrifuged to discriminate between membrane proteins in the pellet (P) and soluble proteins in the supernatant (S). The samples were subjected to SDS/PAGE and immunodecoration with antibodies against OM45 and Mcr1. The latter protein has two isoforms: a 34 kDa form embedded in the OM and a 32 kDa soluble form in the mitochondrial intermembrane space.

attached on the surface of the organelle or also integrated into the membrane. To that end, the mitochondrial fraction was extracted after the binding reaction with alkaline solution and centrifuged. To allow comparison with the variants that lack the SA domain, the binding experiment was performed in a buffer lacking salt where small amounts of the cytosolic domain of OM45 can associate with the organelle (Figure 1C). Notably, whereas the cytosolic domain of OM45 is found solely in the soluble fraction, approximately a third of the full-length protein molecules are embedded in the membrane (Figure 1C). We conclude that binding

and integration of recombinant OM45 into the OM can occur in the absence of cytosolic chaperones, and the assembly into the membrane depends on the SA domain.

The aforementioned experiments demonstrate that the signal-anchor segment is necessary for mitochondrial binding. In addition, we have previously demonstrated that the first 32 amino acid residues of OM45 are sufficient to target *in vivo* a passenger protein to mitochondria [18]. To further investigate the mechanism by which the SA segment integrates into the organelle OM, we used a synthetic peptide corresponding to residues 2–32 of OM45 (OM45-SA). The peptide was selectively labelled at either its N-terminus or at Lys²⁸ with the fluorophore NBD. This fluorophore can be utilized for binding studies since its fluorescence spectrum and intensity reflects the environment in which the NBD group is located. In addition a variant where the N-terminus is labelled with tetramethyl rhodamine was prepared. To serve as control peptides, we also synthesized and labelled a peptide harbouring the charge mutations (R4E and K26E) in the SA segment (Figure 2A). Purified peptides were shown to be homogeneous (>95%) by analytical HPLC and MS (results not shown).

To address the question whether the signal-anchor segment is able by itself to bind to mitochondria, we mixed the rhodamine-labelled peptides with isolated mitochondria. Next, the organelle was re-isolated by sedimentation on a sucrose cushion and fractions were collected. Importantly, rhodamine fluorescence of the native peptide and mitochondrial proteins were enriched in the same fractions. In contrast, the fluorescence of the mutated peptide was not detected in the mitochondria-containing fractions (Figure 2B). Thus this assay demonstrates specific binding of the native SA peptide to the organelle. To monitor whether the peptide is indeed integrated into the membrane, we incubated the isolated organelle with NBD-labelled peptide and then followed the emission spectrum of the NBD moiety. The addition of mitochondria to an aqueous solution of the peptide resulted in a dramatic increase in the fluorescence intensity of the NBD moiety and in the so-called 'blue-shift', a shift of the maximal emission to shorter wavelengths (Figure 2C). Of note these changes that demonstrate a shift of the NBD group to a more hydrophobic environment apparently upon integration into the OM were observed to a highly reduced extent with the mutant peptide (Figure 2C). To verify the insertion into the membrane, samples containing mitochondria-bound native peptide were treated with proteinase K. It is expected that a cleavage of an exposed N-terminus would result in the release of an NBD-containing fragment into the aqueous environment and subsequently a major reduction in the NBD fluorescence. Nevertheless, we observed that approximately 70% of the fluorescence signal remained (Figure 2D). These results suggest that the majority of the peptide molecules were inserted into the membrane.

Secondary structure of the OM45-SA peptide and its orientation within membranes

To better understand the structural requirements for membrane integration, we analysed by the CD method the secondary structure of the peptide in buffer or in the presence of LPC which provides a lipid-like environment, whereas in the former conditions the peptide acquired a mainly β -sheet conformation or was unstructured, the addition of the LPC resulted in conformations with mostly α -helical structure (Supplementary Figure S1 and Supplementary Table S1 available at <http://www.BiochemJ.org/bj/442/bj4420381add.htm>).

To further study the structure of the peptide in a lipid environment, we utilized ATR-FTIR (attenuated total reflectance-

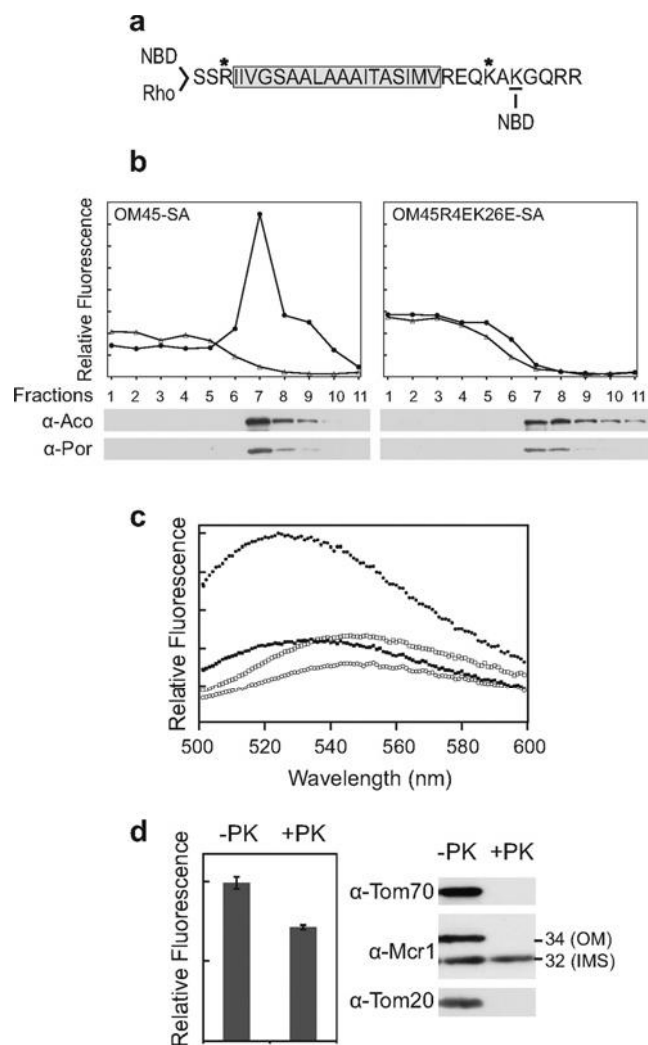


Figure 2 Signal-anchor peptide can bind to mitochondria

(a) Amino acid sequence of residues 2–32 of OM45. The putative TM helix of OM45 is within a box. The positions of the fluorescent probes are shown and the residues mutated in the R4E and K26E mutations are indicated by asterisks. Rho, rhodamine. (b) Mitochondria were incubated with rhodamine-labelled peptides before their re-isolation by centrifugation on top of a sucrose cushion. Ten different fractions were collected, their fluorescence emission was measured at 580 nm, and the relative fluorescence intensity of each fraction is presented. Bottom panels: proteins from the same fractions were precipitated and then analysed by SDS/PAGE and immunodecoration with antibodies against the mitochondrial marker proteins aconitase (Aco) and porin (Por). (c) Fluorescence emission spectra of 1 μ M N-NBD-labelled native peptide and R4EK26E variant in buffer (open circles or open squares respectively) or in the presence of isolated mitochondria (closed circles or closed squares respectively). (d) Mitochondria were incubated with N-NBD native peptide. The samples were divided into two halves and one of them was incubated further on ice with proteinase K (PK) before the fluorescence emission was monitored (left-hand panel). Right-hand panel: proteins from both aliquots were analysed by SDS/PAGE and immunodecoration with antibodies against Tom20 and Tom70 (OM-exposed proteins), and against Mcr1.

Fourier transform IR) spectroscopy. We first tested whether the addition of the peptide to the membrane affects the acyl-chain order of the phospholipid molecules. To that end, polarized ATR-FTIR was used to determine the orientation of the lipid membrane. The phospholipid composition (PC 46%, PE 35%, PI 13%, CL 4% and PS 2%) was according to the published composition of the yeast MOM [19]. The symmetric [$\nu_{\text{sym}}(\text{CH}_2) \approx 2853 \text{ cm}^{-1}$] and the antisymmetric [$\nu_{\text{antisym}}(\text{CH}_2) \approx 2922 \text{ cm}^{-1}$] vibrations of lipid C–H bonds are perpendicular to the molecular axis of a fully extended hydrocarbon chain. The position of these

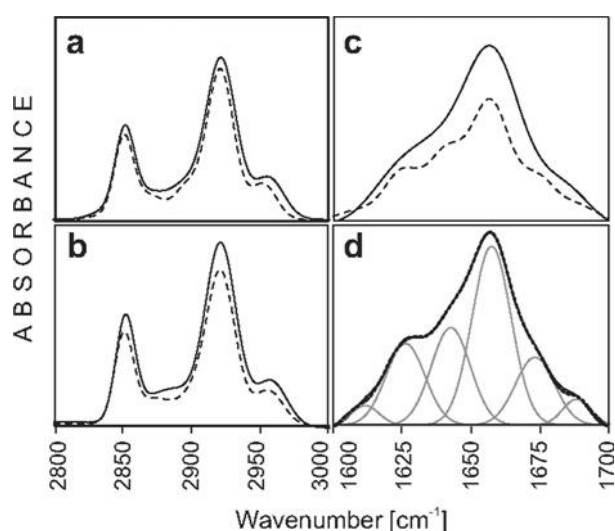


Figure 3 FTIR measurements of OM45-SA peptide in membrane environment

(a and b) ATR dichroism spectra of parallel (continuous lines) and perpendicular (dotted lines) polarized ATR-FTIR absorbance for the lipid CH₂ symmetric and anti-symmetric vibrations of PE/PI/PC/PS/CL multibilayers. (a) Lipids alone and (b) lipids in the presence of OM45-SA peptide. The peptide/lipid molar ratio was fixed at 1:50. (c) FTIR spectra of parallel (continuous line) and perpendicular (dotted line) polarized ATR-FTIR absorbance of amide I band of the OM45-SA peptide in the presence of PE/PI/PC/PS/CL multibilayers. All measurements were taken at a peptide/lipid molar ratio of 1:50. (d) The spectra in (c) were analysed using the curve fitting of the amide I band area assuming Gaussian line shape. The resulting deconvolution peaks are displayed under the fitting (black line).

peaks indicated that the membranes are predominantly in a native-like liquid-crystalline phase [20]. Measurement of the dichroism of IR light absorbance can reveal the order and orientation of the membrane sample relative to the prism surface [21]. The R value based on the stronger $\nu_{\text{antisym}}(\text{CH}_2)$ was 1.18 and the corresponding orientation order parameter, f , was calculated (based on ν_{antisym}) to be 0.62. The effect of OM45-SA peptide on the multibilayer acyl-chains order can be estimated by comparing the CH₂-stretching dichroic ratio of peptide-free multibilayers with that obtained with membranes containing incorporated peptide. The results indicate that integration of the SA peptide into the membranes changed somewhat the lipid order (Figures 3A and 3B). The R values and the corresponding order parameter f , at peptide/lipid molar ratios of 1:50 was 1.12 and 0.59 respectively. Hence the peptide decreased the lipid order, reflecting a reorganization of the lipid molecules probably due to the presence of oblique-inserted peptide molecules.

To determine directly the orientation of the peptides within lipid bilayers, polarized ATR-FTIR was used. Spectra of the amide I region of the peptide bound to the multibilayers and their deconvoluted components are shown in Figures 3(C) and 3(D). According to this analysis 52% of the peptide molecules are in an α -helical structure. This value is in a good agreement with the 58% α -helical structure that was estimated according to the CD measurements (Supplementary Table S1). The R value was 1.63 and the order parameter, f (-0.18) was slightly negative, typical of helices oriented oblique to the membrane surface [22]. According to these parameters, an 'average' angle of 62° between the main axis of the peptide and the bilayer normal was obtained. We propose that this value actually results from a situation where approximately half of the molecules are in a surface conformation and the other half acquired the TM configuration. Such an average

angle is also similar to that of peptides known to acquire a TM conformation [23]. Taken together, these structural studies suggest that the peptide can adopt an α -helical TM conformation in the presence of artificial lipid membranes.

Binding of the OM45-SA peptide to pure lipid vesicles

We next addressed the question whether a proteinaceous element has to be postulated in the insertion of SA proteins. To that end, the interaction of the OM45 peptides with protein-free lipid vesicles was analysed. LUVs were prepared from phospholipids in a composition similar to that of the MOM in yeast [19]. Addition of these LUVs to the NBD-labelled native or mutant peptide resulted in an enhancement in the fluorescence of the NBD group only in the case of the former peptide (Figures 4A and 4D). Hence addition of vesicles to the native peptide resulted in membrane integration of the NBD moiety. Interestingly, although the NBD group at the C-terminus of the native peptide displayed an enhancement of the fluorescence intensity in methanol, it failed to do so upon addition of LUVs (Figure 4B). The absence of such an increase probably indicates that the NBD group and the hydrophobic core of the membrane are distant from each other. While at the N-terminus only three residues separate the NBD group from the last amino acid of the putative TM segment, in the C-terminus this distance corresponds to six amino acids. Of note, we cannot exclude the unfavourable possibility that the NBD group at the C-terminus interferes with peptide binding to the membrane.

We then tested whether the peptide is indeed integrated into the lipid bilayer. The addition of proteinase K to the samples with the bound peptide resulted in an approximately 50% reduction in the fluorescence intensity (Figure 4C). Hence it appears that approximately half of the peptide molecules are in the TM configuration. We excluded the possibility of peptide aggregation since no self-quenching of the rhodamine-labelled peptide was observed under these conditions ([24] and results not shown).

Is the unique lipid composition of the MOM important for the membrane integration of the OM45 peptide? The N-terminally NBD-labelled peptide was titrated with LUVs and the increase in the fluorescence intensity was monitored. Plotting this enhancement as a function of the vesicle concentration allowed us to determine the affinity of the peptide to the vesicles. This affinity was calculated to be $223 \pm 12 \mu\text{M}$ when LUVs lacking ergosterol and having the phospholipid composition of the MOM were used (Figure 4E). The binding of the peptide to CL-free vesicles was comparable with CL-containing LUVs, and the binding of the peptide to mitochondria lacking CL (isolated from the *cdr1*Δ strain) was very similar to its binding to WT (wild-type) organelle (results not shown). Thus CL does not appear to play an important role in binding and integration of the OM45 peptide. We previously observed that elevated ergosterol levels interfere with the insertion of tail-anchored protein into lipid vesicles [9]. To check whether a similar effect can be observed with the signal-anchor peptide, we included 2, 10 or 20% ergosterol in the mixture of the lipid vesicles. Adding these ergosterol-containing vesicles to the NBD-labelled peptide resulted in a strongly reduced enhancement in the fluorescence signal as compared with addition of ergosterol-free LUVs (Figures 4E and 4F).

To further investigate, in a quantitative manner, the role of the lipid composition in the membrane integration process, we studied its thermodynamics using ITC. To this end, a solution containing lipid vesicles with the composition of either the MOM or ER membrane was titrated into an ITC cell containing the

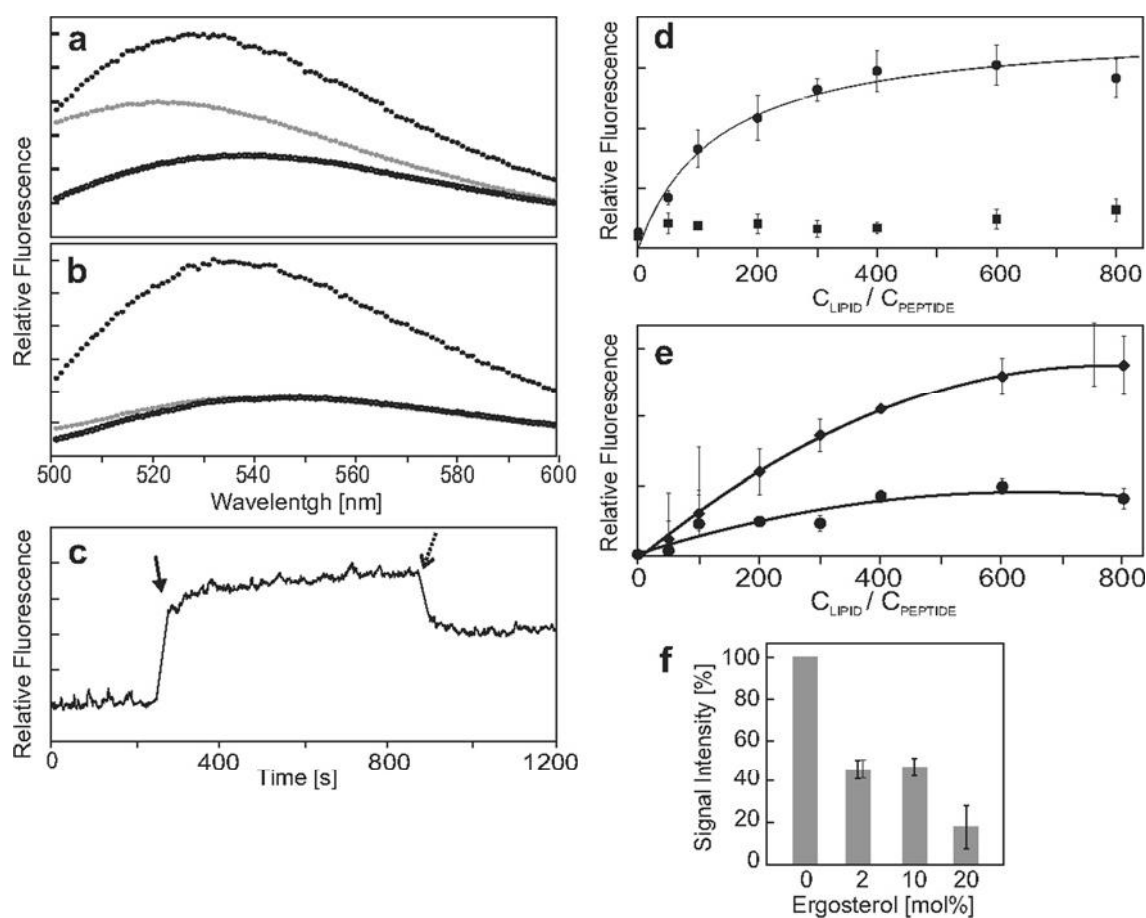


Figure 4 NBD-labelled OM45-SA peptide can integrate into artificial membrane vesicles

(A) Fluorescence emission spectra of 1 μM NBD-labelled native peptide in buffer (open circles), methanol (black closed circles) or in the presence of 100 μM PE/PI/PC/PS/CL LUV (grey closed circles). (B) The C-terminally labelled native peptide was analysed as in (A). (C) Representative experiment of proteolytic digestion of membrane-bound NBD labelled native peptide. The fluorescence emission of NBD-labelled peptide (1 μM) was monitored at 530 nm. The filled arrow indicates addition of 100 μM LUV and the dotted arrow the addition of 125 $\mu\text{g/ml}$ proteinase K. (D) N-terminally NBD-labelled native peptide (circles) and its charge variant (squares) were incubated with increasing amounts of PE/PI/PC/PS/CL LUV. The fluorescence emission was monitored at 530 nm. (E) N-terminally NBD-labelled native peptide (0.5 μM) was incubated with increasing amounts of ergosterol-free PE/PI/PC/PS/CL LUV (diamonds) or with LUV supplemented with 10% ergosterol (circles). The fluorescence emission was monitored at 530 nm. (F) NBD-labelled native peptide (0.5 μM) was incubated with increasing amounts of LUV lacking ergosterol or supplemented with 2, 10 or 20% ergosterol. The fluorescence emission at 530 nm was monitored after each addition and that with the ergosterol-free LUV was set as 100%. The presented values represent an average of all the employed lipid concentrations.

native OM45 peptide, and the heat amount released upon the peptide–lipid binding reaction was recorded (Figures 5A and 5B). Progressive vesicle injections produced decreasing exothermic heats as the availability of the peptide in the cell was gradually exhausted by association with the liposomes. We observed an elevated heat release upon binding of the SA-peptide to the vesicles with the MOM-like lipid composition. Analysis of the data resulted in enthalpy (ΔH) of -31 kcal/mol (1 kcal = 4.184 kJ) for these membranes, whereas the binding to the ER-like vesicles was too weak to allow any fitting (Figures 5C and 5D). These results indicate that the peptide interaction with MOM-like membranes is thermodynamically favoured as compared with its interaction with ER-like membrane.

Next, we turned to investigate the kinetics of membrane binding of the SA peptide by utilizing a stopped-flow setup. The addition of the vesicles to the NBD-labelled peptide resulted in a biphasic increase in the fluorescence intensity. We observed a first phase where the fluorescence increased very fast (within <1 s) to approximately 90% of the final intensity and a second slower phase that lasted several minutes (Figure 6A). Indeed, the first association rate constant was over 100-fold larger than

the second one (Figure 6B). Similar biphasic behaviour was observed also for the membrane-active peptide mastoparan X [25]. Both the initial kinetics and the final fluorescence level were dependent on the amounts of the added vesicles. According to this dependency and considering only k_{obs1} we could calculate the K_d to be 244 μM , which is in an excellent agreement with the value obtained in the previous experiments (223 μM). In agreement with the aforementioned results, addition of vesicles containing 10% ergosterol resulted in slower kinetics and a reduction in the fluorescence increase (results not shown).

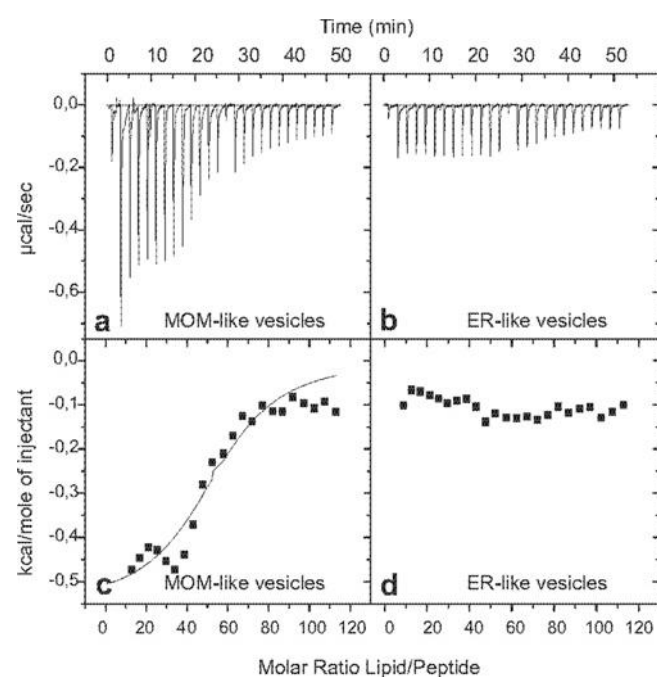
A TM configuration of OM45-SA is thermodynamically more stable than a surface configuration

The results of the ATR-FTIR spectroscopy and the protection of the NBD probe from externally added protease suggest a TM configuration of the peptide. We asked whether this topology is indeed thermodynamically favoured. To that goal we used MC (Monte Carlo) simulations to calculate the free energy of the peptide in two configurations: parallel to the membrane surface

Table 1 Free energy values and energy decomposition for OM45 peptides in TM or surface configurations

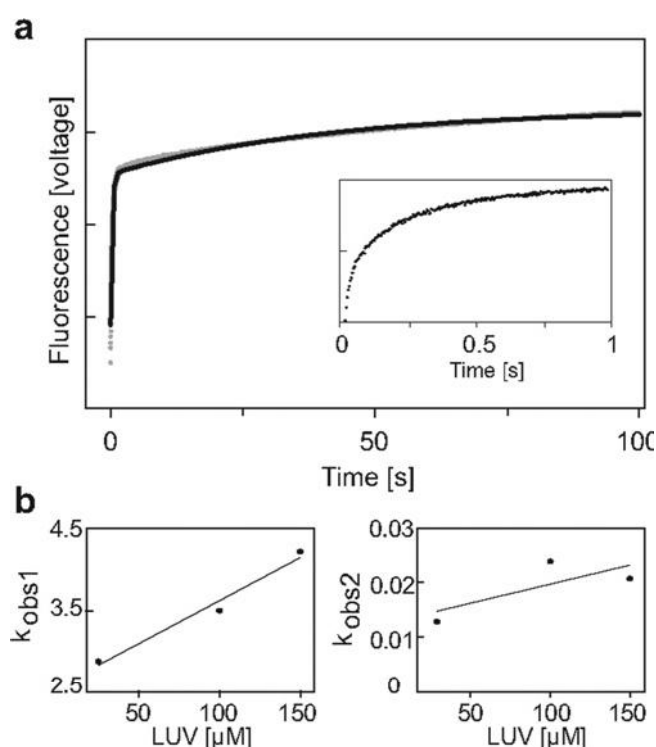
Free energy values are shown in kcal/mol as means \pm S.D. ΔG_{total} is the total free energy of membrane-association of the peptide (in each configuration). ΔG_{conf} is the free energy change due to membrane-induced conformational changes in the peptide. ΔG_{SIL} accounts mostly for the desolvation component of the process, including the favorable contribution of the hydrophobic effect. ΔG_{coul} stands for the Coulombic interactions between charged residues of the peptide and the (negative) surface charge of the membrane. ΔG_{def} is the free energy penalty associated with fluctuations of the membrane width around its resting (average) value.

Peptide/configuration	ΔG_{total}	ΔG_{conf}	ΔG_{SIL}	ΔG_{coul}	ΔG_{def}
OM45/TM	-11.9 ± 0.3	-0.5 ± 0.2	-6.6 ± 0.1	-5.1 ± 0.0	0.2 ± 0.0
OM45/surface	-8.7 ± 0.3	-1.8 ± 0.1	-2.4 ± 0.2	-4.7 ± 0.2	0.2 ± 0.0
R4E,K26E/TM	-6.1 ± 0.2	0.5 ± 0.3	-6.5 ± 0.2	-0.4 ± 0.1	0.3 ± 0.0
R4E,K26E/surface	-1.3 ± 0.2	-0.3 ± 0.2	0.0 ± 0.1	-1.1 ± 0.1	0.2 ± 0.0

**Figure 5** Binding of the SA-peptide to MOM-like and ER-like vesicles

(a) ITC experimental data on MOM LUVs titrated into the SA-peptide solution. (b) ITC experimental data of ER LUV injections. (c and d) Binding enthalpy calculated as an integral of the heat flow peaks and plotted as a function of lipid/peptide ratio for MOM-like LUVs (c) and ER-like LUVs (d).

and in TM orientation. For comparison, similar simulations were performed for the charge variant (R4E, K26E) peptide. The results show that the surface orientation of the native peptide is rather stable (Table 1), explaining the efficient and fast initial binding to lipid membranes (Figure 6). Interestingly, the values of the free energy decomposition obtained by the MC simulations suggest that the surface conformation of the peptide is stabilized by both solvation and electrostatic attractions (Table 1). However, the TM configuration is by far more stable, and therefore a reorganization of the peptide to the TM conformation would be favoured. This transformation is driven mostly by solvation since the electrostatic component is approximately the same in both configurations (Table 1). As the peptide has to cross the lipid core of the membrane, this re-orientation is expected to be slower than the initial binding; however, once occurred it will essentially not be reversible. In sharp contrast, the mutant peptide has less favourable electrostatic interactions with the lipid molecules and

**Figure 6** Kinetics of peptide binding to LUVs monitored using a stopped-flow setup

(a) Reaction of $1 \mu\text{M}$ NBD-labelled OM45-SA peptide with $100 \mu\text{M}$ LUVs under pseudo-first-order conditions. The fluorescence emission of N-NBD peptide was monitored at 530 nm with the excitation set at 467 nm . The inset displays an expansion of the signal in the first second. The solid line is the fit of the experimental data with a double exponential equation. (b) NBD-labelled OM45-SA peptide was incubated with increasing amounts of LUVs and the fluorescence signal was measured as described above. The dependence of the rate constants for the first ($k_{\text{obs}1}$) and second ($k_{\text{obs}2}$) components of the double-exponential reaction on the liposome concentration is presented in the left-hand and right-hand panel respectively.

low stability in both the surface and TM orientations (Table 1). Taken together, these results in combination with the stopped-flow data can support a mechanism where the signal-anchor segment first binds at the surface of the organelle and then gets inserted into the membrane and acquires a TM conformation.

DISCUSSION

In the present study, we investigated the mechanism by which SA proteins are delivered from the cytosol into their final location at the MOM and subsequently inserted into this membrane. We

choose OM45 as a model protein since, in contrast with Tom20 and Tom70, it is not a subunit of the TOM complex. Subunits of this complex might represent a special case and indeed, the correct topology and assembly of the latter two proteins depends on pre-existing TOM complex [11,12]. Our results suggest that cytosolic factors are not required for the membrane integration of OM45. Interestingly, similar independency of cytosolic chaperones was suggested for some ER and mitochondrial tail-anchored proteins [7,26]. Of note, although *in vivo* such cytosolic chaperones might bind newly synthesized SA proteins, the results of the present study suggest that they are not strictly required for specific targeting and integration into the OM.

Our working hypothesis suggests that the SA domain interacts with the membrane according to a two-state model that was suggested for many membrane-active peptides [27–30]. According to this model, the peptide first binds rather fast to the lipid–water interface and forms α -helical structure. Induction of an α -helical structure upon interaction of membrane-active peptides with lipids is a common observation for such peptides [28,30,31]. Previous work [31,32], as well as our MC simulations and present findings with the charge variant, suggest that electrostatic interactions among the positively flanking regions of the SA segment and the anionic headgroups of the phospholipids probably contribute to this interaction. After the initial absorption, the SA segment reorganizes itself within the membrane and adopts a TM configuration. The driving force for this step is the free energy gain thanks to the hydrophobic effect, i.e. the non-polar interactions between the TM region and tails of phospholipid molecules surrounding it. Favourable electrostatic interactions between the flanking regions and the headgroups on both sides of the membrane further stabilize the TM configuration. The importance of the electrostatic interactions is reflected by a reduced calculated thermodynamic stability of a charge variant of OM45 and a reduced insertion of the corresponding protein or peptide into natural and artificial membranes. Furthermore, this working model is also in line with a previous study reporting that physiological membrane concentrations of anionic lipids greatly stabilize the TM configuration of a model hydrophobic segment with positively charged flanking regions [32].

A protein-free membrane-insertion mechanism was proposed to describe the integration of some tail-anchored proteins into the membranes of the ER and mitochondria [9,26,33]. It is also in line with previous studies that failed to identify a mitochondrial protein which is required for the membrane integration of OM45 and momMcr1 [12,13]. In contrast, Mim1 was reported to be required for the membrane insertion of Tom20 and Tom70, and/or for their assembly with the TOM complex [14–16]. However, the request for Mim1 and Tom40 in the biogenesis route of Tom receptors does not have to exclude a unified mechanism of initial insertion of SA proteins into the MOM. It might well be that all SA proteins follow initially a similar pathway of insertion that does not require additional proteins. According to this scenario, Mim1 is required for subsequent steps in the assembly of Tom20 and Tom70 with the rest of the TOM complex [15,34].

The apparently minor importance of proteins in assuring the specificity of the targeting and recognition processes raises the question of what other elements can mediate such distinct mitochondrial location. One such element can be the unique lipid composition of the MOM. Indeed, the SA peptide associated much better with lipid vesicles with the OM composition as compared with vesicles with ER-like composition. Thus we looked more closely at unique features of the lipid content of the MOM. For example, the MOM is the only one among all membranes facing the cytosol that contain the mitochondrial-specific phospholipid CL [19,35]. However, whereas this lipid seems to play a role in the

association of apoptosis-regulating proteins with the OM [36,37], our results do not support a crucial role of CL in assuring specific membrane integration of OM45.

Low levels of ergosterol are another unique feature of the yeast MOM [38,39]. Indeed, our previous results with the tail-anchored protein Fis1 [9] and current findings with OM45 suggest that low ergosterol content is crucial for efficient membrane integration of OM single-span proteins. In addition to its well-known enhancement of the rigidity of the membrane, ergosterol might also influence the compressibility of the headgroups region. It has a relatively small headgroup allowing a more compact packing of the headgroup region of the bilayer [32,40]. Hence the elevated rigidity and reduced compressibility of sterol-containing membrane can result in compromised productive binding of signal-anchor peptides to this membrane.

In summary, we propose that newly synthesized mitochondrial SA protein might associate non-specifically and reversibly with various cellular membranes, but would bind productively, irreversibly and in a TM conformation only to the MOM. Although additional proteins can enhance the membrane integration process or preserve the SA protein in an insertion-competent conformation, we suggest that a distinct lipid composition of the MOM plays a primary role in the specific integration of SA proteins into this membrane.

AUTHOR CONTRIBUTION

Elisa Merklinger, Arnold Driessen, Nir Ben-Tal, Yechiel Shai and Doron Rapaport designed the research. Elisa Merklinger, Yana Gofman, Alexej Kedrov and Yechiel Shai performed the research. All authors analysed the data. Elisa Merklinger and Doron Rapaport wrote the paper.

ACKNOWLEDGEMENTS

We thank K. Rehn, E. Kracker and B. Zarni for technical support, G. Schreiber and M. Harel for help with the stopped-flow setup, and K.S. Dimmer and M. Schuldiner for helpful discussions.

FUNDING

This work was supported by the Deutsche Forschungsgemeinschaft [grant number RA 1048/4–1 to D.R.] and a short-term fellowship from the Minerva Stiftung (to E.M.).

REFERENCES

- Pfanner, N., Wiedemann, N., Meisinger, C. and Lithgow, T. (2004) Assembling the mitochondrial outer membrane. *Nat. Struct. Mol. Biol.* **11**, 1044–1048
- Endo, T. and Yamano, K. (2009) Multiple pathways for mitochondrial protein traffic. *Biol. Chem.* **390**, 723–730
- Walther, D. M. and Rapaport, D. (2009) Biogenesis of mitochondrial outer membrane proteins. *Biochim. Biophys. Acta* **1793**, 42–51
- Shore, G. C., McBride, H. M., Millar, D. G., Steenaart, N. A. E. and Nguyen, M. (1995) Import and insertion of proteins into the mitochondrial outer membrane. *Eur. J. Biochem.* **227**, 9–18
- Borgese, N., Colombo, S. and Pedrazzini, E. (2003) The tale of tail-anchored proteins: coming from the cytosol and looking for a membrane. *J. Cell Biol.* **161**, 1013–1019
- Isenmann, S., Khew-Goodall, Y., Gamble, J., Vadas, M. and Wattenberg, B. W. (1998) A splice-isoform of vesicle-associated membrane protein-1 (VAMP-1) contains a mitochondrial targeting signal. *Mol. Biol. Cell* **9**, 1649–1660
- Lan, L., Isenmann, S. and Wattenberg, B. W. (2000) Targeting and insertion of C-terminally anchored proteins to the mitochondrial outer membrane is specific and saturable but does not strictly require ATP or molecular chaperones. *Biochem. J.* **349**, 611–621
- Horie, C., Suzuki, H., Sakaguchi, M. and Mihara, K. (2002) Characterization of signal that directs C-tail-anchored proteins to mammalian mitochondrial outer membrane. *Mol. Biol. Cell* **13**, 1615–1625

- 9 Kemper, C., Habib, S. J., Engl, G., Heckmeyer, P., Dimmer, K. S. and Rapaport, D. (2008) Integration of tail-anchored proteins into the mitochondrial outer membrane does not require any known import components. *J. Cell Sci.* **121**, 1990–1998
- 10 Schneider, H., Sollner, T., Dietmeier, K., Eckerskorn, C., Lottspeich, F., Trulzsch, B., Neupert, W. and Pfanner, N. (1991) Targeting of the master receptor MOM19 to mitochondria. *Science* **254**, 1659–1662
- 11 Schlossmann, J. and Neupert, W. (1995) Assembly of the preprotein receptor MOM72/MAS70 into the protein import complex of the outer membrane of mitochondria. *J. Biol. Chem.* **270**, 27116–27121
- 12 Ahting, U., Waizenegger, T., Neupert, W. and Rapaport, D. (2005) Signal-anchored proteins follow a unique insertion pathway into the outer membrane of mitochondria. *J. Biol. Chem.* **280**, 48–53
- 13 Meineke, B., Engl, G., Kemper, C., Vasiljev-Neumeyer, A., Paulitschke, H. and Rapaport, D. (2008) The outer membrane form of the mitochondrial protein Mcr1 follows a TOM-independent membrane insertion pathway. *FEBS Lett.* **582**, 855–860
- 14 Becker, T., Pfannschmidt, S., Guiard, B., Stojanovski, D., Milenkovic, D., Kutik, S., Pfanner, N., Meisinger, C. and Wiedemann, N. (2008) Biogenesis of the mitochondrial TOM complex: Mim1 promotes insertion and assembly of signal-anchored receptors. *J. Biol. Chem.* **283**, 120–127
- 15 Hulett, J. M., Lueder, F., Chan, N. C., Perry, A. J., Wolynec, P., Likic, V. A., Gooley, P. R. and Lithgow, T. (2008) The transmembrane segment of Tom20 is recognized by Mim1 for docking to the mitochondrial TOM complex. *J. Mol. Biol.* **376**, 694–704
- 16 Popov-Celeketic, J., Waizenegger, T. and Rapaport, D. (2008) Mim1 functions in an oligomeric form to facilitate the integration of Tom20 into the mitochondrial outer membrane. *J. Mol. Biol.* **376**, 671–680
- 17 Dukanovic, J. and Rapaport, D. (2011) Multiple pathways in the integration of proteins into the mitochondrial outer membrane. *Biochim. Biophys. Acta* **1808**, 971–980
- 18 Waizenegger, T., Stan, T., Neupert, W. and Rapaport, D. (2003) Signal-anchor domains of proteins of the outer membrane of mitochondria: structural and functional characteristics. *J. Biol. Chem.* **278**, 42064–42071
- 19 De Kroon, A. I. P. M., Koorengel, M. C., Goerdal, S. S., Mulders, P. C., Janssen, M. J. and De Kruijff, B. (1999) Isolation and characterization of highly purified mitochondrial outer membranes of the yeast *Saccharomyces cerevisiae*. *Mol. Membr. Biol.* **16**, 205–211
- 20 Ishiguro, R., Matsumoto, M. and Takahashi, S. (1996) Interaction of fusogenic synthetic peptide with phospholipid bilayers: orientation of the peptide alpha-helix and binding isotherm. *Biochemistry* **35**, 4976–4983
- 21 Sharon, M., Oren, Z., Shai, Y. and Anglister, J. (1999) 2D-NMR and ATR-FTIR study of the structure of a cell-selective diastereomer of melittin and its orientation in phospholipids. *Biochemistry* **38**, 15305–15316
- 22 Tamm, L. K. and Tatulian, S. A. (1997) Infrared spectroscopy of proteins and peptides in lipid bilayers. *Q. Rev. Biophys.* **30**, 365–429
- 23 Ghosh, J. K., Peisajovich, S. G. and Shai, Y. (2000) Sendai virus internal fusion peptide: structural and functional characterization and a plausible mode of viral entry inhibition. *Biochemistry* **39**, 11581–11592
- 24 Rosenfeld, Y., Barra, D., Simmaco, M., Shai, Y. and Mangoni, M. L. (2006) A synergism between temporins toward Gram-negative bacteria overcomes resistance imposed by the lipopolysaccharide protective layer. *J. Biol. Chem.* **281**, 28565–28574
- 25 Tang, J., Signarvic, R. S., DeGrado, W. F. and Gai, F. (2007) Role of helix nucleation in the kinetics of binding of mastoparan X to phospholipid bilayers. *Biochemistry* **46**, 13856–13863
- 26 Colombo, S. F., Longhi, R. and Borgese, N. (2009) The role of cytosolic proteins in the insertion of tail-anchored proteins into phospholipid bilayers. *J. Cell Sci.* **122**, 2383–2392
- 27 Huang, H. W. (2000) Action of antimicrobial peptides: two-state model. *Biochemistry* **39**, 8347–8352
- 28 White, S. H., Ladokhin, A. S., Jayasinghe, S. and Hristova, K. (2001) How membranes shape protein structure. *J. Biol. Chem.* **276**, 32395–32398
- 29 Shai, Y. (2002) Mode of action of membrane active antimicrobial peptides. *Biopolymers* **66**, 236–248
- 30 Andreev, O. A., Karabadzak, A. G., Weerakkody, D., Andreev, G. O., Engelman, D. M. and Reshetnyak, Y. K. (2010) pH (low) insertion peptide (pHLIP) inserts across a lipid bilayer as a helix and exits by a different path. *Proc. Natl. Acad. Sci. U.S.A.* **107**, 4081–4086
- 31 van Klompenburg, W., Nilsson, I., von Heijne, G. and de Kruijff, B. (1997) Anionic phospholipids are determinants of membrane protein topology. *EMBO J.* **16**, 4261–4266
- 32 Shahidullah, K. and London, E. (2008) Effect of lipid composition on the topography of membrane-associated hydrophobic helices: stabilization of transmembrane topography by anionic lipids. *J. Mol. Biol.* **379**, 704–718
- 33 Brambillasca, S., Yabal, M., Makarow, M. and Borgese, N. (2006) Unassisted translocation of large polypeptide domains across phospholipid bilayers. *J. Cell Biol.* **175**, 767–777
- 34 Dimmer, S. K. and Rapaport, D. (2009) The enigmatic role of Mim1 in mitochondrial biogenesis. *Eur. J. Cell Biol.* **89**, 212–215
- 35 Gebert, N., Joshi, A. S., Kutik, S., Becker, T., McKenzie, M., Guan, X. L., Mooga, V. P., Stroud, D. A., Kulkarni, G., Wenk, M. R. et al. (2009) Mitochondrial cardiolipin involved in outer-membrane protein biogenesis: implications for Barth syndrome. *Curr. Biol.* **19**, 2133–2139
- 36 Kim, T. H., Zhao, Y., Ding, W. X., Shin, J. N., He, X., Seo, Y. W., Chen, J., Rabinowich, H., Amoscato, A. A. and Yin, X. M. (2004) Bid-cardiolipin interaction at mitochondrial contact site contributes to mitochondrial cristae reorganization and cytochrome C release. *Mol. Biol. Cell* **15**, 3061–3072
- 37 Gonzalez, F., Schug, Z. T., Houtkooper, R. H., MacKenzie, E. D., Brooks, D. G., Wanders, R. J., Petit, P. X., Vaz, F. M. and Gottlieb, E. (2008) Cardiolipin provides an essential activating platform for caspase-8 on mitochondria. *J. Cell Biol.* **183**, 681–696
- 38 Zinser, E., Sperka-Gottlieb, C. D., Fasch, E. V., Kohlwein, S. D., Paltauf, F. and Daum, G. (1991) Phospholipid synthesis and lipid composition of subcellular membranes in the unicellular eukaryote *Saccharomyces cerevisiae*. *J. Bacteriol.* **173**, 2026–2034
- 39 Schreiber, R., Brugger, B., Sandhoff, R., Zellnig, G., Leber, A., Lampl, M., Athenstaedt, K., Hraštnik, C., Eder, S., Daum, G. et al. (1999) Electrospray ionization tandem mass spectrometry (ESI-MS/MS) analysis of the lipid molecular species composition of yeast subcellular membranes reveals acyl chain-based sorting/remodeling of distinct molecular species en route to the plasma membrane. *J. Cell Biol.* **146**, 741–754
- 40 Egashira, M., Gorbenko, G., Tanaka, M., Saito, H., Molotkovsky, J., Nakano, M. and Handa, T. (2002) Cholesterol modulates interaction between an amphipathic class A peptide, Ac-18A-NH₂, and phosphatidylcholine bilayers. *Biochemistry* **41**, 4165–4172

General Discussion: Limitations and Implications

I employed a MC simulations model based on reduced representation of both the peptide and membrane (1). As expected from a computational model, it captures only certain characteristics of the complex peptide-lipid system. For instance, the phospholipids bilayer is described by three quantities, namely thickness, hydrophobicity and surface charge (1, 2). Clearly, other properties that might affect peptide-lipid interactions are missing in the model. One of these is membrane curvature. The flat representation of the membrane surface can roughly describe a cell membrane. However, the curvature of small vesicles or micelles cannot be overlooked and might play a significant role in the interaction with peptides. Another example is the lipid phase which affects the fluidity and rigidity of the bilayer. The MC model describes lipids in their crystalline-liquid phase, which are more susceptible to stretching and bending than gel phase lipids (3). Accordingly, liquid phase bilayer can adjust easier to incorporation of membrane proteins. Lipids' de-mixing refers to migration of negatively charged lipids to the interaction zone with cationic peptides (4-6). As a consequence, the local charge density alters, which may increase the local concentration of the peptide on the membrane's surface.

In order to examine the consequences of the limitations of the model, abovementioned and discussed in details in *Papers I to V*, the computational results were correlated with empiric data, either from previous experiments or experiments specifically designed and performed to evaluate the calculations. In fact, one of the main strengths of the presented studies is the integrated approach that combines insights from calculations and experiments to create a realistic, accurate and trustworthy sketch of the investigated systems.

As a part of my thesis I made the MC simulations model available to the wide scientific community as a web-server (MCPep; <http://bental.tau.ac.il/MCPep/>), and I am hopeful that users will apply it as cautiously as I did. It is essential to correlate the simulations with empiric data, and, thus, the calculations should be conducted in conditions similar to the experiments. The available parameters for matching to the experimental conditions are the fraction of acidic lipids in the membrane, the ionic strength of the surrounding aqueous solution and the native width of the membrane hydrocarbon core. Furthermore, the model describes a single peptide interacting with a single membrane, and, hence, the simulations are analogous to experiments with high lipid and low peptide concentrations (high lipids/peptides ratio). Lastly, one should keep in mind that the model describes lipids in their crystalline-liquid phase. As discussed above, lipids phases are characterized by different molecules packing (3), which may affect the bilayer interaction with the peptides.

In addition to the abovementioned parameters, the user is asked to provide the sequence or 3D structure of the query peptide; if the sequence is provided, an initial canonical α -helix model structure of the peptide is constructed. The server performs three separate simulations of the peptide in water. In membrane the peptide is simulated with its principal axis approximately perpendicular to the membrane normal (surface orientation) and with its principal axis in parallel to the membrane normal (TM orientation). These are two typical configurations of a helical peptide in membrane, and the transition between them is associated with a high free energy barrier. Thus, for simulations in the membrane environment, each of the two configurations is used as the initial orientation for three independent simulations. The output of the server includes energetically favorable orientation(s) of the peptide in the membrane; this could be either surface or TM

orientation. The free energy of membrane association and its decomposition for the favorable orientation(s) are reported as well. Besides, the helical content of the peptide in water and in the membrane are provided. In addition, snapshots of example simulations, both in water and in the membrane, are presented.

It should also be noted that the server was designed for rather short, up to 40 amino acids, linear helical peptides. It was tested on a small set of peptides described herein; there was no systematic research on a larger set of peptides. The recently published AMPad database (7) offers a perfect dataset of membrane-active cationic peptides to perform a systematic testing of the MCPep server. The database includes 36 sequences of natural α -helical AMPs. The peptides are non-homologous, with less than 70% identity between each other. All peptides are cationic and less than 50 amino acids in length. Additionally, the database contains minimal inhibitory concentration (MIC) of each peptide required to apply against various *E. Coli* strains; the MIC values were taken from the available literature. The MC simulations of these peptides in membrane corresponding to *E.Coli* cell wall can provide interesting insights on their action. Moreover, the MIC values can be correlated to the computed free energy of peptide-membrane association. The preliminary results that I obtained with NK-CS derivatives (*Paper II*) indicated that such correlation is possible; the lower the free energy, the more effective the peptide is against bacteria. Such systematic examination could determine whether the MC simulations can provide a rough estimate of the antimicrobial activity of new peptides and become a simple, fast and efficient method for initial filtering of possible candidates for antibiotics.

Additional putative application of the methodology is related to TM proteins structure prediction. Due to difficulties in experimental structure determination, computational structure prediction takes places as a useful approach. The most accurate models of

protein structures are achieved through homology modeling, where the models are referred from a known high-resolution structure of a homologous protein (8). The crucial step in the modeling is alignment of the query sequence to the template sequence (9), required to identify the TM helices of the query protein and match them to the template. This is especially challenging if the query and target proteins share low sequence identity (10). Attempting to create a model-structure of homocysteine-induced endoplasmic reticulum protein (Herp), I applied algorithms for the identification of TM segments on its sequence. Two putative TM helices emerged, with a short loop approximately between Y283 and S288. However, owing to the presence of the highly hydrophilic Arginine in position 289, I deduced that the loop includes residues S288, R289, and F290 and modeled this region as helix-loop-helix motif. This structure was used as the starting conformation for the MC simulations. Surprisingly, the short loop that connects the two TM helices shifted a few residues to Y284, S285, S286, in agreement with the predictions of algorithms for the identification of TM segments. This case-study suggests that the MCPep server could be used for identification of TM helices. It could also predict the membrane boundaries for the existing structures of TM proteins. Further investigation is required to explore these possibilities.

In conclusion, the model exploited here is capable of exploring the interactions of a range of peptides with different physicochemical characteristics with membranes of various types. The model is available via the MCPep server, and even inexperienced users can apply it, preferably correlating the results with other existing data. Furthermore, the model may be useful for prediction of AMPs' efficiency and the identification of putative TM helices.

References

1. Kessel, A., D. Shental-Bechor, T. Haliloglu, and N. Ben-Tal. 2003. Interactions of hydrophobic peptides with lipid bilayers: Monte Carlo simulations with M2delta. *Biophys J* 85:3431-3444.
2. Shental-Bechor, D., T. Haliloglu, and N. Ben-Tal. 2007. Interactions of cationic-hydrophobic peptides with lipid bilayers: a Monte Carlo simulation method. *Biophys J* 93:1858-1871.
3. Marsh, D. 2006. Elastic curvature constants of lipid monolayers and bilayers. *Chem Phys Lipids* 144:146-159.
4. Haleva, E., N. Ben-Tal, and H. Diamant. 2004. Increased concentration of polyvalent phospholipids in the adsorption domain of a charged protein. *Biophys J* 86:2165-2178.
5. May, S., D. Harries, and A. Ben-Shaul. 2000. Lipid demixing and protein-protein interactions in the adsorption of charged proteins on mixed membranes. *Biophys J* 79:1747-1760.
6. Heimburg, T., B. Angerstein, and D. Marsh. 1999. Binding of peripheral proteins to mixed lipid membranes: effect of lipid demixing upon binding. *Biophys J* 76:2575-2586.
7. Juretic, D., D. Vukicevic, N. Ilic, N. Antcheva, and A. Tossi. 2009. Computational design of highly selective antimicrobial peptides. *J Chem Inf Model* 49:2873-2882.
8. Petrey, D., and B. Honig. 2005. Protein structure prediction: inroads to biology. *Mol Cell* 20:811-819.
9. Schushan, M., and N. Ben-Tal. 2010. Modeling and Validation of Transmembrane Protein Structures. In *Introduction to Protein Structure Prediction*. John Wiley & Sons, Inc. 369-401.
10. Forrest, L. R., C. L. Tang, and B. Honig. 2006. On the accuracy of homology modeling and sequence alignment methods applied to membrane proteins. *Biophys J* 91:508-517.

Appendix A: Supplementary Material for Paper I

A combined pulse EPR and Monte Carlo simulation study provides molecular insight on peptide-membrane interactions.

Michal Gordon-Grossman, Yana Gofman, Herbert Zimmermann, Veronica Frydman, Yechiel Shai, Nir Ben-Tal and Daniella Goldfarb

Published in *J Phys Chem B*, 2009, 113(38):12687-12695.

Experimental methods

Materials for peptide synthesis

The Rink amide MBHA resin and 9-fluorenylmethoxycarbonyl (Fmoc) amino acids for peptide synthesis were purchased from Calbiochem-Novabiochem AG. Other reagents used for the synthesis included trifluoroacetic acid (TFA, Sigma), N,N-diisopropylethylamine (DIEA, Aldrich), methylene chloride (peptide synthesis grade, Biolab), dimethylformamide (peptide synthesis grade, Biolab), and benzotriazolyl-noxytris(dimethylamino) phosphonium hexafluorophosphate (BOP, Sigma).

Peptide synthesis and purification

Peptides were synthesized by a solid phase method on rink amide MBHA resin (0.68 mequiv) by using an ABI 433A automatic peptide synthesizer. The resin bound peptides were cleaved from the resins by a mixture composed of 95% trifluoroacetic acid (TFA, Biolab), 1.25% triethylsilane (Tis, Fluka), 1.25% thioanisole (TA, Aldrich) and 2.5% ethanedithiol (EDT, Aldrich), washed with dry ether (Biolab), and extracted with a mixture of 30% acetonitrile (Biolab) and 0.1% TFA, both in water. Peptide disulfide bonds were reduced with 5mM tris (2-carboxyethyl) phosphine Hydrochloride (TCEP·HCl tris, calbiochem) before purification. The peptides were purified by reversed phase (RP)-HPLC on a C18 reverse phase Vydac analytical column (250 x 4.6mm, 300 Å pore size, 5 µm particle size). The column was eluted in 50 min, using a linear gradient of 20-70% acetonitrile in 0.1% TFA (v/v), at a flow rate of 0.6 ml/min. The purified peptides were shown to be homogeneous (>97%, by weight), by the analytical HPLC. The peptides were analyzed by electrospray mass spectroscopy to confirm their composition and molecular weight. The crude peptides were lyophilized and were stored in a freezer at -20°C.

Peptide spin labeling and purification

The peptides were labeled with (MTSL) through attachment to the cystein SH group as reported earlier.¹ A tenfold molar excess of spin probe was added to the reaction buffer (0.1M phosphate buffer (PH 7.2) and 0.1M NaCl). The suspension was shaken for 12 hr, at room temperature. Excess spin label and unlabeled peptides were separated from the labeled peptide by RF-HPLC with the same analytical column that was used for the unlabeled peptide. Labeled peptides were analyzed using electrospray mass spectroscopy. The peptide solution was subdivided into aliquots that were lyophilized and were stored at -20°C. The purified labeled peptides were shown to be homogeneous by analytical HPLC (>97%, by weight). Further purification was performed in case of unlabeled spin probes were detected by CW-EPR.

DEER measurements

The constant time four-pulse DEER experiment, $\pi/2 (v_{\text{obs}}) - \tau_1 - \pi (v_{\text{obs}}) - t - \pi (v_{\text{pump}}) - (\tau_1 + \tau_2 - t) - \pi (v_{\text{obs}}) - \tau_2$ -echo was employed with a +x/-x phase cycle on the first pulse and averaging over 25 increments of τ_1 ($\tau_1 = 400$ ns, $\Delta\tau_1 = 8$ ns) to suppress nuclear modulations. The echo was measured as a function of t , while τ_2 was

kept constant. The pump frequency, ν_{pump} , was set to the center of the resonator bandwidth and the static magnetic field was set to the maximum of the nitroxide spectrum at the pump frequency. The observer frequency, ν_{obs} , was set at 60 MHz higher than ν_{pump} . The length of all mw pulses was 40 ns, and the dwell time was 20 ns. Typical numbers of shots per point and scan number were 30 and 50-600 respectively. Accumulation times for the data sets varied from 12 to 48 hr.

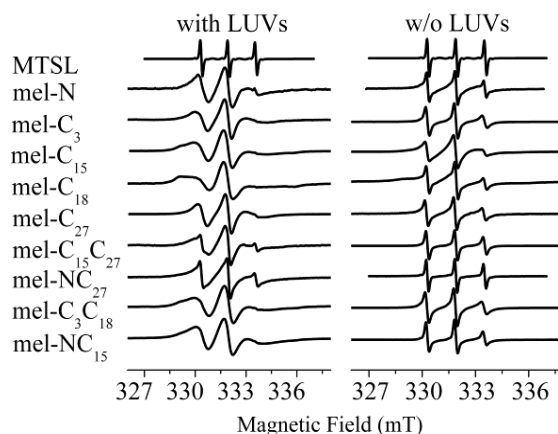


Figure S1. X-band EPR spectra of melittin that is labeled at different locations along the peptide and of MTSL, in the presence (*left*) and absence (*right*) of vesicles.

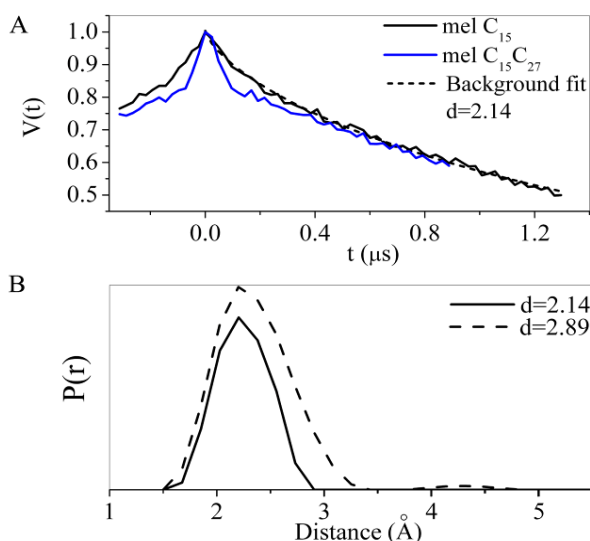


Figure S2. (A) DEER traces obtained from the singly labeled melittin, mel-C₁₅ (*black*), and the doubly labeled melittin, mel-C₁₅C₂₇ (*blue*), both within DPPC/PG/D₂O LUVs. The trace of mel-C₁₅ is fitted with an exponential decay with a dimensionality of 2.14. (B) Distance distributions $P(r)$ obtained for mel-C₁₅C₂₇ after subtraction of background exponential decay with a dimensionality of $d=2.14$ (*solid curve*) and $d=2.89$ (*dashed curve*).

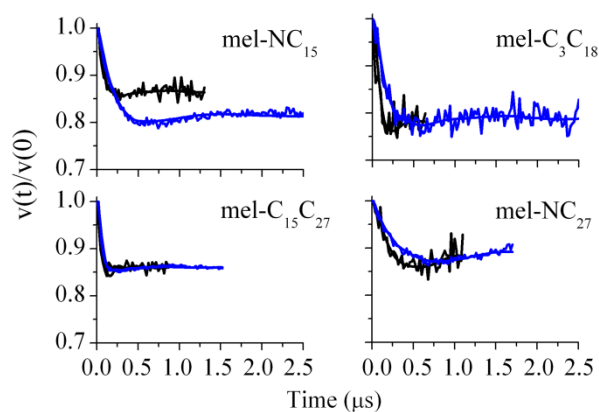


Figure S3. Normalized DEER decays for the doubly labeled melittin peptides within DPPC/PG/D₂O LUVs (*black*) and in D₂O/30% glycerol solution (*blue*) after background correction.

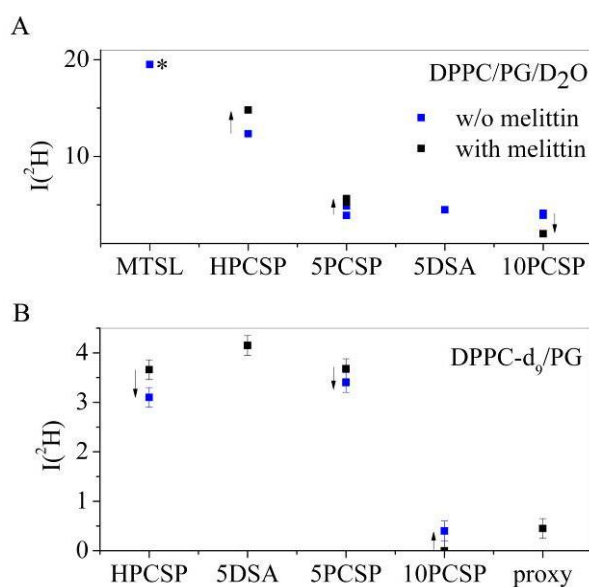


Figure S4. The $I(^2H)$ values of the spin probes examined in this work in (A) DPPC/PG/D₂O and (B) DPPC-d₉/PG LUVs, with (*black squares*) and without (*blue squares*) melittin. MTSL in 70% D₂O /30% glycerol (The value for is marked with *). The arrows designate the direction of the change in $I(^2H)$ value upon melittin addition. The standard errors are marked as bars in "B". The standard errors in "A" were smaller than the symbols.

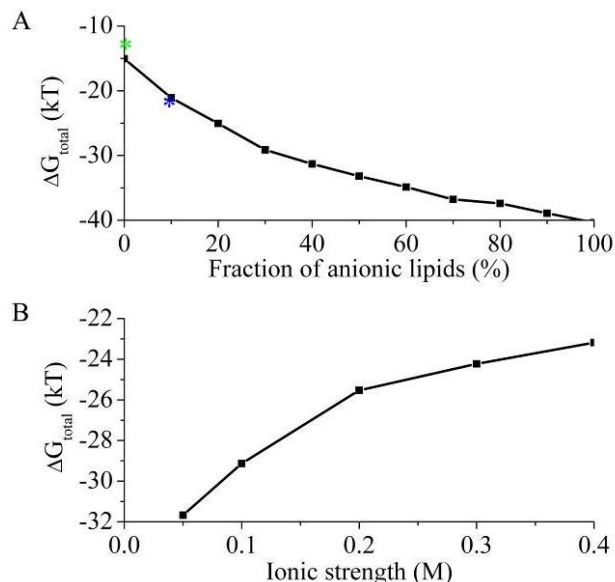


Figure S5. The calculated free energy of melittin-membrane association as a function of: (A) the fraction of anionic lipids (at constant ionic strength of 0.1 M) and (B) the ionic strength (at constant acidic lipid fraction of 30%). The green asterisk marks the experimental value in zwitterionic membrane, and the blue asterisk the value calculated based on MD simulation in 10% acidic lipid.²

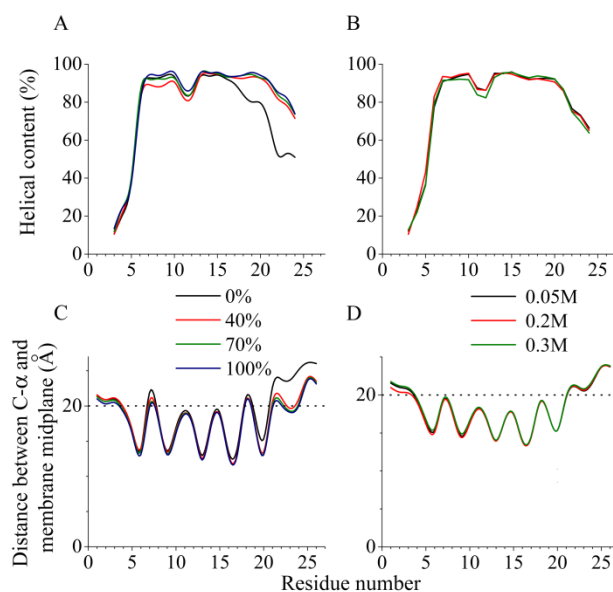


Figure S6. Melittin's helicity and location near the membrane is independent of the ionic strength and acidic lipid fraction. (A) The calculated (average) helicity along melittin's amino acid sequence at constant ionic strength of 0.1 M. Each curve marks the results obtained using different acidic lipid fraction according to the color legend. (C) The average location of the amino acids along the membrane normal at ionic strength of 0.1 M. The fraction of acidic lipids varied between 0-100% using the same color legend. (B) The calculated helicity along melittin's amino acid sequence for acidic lipid fraction of 30%. The different curves mark the results at different ionic strengths according to the color legend. (D) The average location of the amino acids along the membrane normal at acidic lipid fraction of 30%. The curves mark the results at different ionic strengths according to the color legend.

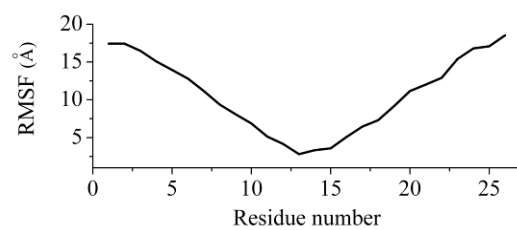


Figure S7. Calculated RMS fluctuations of the α -carbon atoms of native melittin in association with a membrane composed of 30% anionic lipids at ionic strength of 0.1 M. The termini are significantly more mobile than the center.

Appendix B: Supplementary Material for Paper II

Interaction of an antimicrobial peptide with membranes: experiments and simulations with NKCS

Yana Gofman, Sebastian Linser, Agnieszka Rzeszutek, Dalit Shental-Bechor, Sergio S. Funari, Nir Ben-Tal and Regine Willumeit

Published in *J Phys Chem B*, 2010, 114(12):4230-4237.

Theoretical calculations

The total free energy difference between a peptide in the aqueous phase and in the membrane (ΔG_{tot}) can be divided into several terms according to Eq. 1:¹

$$\Delta G_{\text{tot}} = \Delta G_{\text{con}} + \Delta G_{\text{def}} + \Delta G_{\text{Coul}} + \Delta G_{\text{sol}} + \Delta G_{\text{imm}} + \Delta G_{\text{lip}} \quad (1)$$

The free energy terms and the approach taken to calculate them were previously described in details.^{1,2} Generally speaking, ΔG_{con} is the free energy change due to membrane-induced conformational changes in the peptide. It can be calculated as:

$$\Delta G_{\text{con}} = \Delta E - T\Delta S \quad (2)$$

Where, ΔE is calculated as a sum of the internal energy changes between the water- and membrane-bound states of the peptides. The internal energy is derived from a statistical potential based on available 3D structures.^{3,4} The energy function assigns a score (energy) to each conformation of the peptide according to its abundance in the PDB. Common conformations receive high scores (low energy) while rare conformations receive lower scores (higher energy). ΔS refers to the entropy changes between the states, while S in each state is determined by the distribution of the virtual bonds in the reduced peptide representation. As the virtual bonds for the first and last two amino acids are not defined, those are omitted from the calculation. ΔG_{def} is the free energy penalty associated with fluctuations of the membrane width around its resting (average) value of 30 Å.

ΔG_{Coul} stands for the electrostatic interactions between titratable residues of the peptide and the (negative) surface charge of the membrane. We calculate this energetic term using the Gouy-Chapman theory, that describes how the electrostatic potential depends on the distance from the membrane surface in an electrolyte solution.¹ To this end, we considered the solution neutral, containing monovalent salt at a concentration of 0.1M. POPE surface potential was calculated as -2.1kT/e based on previous Z-potential measurements.⁵ The protonation state of the side chains of the titratable residues in the solution was set according to pH=7.

ΔG_{sol} is the free energy of transfer of the peptide from water to the membrane. It accounts for electrostatic contributions resulting from changes in the polarity of the solvent, as well as for nonpolar (hydrophobic) effects, which result from both differences in the van der Waals interactions of the peptide with the membrane and aqueous phases, and from solvent structure effects. ΔG_{imm} is the free energy penalty resulting from the confinement of the external translational and rotational motion of the peptide inside the

membrane. ΔG_{lip} is the free energy penalty resulting from the interference of the peptide with the conformational freedom of the aliphatic chains of the lipids in the bilayer.

The latter three terms are included in ΔG_{SIL} and are calculated based on a previously developed hydrophobicity scale.¹ The scale accounts for the free energy of transfer of the amino acids, located in the center of a polyalanine α -helix, from the aqueous phase into the membrane midplane. In order to avoid excessive penalty associated with charge transfer into the bilayer, the titratable residues were neutralized gradually when located closer to the membrane, so that a nearly neutral form was desolvated into the hydrophobic core.¹ Exceptionally, the charge was retained when the model was applied to calculate the interaction between a charged peptide and an anionic membrane, as described above.

Sampling protocol

To calculate the membrane interaction energy of each peptide, we simulated the peptides both in water and in membrane environments. The values were averaged over four different simulations of 900,000 Monte Carlo (MC) cycles each. In water simulations, the peptide was subjected solely to internal conformational modifications. In membrane simulations, additional external rigid body rotational and translational motions were also generated to allow the peptide to change its location in- and orientation with respect to the membrane. New peptide structures were generated by simultaneous perturbing the generalized coordinates.

The maximal step of the virtual backbone torsion angle was 3° and 0.5° for both the side-chain torsion angle and its angle with respect to the backbone. New configurations were generated by perturbing both the Euler angles that describe the peptide orientation by a maximal step of 5° , and the Cartesian coordinates of its geometric center by a maximal step of 0.5 \AA . A detailed description of the sampling protocol is available in references.^{1,2,6} Clustering of conformations and the calculation of the average helicity were carried out following the methodology described in reference.⁶

References

- (1) Shental-Bechor, D.; Haliloglu, T.; Ben-Tal, N. *Biophys J* **2007**, *93*, 1858-71.
- (2) Kessel, A.; Shental-Bechor, D.; Haliloglu, T.; Ben-Tal, N. *Biophys J* **2003**, *85*, 3431-44.
- (3) Bahar, I.; Jernigan, R. L. *Fold Des* **1996**, *1*, 357-70.
- (4) Bahar, I.; Kaplan, M.; Jernigan, R. L. *Proteins* **1997**, *29*, 292-308.
- (5) Willumeit, R.; Kumpugdee, M.; Funari, S. S.; Lohner, K.; Navas, B. P.; Brandenburg, K.; Linser, S.; Andra, J. *Biochim Biophys Acta* **2005**, *1669*, 125-34.
- (6) Shental-Bechor, D.; Kirca, S.; Ben-Tal, N.; Haliloglu, T. *Biophys J* **2005**, *88*, 2391-402.

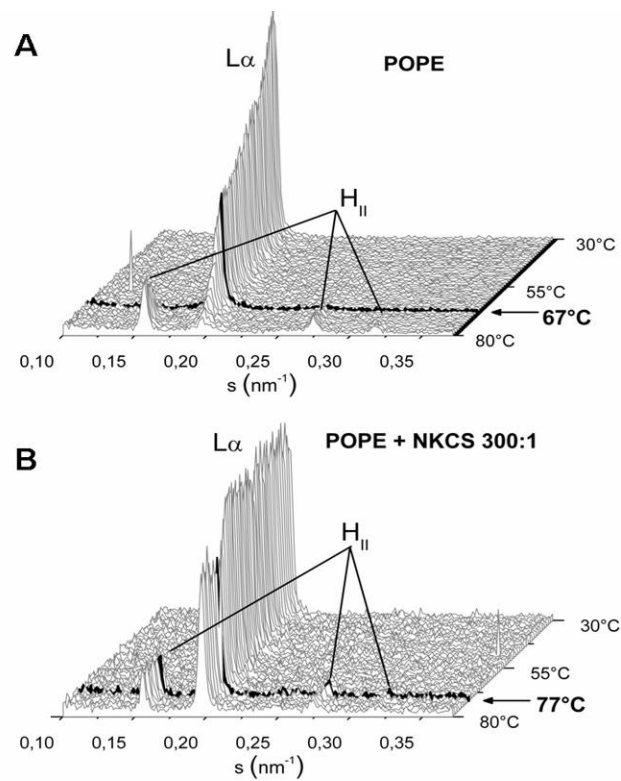


Figure S1. The influence of the peptide NKCS on the POPE phase transition temperature (10 mM sodium phosphate buffer pH 7.4). SAXS pattern for POPE (A) and POPE + NKCS (300:1) (B). The phases are indicated and the onset of the HII phase is highlighted.

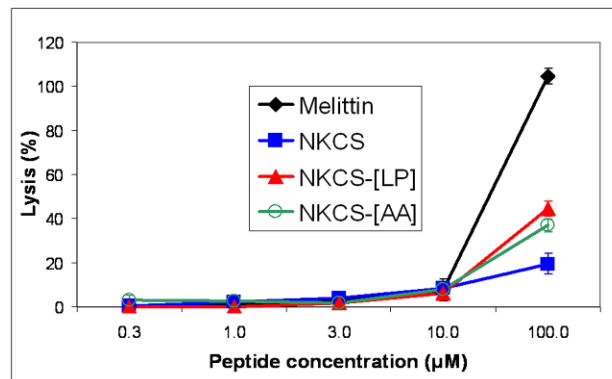


Figure S2. Hemolytic activity of the peptides in comparison to melittin.

Table S1. Energy decomposition. Energy values are shown in kT as average \pm standard deviation.

peptide	conformations	ΔG_{con}	ΔG_{SIL}	ΔG_{def}	ΔG_{Coul}
NKCS	inner	-2.3 \pm 1.0	-5.6 \pm 0.7	0.5 \pm 0.01	-14.2 \pm 0.1
	outer	4.2 \pm 0.9	0.0 \pm 0.1	0.7 \pm 0.1	-11.4 \pm 0.3
	all	-2.5 \pm 1.0	-4.7 \pm 0.8	0.5 \pm 0.01	-13.8 \pm 0.2
NKCS-[LP]	inner	-2.6 \pm 1.4	-1.9 \pm 0.2	0.5 \pm 0.01	-13.3 \pm 0.1
	outer	-0.3 \pm 1.0	0.1 \pm 0.1	0.6 \pm 0.01	-11.3 \pm 0.1
	all	-2.8 \pm 1.3	-1.2 \pm 0.2	0.5 \pm 0.02	-12.6 \pm 0.1
NKCS-[AA]	inner	-5.7 \pm 0.6	-14.4 \pm 0.3	0.5 \pm 0.01	-14.8 \pm 0.04
	outer	48.7 \pm 19.1	0.3 \pm 0.1	0.1 \pm 0.02	-10.2 \pm 0.1
	all	-5.7 \pm 0.6	-14.4 \pm 0.3	0.5 \pm 0.02	-14.8 \pm 0.1

Appendix C: Supplementary Material for Paper III

Membrane interactions of novacidin, a novel antimicrobial peptide: phosphatidylglycerol promotes bilayer insertion

Jerzy Dorosz, Yana Gofman, Sofiya Kulusheva, Daniel Otzen, Nir Ben-Tal, Niels Chr. Nielsen, Raz Jelinek

Published in *J Phys Chem B*, 2009, 114(34):11053-11060.

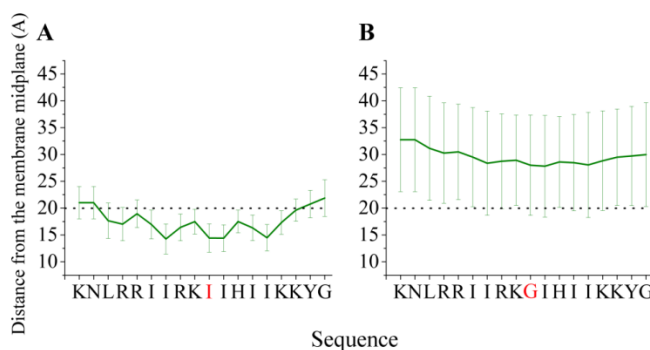


Figure S1. Location of ovispirin and novispirin in a neutral lipid bilayer based on MC simulations. The average conformations of ovispirin (**A**) and novispirin (**B**) in association with neutral (equivalent to pure PC) lipid bilayer determined as the average distance of each residue's alpha-carbon from the bilayer midplane. The error bars mark the standard deviation. The residues are indicated using a one-letter code. The horizontal dotted line marks the location of the phosphate group of the lipids polar heads. Novispirin hardly associates with the lipid bilayer but ovispirin resides in the polar headgroups region. It is remarkable that a single substitution of G to I (position 10; marked in red) is responsible for the different membrane behavior of the peptides. Apparently, novispirin is almost hydrophobic enough to partition into the membrane, and the addition of a single hydrophobic residue is enough to shift the balance.

Computational methods

The total free energy difference between a peptide in the aqueous phase and in the membrane (ΔG_{tot}) can be divided into several terms according to Eq. 1:

$$\Delta G_{\text{tot}} = \Delta G_{\text{con}} + \Delta G_{\text{def}} + \Delta G_{\text{Coul}} + \Delta G_{\text{sol}} + \Delta G_{\text{imm}} + \Delta G_{\text{lip}} \quad (1)$$

Where ΔG_{con} is the free energy change due to membrane-induced conformational changes in the peptide. ΔG_{def} is the free energy penalty associated with fluctuations of the

membrane width around its resting (average) value of 30\AA . ΔG_{Coul} stands for the electrostatic interactions between titratable residues of the peptide and the (negative) surface charge of the membrane. ΔG_{sol} is the free energy of transfer of the peptide from water to the membrane. It accounts for electrostatic contributions resulting from changes in the polarity of the solvent, as well as for nonpolar (hydrophobic) effects, which result from both differences in the van der Waals interactions of the peptide with the membrane and aqueous phases, and from solvent structure effects. ΔG_{imm} is the free energy penalty resulting from the confinement of the external translational and rotational motion of the peptide inside the membrane. ΔG_{lip} is the free energy penalty resulting from the interference of the peptide with the conformational freedom of the aliphatic chains of the lipids in the bilayer.

Appendix D: Supplementary Material for Paper IV

W-band pulse EPR distance measurements in peptides using Gd^{3+} -dipicolinic acid derivatives as spin labels

Michal Gordon – Grossman, Ilia Kaminker, Yana Gofman, Yechiel Shai and Daniella Goldfarb

Published in *Phys Chem Chem Phys*, 2011, 13(22):10771-10780.

Titration of 4MMDPA-mel- $C_{15}C_{27}$ with Gd^{3+}

To 50 μ l of 0.01 mM 4MMDPA-mel- $C_{15}C_{27}$ with 5 μ l of 2.2 mM arsenazo (1:22 peptide/arsenazo molar ratio), n aliquots of 21.6 μ M $GdCl_3$ in DDW, at the required volume to keep $[Gd^{3+}] = 1.8 \mu$ M, were added. After each addition, the sample was vortexed intensively for one minute and then vortexed occasionally during the next 10 minutes. Then, UV-Vis absorption measurements were carried out on 1.5 μ l of the total sample using UV-Vis Nanodrop[®] ND-1000 spectrometer. The spectra are shown in Fig. S1a. The originally bright pink arsenazo III solution turn light-to-dark purple with the formation of chelated arsenazo- Gd^{3+} . The addition of $GdCl_3$ was stopped when arsenazo III began turning purple-to-green, which indicates the presence of Gd^{3+} not coordinated to the 4MMDPA labeled peptide. The titration curve is shown in Fig. S1b and the compositions chosen for DEER measurements are indicated in the Figure.

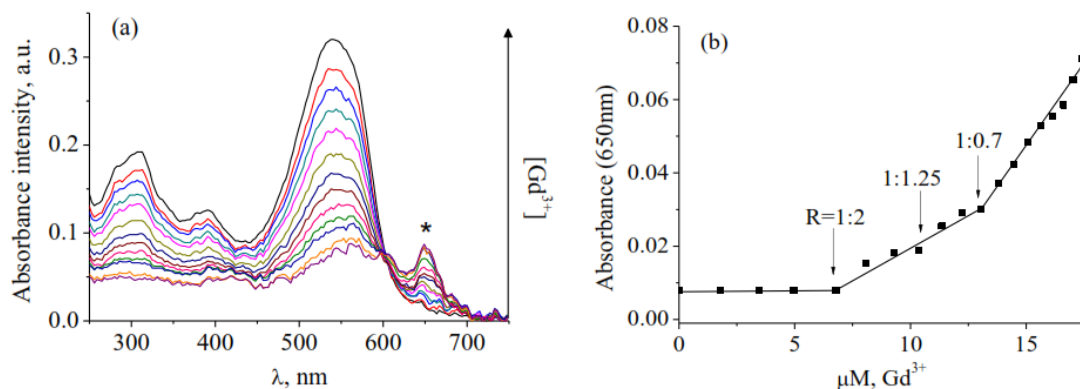


Figure S1. (a) UV-Vis absorbance spectra of 4MMDPA-mel $C_{15}C_{27}$ and arsenazo with gradual amounts of added $GdCl_3$ (The asterisk at 650 nm indicates the band of Gd^{3+} -arsenazo). (b) The corresponding plot of the UV-Vis absorbance intensity at 650 nm as a function of total $[Gd^{3+}]$ added. The arrows indicate the molar ratios of $[Gd^{3+}]/2[4MMDPA-melC_{15}C_{27}]$ examined in this work.

Speciation of Gd^{3+} - (4MMDPA) $_{1-3}$ in solution

The 4MMDPA tag has only three coordination sites, therefore depending on the $[\text{Gd}^{3+}]/[\text{tag}]$ ratio, complexes of $\text{Gd}^{3+}\text{-(4MMDPA)}_{0-3}$ can be formed. Using the literature reported room temperature equilibrium constants; $\text{pK}_{i(i=1-3)}=8.74\pm 0.01, 7.32\pm 0.03, 5.77\pm 0.03$, respectively,¹ we calculated the relative concentration of each of the $\text{Gd}^{3+}\text{-(4MMDPA)}_n$ ($n=0-3$) complexes for a total concentration, (0.2 mM) of the ligand, [4MMDPA], as a function of $R'=[\text{Gd}^{3+}]/[\text{4MMDPA}]$ (Fig. S2a). The chosen concentrations are typical for protein and peptide concentrations used in DEER measurements. These calculations show that for $R'=1:1$ the major component in solution is the $n=1$ complex but there is a significant contribution from both the $n=0,2$ complexes ($\sim 15\%$ each). For $R'=1:2$ the contribution of the $n=0$ (free Gd^{3+}) is negligible, but the amounts of the $n=1,2$ complexes are comparable. For $R'=1:0.7$ there is approximately 40% free Gd^{3+} in the sample.

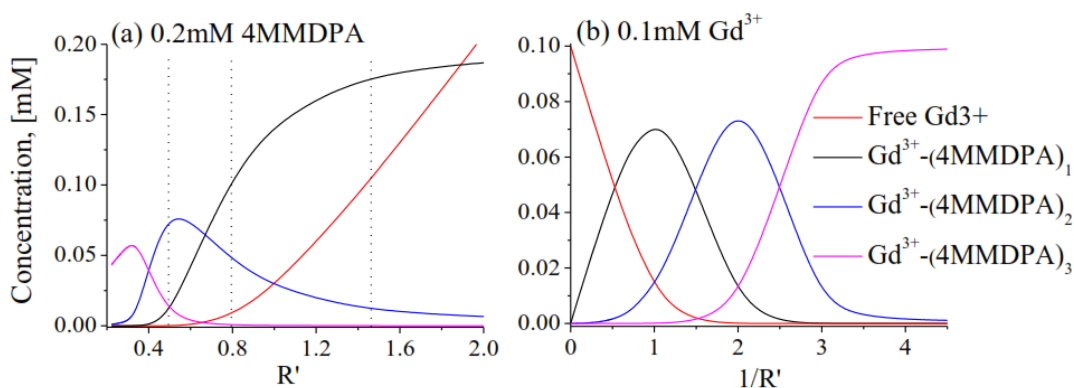


Figure S2. The calculated concentration of $\text{Gd}^{3+}\text{-(4MMDPA)}_1$, $\text{Gd}^{3+}\text{-(4MMDPA)}_2$ and $\text{Gd}^{3+}\text{-(4MMDPA)}_3$ and free Gd^{3+} in solution vs. (a) R' , with $[\text{4MMDPA}]=0.2$ mM and (b) $1/R'$ with $[\text{Gd}^{3+}]=0.1$ mM. The dotted lines in figure a indicate the R values (1:2, 1:1.25, 1:0.7) for the labeled melittin examined in this work.

To verify the actual composition of the frozen solutions in terms of the $\text{Gd}^{3+}\text{-(4MMDPA)}_n$ complexes we prepared solutions of $R'=[\text{Gd}^{3+}]/[\text{4MMDPA}]$ ratios of 1:100, 1:10, 1:5, 1:2, 1:1 and 1:0.5 and $[\text{Gd}^{3+}]=0.1\text{mM}$ by dissolving GdCl_3 and the tag in D_2O (70%) /perdeuterated d_8 - glycerol (30%). The speciation for such a system as a function of $1/R'=[\text{4MMDPA}]/[\text{Gd}^{3+}]$ is represented by the plots in Fig. S2b. Samples were vortexed and sonicated for one minute. These were characterized by W-band EPR and 1H ENDOR (electron-nuclear double resonance).

The 10 K ED-EPR spectra of free Gd^{3+} ($n=0$) and the series listed above are depicted in Fig S3a,b. The spectra exhibit a clear broadening of the central transition and of the background due to all other transitions with decreasing R' . From this series we can isolate the spectra of free Gd^{3+} and of $\text{Gd}^{3+}\text{-(4MMDPA)}_3$ given by the spectrum of $R'=1:100$. The aquo Gd^{3+} spectrum was simulated with the ZFS parameters $D=850$ MHz and $E=270$ MHz with the D and E Gaussian distributions of 700 MHz and 130 MHz, respectively. The spectrum of the $R'=1:100$ sample was simulated with $D=1800$ MHz and $E=180$ MHz with the D and E distributions of 725 MHz and 60 MHz, respectively, as shown in Fig S4a,b.

We could not reproduce the spectra of $R'=1:1$ and $1:2$ just by a superposition of the spectra of free Gd^{3+} and the $1:100$ samples. This and the comparison of the total width of the central transition of the spectra shown in Fig. S3, particularly the low field edge, indicate that spectra of $Gd^{3+}-(4MMDPA)_{1,2}$ are different and narrower than the spectrum of $Gd^{3+}-(4MMDPA)_3$, namely D is smaller.

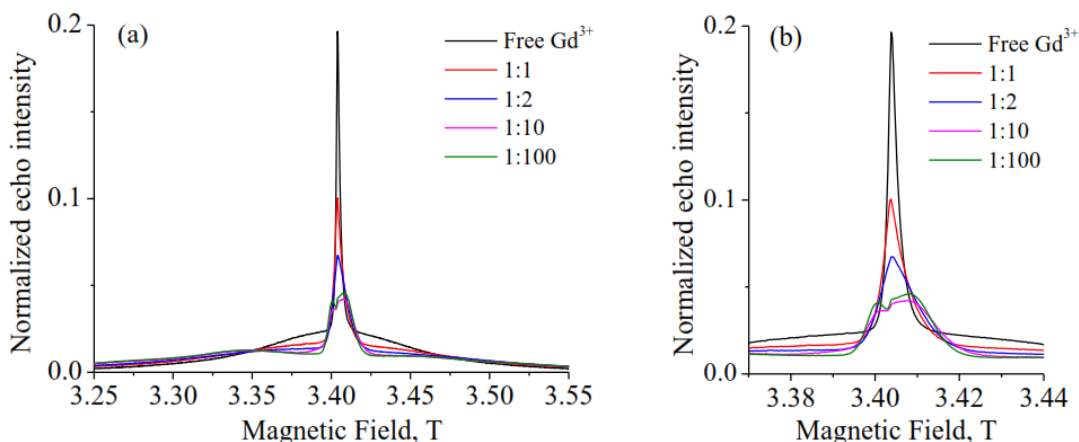


Figure S3. 10 K W-band ED-EPR spectra of frozen solutions of $Gd^{3+}-(4MMDPA)$ as a function of $[Gd^{3+}]/[4MMDPA]$. (a) Full scale and (b) the region of the central transition. The spectra were normalized by equalizing the area under the curve to unity.

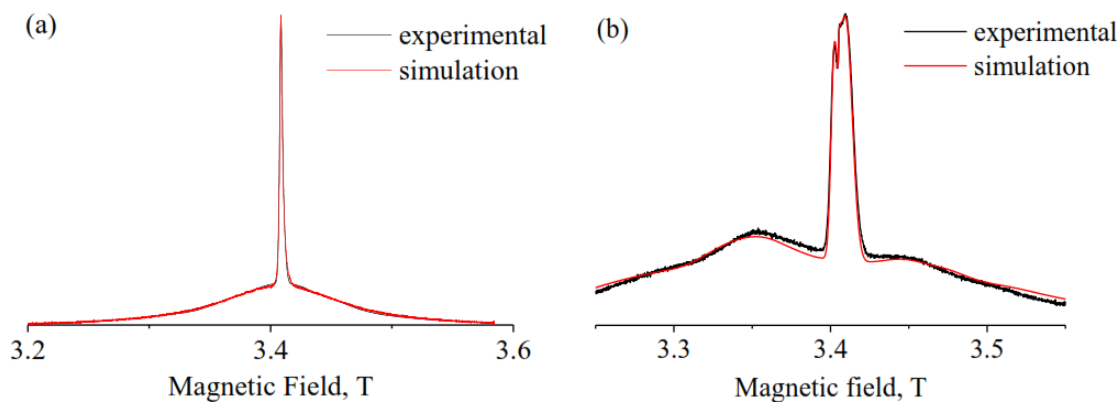


Figure S4. 10 K W-band ED-EPR spectra of (a) aquo Gd^{3+} and (b) $Gd^{3+}-(4MMDPA)_3$ ($R'=1:100$) and the corresponding simulations obtained from Easyspin² and the parameters listed in the text.

ENDOR measurements

In further attempts to determine the composition of the frozen samples subjected to the DEER measurements in terms of the number of 4MMDPA ligands that binds to Gd^{3+} we have performed 1H ENDOR measurements that count the number of water

ligands, m .³ Measurements were performed with the magnetic field set to the maximum of the $Gd^{3+} | -1/2 \rangle \leftrightarrow | +1/2 \rangle$ central transition. The 1H ENDOR spectra were measured using the Mims ENDOR sequence $\pi/2 - \tau - \pi/2 - T - \pi/2 - \tau - \text{echo}$, with an RF pulse applied during the time interval T . The duration of the $\pi/2$ pulses was 12.5 ns, τ was 130 ns and $t_{RF} = 30 \mu s$. All ENDOR spectra were recorded using the random acquisition mode,⁴ with one shot for each RF point and the repetition time was 1 ms. The data accumulation time varied from 20 min to 2 hr depending on the S/N. All ENDOR measurements were carried out at 10 K.

The aquo complex of Gd^{3+} ($n=0$) has a total of 9 water ligands ($m=9$)⁵ whereas for the $Gd^{3+}-(4MMDPA)_n$ complexes we get for $n=1,2,3$ $m=6,3,0$ respectively. Figure S6a shows the 1H ENDOR spectra of solutions of $Gd^{3+}-(4MMDPA)$ with various R 's. These spectra are normalized according to the ENDOR effect, E , that is defined according to:

$$E = \frac{I(RF_{on}) - I(RF_{off})}{I(RF_{off})}$$

where $I(RF_{on})$ and $I(RF_{off})$ are the echo intensity with RF on and off. In Fig. 6b,c we plot E at ± 2.4 MHz and ± 1.3 MHz, corresponding to the $\frac{1}{2}A_{\parallel}$ and $\frac{1}{2}A_{\perp}$ features of the $M_S = \pm 1/2$ manifolds. Taking into account that under the same experimental conditions E is proportional to m , the y scale on the right shows the averaged m values for each sample. These plots show that indeed for $R'=1:10$ and $1:100$ the sample contains mainly $Gd^{3+}-(4MMDPA)_3$ because $m \sim 1-2$. For $R'=1:2$ and $1:1$ we obtained $m=4.7$ and $m=5.5$ respectively. If we use the relative amounts of each $Gd^{3+}-(4MMDPA)_n$ species for $R'=1:2$ from Fig. S2b and assume the same lineshape for the $n=1$ and 2 complex, a weighted average yields $m=3$ which does not agree with the experimental value. Alternatively, to obtain $m=4.7$ we find that the linewidth ratio of the $n=1,2$ complexes, $\Delta H_2/\Delta H_1$, should be ~ 7.84 . This ratio is far too large and inconsistent the spectra shown in Fig. S3. The width of the central transition of free Gd^{3+} ($n=0$) is 29 G and for the $n=3$ complex it is 160 G. Since $29 G < \Delta H_2$ and $\Delta H_1 < 160 G$ the above ratio is considerably overestimated. To reduce this ratio the concentration of the $n=1$ complex has to increase. Similarly, for the $R'=1:1$ sample $m=5.5$ cannot be obtained from the relative concentrations obtained from Fig. S2 and the contribution from free Gd^{3+} must increase.

The calculated speciation curves used in above arguments were derived from room temperature equilibrium constants. Our samples however, were rapidly frozen from room temperature and the equilibrium constants that are relevant for our experimental conditions are probably those of just above the freezing temperature, and may well be different than those determined at room temperature. Moreover our solutions include 30% glycerol which may have an effect as well.

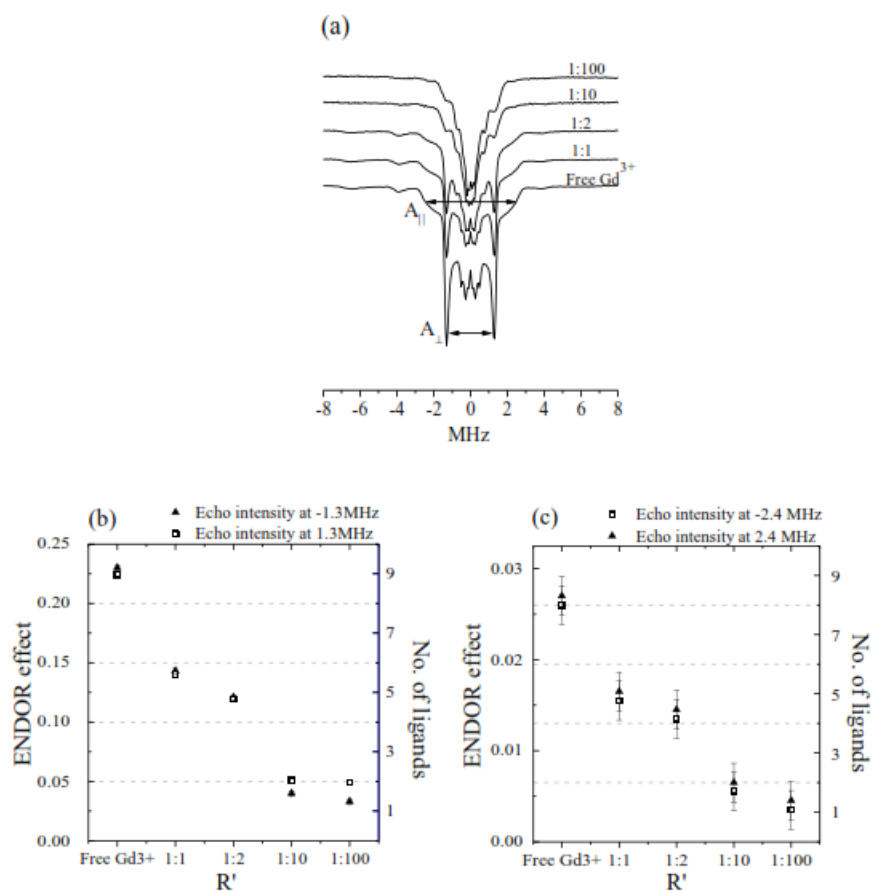


Figure S5. (a) Mims ENDOR spectra of solutions of Gd³⁺-4MMDPA with R'=1:100, 1:10, 1:2, 1:1 and free Gd³⁺. The water hyperfine couplings corresponding to the $M_S = \pm 1/2$ are indicated. (b) The ENDOR effect at ± 1.3 MHz (error bars are in the same size of the symbol) and (c) at ± 2.4 MHz and m as a function of R'.

From the EPR and ENDOR measurements we conclude that the room temperature binding constants obtained do not describe the speciation in frozen solutions well enough and the binding constants are lower at the temperature at which the samples freeze. Nonetheless, these curves are useful as guidelines and give idea on the compositions of these solutions.

In principle, simulations of the EPR spectra should provide the relative contributions of the various complexes. Such a simulation, however, involves a rather large number of parameters, D and E and their distributions for the $n=1$ and $n=2$ complexes (a total of 8 parameters) along with the relative contributions of the $n=0-3$ complexes for each R'. This is not a trivial task and it is beyond the scope of this work.

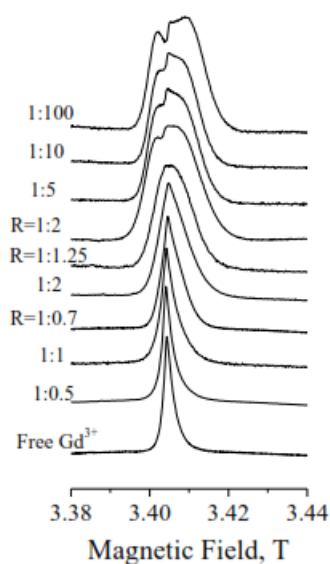


Figure S6. Comparison of the 10 K W-band ED-EPR spectra of solutions of Gd^{3+} -4MMDPA with $R=1:100$, $1:10$, $1:5$, $1:2$, $1:1$, $1:0.5$ and 0.1 mM free Gd^{3+} , in $\text{D}_2\text{O}/30\%$ glycerol, and of Gd^{3+} -4MMDPA- $\text{meI}\text{C}_{15}\text{C}_{27}$, where $R=1:2$ (25 K), $1:1.25$ (10 K) and $1:0.7$ (25 K). Here $[\text{Gd}^{3+}]$ was 0.1 , 0.16 , 0.28 mM, respectively, and $[\text{4MMDPA-meI}\text{C}_{15}\text{C}_{27}]=0.2$ mM.

Relaxation times and DEER control measurements

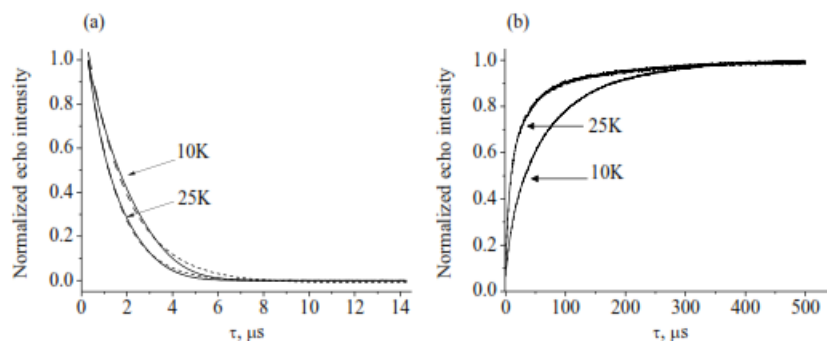


Figure S7. (a) W-band two pulse echo decay of Gd^{3+} -4MMDPA- $\text{meI}\text{C}_{15}\text{C}_{27}$ with $R=1:1.25$, measured at 10 K and 25 K and their exponential fit (*dashed*) where $T_M(10\text{ K})=1.8\ \mu\text{s}$ and $T_M(25\text{ K})=1.3\ \mu\text{s}$. (b) Saturation recovery time domain traces the same sample at the same temperatures their bi-exponential fit (*dashed*) obtained with the time constants $100\ \mu\text{s}$ ($22\ \mu\text{s}$) and $91\ \mu\text{s}$ ($12\ \mu\text{s}$) for 10 K and 25 K respectively.

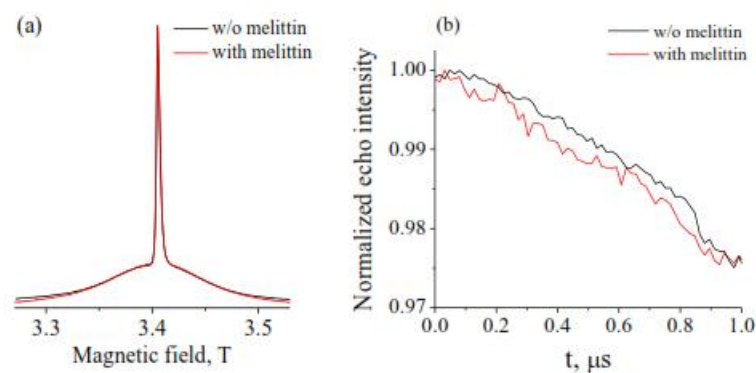


Figure S8. (a) 25 K W-band ED EPR spectra of 0.2 mM Gd^{3+} solution in D_2O /glycerol with 0.4 mM native melittin (red) and w/o (black), and (b) the corresponding W-band four pulse DEER traces.

Literature

- 1 I. Grenthe, *J. Am. Chem. Soc.*, 1961, **83**, 360.
- 2 S. Stoll and A. Schweiger, *J. Magn. Reson.*, 2006, **178**, 42.
- 3 A. Potapov and D. Goldfarb, *Inorg Chem*, 2008, **47**, 10491.
- 4 B. Epel, D. Arieli, D. Baute and D. Goldfarb, *J. Magn. Reson.*, 2003, **164**, 78.
- 5 A. M. Raitsimring, A. V. Astashkin, D. Baute, D. Goldfarb, O. G. Poluektov, M. P. Lowe, S. G. Zech and P. Caravan, *Chemphyschem*, 2006, **7**, 1590.

Appendix E: Supplementary Material for Paper V

Membrane-integration of a mitochondrial signal-anchored protein does not require additional proteinaceous factors

Elisa Merklinger, Yana Gofman, Alexej Kedrov, Arnold J.M. Driessen, Nir Ben-Tal, Yechiel Shai and Doron Rapaport

Published in *Biochem J*, 2011.

Experimental Methods

Isolation of mitochondria by enzymatic spheroblastation

Preparation of crude mitochondria from cultures grown in lactate medium was performed as described before (1). Cells were harvested (3000g, 5 min, 20°C), washed once in water, resuspended in 2 ml per gram cell weight of resuspension buffer (100 mM Tris base, 10 mM dithiothreitol (DTT)) and sedimented again. Cells were then washed with spheroblasting buffer (1.2 M sorbitol, 2 mM potassium phosphate buffer, pH 7.2) and cell walls were subsequently digested at 30°C for 45 min in suspension of 6 ml per gram cell weight of the spheroblasting buffer supplemented with 1.1 mg/ml zymolyase (Seikagaku). All further steps were performed on ice or at 4°C. Spheroblasts were collected by centrifugation (2000g, 5 min) resuspended in 100-200 ml homogenization buffer (0.6 M sorbitol, 1 mM EDTA, 1 mM PMSF, 0.2% (w/v) fatty acid free BSA (Sigma), 10 mM Tris/HCl, pH 7.4) and lysed by ten strokes in a tight fitting Potter glass-glass homogenizer. Cell lysates were clarified by two centrifugation steps as described before and mitochondria were sedimented by centrifugation (18000g, 12 min). Mitochondrial pellets were resuspended in 30 ml SEM buffer (250 mM sucrose, 1 mM EDTA, 10 mM MOPS-KOH, pH 7.2) containing 2 mM PMSF and clarified twice by centrifugation (2000g, 5 min). Mitochondria were reisolated by centrifugation (18000g, 12 min), resuspended in SEM buffer, aliquoted, snap-frozen in liquid nitrogen and stored at –80°C.

CD spectroscopy

The circular dichroism (CD) spectra of the peptide were recorded in an Aviv 202 spectropolarimeter in a thermostatted quartz optical cell with a path length of 1 mm. Spectra were recorded at a wavelength range of 190-260 nm at 1 nm intervals with an average time of 6 s and 3 repetitions. The peptide was scanned at a concentration of 10 µM in two different environments: 5 mM HEPES buffer (pH 7.4), and the above buffer with 1% LPC. The signals of the buffer and 1% LPC, before adding the peptide were subtracted from the signals after peptide addition.

Polarized ATR-FTIR analysis of the Peptides

To determine the orientation of the peptide in lipid multibilayers, we used polarized attenuated total reflectance fourier transform infrared (ATR-FTIR) spectroscopy. Spectra were recorded with a Bruker equinox 55 FTIR spectrometer equipped with a deuterated triglyceride sulfate detector coupled to an ATR device as previously described (2).

Briefly, prior to sample preparations, the TFA counter ions, which associate with the peptides, were replaced with chloride ions through several lyophilizations of the peptides in 0.1 M HCl. After the ion exchange, a mixture of phospholipid (1 mg) alone or with peptide (100 µg) was deposited on a germanium prism. The aperture angle of 45° yielded 25 internal reflections. Lipid/peptide mixtures were prepared by dissolving them together in a 1:2 MeOH/CH₂Cl₂ mixture and drying under vacuum for 15 min. Polarized spectra were recorded and the respective spectrum of pure phospholipid in each polarization was subtracted to yield the difference spectra in order to determine the amide I absorption peaks of the peptide. For each spectrum 60 scans were collected with resolution of 4 cm⁻¹.

ATR-FTIR data analysis

Prior to curve fitting, a straight baseline passing through the ordinates at 1700 and 1600 cm⁻¹ for the peptide, or 2800 and 3000 cm⁻¹ for the lipids was subtracted. To resolve overlapping bands, we processed the spectra using PEAKFIT software (Jandel Scientific). Second-derivative spectra were calculated to identify the positions of the component bands. These wavenumbers were then used as initial parameters for curve fitting with Gaussian component peaks. Positions, band widths, and amplitudes of the peaks were varied until (i) the resulting bands shifted by no more than 2 cm⁻¹ from the initial parameters, (ii) all the peaks had reasonable half-widths (<20-25 cm⁻¹), and (iii) there was good agreement between the calculated sum of all the components and the experimental spectra ($r^2 > 0.99$). The ATR electric fields of incident light were calculated as follows (3):

$$E_x = \frac{2 \cos \theta \sqrt{\sin^2 \theta - n_{21}^2}}{\sqrt{(1 - n_{21}^2)(1 + n_{21}^2) \sin^2 \theta - n_{21}^2}}$$

$$E_y = \frac{2 \cos \theta}{(1 - n_{21}^2)}$$

$$E_z = \frac{2 \sin \theta \cos \theta}{\sqrt{(1 - n_{21}^2)(1 + n_{21}^2) \sin^2 \theta - n_{21}^2}}$$

where θ is the angle of incidence between the light beam and the prism normal (45°) and n_{21} is the reflective index of the Ge (taken to be 4.03) divided by the reflective index of the membrane (taken to be 1.5). Under these conditions E_x , E_y and E_z are 1.40, 1.52 and 1.64, respectively. The electric field components together with the dichroic ratio (defined as the ratio between absorption of parallel (A_{\parallel}) and perpendicular (A_{\perp}) polarized light, $R^{\text{ATR}} = A_{\parallel}/A_{\perp}$) are used to calculate the orientation order parameter, f , by the following formula:

$$R = \frac{A_{\parallel}}{A_{\perp}} = \frac{E_x^2}{E_y^2} + \frac{(E_z^2/E_y^2)(f \cos^2 \alpha + (1-f)/3)}{(f \sin \alpha)/2 + (1-f)/3}$$

where α is the angle between the transition moment of the amide I vibration of the α -helix and the helix axis. We used the value of 27° for α as was previously suggested (3-4). The orientation order parameter f allows calculating the “average” angle of the peptide α -helices relative to the membrane normal by the following formula:

$$f = \frac{1}{2}(3(\cos^2 \gamma)) - 1$$

Lipid order parameters were obtained from the lipid symmetric (2850 cm^{-1}) and asymmetric (2921 cm^{-1}) stretching mode using the same equations differing only by setting $\alpha = 90^\circ$ (3).

Fluorescence measurements with a stopped-flow setup

The kinetic of peptide binding to LUVs was measured in a stopped-flow fluorimeter. The measurements were done at 25°C with a slit width of 5 nm. The excitation wavelength was 467 nm and emission was detected using a cutoff filter of 520 nm. Every reaction was repeated at least six times, and the average signal was considered as the representative signal for the reaction. The association rate constants were measured in PBS under pseudo-first-order rate conditions. The data were fitted using a double exponent equation:

$$F(t) = \Delta F_1 \exp(-k_{\text{obs}1}t) + \Delta F_2 \exp(-k_{\text{obs}2}t) + F_\infty$$

where $k_{\text{obs}1}$ and $k_{\text{obs}2}$ are the observed rate constants for the first and second components of a double-exponential reaction and ΔF_1 and ΔF_2 are the amplitudes for the first and second components of a double-exponential reaction.

Monte Carlo (MC) simulations

MC simulations of the *OM45-SA* peptide and its double mutant R4E,K26E were performed using the MCPep server² (available online at <http://bental.tau.ac.il/MCPep/>). The membrane was represented as a smooth hydrophobic profile of native width of 30 Å, corresponding to the hydrocarbon region. A negative surface charge was located on both sides of the membrane at a distance of 20 Å from the midplane. Its magnitude was estimated based on the relative fraction of charged lipids in the mitochondrial OM, i.e., 13% (PI)+2× 4% (CL)+2% (PS)= 23%. The membrane was embedded in an aqueous solution of 0.1 M monovalent salt and pH=7.0, corresponding to physiological conditions. The initial peptides' structure was constructed as canonical α -helix and placed either in TM orientation with its principle axis roughly along the membrane normal or surface orientation with its axis roughly in the membrane surface. The MCPep server calculated the free energy of each configuration in comparison to the free energy in the aqueous phase.

References

1. Daum, G., Gasser, S., and Schatz, G. (1982) Import of proteins into mitochondria: energy-dependent, two-step processing of the intermembrane space enzyme cytochrome b_2 by isolated yeast mitochondria, *J. Biol. Chem.* 257, 13075-13080.
2. Gazit, E., Miller, I. R., Biggin, P. C., Sansom, M. S., and Shai, Y. (1996) Structure and orientation of the mammalian antibacterial peptide cecropin P1 within phospholipid membranes, *J Mol Biol* 258, 860-870.

3. Ishiguro, R., Matsumoto, M., and Takahashi, S. (1996) Interaction of fusogenic synthetic peptide with phospholipid bilayers: orientation of the peptide alpha-helix and binding isotherm, *Biochemistry* 35, 4976-4983.
4. Rothschild, K. J., and Clark, N. A. (1979) Polarized infrared spectroscopy of oriented purple membrane, *Biophys J* 25, 473-487.

Table S1. Peptide secondary structure in buffer (pH 7.4) and in buffer + 1% LPC determined by CD spectroscopy.

	Secondary structure [%]	
	Buffer	Buffer+1% LPC
α -helix	17	58
β -sheet	32	9
random coil	33	18
other	18	15

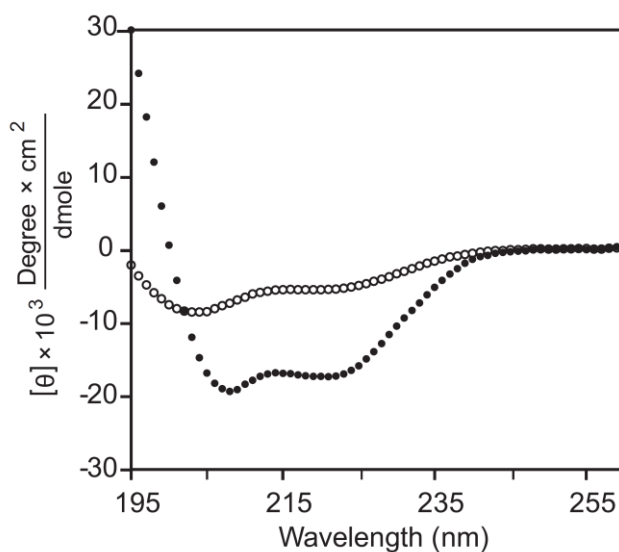


Figure S1. CD spectra of OM45-SA peptide. Lyophilized samples of peptide were dissolved directly in buffer (pH 7.4) (open circles) or in buffer containing 1% (w/v) LPC (closed circles). The spectra were taken at peptide concentrations of 10 μM .

Acknowledgements

I thank Prof. Regine Willumeit for the endless patience, support, empathy and generosity

I thank Prof. Uli Hahn for the help and support

I thank Prof. Nir Ben-Tal for the support and sharing his knowledge and wisdom

I thank Prof. Turkan Haliloglu for her wisdom and careful and fun guidance

I thank Dr. Dalit Shental-Bechor for sharing her knowledge and her support

I thank all collaborators for the opportunity to work together:

Dr. Agnieszka Rzeszutek

Dr. Sebastian Linser

Prof. Daniella Goldfarb

Dr. Michal Gordon-Grossman

Prof. Raz Jelinek

Dr. Jerzy Dorosz

Prof. Doron Rapaport

Special thanks to Dr. Frank Feyerabend for his kindness and care

Declaration of Oath (Eidesstattliche Versicherung)

Hiermit versichere ich Eides Statt, die vorliegende Doktorarbeit selbstständig und nur unter Verwendung der angegebenen Literatur und Hilfsmittel angefertigt zu haben.

Hamburg, Januar 2012

Yana Gofman

Signature

Erklärung über frühere Promotionsversuche

Hiermit erkläre ich, dass vorher keine weiteren Promotionsversuche unternommen worden sind, oder an einer anderen Stelle vorgelegt wurden.

Hamburg, Januar 2012

Yana Gofman

Signature

List of Hazardous Substances (Gefahrstoffliste)

Keine Substanzen verwendet.

No Hazardous Substances were used.

List of Papers and Contribution

Paper	Contribution
1. Gofman Y. [*] , Gordon-Grossman M. [*] , Zimmermann H., Frydman V., Shai Y., Ben-Tal N., Goldfarb D. Melittin-membrane interactions: insight from pulse EPR and Monte Carlo simulations studies. <i>J Phys Chem B</i> 2009 , 113, 12687–12695.	50%
2. Gofman Y. , Linser S., Rzeszutek A., Shental-Bechor D., Funari S.S., Ben-Tal N., Willumeit R. Interaction of an antimicrobial peptide with membranes: experiments and simulations with NKCS. <i>J Phys Chem B</i> 2010 , 114, 4230-4237.	50%
3. Dorosz J., Gofman Y. , Kolusheva S., Otzen D., Ben-Tal N., Nielsen C.N., Jelinek R. Membrane interactions of novicidin, a novel antimicrobial peptide: phosphatidylglycerol promotes bilayer insertion. <i>J Phys Chem B</i> 2010 , 114, 11053–11060.	40%
4. Gordon-Grossman M., Kaminker I., Gofman Y. , Shai Y., Goldfarb D. W-band pulse EPR distance measurements in peptides using Gd ³⁺ -dipicolinic acid derivatives as spin labels. <i>Phys Chem Chem Phys</i> 2011 , 13, 10771-10780.	20%
5. Merklinger E., Gofman Y. , Kedrov A., Driessen A.J.M., Ben-Tal N., Shai Y., Rapaport D. Membrane-integration of a mitochondrial signal-anchored protein does not require additional proteinaceous factors. Accepted <i>Biochem J</i> 2011 .	40%

* - equal contributors. All works were performed in collaboration with an experimental lab, therefore maximal contribution possible is 50%.

Curriculum Vitae

Personal Data

Name Yana Gofman
Date & place of birth: 15.07.1981, Yekaterinburg, Russia
Citizenship: Israel, Russia

Education

2008 - 2011 Studies towards Ph.D in Biochemistry under the supervision of Prof. Ulrich Hahn and Prof. Regine Willumeit, Hamburg University
2004 - 2006 M.Sc. in Pharmacology under the supervision of Prof. Daniel Khananshvili, Tel-Aviv University.
2001 - 2004 B.Sc. in Biology, Tel-Aviv University.

Academic awards

2011 Katzir Travel Scholarship, Weizmann Institute
2010 Trotsky Scholarship, Tel Aviv University
2010 Constantiner Travel Scholarship, Tel Aviv University
2005 - 2006 Achievement scholarship, Tel-Aviv University
2001- 2002 Outstanding students program scholarships, Tel-Aviv University

Publications

Merklinger E., **Gofman Y.**, Kedrov A., Driessen A.J.M., Ben-Tal N., Shai Y., Rapaport D. Membrane-integration of a mitochondrial signal-anchored protein does not require additional proteinaceous factors. Accepted *Biochem J*, **2011**.

Gordon-Grossman M., Kaminker I., **Gofman Y.**, Shai Y., Goldfarb D. W-band pulse EPR distance measurements in peptides using Gd^{3+} -dipicolinic acid derivatives as spin labels. *Phys Chem Chem Phys* **2011**, 13, 10771-10780.

Dorosz J., **Gofman Y.**, Kolusheva S., Otzen D., Ben-Tal N., Nielsen C.N., Jelinek R. Membrane interactions of novicidin, a novel antimicrobial peptide: phosphatidylglycerol promotes bilayer insertion. *J Phys Chem B* **2010**, 114, 11053–11060.

Gofman Y.*, Peretz A.*, Pell L.*, Haitin Y., Patrich E., Ben-Tal N., Attali B. Targeting the voltage sensor of Kv7.2 channels with a new gating-modifier. *PNAS* **2010**, 107, 15637–15642.

Gofman Y., Linser S., Rzeszutek A., Shental-Bechor D., Funari S.S., Ben-Tal N., Willumeit R. Interaction of an antimicrobial peptide with membranes: experiments and simulations with NKCS. *J Phys Chem B* **2010**, 114, 4230-4237.

Gofman Y.*, Gordon-Grossman M.*, Zimmermann H., Frydman V., Shai Y., Ben-Tal N., Goldfarb D. Melittin-membrane interactions: insight from pulse EPR and Monte Carlo simulations studies. *J Phys Chem B* **2009**, 113, 12687–12695.

Gofman Y.*, Shpak B.*, Shpak C., Hiller R., Boyman L., Khananshvili D. Effects of purified endogenous inhibitor of the Na^+/Ca^{2+} exchanger on ouabain-induced arrhythmias in the atria and ventricle strips of guinea pig. *Eur J Pharmacol* **2006**, 553, 196-204.

* - equal contributors.